Julius-Maximilians-Universität Würzburg

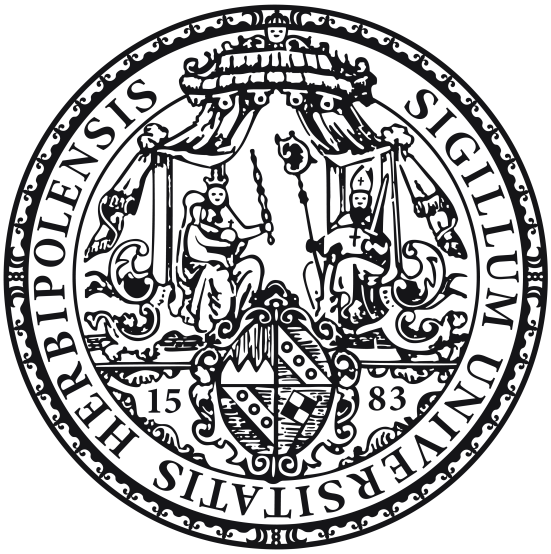

Structure and dynamics of the plasma membrane: a single-molecule study in *Trypanosoma brucei*

Die Struktur und Dynamik der Plasmamembran:
eine Einzelmolekülstudie in *Trypanosoma brucei*

Doctoral thesis

for a doctoral degree
at the Graduate School of Life Sciences

Section: Integrative Biology

submitted by
Marie Schwebs
from
Forchheim (Obfr.)

Würzburg, February 2022

Submitted on:

Members of the Thesis Committee

Chairperson:	**Prof. Dr. Christian Janzen** Department for Cell and Developmental Biology Julius-Maximilians-Universität Würzburg
Primary supervisor:	**Dr. Susanne Fenz** Department for Cell and Developmental Biology Julius-Maximilians-Universität Würzburg
Supervisor (second):	**Prof. Dr. Philip Kollmannsberger** Center for Computational and Theoretical Biology Julius-Maximilians-Universität Würzburg
Supervisor (third):	**Prof. Dr. Markus Engstler** Department for Cell and Developmental Biology Julius-Maximilians-Universität Würzburg
Supervisor (fourth):	**Prof. Dr. Matthias Weiss** Experimental Physics I Universität Bayreuth

Affidavit

I hereby confirm that my thesis entitled 'Structure and dynamics of the plasma membrane: a single-molecule study in *Trypanosoma brucei*' is the result of my own work. I did not receive any help or support from commercial consultants. All sources and/or material applied are listed and specified in the thesis.

Furthermore, I confirm that this thesis has not yet been submitted as part of another examination process neither in identical nor in similar form.

Date: _____ Signature _____

Eidesstattliche Erklärung

Ich erkläre hiermit an Eides statt, dass ich die vorliegende Dissertation „Die Struktur und Dynamik der Plasmamembran: eine Einzelmolkülstudie in *Trypanosoma brucei*“ eigenständig, d.h. insbesondere ohne die Hilfe oder Unterstützung von kommerziellen Promotionsberatern, angefertigt habe. Ergänzend bestätige ich, dass ich keine anderen als die von mir angegebenen Quellen oder Hilfsmittel verwendet habe.

Ich erkläre außerdem, dass diese Dissertation weder in gleicher noch in ähnlicher Form bereits in einem Prüfungsverfahren vorgelegen hat.

Datum: _____ Unterschrift _____

Abstract

The unicellular, flagellated parasite *Trypanosoma brucei* is the causative agent of human African sleeping sickness and nagana in livestock. In the last decades, it has become an established eukaryotic model organism in the field of biology, as well as in the interdisciplinary field of biophysics. For instance, the dense variant surface glycoprotein (VSG) coat offers the possibility to study the dynamics of GPI-anchored proteins in the plasma membrane of living cells. The fluidity of the VSG coat is not only an interesting object of study for its own sake, but is critically important for the survival of the parasite in the mammalian host. In order to maintain the integrity of the coat, the entire VSG coat is recycled within a few minutes. This is surprisingly fast for a purely diffusive process with the flagellar pocket (FP) as the sole site for endo- and exocytosis. Previous studies characterising VSG dynamics using FRAP reported diffusion coefficients that were not sufficient to to enable fast turnover based on passive VSG randomisation on the trypanosome surface.

In this thesis, live-cell single-molecule fluorescence microscopy (SMFM) was employed to elucidate whether VSG diffusion coefficients were priorly underestimated or whether directed forces could be involved to bias VSGs towards the entrance of the FP. Embedding the highly motile trypanosomes in thermo-stable hydrogels facilitated the investigation of VSG dynamics on living trypanosomes at the mammalian host's temperature of 37 °C. To allow for a spatial correlation of the VSG dynamics to the FP entrance, a cell line was employed harbouring a fluorescently labelled structure as a reference. Sequential two-colour SMFM was then established to allow for recording and registration of the dynamic and static single-molecule information.

In order to characterise VSG dynamics, an algorithm to obtain reliable information from short trajectories was adapted (shortTrAn). It allowed for the quantification of the local dynamics in two distinct scenarios: diffusion and directed motion. The adaptation of the algorithm to the VSG data sets required the introduction of an additional projection filter. The algorithm was further extended to take into account the localisation errors inherent to single-particle tracking. The results of the quantification of diffusion and directed motion were presented in maps of the trypanosome surface, including an outline generated from a super-resolved static structure as a reference. Information on diffusion was displayed in one map, an ellipse plot. The colour code represented the local diffusion coefficient, while the shape of the ellipses provided an indication of the diffusion behaviour (aniso- or isotropic diffusion). The eccentricity of the ellipses was used to quantify deviations from isotropic diffusion. Information on directed motion was shown in three maps: A velocity map, representing the amplitude of the local velocities in a colour code.

A quiver plot, illustrating the orientation of directed motion, and a third map which indicated the relative standard error of the local velocities colour-coded. Finally, a guideline based on random walk simulations was used to identify which of the two motion scenarios dominated locally. Application of the guideline to the VSG dynamics analysed by shortTrAn yielded supermaps that showed the locally dominant motion mode colour-coded.

I found that VSG dynamics are dominated by diffusion, but several times faster than previously determined. The diffusion behaviour was additionally characterised by spatial heterogeneity. Moreover, isolated regions exhibiting the characteristics of round and elongated traps were observed on the cell surface. Additionally, VSG dynamics were studied with respect to the entrance of the FP. VSG dynamics in this region displayed similar characteristics compared to the remainder of the cell surface and forces biasing VSGs into the FP were not found.

Furthermore, I investigated a potential interference of the attachment of the cytoskeleton to the plasma membrane with the dynamics of VSGs which are anchored to the outer leaflet of the membrane. Preliminary experiments were conducted on osmotically swollen trypanosomes and trypanosomes depleted for a microtubule-associated protein anchoring the subpellicular microtubule cytoskeleton to the plasma membrane. The measurements revealed a trend that detachment of the cytoskeleton could be associated with a reduction in the VSG diffusion coefficient and a loss of elongated traps. The latter could be an indication that these isolated regions were caused by underlying structures associated with the cytoskeleton.

The measurements on cells with an intact cytoskeleton were complemented by random walk simulations of VSG dynamics with the newly determined diffusion coefficient on long time scales not accessible in experiments. Simulations showed that passive VSG randomisation is fast enough to allow for a turnover of the full VSG coat within a few minutes. According to an estimate based on the known rate of endocytosis and the newly determined VSG diffusion coefficient, the majority of exocytosed VSGs could escape from the FP to the cell surface without being immediately re-endocytosed.

Zusammenfassung

Der einzellige, begeißelte Parasit *Trypanosoma brucei* ist der Erreger der humanen Afrikanischen Schlafkrankheit und Nagana bei Nutztieren. In den vergangenen Jahrzehnten hat er sich sowohl in der Biologie als auch im interdisziplinären Bereich der Biophysik als eukaryotischer Modellorganismus etabliert. So bietet der dichte *variant surface glycoprotein* (VSG) Mantel beispielsweise die Möglichkeit, die Dynamik von GPI-verankerten Proteinen in der Plasmamembran von lebenden Zellen zu untersuchen. Die Fluidität des VSG-Mantels ist nicht nur um ihrer selbst Willen ein interessantes Studienobjekt, sondern auch von entscheidender Bedeutung für das Überleben des Parasiten im Säugetierwirt. Damit die Integrität des Mantel erhalten bleibt, wird der gesamte VSG Mantel kontinuierlich innerhalb weniger Minuten ausgetauscht. Dies ist erstaunlich schnell für einen rein diffusiven Prozess, bei welchem die Geißeltasche (GT) der einzige Ort für Endo- und Exozytose ist. Bisherige Studien zur Charakterisierung der VSG Dynamik mit FRAP ermittelten Diffusionskoeffizienten, welche nicht ausreichten, um eine schnellen Austausch durch eine passive Randomisierung der VSG auf der Trypanosomenoberfläche zu ermöglichen.

In dieser Arbeit wurde die Einzelmolekül-Fluoreszenzmikroskopie (EMFM) an lebenden Zellen eingesetzt, um herauszufinden, ob die VSG Diffusionskoeffizienten zuvor unterschätzt wurden oder ob gerichtete Kräfte beteiligt sein könnten, um VSGs zum Eingang der GT zu leiten. Die Einbettung der hochmotilen Trypanosomen in thermostabilen Hydrogelen erlaubte die Analyse der VSG Dynamik auf lebenden Trypanosomen bei einer Temperatur des Säugetierwirts von 37 °C. Um eine räumliche Korrelation der VSG Dynamik mit dem Eingang zur GT zu ermöglichen, wurde eine Zelllinie verwendet, die eine fluoreszenzmarkierte Struktur als Referenz besaß. Anschließend wurde die sequnezielle EMFM in zwei Farben etabliert, um sowohl die Aufzeichnung als auch die Registrierung der dynamischen und statischen Einzelmolekülinformationen zu gewährleisten.

Um die VSG Dynamik zu charakterisieren, wurde ein Algorithmus zur Gewinnung von zuverlässigen Informationen aus kurzen Trajektorien adaptiert (shortTrAn). Dieser ließ die Quantifizierung der lokalen Dynamik anhand zweier unterschiedlicher Szenarien zu: Diffusion und gerichtete Bewegung. Die Anpassung des Algorithmus an die VSG Datensätze erforderte die Einführung eines zusätzlichen Projektionsfilters. Darüber hinaus wurde der Algorithmus erweitert, um die Lokalisierungsfehler zu berücksichtigen, die bei der Verfolgung von Einzelpartikeln unvermeidbar auftreten. Anschließend wurden die Ergebnisse der Quantifizierung von Diffusion und gerichteter Bewegung in Karten präsentiert, die die Trypanosomenoberfläche abbildeten, einschließlich eines Umrisses, der als Referenz aus einer hochaufgelösten statischen Struktur generiert wurde. Die Informationen zur Diffusion wurden in einer Karte, einem Ellipsenplot, dargestellt. Dabei repräsentierte eine

Farbkodierung die lokalen Diffusionskoeffizienten, während die Form der Ellipsen einen Hinweis auf das Diffusionsverhalten (aniso- oder isotrope Diffusion) gab. Die Exzentrizität der Ellipsen wurde hierbei genutzt, um die Abweichung von isotroper Diffusion zu quantifizieren. Die Informationen zur gerichteten Bewegung wurden in drei Karten wiedergegeben: Eine Karte für die Geschwindigkeit zeigte die Amplitude der lokalen Geschwindigkeiten farbkodiert. Ein Köcherplot veranschaulichte die Richtung der Geschwindigkeit und eine dritte Karte zeigte den relativen Standardfehler der lokalen Geschwindigkeiten farblich kodiert an. Abschließend wurde ein auf *Random-Walk*-Simulationen basierender Leitfaden herangezogen, um zu entscheiden, welches der beiden Szenarien lokal dominierte. Die Anwendung des Leitfadens auf die mit shortTrAn analysierte VSG Dynamik ergab Übersichtskarten, in denen der lokal dominierende Bewegungsmodus farblich kodiert war.

Ich konnte zeigen, dass die VSG Dynamik von der Diffusion dominiert wird. Jedoch war diese um ein Vielfaches schneller als bisher angenommen. Das Diffusionsverhalten war zudem durch eine räumliche Heterogenität charakterisiert. Des Weiteren wurden auf der Zelloberfläche isolierte Regionen beobachtet, die die Eigenschaften von runden und länglichen Fallen aufwiesen. Zusätzlich wurde die VSG Dynamik in Bezug auf den Eingang der GT untersucht. Die VSG Dynamik in dieser Region wies ähnliche Kennwerte auf wie die restliche Zelloberfläche, und es konnten keine Kräfte festgestellt werden, welche die VSGs in die GT dirigieren.

Des Weiteren habe ich den potentiellen Einfluss der Verankerung des Zytoskeletts an der Plasmamembran auf die Dynamik der VSGs untersucht, die in der äußeren Membranschicht verankert sind. Hierzu wurden vorläufige Experimente auf osmotisch geschwollenen Trypanosomen und Trypanosomen durchgeführt, denen ein Mikrotubuli assoziiertes Protein fehlte, welches das subpellikuläre Mikrotubuli-Zytoskelett an der Plasmamembran verankert. Bei den Messungen wurde ein Trend festgestellt, wonach die Ablösung des Zytoskeletts mit einer Verringerung des VSG Diffusionskoeffizienten und dem Verlust der länglichen Fallen korrelieren könnte. Letzteres könnte ein Hinweis darauf sein, dass diese isolierten Regionen durch darunter liegende, mit dem Zytoskelett verbundene Strukturen verursacht wurden.

Die Messungen auf Zellen mit intaktem Zytoskelett wurden durch *Random-Walk*-Simulationen von VSG Trajektorien mit dem neu ermittelten Diffusionskoeffizienten auf langen, experimentell nicht zugänglichen Zeitskalen ergänzt. Die Simulationen zeigten, dass die passive Randomisierung der VSGs schnell genug ist, um einen Austausch des gesamten VSG Mantels innerhalb weniger Minuten zu ermöglichen. Einer Schätzung zufolge, die auf der bekannten Endozytoserate und dem neu ermittelten VSG Diffusionskoeffizienten basierte, könnte der Großteil der exozytierten VSGs aus der GT zur Zelloberfläche gelangen, ohne unmittelbar wieder endozytiert zu werden.

Contents

1 Introduction

1.1 Background on single-molecule fluorescence microscopy

1.1.1 The way from basic light microscopy to single-molecule fluorescence microscopy

Biology, like all natural sciences, is based on observations. Observations raise questions, hypotheses are proposed to provide explanations, which are tested with experiments, and finally conclusions are drawn from the results to the original observation. In order to allow for observations on scales below the resolution of the human eye, a lens system for magnification had to be invented: the microscope. The importance of this new technology for natural scientists was confirmed by the famous work *Micrographia* by Hooke in 1665 with his detailed drawings of minuscule objects. However, it was Antony van Leeuwenhoek who systematically utilised microscopy for new discoveries. At that time, his own setup consisted of only one lens, but with a very strong resolving capacity. Thus, he was the first scientist to discover bacteria and protozoa in water droplets, which he called *animalcules* (van Leeuwenhoek, 1677). Herein, Antony van Leeuwenhoek is acknowledged as the father of microbiology. Since then, light microscopy has evolved and become one of the most widely used techniques in life sciences. Hereby, establishment of histological staining methods provided an important contribution to surpassing poor contrast by altering the light absorption capabilities of different cellular structures.

However, further discoveries were needed to lay the foundations for today's state of the art fluorescence microscopy. This includes the discovery of fluorescence. It was John Frederick William Herschel who discovered the fluorescent property of quinine sulphate in 1845 (Herschel, 1845). George Stokes investigated this phenomenon in more detail and already characterised fluorescence as the emission of light, which results from excitation by light (Stokes, 1852). Moreover, he observed that the absorption and the emission spectrum of a fluorophore diverged. This difference is nowadays well-known as Stokes shift. The emitted fluorescence exhibits a longer wavelength and thus less energy than the absorbed photon. Furthermore, he discovered a collection of fluorescent probes in the following years. The physical background of fluorescence was explained by Alexander Jablonski in 1935, which is illustrated by the Jablonski diagram shown in Figure 1 (Jablonski, 1935). Upon the absorption of light (hv_A), the fluorophores electrons are excited from the singlet ground state (S_0) to a higher vibrational/rotational level (0, 1, 2) of the first (S_1) or second (S_2) electronic state. This is followed commonly by rapid internal conversion

to the lowest vibrational level of S_1. The subsequent return to one of the vibrational energy levels of the electronic ground state is accompanied by the emission of fluorescence (hv_F). For this reason, the emission of light is accompanied by the loss of energy and therefore the spectrum is red-shifted, which explains the Stoke shift. The described process takes place in the regimes of several nanoseconds, which resembles the typical fluorescence lifetime values of fluorophores (Lakowicz, 2010). In addition, fluorophores in S_1 can undergo intersystem crossing by conversion to the first triplet state (T_1), which is followed by the emission of phosphorescence (hv_P). The time scales leading to phosphorescence are several orders of magnitude greater than that for fluorescence (Lakowicz, 2010). An example in which phosphorescence is exploited are *glow-in-the-dark* toys. The discovery that emission light is shifted into the long-wave range compared to absorption light is advantageously employed in fluorescence microscopy to separate perturbing excitation light from emitted light utilising dichroic mirrors.

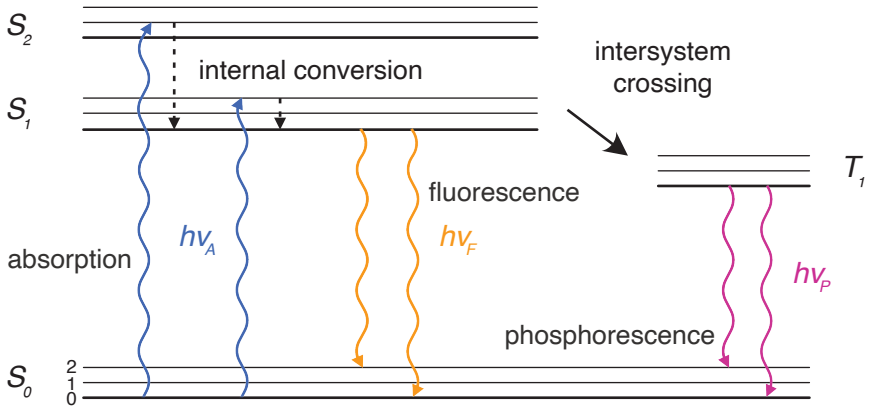

Figure 1: Scheme of a Jablonski diagram. It illustrates the processes from light absorption including transition in energetic and vibrational/rotational states to emission. The absorption of light (hv_A) results in the electrons of the fluorophore being excited from the singlet ground state to a level $(0, 1, 2)$ of the first (S_1) or second (S_2) electronic state. Internal conversion followed by return to a level of the singlet ground state leads to the emission of fluorescence (hv_F). Intersystem crossing to the triplet state (T_1) can occur which is then followed by the emission of phosphorescence (hv_P).

All developments up to this point have improved resolution and signal-to-noise ratio in fluorescence microscopy, but resolution to the smallest detail still remained elusive. This can be attributed to the physical diffraction limit of light which was described by George Airy in 1835 and later mathematically founded by Ernst Abbe in 1873. The diffraction limit according to Abbe is shown in Equation 1 (Abbe, 1873):

$$d = \frac{\lambda}{2 * n * sin\,\alpha} = \frac{\lambda}{2\,NA}. \tag{1}$$

He stated that the minimal resolvable distance d of two lines in a grating depends on the wavelength of light λ divided by 2 times the refractive index n multiplied the sine of the half-angular α of the objective. Alternatively, the nominator can be expressed as two times the numerical aperture (NA) of the objective. The numerical aperture of a modern immersion objective is typically 1.4 or higher. For self-emitting fluorescent objects, the diffraction limit should be calculated according to the heuristic Rayleigh criterion, which is described in Equation 2 (Rayleigh, 1903):

$$d = \frac{1.22}{2} * \frac{\lambda}{NA} = \frac{0.61\,\lambda}{NA}. \tag{2}$$

The equation is derived from Rayleigh's assumption on spatial resolution. It states that two point-like emitters can be distinguished from one another if the distance of both intensity maxima is equal to or greater than the radius of the Airy disk (Figure 2). The airy disk on the other hand is an interference pattern of a point like source. It exhibits a local intensity maximum in the centre which is surrounded by concentric rings of less intensity (Airy, 1835). Consequently, a resolution of 160 - 330 nm can be achieved for visible light (400 - 800 nm). However, if cellular processes occurring at the nanometre scale were of particular interest, it was impossible to study these until new techniques were available to circumvent the natural diffraction limit of light.

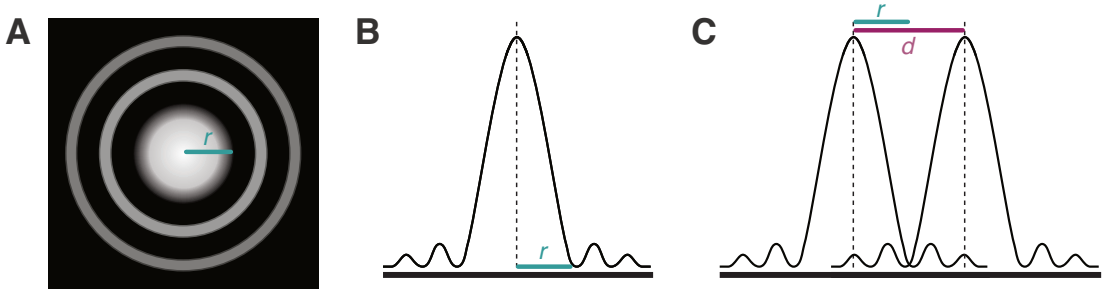

Figure 2: Illustration of the Rayleigh criterion. **A** Schematic representation of an airy disk of a point-like light source. The radius (r) of the airy disk is depicted by a cyan line. **B** Intensity profile of an airy disk with the radius shown by a cyan line. **C** Example of two light sources that fulfil the Rayleigh criterion as the distance (d, magenta line) between both intensity maxima is greater than the radius of the Airy disk (r, cyan line). Thus, the light sources can be distinguished from each other.

The most obvious approach to improve resolution is to exploit the dependency of resolution on wavelength. Implementation of this principle resulted in the development of electron microscopy. By using electron beams ($\lambda = 0.0037$ nm at 100 keV [1]) which are significantly shorter in wavelength compared to visible light ($\lambda = 400$ - 800 nm), structures below 1 Å are potentially resolvable. Nowadays, two types of electron mi-

[1] Reviewed by the University of Utah, Advanced Microscopy (2011). Electron Microscopy Tutorial. *https://advanced-microscopy.utah.edu/education/electron-micro/* (accessed in Dec. 2021)

croscopy have become the most widely used: scanning electron microscopy (SEM) and transmission electron microscopy (TEM). When one is interested in cellular structures within cells, TEM is the technique of choice. For instance, to study a protein of interest, sections of fixed preparations are required. The protein of interest is labelled with gold particles so its location in the cell can be examined. However, it is difficult to investigate a protein or even a lipid of interest whilst taking into account the surrounding molecules. In addition, preparation of specimens is extremely elaborate and time-consuming and the protein cannot be examined in living cells. Nevertheless, a combination of fluorescence microscopy and electron microscopy, correlative light and electron microscopy (CLEM), permits the possibility to study the protein of interest in the complex organisation of cells. It exploits the variety of highly specific fluorescent labelling methods in combination to the super-resolved cellular structures. However, this technique is also limited to the prerequisite of fixed samples.

Here, fluorescence microscopy offers a distinctive advantage, because if special chambers for living cells are used, molecules can be examined in living cells. Structures below the diffraction limit were first studied by fluorescence microscopy using structured light (Lukosz, 1966). However, it was single-molecule detection that led to the breakthrough of super-resolution fluorescence microscopy (Moerner and Kador, 1989; Orrit and Bernard, 1990; Shera et al., 1990). For this, the principle of isolating single emitters was exploited, which was already used to study single-molecule dynamics. Two approaches have been established that use either stochastic or deterministic procedures for the detection of individual molecules.

Stimulated emission depletion (STED) is considered as a deterministic method and was developed in the 1900s (Hell and Wichmann, 1994). As an adaption of confocal laser scanning microscopy (CLSM), a doughnut shaped depletion beam is additionally used to the excitation beam to narrow the emission spot. The final obtained fluorescence from the centre of the object is below the diffraction limit. This allows single molecule positions to be determined down to 20 nm without requiring fitting-based single molecule localisation. The highest resolution of up to $\sim 1\,\mathrm{nm}$ available today is provided by a fluorescence microscopy method that also originates from the Hell laboratory. MINFLUX probes the emitter with a local intensity minimum of excitation light (Balzarotti et al., 2017).

The stochastic approach separates the emission patterns spatiotemporally in a densely labelled sample. For this purpose, the active-on and inactive-off state of the fluorophores are exploited that can be initiated by photoconversion, photoswitching, and photoactivation. This allows for recording isolated but diffraction limited spots. The emitter's localisation can then be determined using algorithms with a better

resolution than the Abbe limit. Single emitters are collected over a period of time and a high-resolution image of the structure is reconstructed with a resolution of ~25 nm. To eventually completely resolve a structural feature, the distance between two emitters needs to be less than half the feature size as stated by the Nyquist-Shannon theorem (Shannon, 1949). There are two techniques, which are mainly distinguished by the fluorophores used: Synthetic organic fluorophores are utilised in direct stochastic optical reconstruction microscopy (dSTORM) (Heilemann et al., 2008) and STORM (Rust et al., 2006), while fluorescent proteins are used in photoactivated localisation microscopy (PALM) (Betzig et al., 2006; Hess et al., 2006). Both techniques were developed in the early 2000s. Development of PALM is based on the discovery of GFP (Shimomura et al., 1962), its cloning (Chalfie et al., 1994), and characterisation (Ormö et al., 1996). Chemical modification of GFP (Patterson and Lippincott-Schwartz, 2002) yielded a photoactivatable variant and eventually allowed it to be used in a wide and versatile range of scenarios. Furthermore, the intrinsic blinking behaviour of GFP at high illumination intensities (photoswitch) can be exploited (Dickson et al., 1997; Zhou and Lin, 2013) to separate individual GFP molecules even without the use PALM. The importance of the discovery of GFP was acknowledged in 2008 with the award of the Nobel Prize.

1.1.2 Fluorescent labelling strategies

The progress in microscopy was accompanied by a development of new labelling methods, which were additionally necessary to increase the accuracy of measurements. In conventional fluorescence microscopy, the first fluorescent labels were fluorophore-labelled antibodies and are still used today. An immunoglobulin G (IgG) has a molecular weight and size of ~148 kDa and 10 - 15 nm. Thus, the size of the IgG alone induces a significant label uncertainty between the fluorophore and the protein of interest, leading to an erroneous localisation, especially in single-molecule measurements. A good alternative for immunostaining with a reduced linkage error are nanobodies. Nanobodies are single-domain antibodies and substantially smaller than IgGs with ~14 kDa and a size of ~2.5 - 4 nm (Harmsen and De Haard, 2007). When labelling intracellular structures with antibodies or nanobodies, the cells require fixation and membrane permeabilisation to access the target protein. Microscopy in living cells is therefore limited to the labelling of extracellular or membrane proteins. The endogenous expression of GFP or one of its derivatives offers the great advantage that live-cell imaging is possible and the strict 1:1 stoichiometry allows for quantification of traget molecules. In addition, GFP is significantly smaller than antibodies with ~27 kDa and the dimensions of the barrel are 4.2 nm in length and 2.4 nm in diameter (Ormö et al., 1996). Nevertheless, the size of the fluorescent protein can impair the physiological function of the tagged protein (Rodriguez

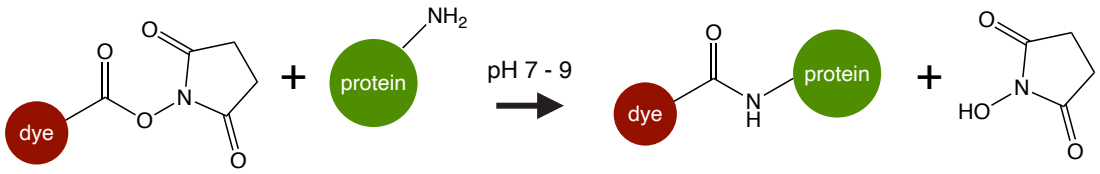

Figure 3: Reaction scheme of NHS-ester based protein labelling. The NHS group of a fluorescent dye reacts with a primary amine of a target protein. Reaction takes place at pH 7 - 9 and results in a stable, covalent bond.

et al., 2017) due to steric hindrance. That is why, synthetic, organic fluorophores are often favoured because of their small size, increased brightness, and photostability. Depending on their chemical properties, these can be membrane permeable and suitable for live-cell experiments. Different strategies can be pursued for labelling the protein of interest with synthetic dyes. The incorporation of SNAP- (~ 20 kDa) and Halo-tags (~ 33 kDa), so-called protein tags, enables specific binding. An endogenous labelling sequence expressed together with the protein of interest is combined with an organic fluorophore having a compatible binding sequence, enabling for instance long-time observations. The endogenous binding sequence restricts the linkage error to a few nanometres, but can also perturb the function of the tagged protein. In order to achieve the smallest label uncertainty, conjugated organic fluorophores are preferentially used to label proteins. Here, small conjugated fluorophores possess a functional group such as a maleimide or NHS (N-hydroxysuccinimide) group, which target suitable reactive groups like primary amines or thiol groups at the protein. The reaction of an NHS-functionalised dye with a primary amine is shown in Figure 3. This allows for direct labelling and is preferably used for *in vitro* labelling in purified protein samples. Specific labelling of a protein of interest using conjugated fluorophores in crowded cellular environments is usually difficult and requires specific conditions, like an excessive abundance of the protein in relation to the other cellular molecules. Labelling methods introduced here represent only a selection of existing labelling methods and fluorophores and are reviewed in Terai and Nagano (2013), Rodriguez et al. (2017), and Lelek et al. (2021). Selection of the appropriate fluorophore and the associated labelling method has to be chosen specifically for each experimental set-up and the addressed biological question.

1.1.3 Single-molecule localisation, tracking and its limitations

To investigate structures or dynamics with single-molecule microscopy, a large number of consecutive image series of diffraction limited, blurred spots are recorded. Blurring can be characterised by the point spread function (PSF). In turn, the PSF of each microscope describes how a single molecule emitter appears in an image

acquired by the microscope. To extract the precise position of the emitter, the local intensity maximum of the emitter is determined by image processing. In order to determine the exact position of the intensity maximum, a sufficient number of photons is required to achieve a good signal-to-noise ratio (Bobroff, 1986). Two categories of noise sources exist. The first noise source is associated with the camera and includes the dark current noise, the usually negligible read-out noise and the multiplicative noise from stochastic amplification of photoelectrons (Quan et al., 2010; Chao et al., 2013). The second noise source is associated with the sample, such as cell autofluorescence and out-of-focus signals (Deschout et al., 2014). Additionally, the finite number of photons limits the determination of the precise position and is leading to Poisson noise. The precision in detection is quantified by the localisation precision σ, which can be particularly well visualised for immobile emitters. There are multiple approaches to determine σ, e.g. from the error of the x- and y-position in the Gaussian fit, from theory (Ober et al., 2004), and from the standard deviation in the x- and y-position of an immobile emitter (Manzo and Garcia-Parajo, 2015).

In recent decades, robust tracking algorithms have been developed for measuring the dynamics of individual moving particles in consecutive image sequences, generating trajectories from the single-molecule localisations (Schmidt et al., 1996; Manzo and Garcia-Parajo, 2015). The rapid development of algorithms also permits the tracking of particles with an exceptionally high diffusion coefficient (Semrau et al., 2011), in an environment with a high particle density or with heterogeneous dynamics (Slator et al., 2015). Fundamentally, classical tracking is based on calculating probabilities that particle m in image i is particle n in image j which are then maximised. Subsequently, trajectories can be analysed in detail to study the dynamics of the single molecules. Usually it includes the determination of a diffusion coefficient or the velocity of a single particle or a set of particles.
The mean-squared displacement (MSD) is regularly used to characterise the single-molecule tracking data and to derive a diffusion coefficient. The relation of the diffusion coefficient to the MSD is defined in $1D$ as follows:

$$2D = \frac{MSD}{\Delta t} \tag{3}$$

with Δt indicating the time lag between the consecutive images. The definition of the MSD in $1D$ is:

$$MSD(n\Delta t) = \frac{1}{N-n} \sum_{i=1}^{N-n} (x_{i\Delta t+n\Delta t} - x_{i\Delta t})^2 \tag{4}$$

with N denoting the number of consecutive steps at a time lag $n\Delta t$, x the position of a particle within the trajectory at a time t, and Δt the smallest time interval resolved. The MSD is calculated for each dimension separately and by adding up

the two-dimensional MSD can be derived. Subsequently, the MSD is determined for each trajectory and averaged to derive the population MSD as a function of time. However, to obtain statistically relevant results from the MSD analysis, only the first 10 - 20 % of the time lags of each trajectory should be included for the derivation of the diffusion coefficient or a motion model, as the error in the MSD increases with increasing time lags (Qian et al., 1991). If the MSD is plotted as a function over time, the diffusion coefficient can be determined from the slope of the fit. If the tracking algorithm yields a large number of long trajectories, the $MSD\,vs\,\Delta t$ plot can be interpreted as a reliable indicator of the motion type (Figure 4). It is Brownian motion, if the plot results in a straight line. Is the MSD increasing sub- or supralinear additional contributions as confined diffusion or active transport have to be considered. Alternatively, the distribution of the $1D$ steps can be employed to conclude on the type of motion. Free diffusion can be assumed from a Gaussian distribution.

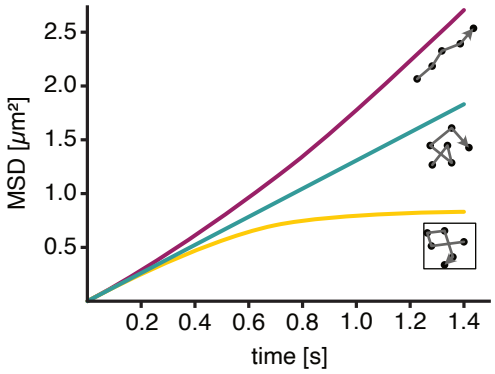

Figure 4: Illustration of different motion types in MSD plots. A linear plot (cyan line) represents Brownian motion. A supralinear MSD curve (magenta line) can arise from directed, active motion of a particle, whereas a sublinear MSD progression indicates restricted particle motion within a given area (yellow line).

Analogous to single-molecule localisation, tracking suffers from sampling errors due to the single-molecule technique. These are known as the (i) static and (ii) dynamic localisation error and affect the measured MSD (Savin and Doyle, 2005). Both errors also will have an impact on the diffusion coefficient if it is derived from a single MSD value instead of the slope of the fit to the MSD curve. (i) The source of the static localisation error is the limited localisation precision σ. This error was already recognised two decades ago in the community and considered in the calculation of the one-dimensional MSD as $MSD_{stat\_corr} = MSD - 2\sigma^2$ (Martin et al., 2002; Savin and Doyle, 2005; Backlund et al., 2015). Thus, the static localisation error adds a constant offset to the real MSD. If the diffusion coefficient is determined from a single MSD value, the diffusion coefficient is consequently overestimated especially at small time lags and diffusion coefficients if it is not corrected for ($D_{stat\_corr} < D$). (ii) The dynamic localisation error originates from

the exposure time required to collect enough photons from a single emitter. Hence, a moving emitter is imaged at positions averaged over the exposure time. The dynamic localisation error can be corrected by adjusting the effective time point of the localisation: $\Delta t_{dyn\_corr} = \Delta t - \frac{1}{3}\frac{t_{exp}}{\Delta t}t_{exp}$ with t_{exp} indicating the exposure time (Savin and Doyle, 2005; Berglund, 2010; Michalet and Berglund, 2012; Backlund et al., 2015). In contrast to the static localisation error, the dynamic localisation error leads to an underestimation of the diffusion coefficient, if it is not considered properly ($D_{dyn\_corr} > D$). Including both error corrections in the calculation of the one-dimensional diffusion coefficient as a function of the MSD stated by Equation 3 yields Equation 5:

$$2D = \frac{MSD - 2\sigma^2}{\Delta t - \frac{1}{3}\frac{t_{exp}}{\Delta t}t_{exp}} \tag{5}$$

Both errors have the largest impact on $MSD(\Delta t = 1)$ and $D(\Delta t = 1)$, as the share of errors decreases with increasing time lags. In conclusion, the two errors have an inverse impact on the measured MSD and diffusion coefficient. It is worth noting that the relative contribution of both errors is unique to each experimental set-up and thus, the errors as well as their effect must be determined for each experiment.

1.2 Evolution of the membrane model

Microscopy has become an important tool in today's research. It has been and still is of crucial relevance in the study of the plasma membrane of cells. This includes the elucidation of the structure and the composition of the plasma membrane, interactions of the individual components as well as studies on the dynamics of components. The following section provides an overview of how the view on the plasma membrane has evolved over the last decades.

In general, plasma membranes consist of two main components, lipids and proteins. Lipids possess a hydrophilic head with a hydrophobic tail consisting of two fatty acid chains. In the conserved lipid bilayer, the lipids are oriented to form a hydrophobic core with the hydrophilic heads pointing outwards. Membrane-embedded proteins can be categorised into peripheral, lipid-anchored, and integral proteins which also include transmembrane proteins. Both components work together to fulfil the various functions of the membrane, which can be broken down to four basic functions: (i) Separation by forming a semi-permeable diffusion barrier, (ii) exchange, e.g. of metabolites and macromolecules from inside and outside the cell, (iii) integration of cells into cell populations or higher organisations like tissues, including cell adhesion and receptor-mediated signalling, and (iv) participation in the metabolism, such as harvesting and conversion of cellular energy (Buehler, 2016).

Georg Quincke was the first to postulate the plasma membrane is of a lipid nature. In 1888, he observed that a cell behaves like oil when broken into two parts and described it as a liquid layer of fat less 100 nm thin (Quincke, 1888; Loeb, 1904). Independently, Hans Horst Meyer and Ernest Overton reported that anesthetics can overcome the cell barrier if they are soluble in oil and in water (Meyer, 1899, 1901; Overton, 1901). This supported the hypothesis of membranes consisting of lipids. The origin of the assumption of a bilayer organisation was set by an experiment by Evert Gorter and François Grendel. To this end, the scientists isolated the membrane of erythrocytes and determined the area covered by the extract when spread on a water surface in a Langmuir trough (Gorter and Grendel, 1925). They calculated that the number of extracted lipids would be sufficient to cover twice the measured area. Although their calculation contained a number of errors that canceled each other out, they correctly concluded that the membrane consisted of a lipid bilayer.

At the same time, the model of Gorter and Grendel could not provide answers to the questions of surface tension, permeability and electrical resistance of cell membranes, which led to scepticism. Hugh Davson and James Danielli assumed that membrane proteins mediate the before mentioned properties in a membrane. In 1935, they proposed an extended hypothesis that the plasma membrane consists of

a lipid bilayer covered by a thin protein layer on either side resulting in a trilaminar architecture of the plasma membrane (Danielli and Davson, 1935).
The invention of electron microscopy enabled scientists to view the plasma membrane in its details for the first time. Electron microscopy images showed a trilaminar appearance of the plasma membrane (Robertson, 1957, 1967), which J. David Robertson interpreted as a support for the model by Danielli and Davson. However, Stoeckenius was able to explain and illustrate how the lipid bilayer resulted in a trilaminar appearance. He pointed out that the inner and outer areas of the lipid membrane are stained to different intensities due to their different compositions (Stoeckenius, 1962).

In 1972, S. Jonathan Singer and Garth Nicolson postulated a new model that reconciled the key features of the previous discoveries: the fluid mosaic model (Singer and Nicolson, 1972). It views the plasma membrane as homogenous, equilibrated lipid bilayer in which a variety of integral, peripheral or lipid anchored proteins are randomly distributed (Figure 5). This composition gives the membrane the appearance of a mosaic. In the model, membranes are also considered as dynamic structures and lipids as well as proteins are able to move laterally in the membrane.

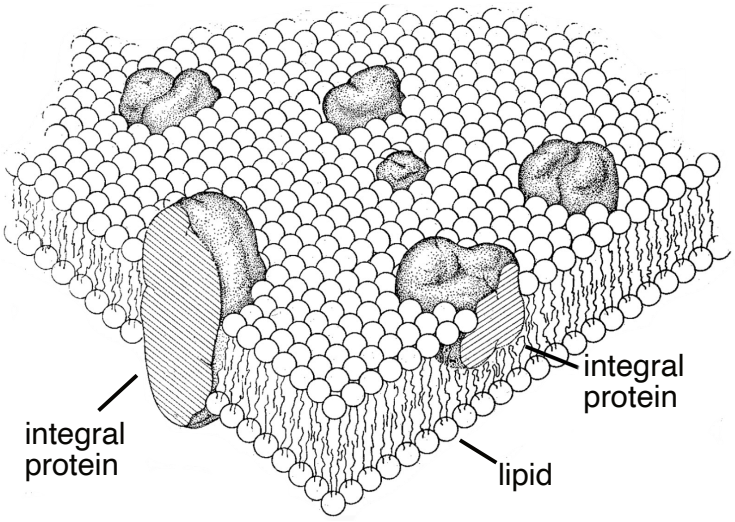

Figure 5: Scheme of the fluid mosaic model introduced by Singer and Nicolson. It shows a three-dimensional, cross-sectional view of the lipid matrix with embedded integral proteins (black stippled and/or striped). Lipids are depicted by their circular head and two jagged lines indicating the fatty acids. Adapted and modified from Singer and Nicolson (1972).

Since the proposal, the understanding of the lipid and protein composition, their interactions in the plasma membrane as well as the interactions with the underlying cytoskeleton or the extracellular matrix of living cells have considerably improved. Today we know that the membrane does not only consist of a large number of a few lipids, but rather a large variety of a hundred different lipids. In addition, thousands of different protein components exist that are densely packed in the membrane (reviewed in Buehler (2016)). The leaflets of the membranes are not in an

equilibrated state either, instead a trans-bilayer asymmetry is actively maintained by transporters (van Meer et al., 2008).

The organisation as well as the dynamics of the lipids were studied, for example, by employing artificial membranes on glass or as giant unilamellar vesicles (GUVs) (Baumgart et al., 2003; Veatch et al., 2008). Depending on the composition and concentration of the used lipids, a phase separation on meso- and nanoscales can be observed. Hereby, the membrane shows two states: lipid disordered and lipid ordered. The latter are termed lipid rafts or lipid domains which were precisely defined by the Keystone Symposium on Lipid Rafts and Cell Function in 2006 as follows: *"Membrane rafts are small (10–200 nm), heterogeneous, highly dynamic, sterol- and sphingolipid-enriched domains that compartmentalize cellular processes. Small rafts can sometimes be stabilized to form larger platforms through protein-protein and protein-lipid interactions."* (Pike (2006), p. 1597). However, the existence of lipid domains in living cells is controversially discussed. Biological membranes consist of a complex mixture of lipids and therefore the estimation of the phase state is difficult. It is implied that the domains can create a sorting or signalling platform by enriching other membrane components via their affinity to them (Simons and Van Meer, 1988; Simons and Toomre, 2000; Sezgin et al., 2017). Furthermore, some proteins harbour lipid-binding motifs that can, for example, regulate their membrane distribution. One such example is the HIV glycoprotein gp41 having cholesterol-binding motifs (Schwarzer et al., 2014). More on the lipid-protein interaction can be found in the reviews Lee (2003), Lee (2011), and Corradi et al. (2019).

Lateral movement of membrane components was initially postulated to be free diffusion. Today, we know that membrane-associated proteins have different modi of diffusion, including simple Brownian motion, confined diffusion and anomalous diffusion. Kusumi and his colleagues showed with high-speed single particle tracking that different modi can be observed for phospholipids and membrane-associated proteins (Kusumi et al., 2011, 2012). They investigated the dynamics of transmembrane proteins, glycosylphosphatidylinositol (GPI)-anchored proteins and phospholipids. The components under investigation exhibited a dependency of diffusion time scales on observation area which did not scale to the expecting simple Brownian motion. The scientists monitored large diffusion coefficients in compartment sizes of less than hundred nanometres, while at the micrometer scale diffusion coefficients were found to be an order of magnitude smaller (Kusumi et al., 2011).
This observation resulted in the development of the hop diffusion model. It implies that molecules in a compartment undergo fast diffusion, but are limited by barriers. To make a transition to the next compartment, the membrane molecule has to hop. For its explanation, the anchored picket fence model of the plasma membrane was proposed by Kusumi et al. (2012) which is shown in Figure 6. It states

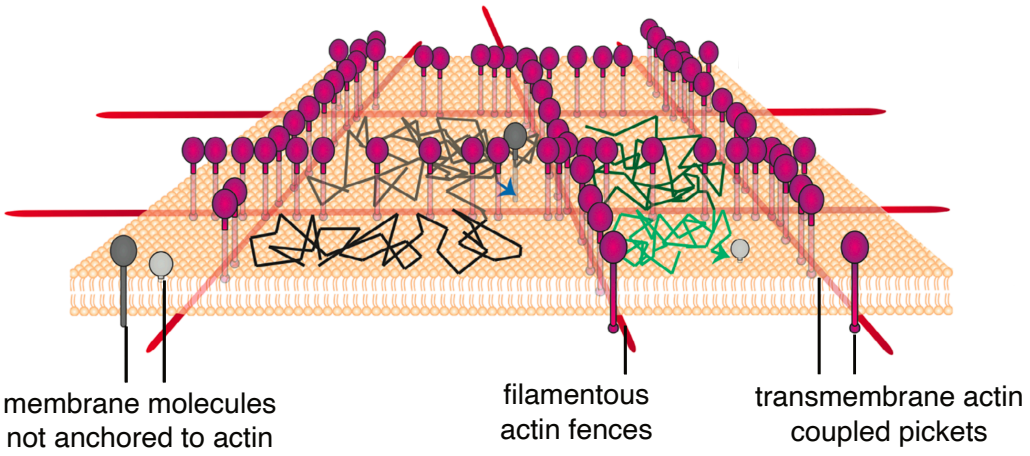

Figure 6: Illustration of the anchored picket fence model stated by Kusumi. A membrane patch of 0.5 x 0.5 µm is displayed. The actin fences (cytoskeleton) are depicted in red and transmembrane actin coupled pickets in magenta. Membrane molecules which are not anchored to the cytoskeleton are shown in grey and light grey. Dynamics of not anchored molecules are illustrated by a black to grey and dark green to green line, while each colour is indicating confined diffusion. Adapted and modified from Kalappurakkal et al. (2020).

that transmembrane proteins (pickets, e.g. actin-binding proteins) are anchored by binding to the underlying cytoskeleton (fences, e.g. cortical actin filaments). The pattern of the cytoskeleton meshwork (fences) is then transferred to the membrane by the transmembrane proteins (pickets), creating compartments. Membrane particles can diffuse freely in the compartment but will collide with the pickets resulting in confined diffusion. To cross the barrier, particles can undergo hop diffusion.

Other studies on the organisation of lipid-anchored proteins indicate a nanoscale organisation which often depends on the cytoskeleton (Plowman et al., 2005; Goswami et al., 2008). However, these cannot be explained by the anchored picket fence model alone. This resulted in the development of the active actin-membrane composite model, which is reviewed in Kalappurakkal et al. (2020). It characterises the cell surface as a composite of a multicomponent plasma membrane resting on a multicomponent cytoskeleton. It considers the dynamics of the cytoskeletal network itself and accounts for the energy-consuming remodelling work, such as the cortical actin-localised acto-myosin-driven processes, in maintaining the non-equilibrated distribution of components in the cell membrane. Furthermore, it adds the possibility that chemical signals are involved in regulation of the remodelling. More generally, the membrane components can be categorised as (i) inert, (ii) passive and (iii) active on the basis of their interaction with the cytoskeleton (Figure 7). (i) Inert components can diffuse randomly in the membrane and do not interact with the underlying cytoskeleton (Figure 7 A). (ii) Passive components are, for example, transmembrane proteins with a cytoskeletal binding domain or GPI-anchored proteins

that affect organisation due to transbilayer interactions, also called interleaflet coupling (Figure 7 B). The latter can be exemplified by the study of Raghupathy et al. (2015). They reported on the interaction of long-chain GPI-anchored proteins with nanodomains of phosphatidylserine in the complementary leaflet in Chinese hamster ovary cells, which in turn were associated with connector proteins of the actin cytoskeleton. (iii) Active components, on the other hand, trigger a signalling cascade through activation by a chemical signal, which in turn triggers the acto-myosin machinery that acts as a template for nanoclusters (Figure 7 C).

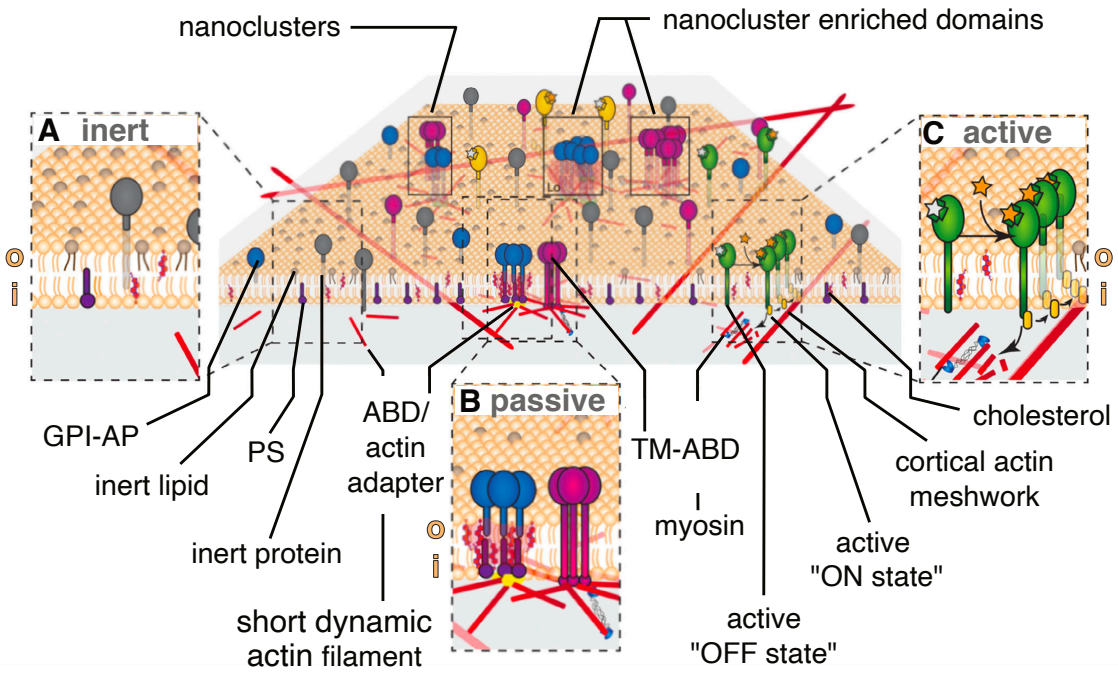

Figure 7: Scheme of the active actin-membrane composite model. Enlarged sections display the three categories of membrane components based on the interaction with the underlying actin cytoskeleton: inert (**A**), passive (**B**), and active (**C**). ABD, actin binding domain; AP, anchored protein; GPI, glycophosphatidylinositol; i, inner leaflet of the plasma membrane; PS, phosphatidylserine; o, outer leaflet of the plasma membrane; TM, transmembrane; Adapted and modified from Kalappurakkal et al. (2020).

In addition to the contact to the interior of the cell, the membrane is also in constant contact with the external environment, such as the extracellular matrix. Considering that the extracellular matrix has binding sites for cell adhesion receptors or that lectins like multivalent Galectins can guide the organisation of glycosylated proteins (Garner and Baum, 2008; Lakshminarayan et al., 2014), it is quite likely that the extracellular matrix and the glycocalyx of the cell also influence the organisation of the cell membrane. Furthermore, the signal transduction pathway via receptors into and out of the cell has a high potential to impact the local membrane organisation.

Since the introduction of the fluid mosaic model by Singer and Nicolson, we have continuously developed our knowledge about the organisation of the cell membrane.

Today we know that the membrane of living cells is highly organised and the interactions with adjacent structures such as the cytoskeleton or the extracellular matrix are intricate. Quoting Kalappurakkal et al. (2020) from their review: *"there's (always) more to this than meets the eye"*.

The cell membrane's link to cellular processes as well as its involvement in signal transduction makes cell membrane proteins a target for therapeutic treatment of diseases in medicine. Membrane-associated proteins can also be implicated in evading the host immune response and facilitating the survival of parasites in the host. An example of this is the eukaryotic parasite *Trypanosoma brucei*, which is discussed in more detail in the following section.

1.3 *Trypanosoma brucei*

1.3.1 African trypanosomes are the causative agent of African Sleeping sickness

Trypanosoma brucei (*T. brucei*) is a unicellular, eukaryotic parasite belonging to the order of Trypanosomatida in the class Kinetoplastida (Fernandes et al., 1993). The class is characterised by the existence of a kinetoplast, a structure containing the mitochondrial DNA (d'Avila Levy et al., 2015). The flagellated parasites are transmitted by the bite of the tsetse fly vector (*Glossina* spp.) and infect a variety of vertebrate hosts. During their life cycle, the African trypanosomes are exclusively extracellular. The geographic distribution of the flagellated parasite is limited by the habitat of the tsetse fly vector to sub-Saharan Africa.

In the fly, five different stages are known to exist. After ingestion of parasites during a blood meal, trypanosomes develop in the midgut of the tsetse fly into proliferative procyclic forms (PCFs). In parallel with the migration in the vector from the posterior midgut to the salivary glands through the proventriculus, the PCFs differentiate into cell cycle arrested mesocyclic cells and subsequently into long epimastigote forms. In the salivary glands, the long epimastigote forms divide asymmetrically, which produces a long and a short daughter cell (Van Den Abbeele et al., 1999; Sharma et al., 2008). The short epimastigote form attaches to the epithelium of the glands and produces by asymmetric division mammalian-infective, cell cycle-arrested metacyclic forms (Rotureau et al., 2012). During a blood meal this infective parasite form is then transmitted back to the vertebrate host and establishes infection. In the vertebrate host, in contrast, there are two forms: The slender trypomastigote, also known as bloodstream form (BSF), and the stumpy form trypomastigote. The BSF is the proliferative stage and is responsible for the level of parasitemia. If the parasite population reaches a certain density, BSF trypanosomes differentiate upon the quorum sensing factor *stumpy inducing factor* (SIF) into stumpy forms (Seed and Sechelski, 1989; Reuner et al., 1997; Vassella et al., 1997). Stumpy cells are cell cycle-arrested and die within 2 - 3 days after differentiation unless they are taken up by the fly (MacGregor et al., 2011). In the fly stumpy cells can develop to procyclic forms and infect the tsetse fly. Stumpy forms were thought to be the only mammalian host-related form to infect the tsetse fly (Fenn and Matthews, 2007). Schuster et al. (2017) showed that also BSF trypanosomes could establish infections. During their life cycle, trypanosomes are exposed to a variety of different environmental conditions. This includes the change in temperature from 27 °C in the vector to 37 °C in the vertebrate host. In addition, the pH value of the environment changes and the available nutrients differ. To survive in the mammalian host, the parasite switches its energy metabolism from oxidative phosphorylation in the

insect vector to glycolysis in the host (reviewed in Bringaud et al. (2006); Tielens and van Hellemond (2009)).

In the vertebrate host, the parasite causes the diseases African sleeping sickness in humans and Nagana in livestock. Nagana is caused by the prevalent subspecies *T. brucei brucei*, *T. congolense*, and *T. vivax* (Rotureau and Van Den Abbeele, 2013). In contrast, human African trypanosomiasis is caused by *T. brucei rhodesiense*, and *T. brucei gambiense*, which can survive in the bloodstream of the human host. This is due to their resistance to human trypanolytic factor (TLF), which is a combination of apolipoprotein L1 (APOL1) and a haptoglobin-related protein (HPR). TLF circulates in the blood as innate immune effector, opposing the trypanosomes by lysis (Perez-Morga et al., 2005; Wheeler, 2010).

Symptoms of the diseases were already recorded before the colonial period. But it was not until 1857 that David Livingstone discovered that a bite from the tsetse fly causes the disease Nagana (Livingstone, 1857). Another 40 years later, it was Sir David Bruce who identified trypanosomes as causative agents in the blood of infected animals (Bruce, 1895). His observation was honoured with the naming *Trypanosoma brucei* spec. It was shortly thereafter that the bite of the tsetse fly and an infection with trypanosomes were linked to human African trypanosomiasis (HAT) (Dutton, 1902; Kleine, 1909).
Progression of HAT occurs in two steps: (i) an hemolymphatic stage which is followed by (ii) a meningoencephalitic stage. (i) After transmission of trypanosomes by the bite of the tsetse fly, the parasites spread in the blood, lymph and various tissue spaces, causing headache, fever, joint pains and shivering. (ii) Once the parasites cross the blood-brain barrier and reside in the brain and central nervous system, the patient is in the second stage. Symptoms associated with the disease emerge, such as a disturbed sleep cycle, which gave the disease its name. Eventually, the patient falls into a coma and dies (Kennedy, 2013). Infections with *T. brucei rhodesiense* have an acute and severe progression, characterised by the infection of the central nervous system within a few weeks and leading to death after a few months (Brun et al., 2010). Infections with *T. brucei gambiense*, on the other hand, are chronic and can last for years (Brun et al., 2010).

Vector control with combined surveillance and treatment of the disease, have reduced annual case numbers of HAT from 25,000 reported cases in 2000 to 1,000 cases in 2018 (Franco et al., 2020). To this day, animal African trypanosomiasis is fatal to many domesticated animals and causes $ 4.5 billion in damage annually to the African economy, livestock and agricultural sectors (Kimaro and Abiola, 2021).

1.3.2 Cell architecture and cell cycle

T. brucei brucei is the most widely studied subspecies and exhibits a high similarity to human-infective trypanosomes.

Trypanosomes have a highly polarised cell structure in which the organelles occupy distinct positions (Figure 8). Cell shape is defined by the highly polarised microtubule skeleton with the minus end facing the anterior part of the cell and the plus end facing the posterior end (Robinson et al., 1995). The sub-pellicular corset of microtubules is regularly spaced, linked to each other as well as to the overlying plasma membrane (Hemphill et al., 1991). Trypanosomes in the mammalian host are covered by a dense coat of glycosylphosphatidylinositol (GPI)-anchored variant surface glycoproteins (VSGs), which provide a protective barrier on the plasma membrane. Similar to other eukaryotes, trypanosomes possess the following organelles: a nucleus, a single mitochondrion, a Golgi apparatus, an endoplasmic reticulum, endosomes and lysosomes. Moreover, mitochondrial DNA is organised in a structure called the kinetoplast. It is located next to the flagellar pocket (FP) at the posterior end and is physically connected to the flagellum by the basal body. The basal body is, for instance, involved in the segregation of the mitochondrial genome (Robinson and Gull, 1991). The FP is a membrane invagination at the posterior end. At the same time, it is the only site for endo- and exocytosis (Overath and Engstler, 2004) and the exit site of the single flagellum. The flagellum extends along the longitudinal axis of the cell body to the anterior end. Its exterior part is attached to the cell body by the flagellum attachment zone and it has a free distal tip at the anterior end (Taylor and Godfrey, 1969). The flagellum is characterised by two structures (Gull, 1999): The paraflagellar rod (PFR), a lattice-like filament, and the axoneme.

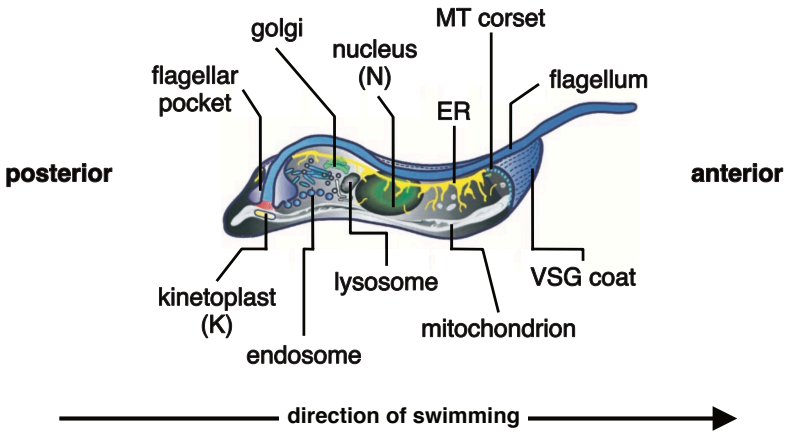

Figure 8: Scheme of the cell architecture of *T. brucei*. It shows a bloodstream form (BSF) trypanosome including the major organelles and their respective cellular location. ER, endoplasmic reticulum; MT corset, microtubule corset; VSG, variant surface glycoprotein; Adapted and modified from Grünfelder et al. (2003).

The PFR is physically connected to the axoneme, which contains an in eukaryotes conserved, canonical arrangement of '9+2' microtubules. For the motility the PFR as well as the axoneme are essential (Bastin et al., 1998, 1999, 2000; McKean et al., 2003) and lead to a helical propulsion in anterior direction (Rodriguez et al., 2009). The flagellar beat can accelerate *T. brucei* to speeds of up to 42 µm/s with a tip-to-base beat frequency of ~20 Hz (Heddergott et al., 2012; Bargul et al., 2016). The motility of the parasite is crucial for its viability (Broadhead et al., 2006), infection of the mammalian host (Shimogawa et al., 2018), its morphogenesis (Kohl et al., 2003), and cell division (Kohl et al., 2003; Ralston et al., 2011).

The cell cycle is precisely timed and can be characterised by the replication of key structures and their distribution to daughter cells (Figure 9). The coordinated process starts with the duplication of the basal body, which acts as a nucleation site for the newly synthesised flagellum (Sherwin and Gull, 1989; Lacomble et al., 2010). The growing daughter flagellum follows precisely the old flagellum and thus transfers the structural information from the old flagellum to the new flagellum (Moreira-Leite et al., 2001). At the same time, the replicated mitochondrial DNA is segregated in the S phase of the cell cycle, resulting in an elongated, v-shaped kinetoplast (1K^{v}1N). The division of the kinetoplast invariably precedes that of the nucleus (2K1N) and characterises cells in the G2 phase. The nuclear DNA is replicated in the G2 phase and separated in the M phase without disassembly of the nuclear envelope, which is termed closed mitosis (Ogbadoyi et al., 2000). After complete separation (post M phase), the cell has two kinetoplasts and two nuclei (2K2N). Cytokinesis is finally initiated at the anterior end when all cell organelles have been duplicated. Cell division is accomplished by a longitudinal binary fission in which a division furrow is formed towards the posterior end. Following cell division, both daughter cells have one kinetoplast and one nucleus (1K1N).

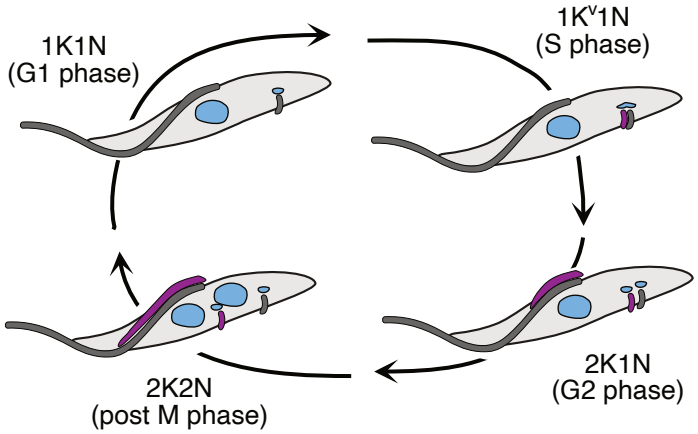

Figure 9: Schematic representation fo the cell cycle of *T. brucei*. Duplication of the key organelles, kinetoplast (K) and nucleus (N) are shown in respect to the duplication of the flagellum. Cytokinesis takes place by binary fission along the longitudinal axis of 2K2N cells, resulting in two 1K1N cells.

1.3.3 Organisation and composition of the plasma membrane of bloodstream form trypanosomes

The knowledge and view of plasma membranes has changed significantly since the fluid mosaic model by Singer and Nicolson in 1972, as explained in Section 1.2. The membrane is no longer considered a separate element of a cell, but is in constant exchange with the environment. This has prompted scientists to investigate the composition and components of *T. brucei's* plasma membrane to contribute to the knowledge of the parasite and its infection strategy.

The central element of the plasma membrane is the lipid bilayer. The lipid composition of trypanosomes is consistent with the usual range of lipids found in eukaryotes., e.g. phospholipids, neutral lipids, and sterols (Dixon and Williamson, 1970; Dixon et al., 1971; Venkatesan and Ormerod, 1976; Patnaik et al., 1993; Smith, 1993; Vial et al., 2003; Richmond et al., 2010). Phospholipid composition in BSF trypanosomes determined from total cell extracts revealed that phosphatidylcholine (PC, 45 - 60 %) and phosphatidylethanolamine (PE, 10 - 20 %) were the most abundant glycerophospholipid classes, while phosphatidylinositol (PI), phosphatidylserine (PS), phosphatidylglycerol (PG) and cardiolipin (CL) represented minor glycerophospholipid classes (Patnaik et al., 1993; Richmond et al., 2010). Sphingolipids were represented by sphingomyelin (SM), inositol phosphorylceramide (IPC) and ethanolamine phosphorylceramide and accounted for 10 - 15 % of the total lipid composition. Additionally, investigations of the flagellar membrane revealed that sterols and raft forming lipids are enriched compared to the remaining cell membrane (Tyler et al., 2009; Serricchio et al., 2015). The precise lipid composition of the plasma membrane is not known due to the difficulty in separating the plasma membrane from the membrane of the organelles.

The lipid membrane is connected to the underlying sub-pellicular microtubule skeleton by microtubule-binding proteins (Hemphill et al., 1991). The only region lacking the underlying skeleton is the FP region, restricting endo- and exocytosis to this part (Overath et al., 1997; Gull, 2003). Insertion of a lipid-anchored eYFP to study the structure of the inner leaflet showed either an accumulation or dilution of the fluorescent probe rather than a homogeneous distribution (Glogger et al., 2017b). It is implied by the authors that presumably the anchoring of the cytoskeleton has a structuring influence and prevents the homogeneous diffusion of the probe as explained by the picket fence model (Glogger et al., 2017b).

Anchored in the outer leaflet of the plasma membrane, the interface to the environment, BSF trypanosomes possess a dense glycocalyx, which is the parasite's key virulence factor (Vickerman, 1969; Cross, 1975). The glycocalyx consists nearly exclusively of a variant of a homodimeric variant surface glycoprotein (VSG) and

is also known as the VSG coat (Figure 10). The coat consists of $\sim 10^7$ monomers, which corresponds to 10 % of the proteome and ~90 % of the proteins found on the cell surface (Jackson et al., 1985; Grünfelder et al., 2002; Bartossek et al., 2017). The VSG homodimer has a molecular weight of 100 - 120 kDa. Each monomer is constituted of one or two small C-terminal domains of 20 - 40 residues, which are connected by a flexible linker region to a large N-terminal domain (Bartossek et al., 2017). The N-terminal domain consists usually of 350 - 400 amino acids. The position and number of conserved cysteine residues allows for a grouping in two VSG classes (type A and B). Usually, VSGs are modified by one or more N-glycosylation sites (Mehlert et al., 2002). Additionally, class B variants can possess an O-glycosylation on top of the N-terminal domain, increasing the virulence of the parasite by impairing the generation of a protective immunity (Pinger et al., 2018). Even though the sequence of the individual VSG variants can differ significantly from each other, which induces the antigenic variation, the tertiary structure is conserved in the individual classes. This suggests that an important structure-function relationship exists. With all its components, the VSG extends 12-15 nm from the cell surface membrane (Vickerman, 1969; Schwede et al., 2015). The size of VSGs and the density of the coat forms eventually a barrier and shields remaining surface proteins from recognition by the host immune system.

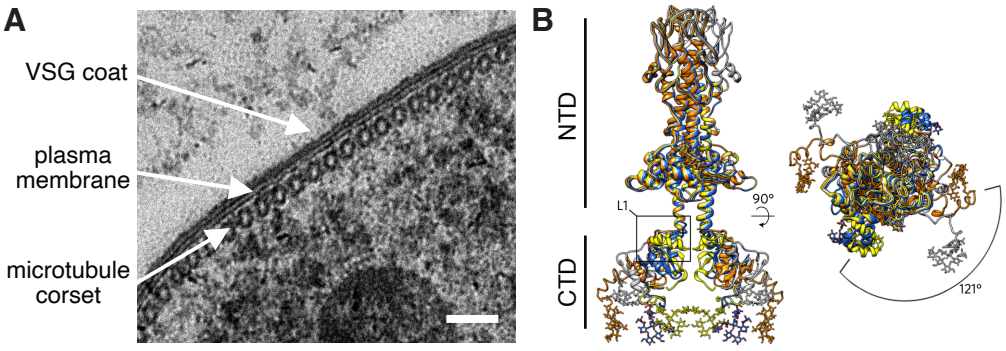

Figure 10: The VSG coat of bloodstream form trypanosomes. **A** Image generated by transmission electron microscopy showing the dense VSG coat as an electron dense structure, the plasma membrane and the subpellicular microtubule skeleton. Scale bar is 0.1 µm. Courtesy of Elisabeth Meyer-Natus. **B** Model of a complete VSG structure. It represents the top and side view of the structure of VSG M1.1 generated from a superposition of different models for the N-terminal domain. The flexibility of the C-terminal domain (CTD) is indicated by the angles. NTD, N-terminal domain; Adapted and modified from Bartossek et al. (2017).

Linkage of a VSG homodimer to the outer leaflet of the membrane is mediated by GPI-anchors at the C-terminal end of each VSG monomer. A GPI-anchor is composed of a glycan part and a lipid part (reviewed in Borges et al. (2021)). The glycan core is conserved for all known protein-linked GPI anchors and can by modified by side chains varying between species and even within different life cycle stages of the

same organism (Ferguson et al., 2015). To generally link a GPI-anchor to a protein, a peptide bond is formed between the amino group of phosphoethanolamine of the glycan part of the anchor and the C-terminal carboxyl group of the polypeptide (Ferguson et al., 1988). The lipid part consists of one or two phospholipids and its composition varies from species to species. Additionally, the length of phospholipids can be different and can range from 14 to 26 carbons (Ferguson et al., 2015). In the case of *T. brucei's* VSG, the final GPI-anchor is composed exclusively of two C14:0 myristate fatty acids. The GPI-anchor provides the high lateral mobility of the VSGs.

Lateral movement is required, for instance, to maintain the integrity of the coat. For this purpose, the VSGs have to be taken up into the cell through the FP, the sole site of endocytosis and exocytosis. The uptake resembles the narrow escape problem (Schuss et al., 2007), which deals with a Brownian particle which is confined to a bounded domain (cell surface), except for a small window (FP) through which it can escape. After the uptake by clathrin-coated vesicles, the VSGs reach early endosomes. Thereafter, two pathways are possible (Engstler et al., 2004; Link et al., 2021): the first option moves the VSGs to recycling endosomes (RE), which then bring the VSG pool back to the surface. The second possibility, is a route that moves the VSG pool to lysosomal endosomes (LE) and then to RE, which eventually redirect the VSG back to the surface. Whilst the liquid phase cargo is transported from the LE to the lysosome to be degraded, it is interesting that no VSG could be found in this organelle (Engstler et al., 2004). The time required to endocytose the entire coat was investigated by fluorescence experiments and determined by extrapolations (Engstler et al., 2004). It takes ~12 minutes to completely absorb and recycle the VSG coat. The determined turnover time is surprisingly fast, considering that the FP only makes up 5 % of the cell surface.

It is also hypothesised that the lateral dynamics of the VSGs are crucial for the survival of the parasite (Hempelmann et al., 2021). Incubation with nanobodies against VSG MITat 1.2 lead to a rapid decrease of the VSG coat mobility, resulting in impaired cell motility and eventually cell death. Furthermore, the fluidity of the coat is a prerequisite for the evasion strategies of the parasite. The evasion strategies are addressed in the following chapter.

The remaining 5 - 10 % of the surface proteins are made up of receptors, Ca^{+2}-regulated adenylate cyclase, glucose transporters, and plasma membrane enzymes. Among these are also GPI-anchored proteins, which include the heterodimeric transferrin receptor, TfR (Steverding et al., 1994, 1995), the haptoglobin-hemoglobin receptor, HpHbR (Vanhollebeke et al., 2008), phospholipase C, GPI-PLC (Bülow et al., 1989), and metalloprotease GP63 (LaCount et al., 2003). The latter two are implicated in VSG shedding (Gruszynski et al., 2003; Grandgenett et al., 2007; Garrison et al., 2021).

Transmembrane proteins are also present in the plasma membrane of BSF trypanosomes. Two examples are an adenylate cyclase encoded by ESAG4 (expression site associated gene 4) (Rolin et al., 1990; Paindavoine et al., 1992) and the family of invariant surface glycoproteins (ISGs) (Ziegelbauer et al., 1992; Ziegelbauer and Overath, 1992; Jackson et al., 1993; Nolan et al., 1997). The recognition of all these proteins by the immune system is prevented by the dense and protruding VSG coat or the accumulation mainly in the invaginated FP. The latter is especially the case for the receptors (Vanhollebeke et al., 2008; Steverding et al., 1995).

The trypanosome plasma membrane can be subdivided into three structurally and functionally distinct regions: the flagellar membrane, the flagellar pocket membrane, and the pellicular membrane. The FP is the specialised region of endo- and exocytosis and exhibits an accumulation of receptors, while the flagellum is the origin of the propulsion and is enriched in cholesterol. All three regions have the highly antigenic, but at the same time protective VSG coat in common.

1.3.4 Contribution of the VSG coat in strategies to escape the host immune system

T. brucei is an exclusively extracellular parasite and thus constantly exposed to the host's immune system. To evade the immune response, it has evolved two strategies that are based on the glycocalyx consisting of GPI-anchored VSGs: Antigenic variation (Cross, 1975; Barry and McCulloch, 2001) and hydrodynamic antibody clearance (Engstler et al., 2007).

Antigenic variation is essential for trypanosomes to establish a persistent infection. It is understood as a stochastic event that changes the expression to an antigenically different VSG and its presentation on the cell surface in place of the previous expressed VSG. The whole VSG coat is replaced and the immune system is exposed to a variant it is not yet familiar with. This provides time for the parasite to proliferate and establish a new wave of parasitemia, while the population recognised by the immune system is cleared (Figure 11 A). The VSG is expressed from one of the 15 existing VSG expression sites (Hertz-Fowler et al., 2008). Additionally, the genome harbours more than 2,000 VSG genes, which form a huge repertoire for antigenic variation (Cross et al., 2014).
Switching can occur in different ways (reviewed in Taylor and Rudenko (2006)): It can happen by an *in situ* switch or recombinational events. The *in situ* switch involves the inactivation of the previously active expression site (ES) and the transcriptional activation of one of the 14 previously inactive ES (Bernards et al., 1984; Myler et al., 1984a,b). Three main paths for recombination-based switching events exist: The first mechanism is referred to as telomere exchange. It is a crossover

event between the active ES and an inactive telomeric VSG ES, leading to the exchange of the telomeric sequences. Hereby, no sequences are lost (Pays, 1985). The second pathway is termed gene conversion. The sequence of the active VSG is replaced by a copy of a silent VSG from a silent ES or the repertoire in the genome. This time, the original VSG sequence is lost. The third process, segmental gene conversion, assembles even novel VSG sequences. Mosaic VSGs are created by copying various segments of VSG sequences into the active ES. This mechanism manifolds the number of antigenically different VSG coats beyond the number of genes in the ES and the repertoire. The switch of the VSG is a passive process which is *in vivo* independent from the host's immune response and occurs with a rate of 10^{-7} to 10^{-6} switches/cell/generation for cell lines cultured *in vitro* or 10^{-3} to 10^{-2} switches/cell/generation for fly-transmitted cells *in vivo* independent from the host's immune response (Doyle et al., 1980; Lamont et al., 1986; Turner, 1997).

Hydrodynamic antibody clearance, on the other hand, utilises hydrodynamic forces generated by the forward propulsion of the parasite (Engstler et al., 2007). Antibody-bound VSGs are pushed to the posterior part of the cell and thus, relocated in close proximity to the FP (Figure 11 B). Thereby increasing the probability of being rapidly endocytosed and degraded intracellularly. This prevents an effective response of the host immune system as antibodies are not exposed to the host immune system long enough. The clearance of antibodies is effective at low to moderate antibody concentrations. However, it can not protect cells at high antibody titres. Nevertheless, it is an important strategy and seems to be of particular importance for the survival of non-proliferating stumpy forms (Engstler et al., 2007). The authors assume that it provides the cells sufficient time for transmission to the tsetse vector

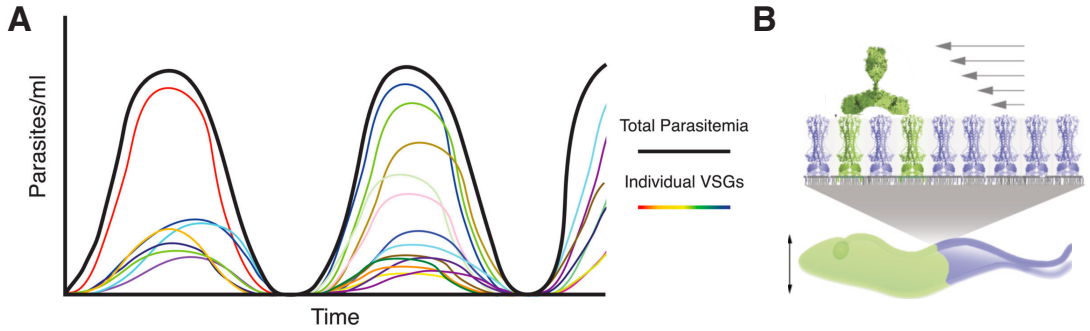

Figure 11: Evasion strategies of bloodstream form trypanosomes. **A** Representation of the wave-like parasitemia over time in relation to the expressed VSGs of individual trypanosomes of a population. Only one variant is expressed by a cell at a time. The underlying mechanism for the expression of a new antigenically VSG variant is termed antigenic variation. Adapted from Mugnier et al. (2016). **B** Illustration of the hydrodynamic antibody clearance. Antibody-VSG complexes are shoved to the posterior part of the trypanosome due to the hydrodynamic flow induced by the swimming of the cell. VSG and Immunoglobulin G are drawn to scale. Adapted and modified from Engstler et al. (2007).

before being cleared by the immune response. The hypothesis is supported by the observation that endocytosis rates are even higher in short stumpy forms (Engstler et al., 2007), facilitating a fast degradation.

For both processes, the lateral mobility of individual VSGs is fundamental for their efficiency as well as for the overall fluidity of the VSG coat. Any interference of these features could eventually lead to a better detection by the immune system and rapid clearance of the whole parasite population. It can be assumed that a large selective pressure is generated to maintain the mobility and fluidity of the coat. At the same time, the coat has to be extremely dense to guarantee its protective barrier. Both aspects seem to be contrary, as it was found that protein density significantly influences the diffusion coefficient of proteins and that crowding leads to a reduction in diffusion (Hartel et al., 2016; Guigas and Weiss, 2016).

1.3.5 Dynamics of the VSG coat of bloodstream form trypanosomes

Various methods have been established to investigate the dynamics of proteins or lipids in membranes. Examples for microscopy-based methods are: fluorescence recovery after photobleaching (FRAP), single-particle tracking (SPT), and fluorescence correlation microscopy (FCS). All techniques require the fluorescent labelling of the lipids or proteins of interest, while the required label density in the sample differs. For instance, FRAP measurements demand a homogeneously and densely labelled sample, which corresponds to micromolar labelling, while the required labelling density for SPT and FCS ranges from nano- to femtomolar to resolve single emitters (Chen et al., 2006; Garcia-Saez and Schwille, 2010). Furthermore, the spatio-temporal resolution at which the methods operate varies. FRAP works at a micrometre and seconds regime, while FCS operates in a submicrometre and sub- to millisecond regime, and SPT at a nanometre and millisecond range (Hess et al., 2002; Chen et al., 2006).

The extensive abundance of VSG molecules in the coat of BSF trypanosomes provides the ideal conditions for FRAP experiments to measure the dynamics of a specific protein in living cells. Bülow et al. (1988), Hartel et al. (2015), Hartel et al. (2016), and Hempelmann et al. (2021) characterised the diffusion with 0.01 - 0.03 $\mu m^2/s$. The proportion of the mobile fraction was 76 - 82 %. In order to meet the requirement of an immobile cell for fluorescence microscopy with the highly motile trypanosomes, the scientists chose two different strategies. Bülow et al. first depleted the global ATP level of the trypanosomes and subsequently embedded the motionless parasites in low-melt agarose. This allowed for monitoring the dynamics at the mammalian physiological temperature of 37 °C. Hartel et al. (2015), Hartel et al. (2016) and Hempelmann et al. (2021) chose gelatine for immobilisation, which

limited the temperature to 20 °C. However, the stiffness of the gelatine gel provided the crucial compromise to study trypanosomes without massive interference in the global ATP household. Hartel and his colleagues characterised the dynamics even further. In the study of Hartel et al. (2015), the scientists showed that dynamics of the GPI-anchored proteins depend on the extracellular molecular length of the protein. Dynamics increased with decreasing extracellular length of the protein, even in living cells. In 2016, Hartel et al. addressed the question of whether N-glycosylation of the VSG has an effect on the molecular crowding threshold (MCT) at which the VSG coat operates. For this, living trypanosomes expressing N-glycosylation deficient VSGs were studied by FRAP. Hereby, a significant reduction in the mobile fraction was shown. This was complemented by studies in artificial membranes which revealed a decreased diffusion coefficient of N-glycosylation deficient VSGs compared to WT VSGs at the MCT. This suggests that N-glycosylations promote a high fluidity as well as mobility of the VSG coat while maintaining a high protein density to ensure its shielding function.

1.4 Aim

In this thesis, I utilised live-cell two-colour SMFM to characterise the dynamics of individual VSG molecules within the dense surface coat of *T. brucei*. This technique has high spatial and temporal resolution. The VSG diffusion coefficients reported in the literature and measured by FRAP are not sufficient to explain the known fast turnover time of the VSG coat. Trypanosomes are special to the extent that they possess only one site for endo- and exocytosis: the FP. Thus, to successfully exchange the VSG coat, exocytosed VSGs have to randomise fast to prevent being immediately re-endocytosed. Concurrently, for a fast turnover of the coat, VSGs have to either diffuse much faster than previously described or utilise directed forces biasing their motion towards the FP. Both aspects will be assessed in this thesis. For this purpose, I used live-cell super-resolution microscopy to resolve the structure of the fluorescently labelled hook complex which served as a reference to identify the FP entrance. Embedding trypanosomes in an irreversible, cross-linkable hydrogel facilitated imaging at the physiological temperature of their host at 37 °C. As stage drift in the nanometre range is unavoidable during the acquisition time required for SMFM, I implemented an approach based on multifluorescent beads to allow for the correction in both colour channels. Trypanosomes are small in size and their surface is highly curved. This is why the VSG trajectories obtained were short. Hence, a reliable method for quantification was needed. To this end, I adapted an approach introduced by Hoze et al. (2012) to our data. Additionally, I will present an important extension of the analysis which is the consideration of the static and dynamic localisation error present in SPT. The evaluation approach allows for the analysis of the VSG dynamics in two distinct scenarios: diffusion and directed motion. The results of the quantification were visualised in maps representing the trypanosome surface, e.g. local diffusion coefficients or velocities. In order to decide which of the two motion scenarios dominated locally, I present a suggestion for a guideline on the basis of random walk simulations. In addition, I aimed to study a potential correlation of VSG dynamics and the cell's cytoskeleton. To this end, single-molecule tracking of VSGs was conducted on osmotically swollen trypanosomes and on a trypanosome cell line deficient in a microtubule associated protein possibly anchoring the cytoskeleton to the plasma membrane.

2 Results

2.1 Immobilisation of living trypanosomes in PEG-VS/HA-SH hydrogels for single-molecule fluorescence microscopy

To study the dynamics of the surface protein VSG (variant surface glycoprotein) of the highly motile parasite *T. brucei in vivo*, living trypanosomes have to be immobilised. This can be accomplished by the use of hydrogels (Bülow et al., 1988; Hartel et al., 2015; Hartel et al., 2016; Glogger et al., 2017a; Glogger et al., 2017b). However, to study for the first time the dynamics at physiological temperatures of 37 °C, an irreversibly cross-linked hydrogel was needed. Three hydrogels with different polymer composition were introduced by Marius Glogger during his doctoral thesis (Glogger, 2018). The hydrogel consisting of the 8-arm poly(ethylen glycol)-vinyl sulfone (PEG-VS, commercial) and thiol-functionalised hyaluronic acid (HA-SH, provided by Simone Stichler and Leonard Forster) appeared to be the best candidate as it was convenient to handle and did not require the initiation of cross-linking by UV light. For this hydrogel, I tested the nanoscale immobilisation efficiency and extended the published protocol by inclusion of multifluorescent beads to allow for drift correction. Subsequently, cytocompatibility was tested for the adjusted hydrogel sample assembly.

2.1.1 Quantification of the immobilisation efficiency

The high motility of a trypanosome originates from its beating flagellum. Hence, fluorescence imaging of hydrogel-embedded trypanosomes expressing a marker for the flagellum was performed over a period of time to monitor any potentially remaining cell movements. Measuring the diameter of the fluorescent signal allowed the determination of the immobilisation efficiency at the nanometre scale.
For this experiment, the 13-90 kinesin-MORN::eYFP cell line established by Ines Subota was employed, as it expressed a marker for the axoneme of the flagellum (Glogger et al., 2017a). The cells were immobilised in hydrogels of 10 % (w/v) PEG-VS and 5.6 % (w/v) HA-SH (~24 kDa, ~54 % SH-substituted, Simone Stichler). The intrinsic blinking behaviour of eYFP (Dickson et al., 1997) at high illumination intensities allowed for the spatial and temporal separation of the individual emitters for single-molecule microscopy. The diameter of the super-resolved structure was then compared to the axonemal diameter of chemically fixed cells and to the axonemal diameter determined by electron microscopy. A remaining flagellar beat of insufficiently immobilised cells should result in a spread distribution of eYFP localisations and thus increase the average axonemal diameter.

In total, 32 cells immobilised in PEG-VS/HA-SH hydrogels were examined. 10,000 frames each were recorded at 28 Hz, and 1 kW/cm^2. Due to the high label density of eYFP molecules at the axoneme, the first ~100 - 200 frames were removed manually from the movies until single emitters became visible. After processing the single-molecule localisations according to Section 4.7.1, super-resolved images were reconstructed as described in Section 4.7.4. An exemplary super-resolved image of the axonemal signal is presented in Figure 12 A. To ensure that the structure was sufficiently resolved, the number of localisations per µm^2 was quantified. As stated by the Nyquist-Shannon theorem (Shannon, 1949), this parameter gives an indication about the minimal extractable information of a structure. Therefore only images with a label density >1,000 localisations per µm^2 were further evaluated. Background noise as well as false-positive signals were also present in the reconstructed super-resolved images and needed to be considered. Therefore, the ratio of false-positive localisations ($r_{false-positive}$) was determined by the comparison of the specific localisation density with the background density. For the 32 cells, the average label density was 2,096 ± 712 localisation per µm^2. At the same time, $r_{false-positive}$ was minor and ranged between 0.6 % and 1.5 % with an average of 0.64 %. To extract the diameter of the axoneme, lines perpendicular to the contour line were used to extract the intensity profiles. Then the average full-width-half-maximum (FWHM) was calculated from these profiles (Section 4.7.5). The FWHM, representative for the axonemal diameter, was 172 ± 18 nm (Figure 12 B). Thus, the diameter was below the diameter of fixed cells (214 ± 39 nm, Glogger (2018)) and the diameters extracted from electron microscopy images (210 - 230 nm, Nicastro et al. (2006); Koyfman et al. (2011)). However, it can be concluded that the cells were efficiently immobilised as the average axonemal diameter was below the average diameters of the reference and no blurring was detected in the axonemal signal.

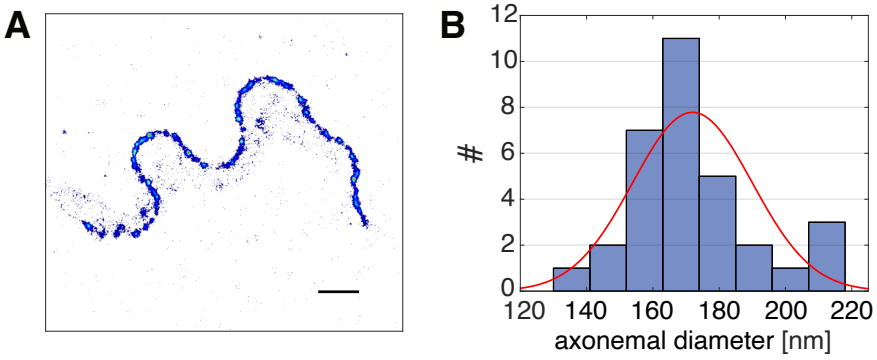

Figure 12: Quantification of the immobilisation efficiency of the PEG-VS/HA-SH hydrogel. **A** Super-resolved image of kinesin-MORN::eYFP localisations depicting the axoneme of the flagellum. The scale bar is 1.6 µm. **B** Distribution of the determined axonemal diameter (n = 32 cells). The average axonemal diameter was determined from the super-resolved images of the kinesin-MORN::eYFP signals and was 172 ± 18 nm.

One reason for the smaller axonemal diameter could be a still too high label density. In single-molecule imaging, a high label density is known to cause artefacts like false structures, multiple features collapsing into one or artificial sharpening (Burgert et al., 2015; Sage et al., 2015; Fox-Roberts et al., 2017). To check whether artificial sharpening caused the smaller axonemal diameter, an analysis for high-density single-molecule data with the HAWK (Haar Wavelet Kernel) algorithm was performed which was established by Marsh et al. (2018). To that end, the movies of the kinesin-MORN::eYFP signals were fed into the HAWK ImageJ plug-in and the filter level 5 was employed. The algorithm enables the separation of emitters on the basis of their blinking behaviour. The output yielded an image sequence containing an increased number of frames with a reduced number of emitters in each frame. This image sequence was then used to retrieve the single-molecule localisations to reconstruct super-resolved images. The diameter of the axoneme was determined by the application of a strict mask to define the axonemal signal as the HAWK algorithm introduces a higher background signal. Four cells were analysed and the axonemal diameter increased by ~34 nm. Taking into account artificial sharpening, the average axonemal diameter increased from 172 nm to 206 nm and was in good agreement with the diameter of fixed cells and extracted from electron microscopy.

Once sufficient immobilisation of the trypanosomes was ensured, the Young's modulus of the hydrogel was determined. It is a measure of the ability of elastic material to withstand changes in length under compressive loads, and thus it is a measure of the stiffness of the material. Hydrogels with a polymer concentration of 10 % (w/v) PEG-VS and 5.0 % (w/v) HA-SH (~10 kDa, ~40 % SH-substituted, Leonard Forster) were casted in cylindrical glass forms. The mechanical properties were determined at the Department for Functional Materials in Medicine and Dentistry (University of Würzburg) with the support of Leonard Forster. The Young's modulus was calculated from the raw data as the slope of the true stress-strain curve in the linear elastic range of 5 - 10 % strain which is depicted in Figure 13. The average Young's modulus of the three PEG-VS/HA-SH hydrogels was 105 ± 29 kPa and was below the determined Young's modulus of 154 ± 22 kPa for the 15 % (w/v) HA-SH/P(AGE-co-G), which was also used for the immobilisation of trypanosomes (Glogger et al., 2017a; Glogger, 2018).

In summary, the PEG-VS/HA-SH hydrogel successfully immobilised trypanosomes at the nanometre scale. Testing the mechanical properties revealed that PEG-VS/HA-SH hydrogels with a Young's Modulus of 105 ± 29 kPa were sufficient for the nanometre immobilisation.

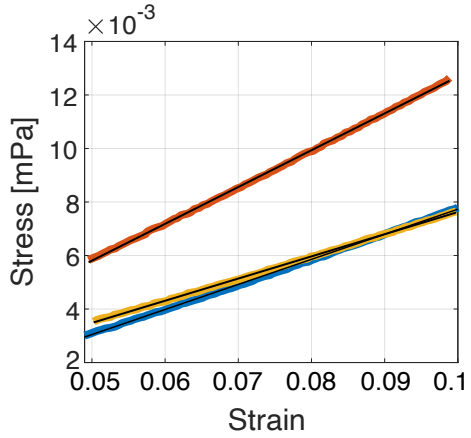

Figure 13: True stress-strain curves of three PEG-VS/HA-SH hydrogels. The graph depicts the raw data from the triplicates (yellow, blue and orange) with their corresponding linear fits (black) of the linear elastic range of 5 - 10 % strain.

2.1.2 Hydrogel sample assembly allowing for drift correction

To perform super-resolution imaging, acquisition times of several minutes are required. During this time, the microscopic stage with the sample under investigation can drift which falsifies the measurements, e.g. a known structure or outline appears smeared. In the case of tracking dynamic particles, for instance, a directionality is introduced to diffusion. The drift did not occur permanently and constantly, rather it was uneven and varying in severity over time. A possibility to track the drift is to use permanent fluorescent fiducial markers in the field of view. The localisations of the reference enabled me to calculate the spatial difference to the preceding positions. The deviation can be then used to correct the single-molecule localisations of the moving particles under investigation *a posteriori*. For this purpose, multifluorescent beads are widely used which posses a long-lasting fluorescence. Additionally, the drift can be corrected in several colour channels, enabling multicolour experiments. The single-molecule setup used for this work was equipped with two laser lines of the wavelength 515 nm and 647 nm and thus TetraSpeck™ beads (TS beads, ⌀ 100 nm) with a diameter below the diffraction limit were suitable.

Several attempts were made to place the beads in the proximity of trypanosomes to allow for recording of the drift. The first attempt was to add TS beads directly to the hydrogel mixture and to place the hydrogel mixture between two cover slips. Surprisingly, the TS beads showed a high affinity to the trypanosome surface and many TS beads accumulated at single cells. This was not ideal, as the signal of the TS beads outshone the fluorescence of single Atto-647 N labelled VSGs and an interaction of the TS beads with the surface coat could not be excluded.
In a second attempt I used a mixture of differently dyed polystyrene beads from Bangs Laboratories. The green and red fluorescent beads were added directly to the

hydrogel mixture before it was placed between two cover slips. Although no affinity of the beads to the trypanosomes could be observed, the likelihood of having two beads with different fluorescence in the field of view was extremely rare.

Based on the previous observations, a hydrogel assembly approach was required to locate the cells in proximity to the lower cover slip and to place a few TS beads next to the trypanosomes without accumulation on the cells. Hence, the TS beads were spin-coated on the bottom cover slip. After the addition of HA-SH to the prepared hydrogel mixture, containing harvested trypanosomes, spacer beads and PEG-VS precursor solution, the polymerisation of the hydrogel was initiated (Section 4.6.6.1). Once the polymerisation started, 90 seconds were left for the final assembly. The hydrogel mixture was placed between a cover slip and the spin-coated cover slip. The viscosity of the hydrogel mixture prevented the sedimentation of the cells close to the bottom cover slip. Therefore, the cover slip sandwich was weighted down with 90 mg to decrease the height of the hydrogel. A subsequent centrifugation step placed the trypanosomes close to the bottom cover slip. To prevent squeezing of the cells, so-called spacer beads (unlabelled calibration FACS beads, ⌀ 6 µm) were added to the hydrogel mixture. Figure 14 illustrates the final procedure for the

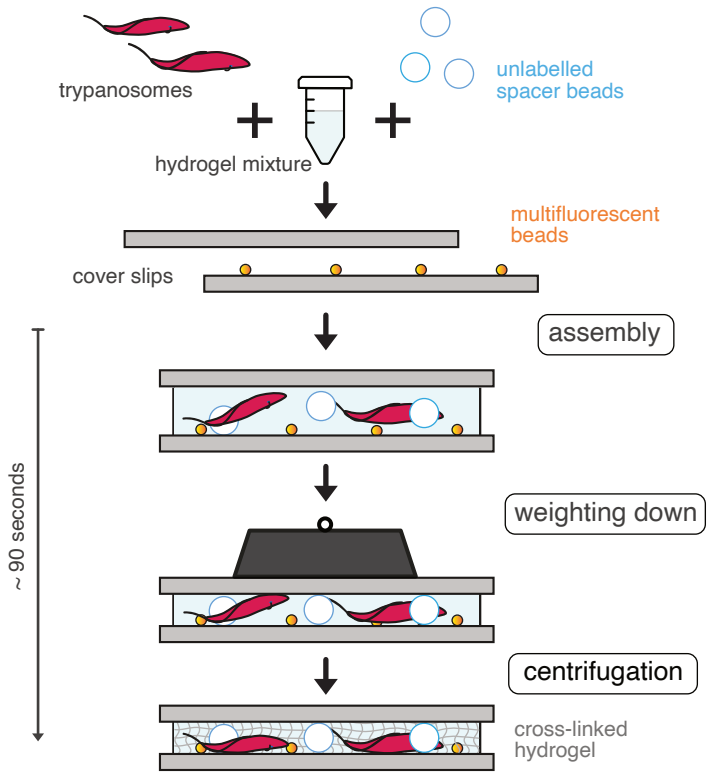

Figure 14: Scheme of the hydrogel sample assembly. Harvested trypanosomes and unlabelled spacer beads were mixed with the hydrogel components. After addition of HA-SH, hydrogel polymerisation was initiated, leaving ~90 seconds for the final assembly. The hydrogel mixture was placed between two cover slips. The bottom cover slip was spin coated with multifluorescent beads to enable drift correction. The top cover slip was weighted down and a centrifugation step facilitated locating living trypanosomes in the same focal plane as multifluorescent beads. Scheme not to scale.

sample assembly. Placing trypanosomes close to the bottom cover slip increased additionally the signal-to-noise ratio in the yellow channel. The closer the cells were to the cover slip, the less the hydrogel had to be traversed by the excitation and emission light and the hydrogel's autofluorescence in the yellow channel was minimised.

For post-processing of the drift, a moving average kernel was employed to dampen fluctuations in the range of the localisation precision (described in Section 4.7.2). Figure 15 depicts the raw x- and y-positions of a TS bead revealing a drift of several nanometre over a total recording time of 100 s and after being post-processed for the drift.

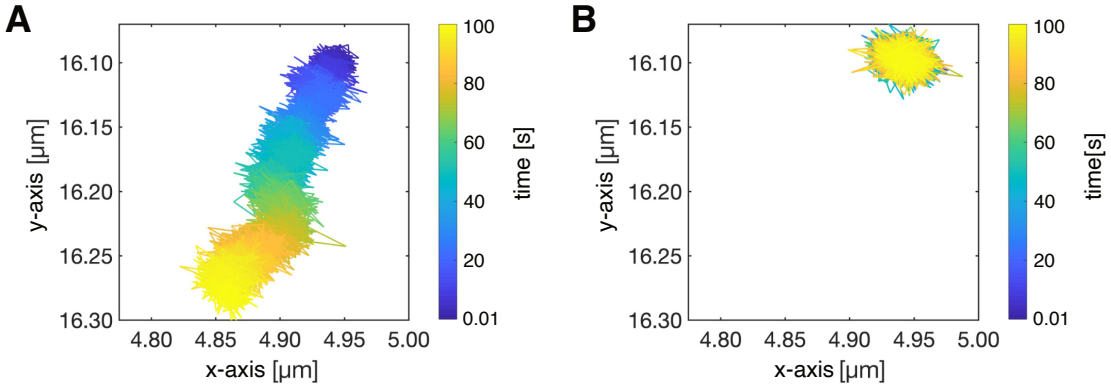

Figure 15: Temporal resolution of the drift. **A** The raw x- and y-positions of a multifluorescent bead are plotted colour-coded over time revealing a drift of several nanometre over a total time period of 100 seconds. **B** illustrates the x- and y-positions after correction of the drift.

A proof-of-principle experiment was then conducted, addressing two questions: (i) Do all immobile objects show a similar drift? (ii) How well does the self-correction work compared to the external correction? To this end, the drift of TS beads in the field of view was compared to the drift of TS beads located directly underneath trypanosomes. The drift was analysed in three measurements. Plotting the raw x- and y-localisations over time demonstrated that the beads showed a similar drift pattern in the nanometre range. Figure 16 shows an exemplary comparison of the bead drift from the reference ($bead_{ref}$) to the bead underneath the trypanosome ($bead_{tryp}$). The drift was extracted from the average position with a moving average kernel of the size 500 frames (see orange line in Figure 16). Even though the manifestation of the drift did not coincide perfectly (Figure 16 A and B, upper graphs), the deviation between both was minor. The drift was then corrected using $bead_{ref}$. In this concrete example, the correction of the drift resulted in minimising the fluctuation in the drift of $bead_{ref}$ from 19.3 & 23.7 nm to 1.7 & 1.7 nm (x- & y-axis). In the case of $bead_{tryp}$, the drift fluctuations were reduced from 19.3 & 23.7 nm to 7.8 & 6.5 nm (x- & y-axis). The time course of the drift-corrected positions is depicted in the lower graphs of Figure 16 A and B. Even though the drift of the $bead_{tryp}$ was not

completely eliminated, it was nevertheless reduced and the precision of the measurements were improved. Thus, a global drift can be assumed and the drift correction can be applied to the single-molecule localisations recorded on the trypanosome embedded in the hydrogels. The correction is described in Section 4.7.2 and rectifies only drifts above the magnitude of the localisation precision.

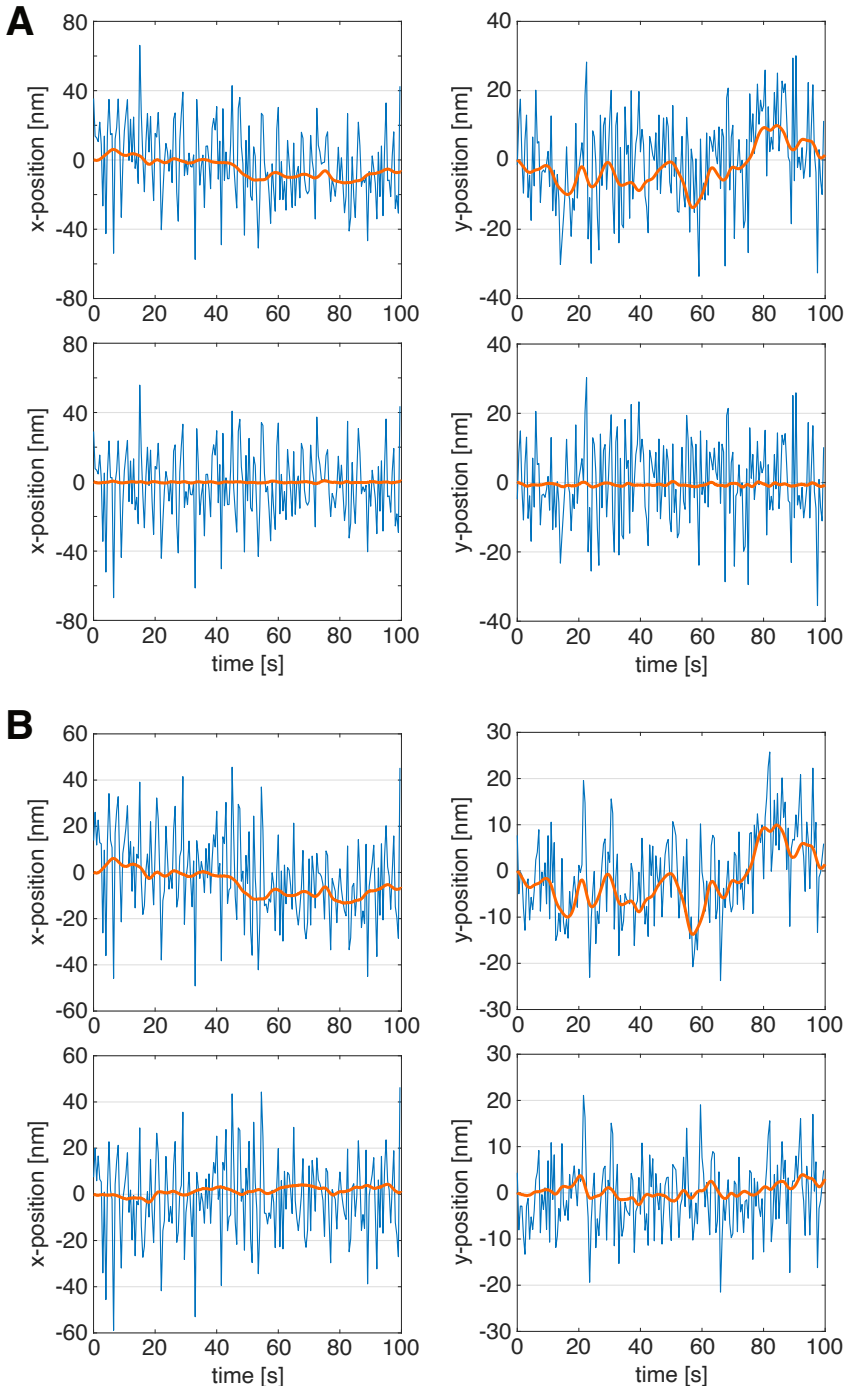

Figure 16: Quantification of the self-correction and the external correction of the drift. The graphs represent the temporal progressions of the x- and y-positions over time (every 0.5 seconds). The drift was extracted using an average box kernel spanning a period of 5 seconds. The orange line depicts the drift. **A** shows the time course of the $bead_{ref}$'s positions in the field of view, while **B** reflects the progression of $bead_{tryp}$. The upper graphs show the time course before drift correction and the lower graphs the time course after the successful application of the drift correction using $bead_{ref}$, respectively.

2.1.3 Cell viability under adjusted conditions in the hydrogel sample assembly

In the course of this work, multifluorescent beads with an average diameter of 100 nm were introduced to correct the drift of the microscopic stage. This required an adjustment in the assembly of the sample. After all components of the hydrogel were mixed and added to the cells, a weight of 90 mg was applied on the cover slip on the top to decrease the diameter of the hydrogel and an additional centrifugation step was required to place the trypanosomes in the proximity of the fiducial markers (multifluorescent beads on the bottom cover slip) used for the drift correction (described in more detail in Section 2.1.2). For this reason, the viability of the transgenic trypanosome cell line 13:90 HASP::eYFP embedded in the hydrogel with the adapted assembly protocol was assayed with propidium iodide (PI). PI is a membrane-impermeable dye that can only integrate into the DNA upon the loss of cell membrane integrity, which is the case for dead cells. The intercalation of PI into DNA is accompanied by an 20 - 30-fold increase in its emission intensity as well as a Stoke shift of its emission, resulting in an excitation and emission maximum of 535 nm and 617 nm, respectively. Expression of the fluorescent probe HASP::eYFP, a marker for the inner leaflet of the plasma membrane, facilitated the quantification of the total cell number embedded in the gel by diffraction limited microscopy. Dead cells showed an additional PI signal. Both values enabled me to calculate the viable fraction (PI negative (-)). For each time point 3 replicate experiments were performed with a total cell number $\geq$ 100 per replicate. The viability of the embedded trypanosomes was monitored up to 60 min at 37 °C.

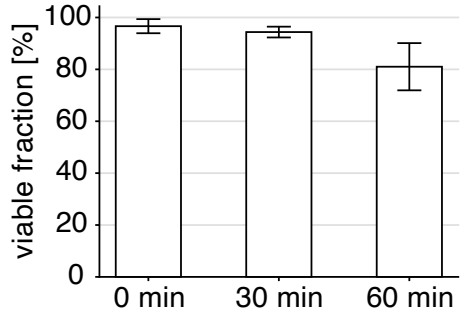

Figure 17: Viability of trypanosomes embedded in PEG-VS/HA-SH hydrogels. The viable fraction was assessed by a live/dead assay with propidium iodide (PI). The bars illustrate the average viable fraction of embedded trypanosomes at 37 °C. Each time point was monitored in three replicate experiments with a total cell number $\geq$ 100 per replicate. The error bars represent the standard deviation.

The viability was found to be high (> 80 %, Figure 17) for up to 60 min and the embedding of trypanosomes with the adjusted hydrogel assembling strategy provided sufficient time for single-molecule microscopy in living trypanosomes.

2.2 Tracking of individual VSGs in the surface coat of living trypanosomes in relation to the flagellar pocket

The dynamics of the variant surface glycoprotein (VSG) surface coat of trypanosomes contributes to the evasion of the host immune system. For this, the lateral mobility of the GPI-anchored protein is necessary to clear VSG-bound antibodies by the generated hydrodynamic flow (Engstler et al., 2007). To guarantee this evasion strategy, the integrity of the VSG coat needs to be maintained. To this end, VSGs are shuffled through the flagellar pocket (FP), the sole site for endo- and exocytosis. So far, the VSG dynamics was investigated with fluorescence after photobleaching (FRAP) on living trypanosomes or membrane VSGs were extracted and studied in supported lipid bilayers at a single-molecule level (Bülow et al., 1988; Hartel et al., 2015; Hartel et al., 2016; Bartossek et al., 2017; Glogger, 2018; Hempelmann et al., 2021). Furthermore, Engstler et al. (2004) determined the time of the turnover of the VSG coat with ~12 min. This time is surprisingly fast for solely diffusion and can not be achieved in theory by the diffusion coefficients determined by FRAP. For this reason, the aim of this work was to study the VSG dynamics on living cells at the host's physiological temperature of 37 °C and at the single-molecule level and in relation to the flagellar pocket.

2.2.1 Generation of a trypanosome cell line expressing a marker for the entrance to the flagellar pocket

To track the surface VSGs in relation to the flagellar pocket, a BSF cell line was established expressing an N-terminally eYFP tagged TbMORN1 (MORN1, accession number Tb427.6.4670). This protein is one component of the hook complex and is distributed over the whole structure (Esson et al., 2012). The hook complex is located directly underneath the plasma membrane and is wrapped around the FP neck (Figure 18). The hook complex was chosen due its location close to the plasma membrane and its asymmetric form (hook and handle) providing information about the orientation. The plasmid for transfection was provided by Brooke Morriswood.

The fluorescent protein eYFP was fused to the MORN1 protein with a hinge region of 4 amino acids (aa). Prior to transfection the plasmid was linearised. The MORN1 reporter construct was established in the trypanosome wild type (WT) strain MITat 1.6 and the transgenic cell line MITat 1.2 13-90. This offered in principle the opportunity to study the dynamics of different surface VSGs on living trypanosomes. VSG MITat 1.6 is expressed by MITat 1.6 and had previously been extracted to investigate the VSG dynamics in supported lipid bilayers. VSG MITat 1.2 is expressed

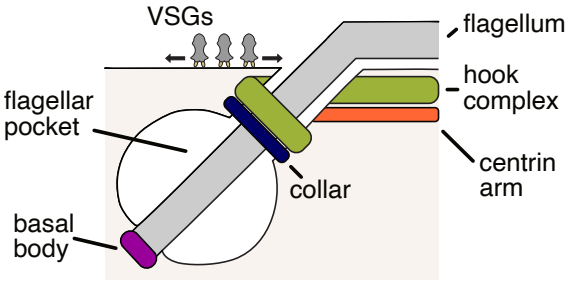

Figure 18: Scheme of the flagellar pocket region of *T. brucei*. The position of the hook complex is shown in regard to other structures present in this region. Scheme not to scale. Inspired by Morriswood (2015).

by the 13-90 cell line and was used by Marius Glogger to study the plasma membrane organisation in *T. brucei*. Only one of the alleles was tagged in both cell lines to ensure detection of single molecules. The correct integration of the constructs into the genome was verified for all clones as well as the transfection pools by PCR. The genomic DNA of both parental cell lines served as negative control (Figure 19 A & B). Further analyses were then performed with two of the clones obtained per cell line, as all showed successful endogenous integration of the reporter construct. The expression and the correct localisation of the fusion protein was verified by Western Blot (WB) analysis, immunofluorescence analysis (IFA), and resolution of the shape of the hook complex in super-resolution microscopy. Additionally, the cell growth of the transgenic cell lines was observed. For the WB analysis, whole cell lysates of the WT and the transgenic cell lines were probed with α MORN1 and α GFP antibodies verifying the expression of eYFP-tagged MORN1 and the presence of the WT protein (Figure 19 C). The population doubling time of the transgenic cell lines (1.6 eYFP::MORN1 clone 1 & 2: 7.4 h, 13-90 eYFP::MORN1 clone 1 & 2: 7.5 h, 6.2 h) was found to be similar to the WT cell lines (1.6 WT: 7.4 h, 13-90: 7.4 h, Figure 19 D). In the IFA analysis, the fixed trypanosomes were treated with α MORN1 antibodies showing the co-localisation of the eYFP signal of the fusion protein with the hook complex (Figure 19 F). In addition, super-resolution microscopy demonstrated the hook-like shape obtained from the sum of localisations of the fusion protein (Figure 19 F). All together, the above experiments verified the expression of the fusion protein, which behaved as expected. For the following tracking experiments, clone 2 of the 13-90 transgenic cell line was employed. The transgenic cell line 13-90 was chosen since the distribution and tracking of surface VSGs should be examined under consideration of a possible influence of the cytoskeleton on the organisation of the plasma membrane as hypothesised in Glogger et al. (2017b).

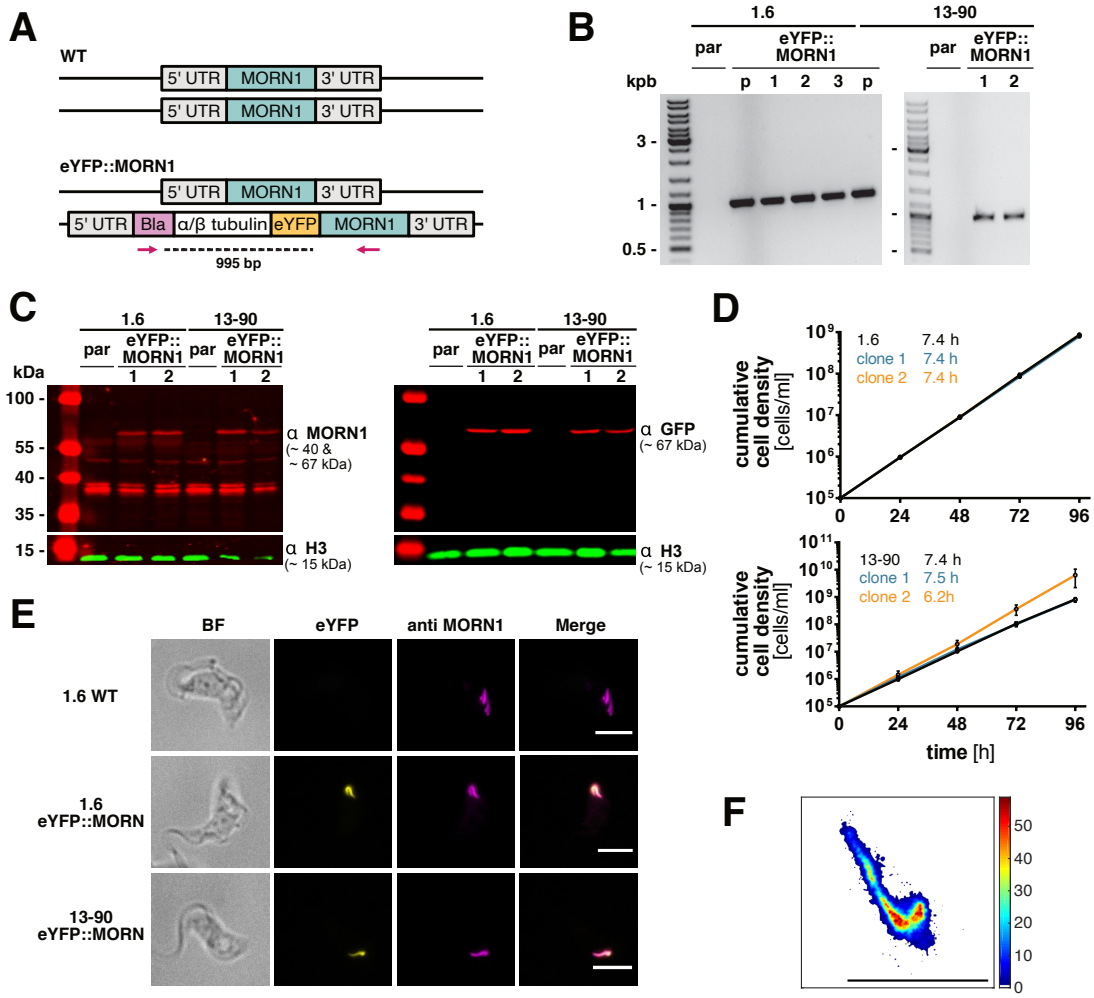

Figure 19: Characterisation of transgenic cell lines expressing eYFP::MORN1. **A** Scheme of the endogenous *MORN1* locus in WT and transgenic cell lines. One allele of MORN1 was N-terminally tagged with eYFP. Magenta arrows indicate the primers used for the verification of the genome integration by PCR. **B** PCR with primers binding in the balsticidin (Bla) resistance gene and the the open-reading frame (ORF) of MORN1. The genomic DNA of the parental cell lines (par) as well as the obtained transgenic eYFP::MORN1 clones and the transfection pools (p) served as template for the PCR reaction. **C** Confirmation of the expression of WT MORN1 and the eYFP fusion protein. Whole cell lysates of the parental cell lines (par) and the eYFP::MORN1 transgenic cell line were analysed by immunoblotting with α MORN1 and α GFP antibodies. As protein loading control, the same blot was probed with α H3 antibodies. **D** Cumulative growth curves of the parental cell lines 1.6 and 13-90 in relation to the transgenic 1.6 eYFP::MORN1 and 13-90 eYFP::MORN1 cell lines. The doubling times are indicated in the graphs. **E** Immunofluorescence analysis to confirm the integration of the fusion protein in the hook complex. The fluorescent signal of the eYFP::MORN1 fusion protein was recorded and its correct localisation was confirmed by co-localisation with the WT MORN1 protein detected by immunofluorescence. **F** Super-resolution image of the hook complex of a living, but immobilised trypanosome expressing eYFP::MORN1. The quantity of single-molecule localisations is displayed by the colour code. The scale bar is 1.6 µm.

2.2.2 Single-molecule tracking of surface VSGs on living trypanosomes

The tracking of single molecules on trypanosomes is particularly challenging. The small size of the parasites (length of ~20 µm, diameter of ~4 µm) and the focus lying on the bottom plasma membrane of the trypanosome provides only a small area of less than 100 µm^2 for the tracking. In addition, tracking was further limited by the strong curvature of the plasma membrane. As a result, emitters were only in focus for a short time. To enable the reconstruction of trajectories, a high acquisition frequency was required. Additionally, I aimed to investigate the surface VSG dynamics with particular interest in the region of the FP entrance by two-colour experiments. Both requirements demanded the *a priori* establishment of high-frequency two-colour single-molecule fluorescence microscopy.

2.2.2.1 Sequential two-colour single-molecule fluorescence microscopy

In order to enable two-colour experiments, the emitted signals of the two colour channels must be separated either spatially or temporally. Spatial separation is usually accomplished by using a dual view unit. The dual view unit enables the projection of the emitted light onto two separated regions on the sensor chip of the camera. However, the area on the sensor chip that is used for imaging is doubled to simultaneously record both colour channels. This limits the acquisition speed, because the larger the area on the sensor chip is, the more time is consumed to read and process the information. For the tracking analysis, I aimed for an acquisition frequency of at least 100 Hz. The simultaneous two-colour imaging established by Marius Glogger could therefore not be utilised, as the occupied region of the sensor chip limited the acquisition to 28 Hz.
Temporal separation can be achieved for example by alternating illumination using an electronic filter changer or an acousto-optic tunable filter (AOTF). An alternating acquisition of the signal would increase the time lag between two images of the same colour channel by a factor of two. A second option, which allows for a temporal separation while maintaining high acquisition frequencies, relies on recording the two-colour channels sequentially. The large temporal offset between the recording of the single-molecule dynamics and the super-resolved structure of the hook complex is not problematic in the given experiment as the structure of the hook complex is durable.

In the following two-colour experiments, the dynamic information was always recorded first and thereafter the structural information. A region of interest (ROI) of the size 120 x 120 px was chosen on the camera sensor to acquire at 100 Hz. This corresponds to a field of view of 19.2 x 19.2 µm in the sample. This was the minimal size allowing to simultaneously place the entire cell body and a TS bead required for drift

correction in the same field of view. The colour channels were superimposed using a registration matrix *a posteriori*. To this end, the laser spots were shifted horizontally to each other by a few pixels on the sensor chip. This allowed a superposition in the nanometre range which would never be achieved by superimposing the colour channels manually on the sensor chip. For the generation of a registration matrix, I collected a large number of localisations of multicolour reference objects with alternating illumination of both colour channels. The principle is depicted in Figure 20. This method was introduced in the lab by Marius Glogger (Glogger, 2018) and was adapted in this work for sequential two-colour imaging.

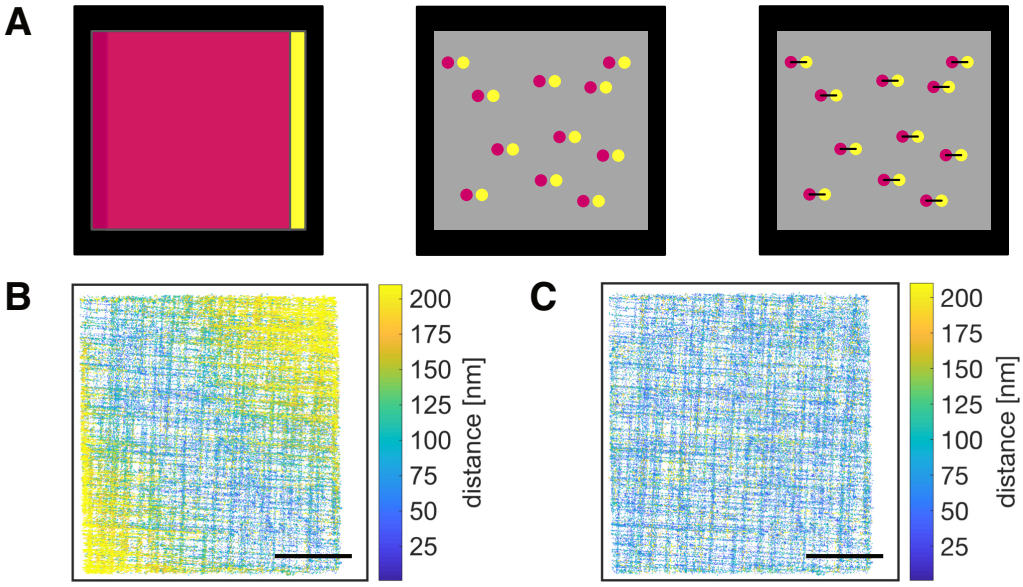

Figure 20: Registration of two-colour information. **A** Scheme of the spatial separation of the red and yellow emission signals on the sensor chip. From left to right. The red and yellow colour-channel are horizontally shifted to each other. Consequently, the red and yellow emission profile of the beads are localised with a horizontal shift of a few pixels. The distance between the two profiles is ascertained and used for the coarse registration. For the correction of the lateral chromatic aberration a transformation matrix is applied. **B** represents the lateral chromatic aberration of the TS bead localisations used for the generation of the transformation matrix. **C** Application of the transformation matrix removed the inhomogeneous lateral chromatic offset. The colour code indicates the range of the spatial error. The scale bar is 5 µm and valid for B and C.

In order to keep the image section on the camera's sensor to a minimum for enabling high acquisition frequencies, the two laser spots were shifted horizontally a few pixels to each other. To enable the generation of the registration matrix, TS beads randomly distributed on a cover slip were used as fiducial markers. Typically, 4 movies with 10,000 consecutive images each were recorded under alternating illumination of the two lasers at the same acquisition frequency used for the later measurements. During the acquisition, the TS bead sample was moved slowly and continuously to sample the ROI. The beads were then localised as described in Section 4.7.1. Since

both colour channels were recorded alternately, the information of the red and yellow channels of a movie were separated for easier processing. As the TS beads are dyed multifluorescent beads, double localisations were present in the frames of the yellow channel due to the emission of bright red light by the excitation with the 515 nm laser. This light passed the dichroic mirror with a cutoff at of 640 nm in the Optosplit and was projected at the sensor simultaneously with the yellow signal. These localisations of the same bead could then be removed by the reference positions in the preceding red channel. First, the profiles were coarsely aligned manually. The offset over the sensor chip between the camera chip varies and is due to the lateral chromatic aberrations and its distorting effect is greater towards the corners of an image. Therefore, the local displacement was determined using the built-in Matlab function 'images.geotrans.LocalWeightedMeanTransformation2D.m'. It fits a local weighted mean transformation to a set of predefined fixed and moving reference data points that are related by a global second degree polynomial across the entire ROI. The red single molecule positions were defined as fixed reference points and the yellow ones were moving reference points. A nearest neighbour distance approach was applied to define reference points in every image. Additionally, a maximum distance between the fixed and moving reference points was introduced to avoid false assignment. The successful generation of the registration matrix was checked by plotting the offset before and after the registration (Figure 20 B and C). The remaining offset after the coarse registration was in extreme cases > 200 nm. After the registration, a mean offset of 55 ± 5 nm was measured for all reference points. This registration matrix was then applied to the obtained localisations of the yellow colour channel of two-colour measurements. Notably, imaging of TS beads prior to every two-colour experiments was a prerequisite to generate a registration matrix and to enable the nanometre registration of the two channels.

2.2.2.2 Localisation and tracking of individual VSGs in relation to the flagellar pocket entrance

For tracking experiments, cells of the 13-90 eYFP::MORN1 cell line were embedded in hydrogels composed of 10 % (w/v) PEG-VS and 5.6 % (w/v) HA-SH. Labelling with a nanomolar quantity of the Atto-647 N NHS dye ensured the indirect detection of single VSGs as 95 % of the cell surface is covered by VSG molecules. Initial tracking experiments by Marius Glogger showed that the supplementation of a picomolar quantity of reactive Atto-NHS dye in the background of the hydrogel allowed constant binding of the dye to the surface. This counteracted the bleaching of the dye and the label density was optimised. Label attempts with Setau-647-NHS were also performed. Setau-647-NHS is one of the brightest fluorophores currently available on the market and outperforms the Atto-dye with a better extinction coefficient. This was promising as a better signal-to-noise ratio could be achieved. NHS dyes

have the best bonding efficiency in the slightly alkaline range of pH 8.3. However, this pH induces stress in trypanosomes and caused the hydrogel to polymerise faster, resulting in a shorter time for the sample assembly. Optimal conditions were found at a pH of 7.0 - 7.5 and the hydrogel was set to this pH range as a standard. At these pH conditions, labelling could be established and reproduced with the Atto-647 N NHS dye. Unfortunately, this was not possible for the Setau-647-NHS dye.

VSG dynamics on 20 living, hydrogel-embedded trypanosomes were analysed with particular interest in the region of the FP entrance. First, the information on the VSG dynamics was recorded in 10,000 - 20,000 consecutive images. Second, the signals of the eYFP labelled hook complex were recorded in 10,000 consecutive images. In addition to identifying the single-molecule localisation by the known width and intensity profile as described in Section 4.7.1, a mask was placed around the profile of the cell or the hook complex to eliminate background signal. At least $2.36\,\mathrm{x}\,10^{4}$ VSG localisations with a localisation precision of 25 ± 10 nm were identified per cell. The localisation precision was determined from the error in the Gaussian fit of the x- and y-position. On average, $5.07\,\mathrm{x}\,10^{4} \pm 2.06\,\mathrm{x}\,10^{4}$ VSG localisations were detected. Overall, VSG localisations were detected on the entire cell surface. Areas were identified that were more densely populated and small areas which had almost no VSG localisations. For imaging of the hook complex, eYFP signals were detected with a localisation precision of 26 ± 9 nm. The eYFP label density was at least $1.1\,\mathrm{x}\,10^{3}$ localisations per µm^2 and was sufficient to map the hook complex. To reference the position of the hook complex in the example cell to the VSG localisations, a super-resolved image was generated from the sum of eYFP signals. Subsequently, the VSG localisations were superimposed on the super-resolved image of the hook complex (Figure 21). The areas of absent VSG localisations did not co-localise with the FP entrance region.

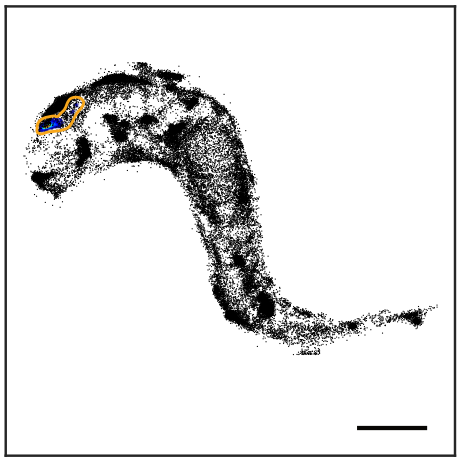

Figure 21: VSG single-molecule localisations in reference to the marker of the flagellar pocket entrance. Position of the hook complex in regard to the obtained eYFP::MORN1 localisations. The super-resolved image of the eYFP localisations is superimposed to the obtained VSG localisations. The position of the hook complex is highlighted by an orange outline. The scale bar is 2 µm.

In a previous study, the organisation of the inner leaflet of the plasma membrane in trypanosomes was examined with a fluorescent probe. Hereby, an inhomogeneous distribution of the probe was observed (Glogger et al., 2017b). In this present work, I investigated whether the inhomogeneous organisation of the inner leaflet has a potential influence on the distribution of GPI-anchored VSGs in the outer leaflet of the plasma membrane using the Ripley's analysis. It is a nearest neighbour approach and determines the deviation from a random distribution. The size of the potential clusters can then be estimated from the plot of the Ripley $L(r) - r$ function and corresponds to the maximum. Potential artificial clusters had to be removed before the approach was applied. Artificial clusters arise when the same immobile molecule was localised several times before it bleached. This situation is characterised by a clustering of localisations within the localisation precision. To ensure that the measured VSG distribution was not biased by artificial clustering, the set of localisations was treated as introduced by Annibale et al. (2011) before Ripley's analysis was performed. To this end, all localisations that re-appeared within the localisation precision within a dark time of 10 s (1,000 frames at 100 Hz) were removed from the data set. The graph of the Ripley $L(r) - r$ function averaged over all cells had its maximum at 225 ± 20 nm (Figure 22 A). The width of the $1\,\sigma$ confidence interval was broad and the associated cluster radii spanned 202 - 240 nm. A super-resolved image of the sample cell was generated from the sum of all localisations, and clusters of varying size were visible (Figure 22 B). This observation correlated with the broad confidence interval of the Ripley's analysis. Furthermore, a Ripley's analysis inherently assumes circular shapes of potential domains and the shape of the

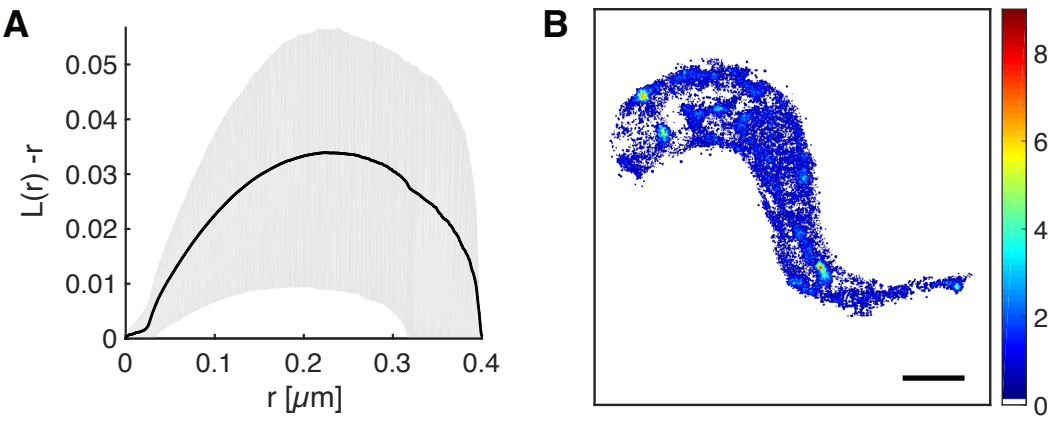

Figure 22: Cluster analysis of labelled surface VSGs. **A** Ripley's $L(r) - r$ analysis was performed on the VSG localisations on the cell surface. The $1\,\sigma$ confidence interval is displayed as grey area. The function averaged over 20 imaged trypanosomes (black line) and exhibited a maximum of 225 ± 20 nm, indicating the presence of clusters with this radius. **B** Super-resolved image generated by the sum of VSG localisations at a localisation precision of 26 nm. The quantity of localisations is colour-coded. The scale bar represents 2 µm and applies for A and B. Artificial clusters were removed in advance.

VSG clusters deviated from a perfect circular shape. On average, 863 ± 307 VSG localisations per µm^2 were present.

Trajectories were calculated from the obtained VSG localisations. On average, $4.3\,\mathrm{x}\,10^4 \pm 1.8\,\mathrm{x}\,10^4$ trajectories were found per cell. Figure 23 A shows the VSG trajectories generated from the localisations of the example cell in Figure 21. The distribution of the trajectory lengths of all 20 cells revealed that the number of long trajectories decreased exponentially and ~69 % of the trajectories were shorter than 10 steps (Figure 23 B). The average step length over all 20 cells was determined to be 13 steps with a maximal trajectory length of 757 steps.

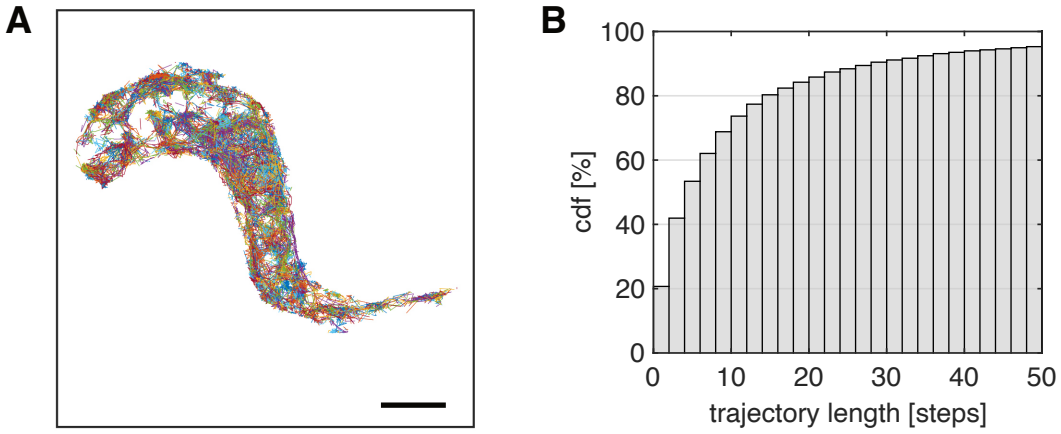

Figure 23: Characterisation of trajectories obtained from VSG localisations. **A** Distribution of trajectories generated from the example cell's single-molecule localisations, displayed in Figure 21. The scale bar is 2 µm. **B** Histogram displays the distribution of trajectory lengths as cumulative density function (cdf). It comprises all obtained trajectories of the 20 trypanosome surfaces studied.

In order to get a preliminary insight into whether deviations from free diffusion were present in the VSG dynamics, the analysis of the $1D$ displacements was conducted, in which free diffusion is characterised by a Gaussian distribution. For this purpose, the $1D$ displacements of all obtained trajectories in x- and y-direction of the 20 cells were pooled and plotted in a histogram (Figure 24). This showed that the distribution deviated from a Gaussian distribution and that a greater number of short steps were present. To evaluate short trajectories for a potential influence of directed forces, an approach was adapted, which is explained in the next section.

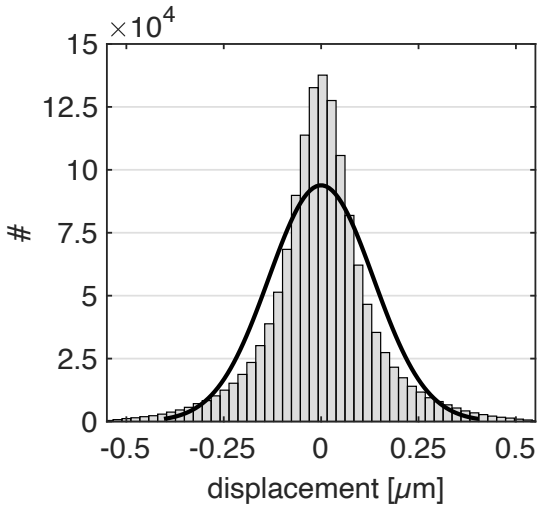

Figure 24: 1D displacements of VSG trajectories obtained from tracking labelled VSGs on eYFP::MORN1 trypanosomes. The histogram comprises the displacements in x- and y-direction of all 20 cells. The black line indicates the fit of a gaussian distribution.

2.3 ShortTrAn: Implementation and validation of an algorithm for the analysis of short trajectories

Most of the trajectories obtained when tracking labelled VSGs on the surface of trypanosomes were less than 10 steps long and thus relatively short. This was primarily due to the small size and strong curvature of the parasites. Therefore, an evaluation method was needed to determine a reliable diffusion coefficient from short trajectories. In addition, it should be investigated whether directional forces are involved in the rapid turnover of the VSG coat. The adaptation and extension of the method introduced by Hoze et al. (2012) enabled me to evaluate the displacements in terms of diffusion and directed motion and will be referred to as shortTrAn (**short** **Tr**ajectory **An**alysis) in the following. The results were then presented in diffusion and directed motion maps. This offered me the opportunity to subsequently draw a conclusion about the locally predominant type of motion on the trypanosome surface. Prior to the evaluation of VSG trajectories by shortTrAn, the adapted algorithm was carefully validated.

2.3.1 Implementation of shortTrAn and its extensions

For implementation, data sets obtained from tracking labelled VSGs on the trypanosome surface of the eYFP::MORN1 cell line were employed. The shortTrAn routine was established in Python in collaboration with Torsten Paul und Philip Kollmannsberger. Each data set contained the positional information of all localisations corresponding to the trajectories collected from one cell. A data set comprised on average, $4.3\,\mathrm{x}\,10^4 \pm 1.8\,\mathrm{x}\,10^4$ trajectories. In addition to the local information, the matrices provided information about the trajectory identity and the temporal information encoded as the frame number. An overview of the implementation of shortTrAn is displayed in Figure 25.

First, the position unit was transformed from camera pixelation to a nanometre resolution. Subsequent padding of 160 empty nm-spaces on each side of the image, corresponding to one camera pixel, provided sufficient space for later binning. In this work, trajectories of all length were analysed to calculate local diffusion coefficients and local velocities. All trajectories were considered reliable due to the fit of the localisation parameters (error, width and intensity) to the Atto-647 N footprint, the application of a cell mask and the verification of the correct connection of the localisations to a trajectory by plotting obtained trajectories onto the corresponding image sequences.

Trajectories were decomposed in one step events and for each the displacement was determined. The diffusion coefficient and velocity was calculated for each displacement. When calculating these quantities, I introduced the first extension namely

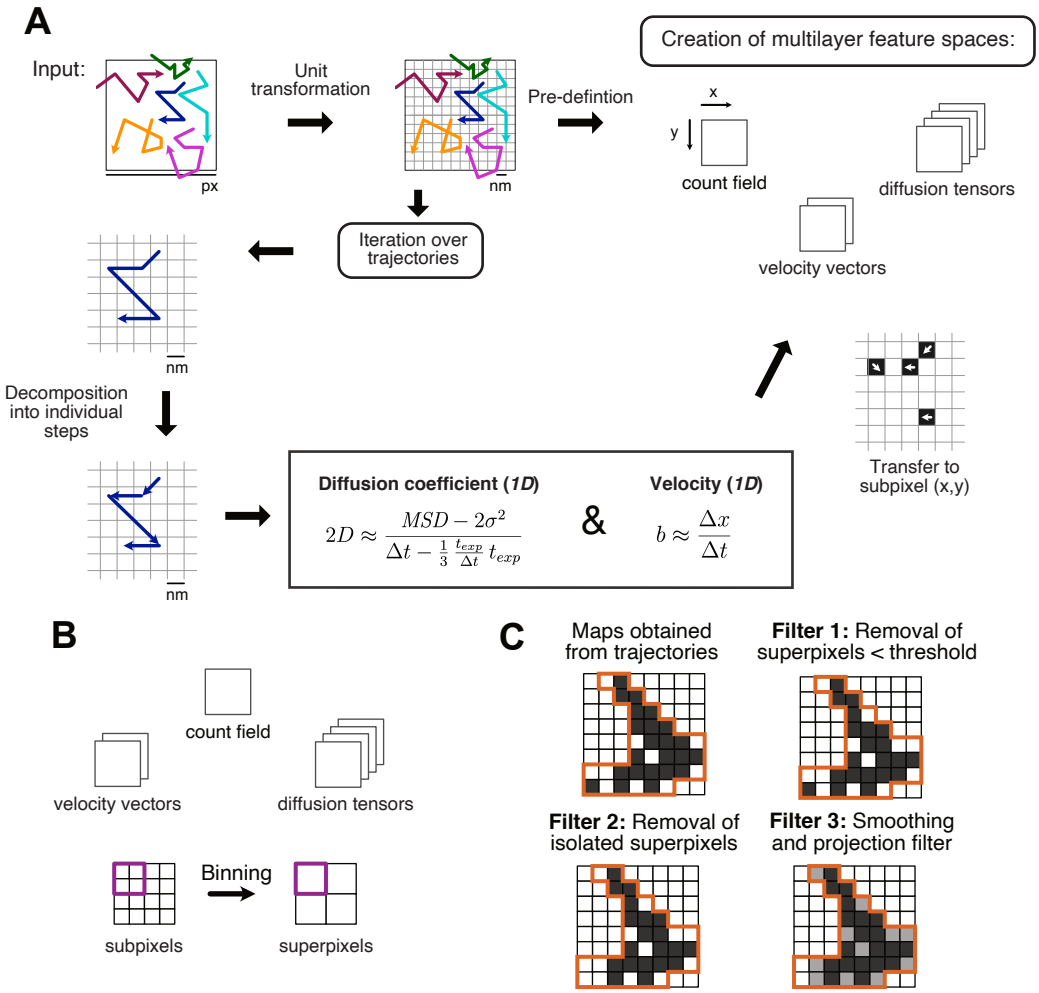

Figure 25: Workflow of the evaluation of trajectories by shortTrAn. **A** For shortTrAn, the positions in pixel (px) of the trajectories and the according temporal information served as input. First, the positional information was refined to a subpixel scale corresponding to one nanometer. Iteration over all trajectories facilitated the analysis. Each trajectory was decomposed into its individual steps and for each the diffusion coefficient and velocity was calculated. The results were then transferred to the subpixel of the steps origin in the pre-defined feature spaces, that represented the image. The count field comprised the number of steps originating from the subpixels. The velocity vector matrices contained the results on the velocities in x- or y-direction. The diffusion tensor matrices corresponded to the diffusion coefficients of the xx-, xy-, yx- or yy-direction. **B** Binning of the subpixels to larger superpixels improved the local statistics. **C** Spatial filters removed superpixels with low statistics and removed entries from isolated superpixels. Finally, the data was smoothed out and a projection filter was applied on the superpixels at the rim of the surface projection. $1D$, one-dimensional; b, velocity; D, diffusion coefficient; MSD, mean-squared displacement; Δx, displacement, Δt, change in time; t_{exp}, exposure time; σ, localisation precision.

taking into account the localisation errors inherent to single-particle tracking (SPT). This is explained in more detail in the following Section 2.3.2. The results were then assigned to the location in predefined multilayer feature spaces of which the substep originated. Three types of predefined feature spaces were created: (i) The count

field contained the number of substeps originating from position x, y. (ii) The tensor field comprised the results of the tensor components D_{xx}, D_{xy} , D_{yx} and D_{yy}. (iii) The one-dimensional velocities of the motion were placed in the corresponding vector fields b_x and b_x. The subsequent binning of the entries in the feature space to superpixels improved local statistics and averaged over the number of contributing entries. Different binning factors 100, 120, 140 and 160 were tested which corresponded to the size of the superpixels, e.g. a binning factor of 100 was equivalent to superpixels of the size 100 x 100 nm. The statistics per superpixel increased significantly with the binning factor. While 50 % of the total superpixels were populated with at least 6 counts for the binning factor 100, 50 % of the total superpixels were populated with at least 8 counts for the binning factor 120. The 50 % benchmark increased further to 10 and 13 counts for the binning factors 140 and 160, respectively. The results are displayed in Figure 26. The binning factor of 160 was chosen as a trade-off to achieve good statistics without loosing to much resolution.

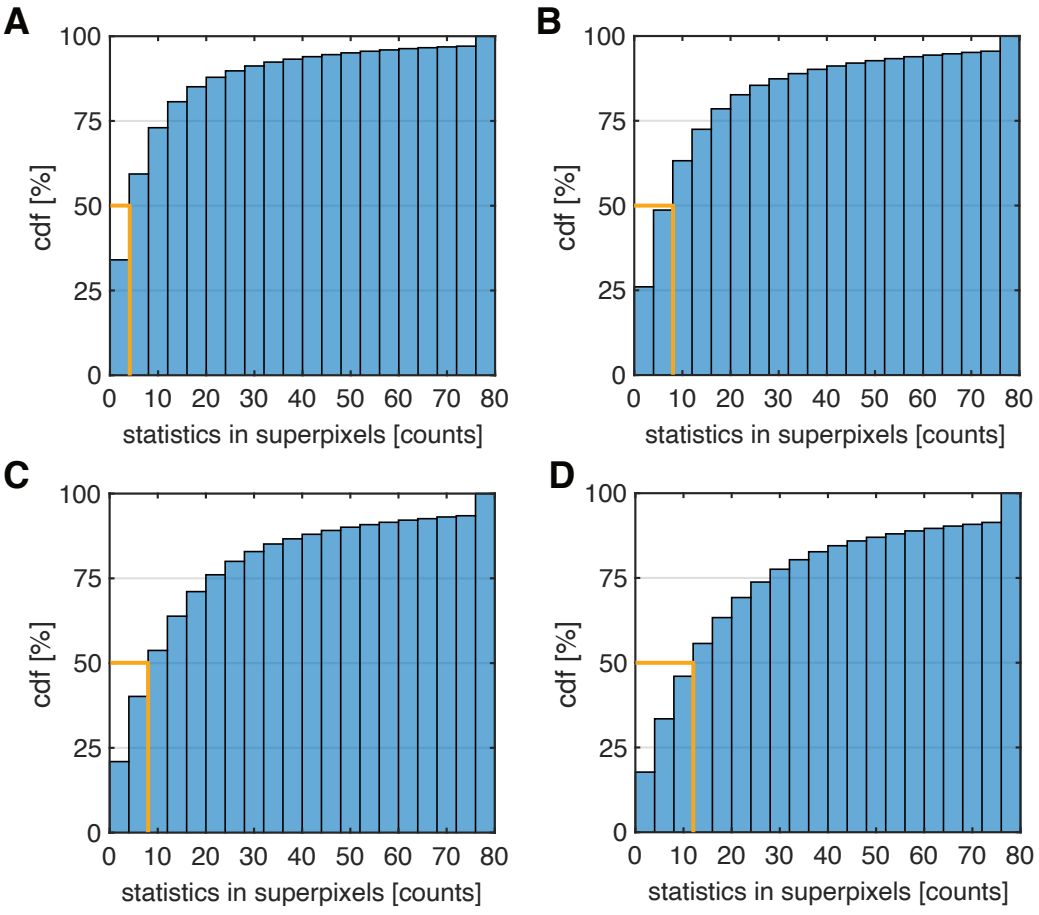

Figure 26: Correlation of binning factors and statistics in superpixels. All 20 data sets were analysed and the statistics of the superpixels are shown as cumulative density functions (cdf). A cut off was set at 80 counts and superpixels with a count value greater than 80 were assigned with 80. Binning factors of 100 (A), 120 (B), 140 (C), 160 (D) were tested. The orange line represents 50 % of the total superpixels.

Three spatial filters were then applied to the feature spaces: The first filter removed entries in superpixels which had low statistics. For this purpose, a threshold was applied which removed entries from superpixels containing ≤ 5 data points (Implementation explained in Section 4.7.11.1, script 7). The second filter removed entries from isolated superpixels. For this, a kernel of the size 3 was utilised as superpixels located diagonally were considered to be within the immediate environment. Its implementation is described in script 7 in Section 4.7.11.1. The third filter was a combination of two filters. Filter 3.1 smoothed out the data assuming similar conditions on the scale of neighbouring superpixels (Section 4.7.11.1, Equation 30). The implementation of Filter 3.2 became necessary as artefacts at the rim of the $3D$ to $2D$ projection of the trypanosome surfaces arose due to the evaluation by shortTrAn. The observed artefacts are more precisely explained in Section 2.3.3.3. Superpixels at the rim of the projection were populated with the results of the projection Filter 3.2, while superpixels of the surface area were filled with the results of the smoothing Filter 3.1 as depicted in Figure 27. The implementation of Filter 3.1 and Filter 3.2 is described in script 8 in Section 4.7.11.1.

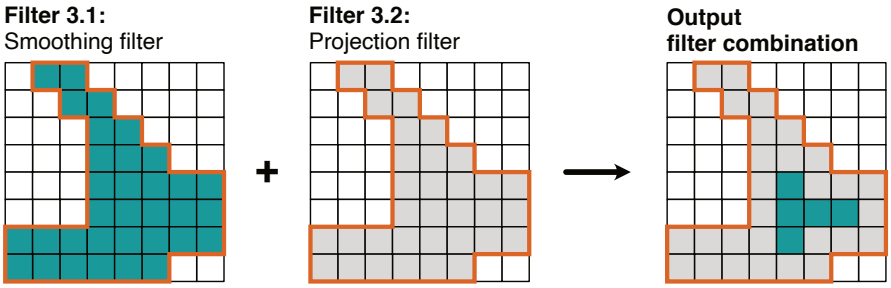

Figure 27: Scheme of the third spatial filter. Illustration of the combination of Filter 3.1 (green) and 3.2 (grey) on the superpixels in the feature spaces resembling the projection of the trypanosome surface.

Finally, the feature spaces were used to built diffusion and directed motion maps of the trypanosome surface. The results of the evaluation in terms of a diffusion scenario were presented in an ellipse plot. This made it possible to obtain information on the (an)isotropy of the diffusion and was an extension to the original method (Hoze et al., 2012; Hoze and Holcman, 2014). The eigenvalues and eigenvectors were calculated from the diffusion tensors using a transformation matrix. The eigenvalues reflected the diffusion value of the major and minor axes, while the eigenvectors defined the angle of entry of the ellipse into the plot. The angle of the orientation was then calculated with a transformation matrix. The validation of the correct orientation is described in Section 2.3.3.1. The ellipses were colour-coded, representing the local diffusion coefficient in $2D$. The results of the evaluation in terms of a directed motion scenario were illustrated in three maps. The local velocities were calculated from the one-dimensional velocities, the directed motion vectors. The first map was a heat map, depicting the amplitude of the local velocity colour-coded, also called

velocity map. The second map was a quiver plot, indicating the direction of the velocity and validation of the quiver orientation is shown in Section 2.3.3.2. The third map was introduced by the consideration of the localisation errors in the measured velocities. The relative standard errors in the local velocities were represented by a colour code. The calculation of the relative standard error is explained in the following Section 2.3.2.

2.3.2 Consideration of the localisation errors in shortTrAn

The technique of SPT suffers from sampling errors which are known as the static localisation error and the dynamic localisation error (Savin and Doyle, 2005). The static localisation error results from the limitation in the detection of a single molecule, the localisation precision σ. For the later consideration of the static localisation error, σ was determined by three approaches. It was obtained (i) from the error associated with the determination of the x- and y-position by the fit of a $2D$ Gaussian to the intensity profile of the single molecules. σ was extracted from all VSG localisations of all 20 analysed data sets and was 25 nm. (ii) In theory, the localisation precision is defined by Ober et al. (2004):

$$\sigma_i = \sqrt{\frac{w_i^2}{N_i} + \frac{a^2/12}{N_i} + \frac{8\pi w_i^4 b^2}{a^2 N_i^2}}. \tag{6}$$

w_i was the width of the Gaussian, N_i was the number of emitted photons, a was the pixel size and b was the background noise. The number of incoming photons for each localisation (N_i) was derived from the counts detected by the EMCCD camera as explained in Section 4.7.6. For the determination of the theoretical σ, localisations of eleven immobile Atto-647 N NHS emitters were extracted with a minimum of 100 localisations and was on average 28 nm. Furthermore, σ can be assessed (iii) from the standard deviation of the x- and y-position of an immobile emitter (Thompson et al., 2002). For this purpose, trypanosomes incubated with a nanomolar quantity of Atto-647 N-dye were fixed with methanol (4.6.4) as Tanaka et al. (2010) showed that formaldehyde is insufficient to immobilise membrane anchored proteins. Fixed trypanosomes were then embedded in hydrogels for the measurements. Trajectories were generated from the obtained localisations to extract localisations belonging to one immobilised emitter. Eleven emitters were analysed, which were of a minimum step length of 100 steps to guarantee that a sufficient number of localisations sampled the range of the localisation precision. The smallest standard deviation found was 26 nm and corresponded to a trajectory of a length of 480 steps. The smallest standard deviation was chosen because by then the emitter was most likely

completely immobilised. For the cases which covered a larger area, a residual movement could not be excluded. The determined localisation precisions by all three approaches were in good agreement with each other. Hence, the averaged σ of all three approaches with 26 nm was used for the consideration of the static localisation error.
The dynamic localisation error originates from the exposure time needed to collect enough photons from a single molecule. Consequently, a moving emitter is imaged at a position averaged over the exposure time.

For the calculated diffusion coefficient by shortTrAn, the correction of both errors is particularly important because the calculation is based on the absolute values of the $MSD\,(\Delta t = 1)$. The diffusion coefficient in one dimension is frequently derived by:

$$2D = \frac{MSD}{\Delta t}. \tag{7}$$

Equation 7 is a simplified version of Equation 25 used to determine the one-dimensional diffusion coefficient in shortTrAn. In the scientific community, the static localisation error was recognised almost two decades ago and is corrected for by $MSD - 2\,\sigma^{\,2}$ for one dimension, where σ denotes the localisation precision (Martin et al., 2002; Savin and Doyle, 2005; Backlund et al., 2015). The dynamic localisation error impacts the effective time point at which a molecule is localised and was accounted by $\Delta t - \frac{1}{3}\frac{t_{exp}}{\Delta t}t_{exp}$ with Δt indicating the time lag, and t_{exp} the exposure time (Savin and Doyle, 2005; Berglund, 2010; Michalet and Berglund, 2012; Backlund et al., 2015). Consideration of both corrections resulted in Equation 8:

$$2D = \frac{MSD - 2\sigma^2}{\Delta t - \frac{1}{3}\,\frac{t_{exp}}{\Delta t}\,t_{exp}}. \tag{8}$$

In contrast to the consideration of the localisation errors in the diffusion coefficient, the consideration of the localisation errors in the calculation of a velocity had not been established before. The static localisation error is taken into account on the basis of the following consideration: For the calculation of the displacement and the associated velocity, the particle has to be localised twice. Each localisation suffers from the limited localisation precision σ. Hence in a conservative estimate, the systematic error (err_Δ) of the measured displacement in one dimension was $\pm\,2\,\sigma$. In order to indicate the share of the error in the mean velocity ($\overline{v}$) registered to a superpixel, the relative error $err_{\overline{v}}$ in $2D$ was calculated by the classical error propagation based on its share in the one-dimensional velocities (v_x, v_y):

$$\overline{v} = \sqrt{{v_x}^2 + {v_y}^2}.$$

The error propagation started with the calculation of the associated error in ${v_x}^2$ or ${v_y}^2$ and resulted in:

$$\Delta({v_x}^2) = |2| * \frac{err_\Delta}{v_x} * {v_x}^2 \qquad \text{or} \qquad \Delta({v_y}^2) = |2| * \frac{err_\Delta}{v_y} * {v_y}^2 \tag{9}$$

with $err_\Delta = (2\sigma)/\Delta t$ in one dimension.
Subsequently, derived errors were added according the error propagation of a sum:

$$\Delta(({v_x}^2) + ({v_y}^2)) = \Delta({v_x}^2) + \Delta({v_y}^2). \tag{10}$$

The result served as input in the error propagation of the square root to yield the relative error and was considered as follows:

$$err_{\overline{v}} = |0.5| * \frac{\Delta(({v_x}^2) + ({v_y}^2))}{({v_x}^2 + {v_y}^2)}. \tag{11}$$

The calculation resulted eventually in the relative standard error of the mean velocity $SE_v = \frac{err_{\overline{v}}}{\sqrt{N}}$ by division by the square root of the number of displacements (N) registered to the corresponding superpixel.

If the resulting velocity is solely due to the inherent localisation precision of the measurement, the relative standard error equaled 1. The results of the local relative standard errors were displayed in a heat map.
The dynamic localisation error could be neglected because neglecting the dynamic localisation error may result in an underestimation of the velocity. Thus, it is more likely that an existing directed motion was rejected in favour of diffusion than that a directed motion was introduced accidentally.

In summary, the successful implementation of the approach by Hoze et al. (2012) to our data sets was complemented by the following extensions: (i) Information on the (an)isotropy of the diffusion was decoded in the diffusion map by ellipses, (ii) the consideration of the static and dynamic localisation error and (iii) the introduction of an spatial projection filter at the trypanosome rim. The shortTrAn algorithm was then further validated which is addressed in the following section.

2.3.3 Validation of the shortTrAn algorithm

In order to validate the shortTrAn algorithm, several aspects were scrutinised: the ellipse orientation in diffusion maps, the quiver orientation in directed motion maps as well as the quiver assignment to the superpixels. Additionally, trajectories of random walk simulations with a defined diffusion coefficient were analysed to identify potential artefacts arising by shortTrAn.

2.3.3.1 Ellipse orientation in diffusion maps

For placing of the ellipses representing the diffusion tensors in the right orientation, the eigenvectors were calculated from the tensor components. The final ellipse angle was determined from the eigenvectors using a transformation matrix. The correct transformation matrix was identified by comparison of ellipses generated with defined axis and angle of orientation (input) with the ellipses generated (output) by using a defined transformation matrix[2]. For this, the eigenvalues and eigenvectors were calculated from the defined ellipse parameters. Then the eigenvectors were used to determine the angle of the ellipse by different transformation matrices. The transformation matrix was approved when the ellipse from the input matched the ellipse generated by the predefined axis as well as the newly determined angle for the orientation. The transformation matrix of [cos,-sin;sin,cos] yielded an ellipse with the same orientation as the ellipse from the input. The validation of the orientation is schematically displayed in Figure 28.

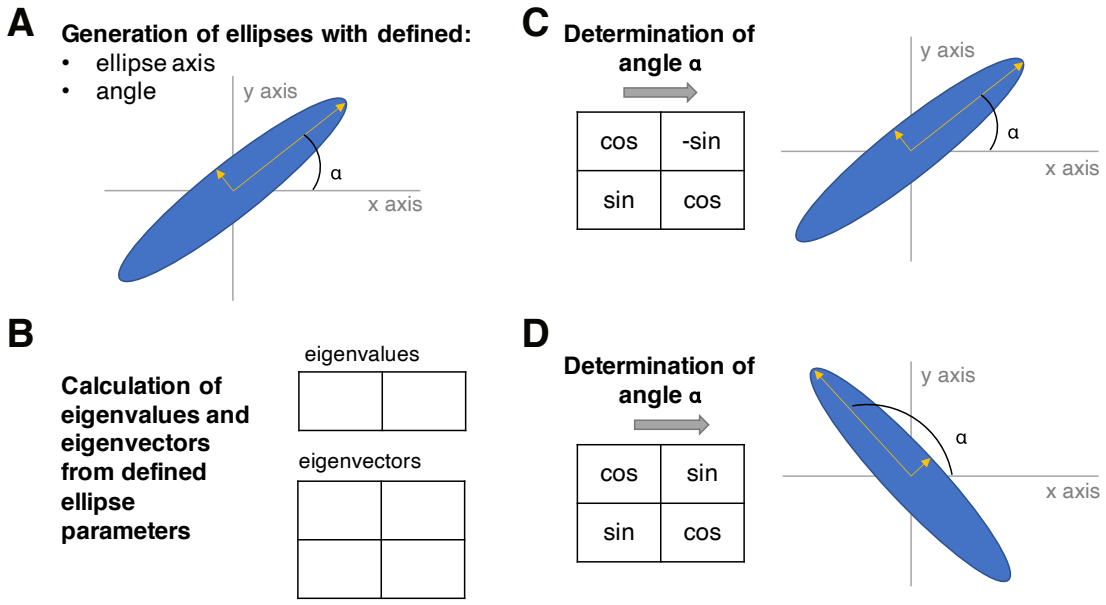

Figure 28: Scheme of the verification of the ellipses' orientation in diffusion maps. Ellipses with defined parameters for the ellipse axis and angles served as input (**A**). The eigenvalues and eigenvectors were calculated from the defined ellipse parameters (**B**). Different transformation matrices were applied to determine the angle of the ellipse orientation (**C** and **D**). The transformation matrix which resulted in a correctly oriented ellipse (matching the input) was chosen for further analysis.

[2]Jupyter Notebook written by Torsten Paul

2.3.3.2 Quiver orientation in directed motion maps

The direction of the individual trajectory steps was encoded using a quiver plot. The arrows in the superpixels should show the direction of the outgoing steps and thus indicate the average direction of the steps taken from the superpixels. To verify that the information was registered in the superpixel of the outgoing step and that it followed the course of the step, an exemplary trajectory was analysed with shortTrAn. The quiver plot was then plotted onto the trajectory course (Figure 29). Inspection of the generated quiver plot verified that the arrows were successfully placed in superpixels of the outgoing step. The arrow orientations followed the course of the trajectory's steps which was colour-coded from black to yellow.

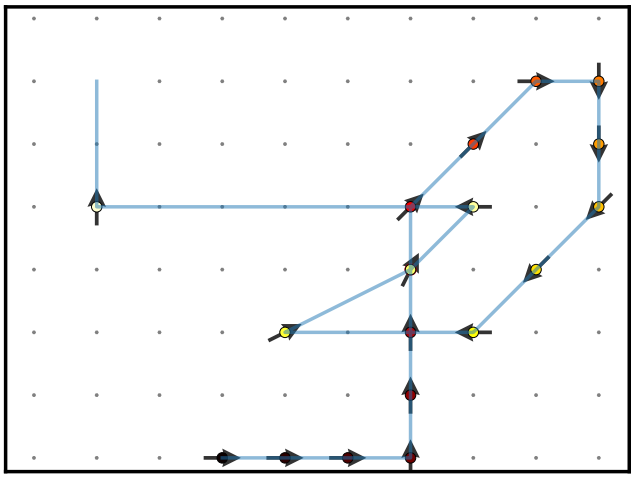

Figure 29: Verification of the arrow insertions in quiver plots of directed motion maps. Arrows indicate the direction of the velocity calculated from substeps of the exemplary trajectory. The blue line represents the course of the trajectory. The temporal progress of the trajectory's substeps is visualised by the colour code of the circles placed at the centre of the superpixels (from black to light yellow). The small dots represent the centre of empty superpixels.

2.3.3.3 Random walk simulations revealed a projection artefact in superpixels at the surface rim

Measurements of VSG dynamics in the plasma membrane of living trypanosomes were a projection of the dynamics information in $3D$ to $2D$. When proteins follow the $3D$ shape of the plasma membrane they move out of focus. Consequently, the information of the dynamics can not be registered. Hence, superpixels at the rim hold only informations pointing in the centre of the surface instead of holding all directions. This can lead to artefacts that need to be taken care of.

To validate the correct representation of local diffusion coefficients and velocities in shortTrAn maps, especially in superpixels at the rim of the surface, random walk simulations were performed on a trypanosome-shaped mask. The mask was obtained from a count field derived from the analysis of VSG trajectories with shortTrAn on

living trypanosomes. For simulations, the resolution of the mask was refined from 160 nm pixels to 10 nm pixels. To resemble the $3D$ plasticity of the trypanosomes in a simplified approach, the mask was doubled. When a particle reached the rim, it was placed on the other mask. 2,000 dimensionless particles were simulated on the mask with a diffusion coefficient of 1.00 µm^2/s and then analysed with shortTrAn.

In the analysis that used only the smoothing filter (Filter 3.1) as third spatial filter (Equation 30), an accumulation of high velocities in superpixels located at the rim of the mask was observed in the velocity maps (Figure 30 A). The comparison of the average velocity of superpixels from the outermost two rows at the rim with 2.39 µm/s with the remaining superpixels in the centre with 1.37 µm/s reflected this observation (Figure 30 B). To this end, a projection filter was introduced on the

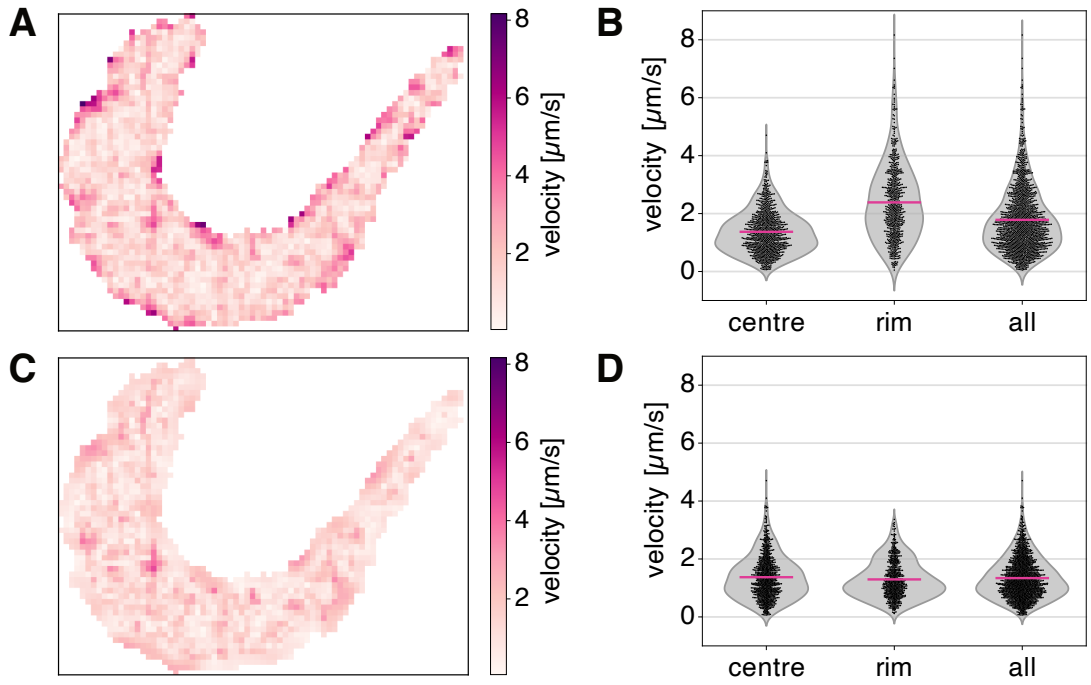

Figure 30: Random walk simulations on a trypanosome mask revealed an accumulation of high velocities at the rim. **A** Velocity map showing the superpixels' velocity after application of the third spatial filter which only smoothed out the data. **B** Violin plots confirmed the increased number of superpixels with a high velocity at the rim compared to superpixels in the centre. The violin representing the velocities of superpixels at the rim includes the outer two rows of superpixels. The group 'centre' comprised all remaining superpixels. Magenta lines indicate the average velocity (centre: 1.37 µm/s, rim: 2.39 µm/s). The averaged velocity comprising all superixels is shown in the right violin (all: 1.78 µm/s). **C** Velocity map after the application of the projection filter to superpixels at the rim that corrected the accumulation of high velocities. **D** Violin plots display the deviation in local velocities of superpixels in the centre, at the rim, and of the entire mask after the application of the projection filter. The magenta line represents the average velocity (centre: 1.37 µm/s (N = 995 superpixels), rim: 1.29 µm/s (N = 681 superpixels), all: 1.34 µm/s (N = 1676 superpixels)).

feature spaces used for the generation of the maps. The filter was a Gaussian filter with a radius of 6 superpixels, a standard deviation σ for the Gaussian kernel of 1, and used a constant mode with a value of 0. These parameters were found by application of the projection filter to the outermost two rows of superpixels and the strength and width of the filter was tuned until the average velocity of 1.29 µm/s fitted the average velocity of the superpixels in the centre (Figure 30 C , D). The average velocity of all superpixels decreased from 1.78 µm/s to 1.34 µm/s.

Next, diffusion maps representing the local diffusion coefficients were examined for artefacts. When the third spatial filter was solely applied to smooth out the data, no accumulation of high diffusion coefficients was observed in superpixels at the surface rim (Figure 31 A). The averaged diffusion coefficient of superpixels at the rim was 0.66 µm^2/s and thus lower than the average diffusion coefficient of the remaining superpixels in the centre with 0.93 µm^2/s (Figure 31 A, C). Although the application of the projection filter slightly reduced the diffusion coefficient from 0.66 µm^2/s to 0.59 µm^2/s in ellipses at the rim, its influence on the averaged diffusion coefficient for the whole cell was minor (Figure 31 C, D). The averaged diffusion coefficient for the whole cell was 0.82 µm^2/s without the projection filter and 0.79 µm^2/s with the filter applied.
The ellipse shape was used to draw conclusions about the diffusion behaviour. Isotropic diffusion is indicated by a circle. If particles diffuse freely through the superpixels, movements in all directions can be registered which results in a circle. If the ellipse is elongated, an anistropic diffusion is implied, which indicates a preferred direction in the diffusion. The deviation from a circle and thus from an isotropic diffusion was determined by means of the eccentricity. The eccentricity is defined in a range $\varepsilon \in [0,1]$ with the extrema 0 and 1 indicating a circle and line, respectively. When the shape of the ellipses at the rim of the surface was examined more closely, the shapes differed noticeably from the ellipses in the centre (Figure 31 B). The eccentricity of the ellipses at the rim was on average 0.70 and hence higher than the eccentricity of ellipses at the centre with 0.58 (Figure 31 E, F). Thus, free simulated diffusion appeared more anisotropic in superpixels at the rim. Application of the introduced projection filter resulted in fitting of the eccentricity of ellipses at the rim to that in the centre and eventually amounted to 0.56. For this reason, the projection filter was also applied to feature spaces which were used to create the diffusion maps. Even though the filter resulted in a minimal decrease in the diffusion coefficient, the correction on the eccentricity was more relevant as it later was used as a decision parameter on the predominant motion.

In conclusion, evaluation of random walk simulations on a trypanosome mask using shortTrAn showed artefacts in the maps, especially at the rim of the cell surface mask. Free diffusion appeared to be anisotropic and an accumulation of high veloc-

ities was observed. Both artefacts were aligned to the parameters in the centre by introducing a projection filter on superpixels at the rim.

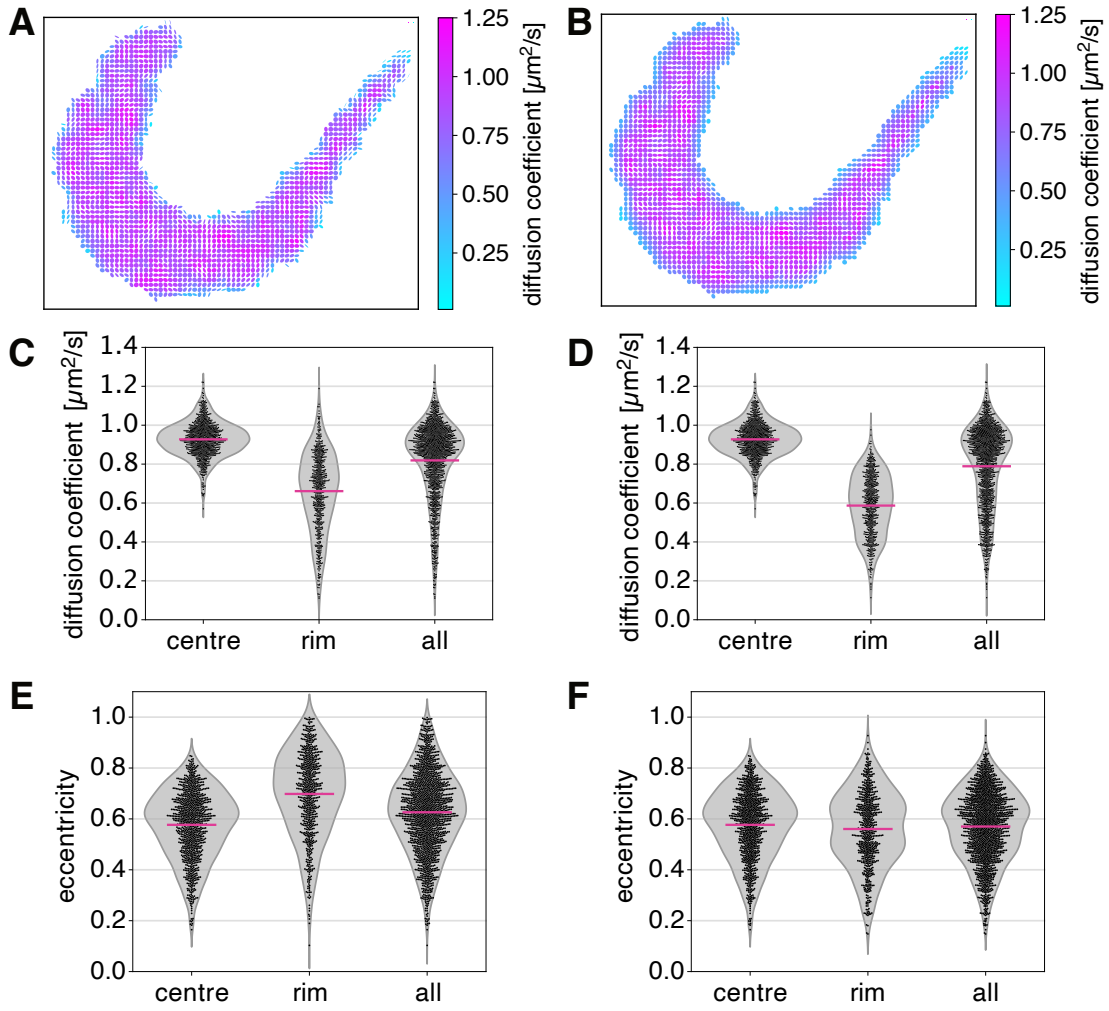

Figure 31: Influence of the projection filter on the local diffusion coefficients and the eccentricities of ellipses. **A-B** Diffusion maps generated from a random walk simulation which where only smoothed out (A) or after the additional application of the projection filter (B). The colour code of the ellipses displays the local diffusion coefficient. The shape of the ellipses indicates anisotropic (elongated) or isotropic (roundish) diffusion behaviour. **C** Violin plots displaying the local diffusion coefficients of superpixels located in the centre in comparison with superpixels of the two outer rows of the surface before the projection filter was applied. Magenta lines depict the average diffusion coefficients (centre: 0.93 µm^2/s, rim: 0.66 µm^2/s, all: 0.82 µm^2/s). **D** Distribution of the local diffusion coefficients after application of the projection filter. Magenta lines represent the average diffusion coefficients (centre: 0.93 µm^2/s; rim: 0.59 µm^2/s, all: 0.79 µm^2/s). **E** Violin plots showing the deviation in the ellipse eccentricity of superpixels in the centre compared to superpixels located in the two outer rows at the rim of the surface before the application of the projection filter. The magenta lines indicate the average eccentricity (centre: 0.70, rim: 0.57, all: 0.63). **F** Distribution of local eccentricities after application of the projection filter with a magenta line depicting the average eccentricity (centre: 0.57 (N = 995 superpixels), rim: 0.56 (N = 1676 superpixels), all: 0.57 (N = 681 superpixels)).

2.4 Evaluation of the single-molecule trajectories using shortTrAn

The trajectories obtained from tracking individual surface VSGs on the cell line 13-90 eYFP::MORN1 were analysed with shortTrAn in two distinct scenarios and the results are presented in the following. The following input parameters were set in the analysis with shortTrAn: the binning factor was 160 nm superpixels, the smoothing filter (Filter 3.1) utilised a box kernel of the size 3 superpixels as well as the projection filter (Filter 3.2) was applied to the two outermost rows of superpixels. In addition, localisation errors were taken into account and the localisation precision was 26 nm.

2.4.1 VSG dynamics evaluated by a diffusion scenario show local heterogeneities on the trypanosome surface

Evaluation of the 20 cells showed a spatial heterogeneity in the local diffusion coefficients. An exemplary ellipse plot is presented in Figure 32 A. The colour code indicates the local $2D$ diffusion coefficient determined by the mean of both diffusion tensor. The shape of the ellipses allowed for the distinction of isotropic (circle) and anisotropic (ellipse) diffusion. The deviation from a circle and thus from isotropic diffusion was determined by means of the eccentricity.
For the exemplary cell, the local diffusion coefficients ranged from $0.07\,\mu m^2/s$ to $2.60\,\mu m^2/s$ with a median of $0.81\,\mu m^2/s$ (Figure 32 C). The overall diffusion coefficient of all 20 cells was comparable and the average over all 20 cells was $1.00 \pm 0.15\,\mu m^2/s$ (Figure 32 C). The outline of the hook complexes were depicted in the diffusion maps to reference the entrance to the FP. The part wrapped around the FP neck was highlighted in red. Extraction of the FP entrance (FPE) region allowed for the comparison of the amplitude of the diffusion coefficients and the eccentricity of the ellipses with the ellipses from the entire surface area (Figure 32 B). The local diffusion coefficients in the FPE region of the exemplary cell varied from $0.20\,\mu m^2/s$ to $1.88\,\mu m^2/s$ with a median of $0.62\,\mu m^2/s$ (Figure 32 C). The average diffusion coefficients of the FPE region over all 20 cells was $0.88 \pm 0.32\,\mu m^2/s$. The averaged diffusion coefficient of the FPE regions was not significant different to the averaged diffusion coefficient of the entire cell surfaces ($1.00 \pm 0.15\,\mu m^2/s$).
Similarly, the eccentricities in the FPE regions were not distinct in comparison to the entire cell surface. For the exemplary cell, the eccentricity ranged from 0.27 to 0.99 with a median of 0.82 for the entire surface area, while the FPE region showed an eccentricity from 0.27 to 0.99 with a median of 0.79. The average eccentricity over all 20 cell surfaces was 0.78 ± 0.04 and over all FP regions was 0.79 ± 0.06. It

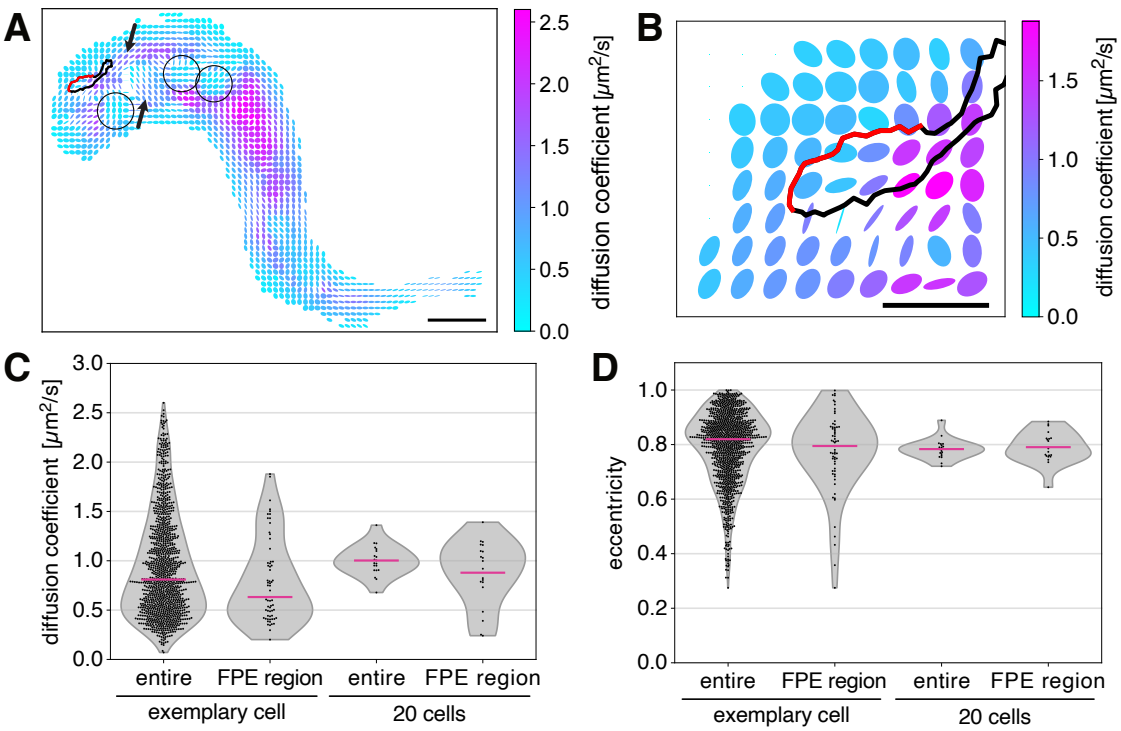

Figure 32: Characterisation of VSG dynamics recorded on 13-90 eYFP::MORN1 trypanosomes in the light of diffusion. **A** Representative diffusion map depicts the local diffusion coefficients colour-coded, while the shape of the ellipses indicates isotropic (circle) or anisotropic (ellipse) diffusion. The outline of the hook complex is shown by a black line with a red highlighting indicating the part wrapped around the FP neck marking the region of the FP entrance (FPE). Circles mark domains of low diffusion coefficients and arrows point to streams of aligned and elongated ellipses. The scale bar is 1.6 µm. **B** FPE region of the exemplary cell. The scale bar is 0.5 µm. **C** Violin plots display the distribution of local diffusion coefficients of the exemplary cell and the averaged coefficients of all 20 trypanosomes. The distribution of the entire surface is compared to the FPE region. Magenta lines depict the median for the exemplary cell (entire: 0.81 $\mu m^2/s$, FPE region: 0.63 $\mu m^2/s$) and the average over all 20 cells (entire: 1.00 $\mu m^2/s$, FPE region: 0.88 $\mu m^2/s$). **D** Violin plots show the distribution of local eccentricities of the exemplary cell and averaged eccentricities of all 20 investigated cells. Hereby, the local eccentricities of the entire surface are compared to the FPE regions. The median of the local eccentricities of the exemplary cell (entire: 0.82 (N = 1124 superpixels), FPE region: 0.79 (N = 63 superpixels)) or the average eccentricity over all 20 cells (entire: 0.78, FPE region: 0.79) is represented by magenta lines.

should be noted that FPE regions were mostly located at the surface rim and thus in the region that is affected by the projection artefact. An overview of all 20 diffusion maps is presented in Figure 51 (Appendix).

However, two observations were made that occurred without a correlation to the FPE regions. In the maps of each cell, at least one well-defined domain with low local diffusion coefficients could be identified, but generally several of these were present. These are encircled in the diffusion map of the exemplary cell in Figure 32 A. Another distinctive feature seen in the ellipse plot were streams of aligned

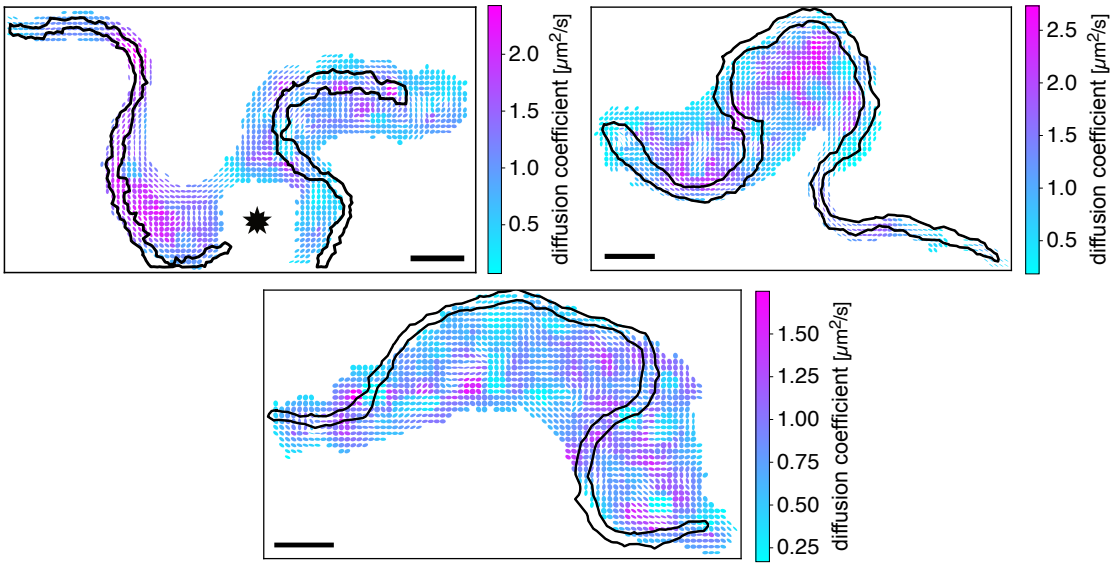

Figure 33: Characterisation of VSG dynamics by the diffusion scenario in relation to the flagellum. Three representative diffusion maps are displayed. The $2D$ diffusion coefficient is colour-coded. The shape of the ellipses indicates isotropic (circle) or anisotropic (ellipse) diffusion. The black outline represents the spatial progression of the flagellum on the surface. The area outshone by a TS bead is marked by a star. The scale bars are 1.6 µm.

elongated ellipses indicating an anisotropic diffusion. In Figure 32 A arrows indicate a stream of elongated ellipses. In order to test a correlation of the streams with the flagellum, the spatial course of the flagellum was determined using the transmitted light images as the 13-90 eYFP::MORN1 cell line did not harbour a fluorescent marker for the flagellum. No correlation was found when it was compared with the regions of the streams. Additionally, tracking of labelled surface VSGs was conducted on 10 cells of the 13-90 cell line expressing kinesin-MORN::eYFP, a marker for the axoneme of the flagellum. Three representative diffusion maps with the outline of the flagellum are depicted in Figure 33. Sporadically anisotropic diffusion runs along the flagellum. At the same time, domains of slow and isotropic diffusion are located at the flagellum. Based on both observations no clear correlation could be found here either.

2.4.2 High velocities are locally present on the trypanosome surface in the evaluation of a directed motion scenario

Evaluation of the displacements by a directed motion scenario showed high velocities were locally present on the trypanosome surface of all 20 cells. The results were displayed in a heat map showing the amplitude of the local velocities (velocity map), a quiver plot indicating the direction of the local velocities and a heat map representing the local relative standard error SE_v, which was a indicator for

the reliability of the measured velocities. A large variety in local velocities was observed within one cell and an exemplary velocity map is shown in Figure 34 A. The velocities of the exemplary cells ranged from 0.05 µm/s to 10.35 µm/s with a median of 1.75 µm/s. In comparison to the local velocities on one cell, the averaged velocity of all 20 cells was similar and found to be 1.99 ± 0.20 µm/s (Figure 34 C). The location of the hook complex was marked by a black outline. The red part of the outline highlights the part which was wrapped around the FP neck and marks the FPE region. In order to identify potential directing forces near the entrance to the FP, the FPE region was extracted and compared to the entire cell surface (Figure 34 B, E). The local velocities of the FPE region of the exemplary cell varied from 0.19 µm/s to 5.07 µm/s with a median of 1.70 µm/s. The average velocity over all 20 FPE regions was 1.95 ± 0.57 µm/s (Figure 34 C). In the quiver plots of a few cells, arrangements of arrows pointed to each other in close proximity of the FPE region. The length of the arrows, which correlated with the amplitude of the velocity, was short, so that arrangements were only recognised on closer inspection. Generally, the region of the FPE did not appear to be very distinctive. However, all cells shared one prominent feature in the quiver plots: so-called sinks. The locations of the sinks were not restricted to a particular area of the cell surface. At least one sink was located on the surface of each trypanosome, but on average 3 sinks were present. The sinks were characterised by a set of arrows pointing to a common centre with small local velocities. Both observations are encircled in Figure 34 A and E. As expected, the sinks correlated with domains of slow diffusion detected in the diffusion analysis (Figure 32). When I examined the movies by eye, I found a correlation with confined emitters in these superpixels. To indicate the dwelling time of particles in these superpixels, intensity maps were generated that confirmed the prolonged residence of the labelled VSGs at these sites (Figure 34 D).

The local relative standard error SE_v was calculated to consider the static localisation error in the local velocity. In all investigated cells, the SE_v varied in a large range of 0.029 to 215. If the relative standard error for a superpixel was equal to or greater than 1, it was concluded that there was no directed motion present or that it was below our detection limit. Thus, a cut off at 1 was set for the representation of the relative standard error in the map (Figure 34 F). The detection limit of a velocity within a superpixel was 5.2 µm/s ($N = 1$) considering the worst case at a localisation precision σ of 26 nm and $\Delta t = 10$ ms. The detection limit decreased with increasing statistics $\sqrt{N}$. An overview of all velocity maps, quiver plots and relative standard error maps is represented in Figure 52 - 54 in the Appendix.

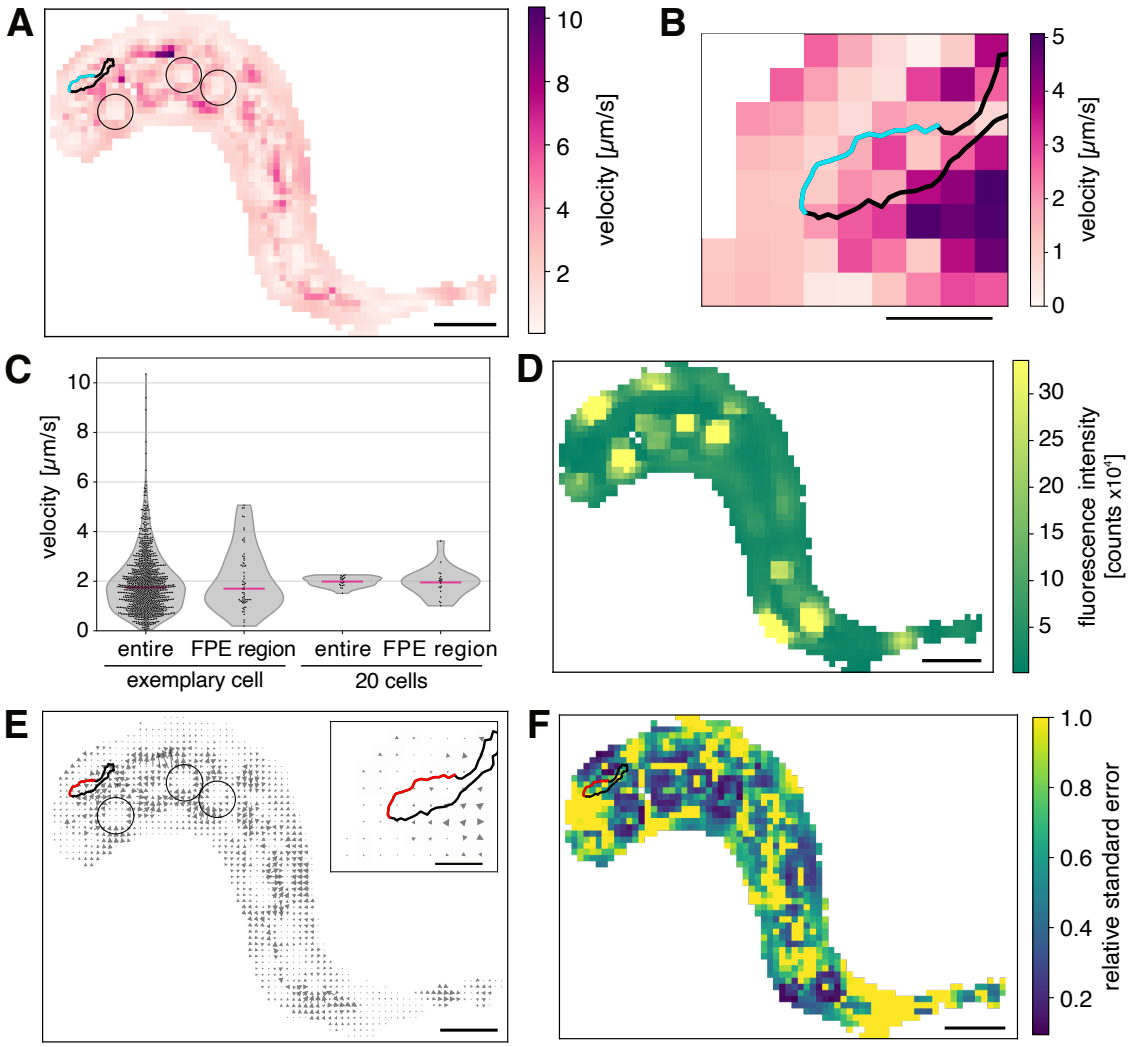

Figure 34: Characterisation of the VSG dynamics on 13-90 eYFP::MORN1 trypanosomes by a directed motion scenario. **A** Velocity map of the local velocities of an exemplary trypanosome. The heat map colour codes the amplitude of local velocities. The outline of the hook complex is depicted by a black line while the cyan part highlights the part which is wrapped around the FP neck marking the FPE region. This accounts also to E and F (highlighting in red). Domains consisting of superpixels attributed with small velocities are encircled. **B** Velocity map of the FP entrance (FPE) region of the exemplary cell. **C** Violin plots showing the distribution of the local velocities of the entire exemplary cell in comparison to the FP region. Additionally, the variance in the average velocity of each cell was compared to the variance in the average velocity of the FP region of all 20 cells. Magenta lines represent the median for the exemplary cell (entire: 1.75 µm/s (N = 1124 superpixels), FPE region: 1.70 µm/s (N = 63 superpixels)) and the average over all 20 cells (entire: 1.99 µm/s, FPE region: 1.95 µm/s). **D** Intensity map displaying the sum of all emitters' fluorescence detected within each superpixel. **E** Quiver plot representing the direction of the local velocities. The arrow size correlates with the amplitude of the local velocity. Sinks are encircled. The box shows the quiver plot of the FPE region of the exemplary cell. **F** Relative standard error map of the exemplary trypanosome. The colour code represents the local relative standard error, for which a cut of at 1 was set. The scale bar in A, D, E, and F is 1.6 µm, whereas the scale bar in B and E (box) is 0.5 µm.

2.4.3 Confined VSGs are not induced by interactions with the glass surface or the hydrogel.

Evaluation of VSG trajectories by shortTrAn revealed the existence of domains that were characterised by a slow diffusion coefficient in diffusion maps and by sinks with a centre of low local velocities in directed motion maps. The visual examination of the movies showed a correlation with confined particles.

In the tracking experiments, the cells were brought close to the bottom cover slip to allow for drift correction. In order to exclude the possibility that the confined particles are caused by an interaction of labelled VSGs with the glass surface, I performed two control experiments. First, I recorded VSG dynamics on cells not spun down to the glass, but located well within the hydrogel separated from the glass by a 10 - 14 µm thick gel layer. The thickness of the hydrogel layer was measured with the help of the fluorescent signal of the TS bead on the bottom cover slip. In this region of the hydrogel, the fluorescent signal of the Atto-647 N dye appeared diffuse. Thus, SPT was not feasible. Instead, the focus was set to a spot where the signal of the cell appeared and the cell was recorded in 10,000 consecutive images. Subsequently, an image stack was generated. If VSGs can diffuse freely,

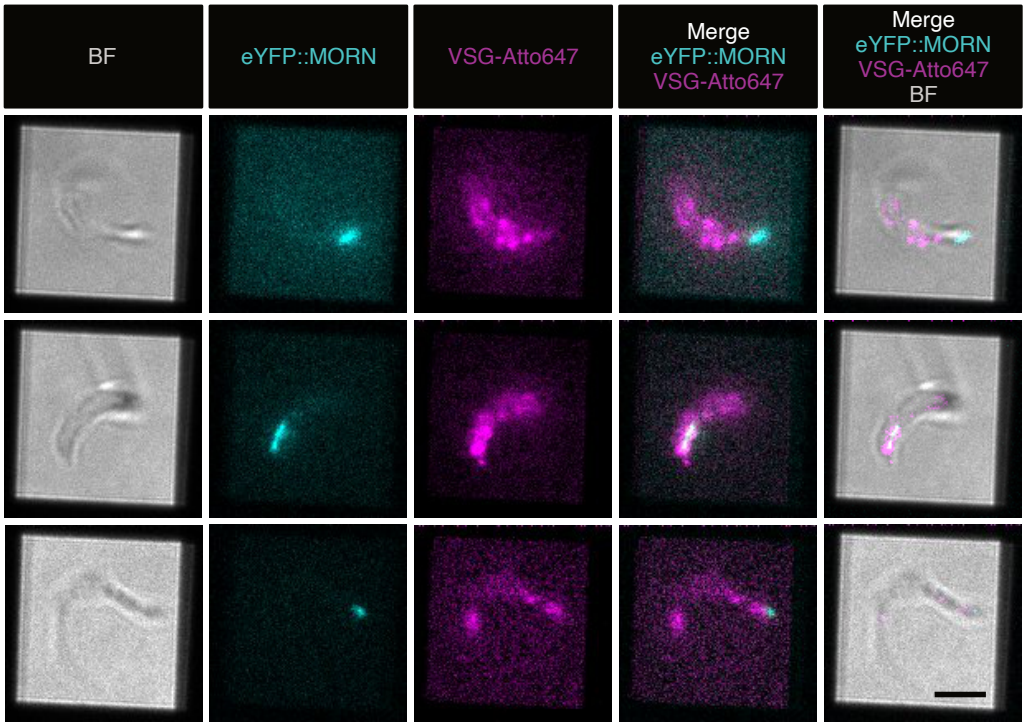

Figure 35: Fluorescence signal of Atto-647 N labelled VSGs in the surface coat of trypanosomes embedded deep inside the hydrogel. Image stacks of the bright field (BF), the eYFP::MORN1 and VSG-Atto-647 N fluorescence are displayed which were recorded at the single-molecule fluorescence microscope. The scale bar is 5 µm and applies to all images.

a homogenous fluorescent signal should be seen in a sum stack. If single emitters are confined, the fluorescent signal at that spot will increase linear with its dwelling time. Hence, the region of the confined particle will be highlighted. 16 cells of the 13-90 eYFP::MORN1 cell line were investigated. Figure 35 shows three representative stacks of the VSG signals from three trypanosomes. The location of the hook complex indicated the posterior part of the cells. For each cell at least one bright spot was observed. However, another explanation for the bright spots could be that labelled VSGs were endocytosed and located in endosomal structures. Due to our widefield SMFT microscopic setup out-of-focus signal is recorded, as well.
Second, VSG dynamics were investigated on top of trypanosomes spun down to the glass, with SPT performed on that side facing the hydrogel to check whether confined particles were also present. Tracking was conducted on four cells in total. At least one confined particle was identified for each cell. Figure 36 displays trajectories generated from one of this measurements and confined particles are indicated by an arrow. Confined particles were still present although interactions of labelled VSGs with the glass could be excluded.

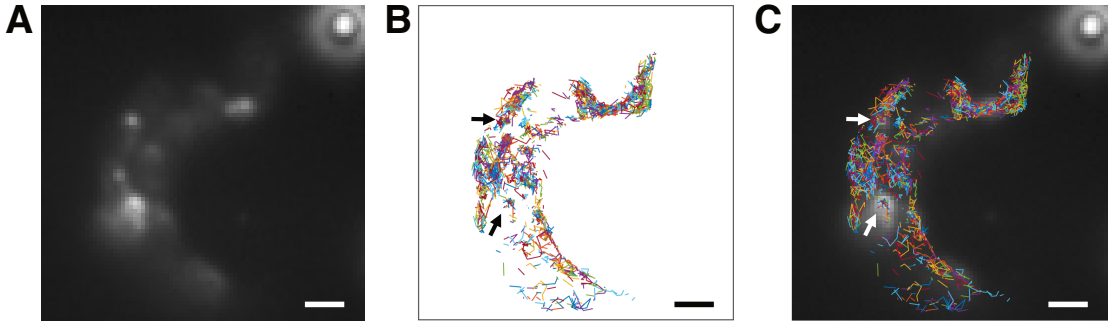

Figure 36: VSG tracking in the dense surface coat facing the hydrogel. **A** Image stack of the VSG-Atto-647 N fluorescence. **B** Trajectories obtained from the tracking of labelled VSGs in the plasma membrane facing the hydrogel. Typically, VSG tracking was conducted on the side facing the bottom cover slip. **C** Overlay of the obtained trajectories with the Atto-647 N fluorescence image. Arrows indicate confined particles. The scale bar is 1.6 µm and is valid for all three images.

Another potential cause for the confined particles could be the interaction of the VSGs with the hydrogel. To test this hypothesis, membrane form VSGs were incorporated in supported lipid bilayers (SLBs) and their dynamics recorded in presence and absence of a gel layer on top. This had the advantage that measurements were performed in a model system instead of on cells. The experiment was performed by Marius Glogger. To this end, he used proteoliposomes consisting of SOPC and VSG 1.6. The lipid-to-protein ratio was 75 - 95, representing the dense coat of living trypanosomes (Bartossek et al., 2017). SLBs were prepared from proteoliposomes with unstained VSGs. When SLBs were prepared, 3 µl of a 1:1000 dilution of Atto-647 N labelled VSGs were added to the supernatant, which integrated into the SLBs

after a few minutes. The supernatant was changed extensively to remove free VSGs. To investigate the influence of the hydrogel on the dynamics of the VSGs in SLBs, the hydrogel was formed on top of the SLBs. Tracking of VSGs in SLBs without the formation of an hydrogel on top served as control. Trajectories were generated from the obtained single-molecule localisations and the fraction of immobile particles was determined in two independent analyses.

The first analysis was performed by Susanne Fenz. Trajectories with a length of minimum 20 steps served as input. To identify immobile trajectories, the squared-displacement (SD) was calculated for each trajectory. Plotting the determined SDs in ascending order and looking for characteristic changes in the curve, allowed for the identification of the threshold to split immobile trajectories from the mobile trajectories (Figure 37). Trajectories with a SD $\leq 0.13\,\mu m^2$ were considered as immobile. In the simple model system, the only cause of immobile particles is the interaction with the glass at defect sites in the membrane. The proportion of these defects on the total surface is similar in the presence ($13 \pm 6\,\%$, $N = 41$) and absence ($16 \pm 8\,\%$, $N = 39$) of the gel. Thus, the gel does not provide any additional immobilisation, which would then be interpreted as an increase in the defect area.

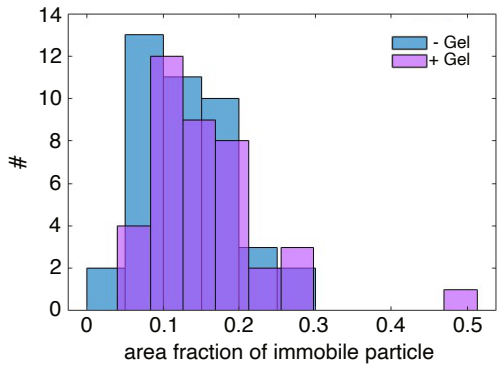

Figure 37: Histogram of the deviation of immobile VSGs fractions integrated in SLBs with and without hydrogel (+ Gel: $N = 41$, - Gel: $N = 39$).

The second analysis to identify the immobile fraction of VSGs was based on shortTrAn. The analysis of the VSG tracking on trypanosomes by shortTrAn revealed that immobile particles can be identified by the algorithm. Data sets were pooled according to whether a hydrogel ($N = 21$) or no hydrogel ($N = 29$) was formed on top as the algorithm needed a good coverage of the field of view. The parameters for the evaluation by shortTrAn were the following: The binning factor was 160 and the projection filter was applied to the outer two rows of superpixels. Immobile particles were characterised by a slow diffusion coefficient. Superpixels having a diffusion coefficient $\leq 0.375\,\mu m^2/s$ were extracted to identify superpixels belonging to immobile VSGs (Figure 38). This threshold was determined by visual examination of the diffusion map obtained from VSG dynamics in the absence of a hydrogel layer.

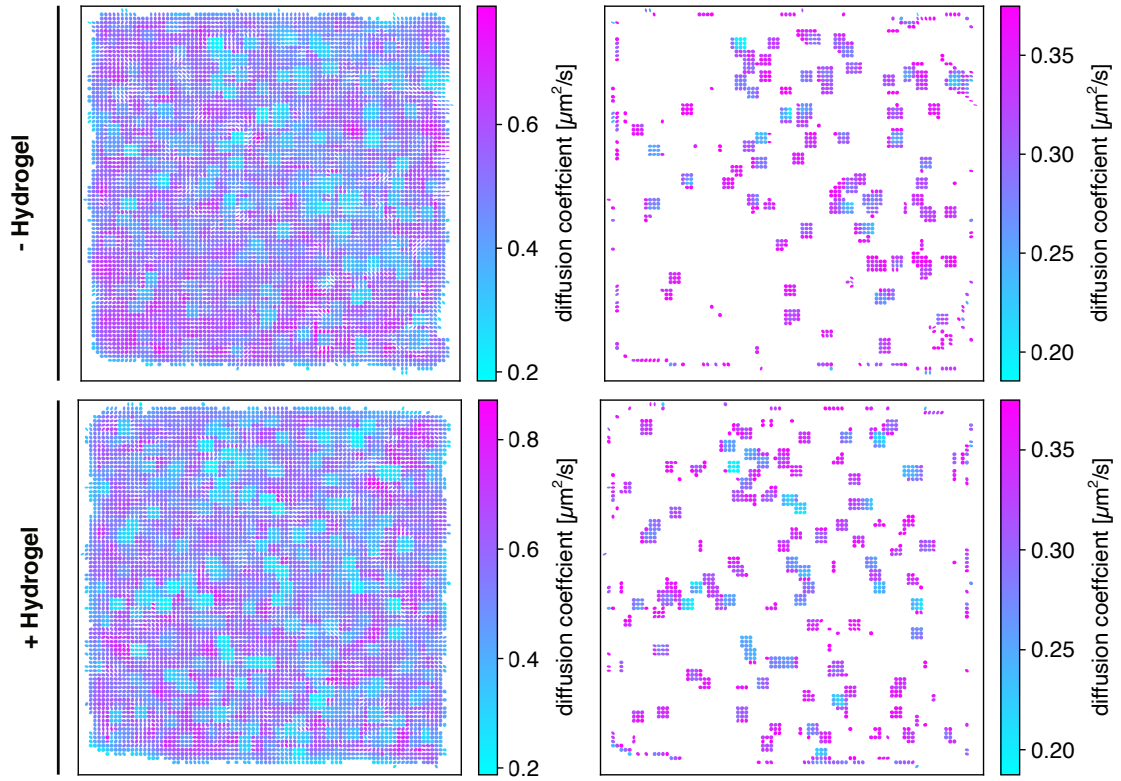

Figure 38: Identification of the immobile fraction of VSGs integrated in SLBs with and without hydrogel by. shortTrAn. Diffusion maps are representing the local diffusion coefficients. To extract the number of superpixels representing immobile particles, superpixels with a diffusion coefficient $\leq 0.375\,\mu m^2/s$ were extracted.

Thereby, the threshold of the diffusion coefficient was chosen so that the number of easily identifiable domains characterised by a slow diffusion coefficient matched the number of the remaining domains after the threshold was applied. This threshold was then transferred to the diffusion map generated from VSG dynamics in the presence of a hydrogel layer. Quantification of the immobile fraction was then performed by comparing the number of superpixels representing immobile VSGs to the total number of superpixels when no threshold was applied (Figure 38). In case of the SLBs without the formation of a hydrogel, the fraction of the immobile VSGs was 13 %. The fraction of immobile VSGs was 15 % in SLBs with a hydrogel formed on top. Similarly to the first analysis of the immobile fraction, the proportion of immobile VSGs was comparable in both SLBs with or without hydrogel.

In summary, the VSG coat of cells embedded deep inside the hydrogel or tracking of VSGs on the surface facing the hydrogel of trypanosomes spun to the glass also showed immobile particles as observed in tracking VSGs on the surface facing the glass cover slip. The formation of a hydrogel on top of SLBs which had labelled VSGs incorporated exhibited a similar number of immobile particles compared to VSGs in SLBs that did not have a hydrogel on top.

2.4.4 Supermaps - the decision on the dominating motion mode

Hitherto, the measured displacements of the steps of all trajectories were interpreted as diffusion or as directed motion, respectively. Local diffusion coefficients and local velocities were extracted from an ensemble of displacements originating from the specific superpixels. To answer the question whether VSG dynamics were characterised by solely Brownian motion or whether directed contributions were present, it was necessary to identify superpixels in which one type of motion clearly dominated. To this end, a guideline on the basis of the previously determined key figures of diffusion and directed motion, namely the eccentricity and the relative standard error, was developed and the final results were presented in so-called supermaps. In these maps, each superpixel was colour-coded according to the type of motion which was dominant.

2.4.4.1 Decision guideline on the basis of the eccentricity and the relative standard error

The representation of the local diffusion tensor as ellipses allowed the characterisation of diffusion by their shape. Isotropic diffusion is indicated by a circle, while an elongated ellipse denoted anisotropic diffusion. The deviation from a circle was determined by means of the eccentricity ε, which was obtained from the two axes of the ellipses representing the diffusion coefficients in one dimension (see Equation 31). The eccentricity is defined in a range $\varepsilon \in [0,1]$ and the extrema 0 and 1 indicate a circle and a line, respectively. If the eccentricity approaches 1, this may imply the possibility of directed motion or may be falsely induced by bad statistics.

The relative standard error SE_v of the local velocity reflects the likelihood of directed motion. If the relative standard error equals 1, the measured velocity is caused solely by the inherent localisation precision of the measurement. Two reasons exist for a large SE_v: (i) either if the average velocity in a superpixel is very small or (ii) if the corresponding error is very large. The first reason of a small velocity will be true if either slow directed motion exists or in case of diffusion because random displacements add up to a zero net displacement. In contrast, a very small SE_v results from a fast directed motion ($SE_v \to 0$).

To determine appropriate threshold values for ε and SE_v to decide on the presence or absence of diffusion, random walk simulations were performed as described in Section 4.8.2. Simulations were conducted on a trypanosome mask to account for rim effects. Trajectories were simulated with a $D = 1.00\,\mu m^2/s$ and $\Delta t = 10\,ms$ from starting points randomly distributed on the trypanosome mask. The specific diffusion coefficient was chosen equal to the average diffusion coefficient over all 20 investigated cells. Subsequently, the data sets were analysed with shortTrAn.

Statistics per superpixel were varied by either choosing a trajectory length (TL) of 15 and/or 50 or the compilation of different numbers of trajectories within a data set (2,000 - 10,000). The dependency of the eccentricity and the relative standard error on the statistics is plotted in Figure 39 A and B. It can be recognised that no general threshold value can be set, instead the threshold values have to be chosen as a function of the statistics. Since diffusion was simulated, the thresholds were chosen under the premises that 99 % of the superpixels would be assigned to diffusion and only 1 % would be false-positively assigned to directed motion (Figure 39 C). For the eccentricity, a 99 % threshold could be used as a value of 0 represents isotropic diffusion. For example, all superpixels with a statistics of $N = 20$ and an eccentricity smaller than 0.79 were categorised as diffusion (black arrow, Figure 39 C). In case of the relative standard error, the threshold was set at 1 % because a large relative error indicated diffusion whereas a relative error close to 0 signified directed motion. Consequently, all superpixels with a statistics of $N = 20$ and a relative standard error larger than 0.45 were assigned to diffusion (black arrow, Figure 39 C).

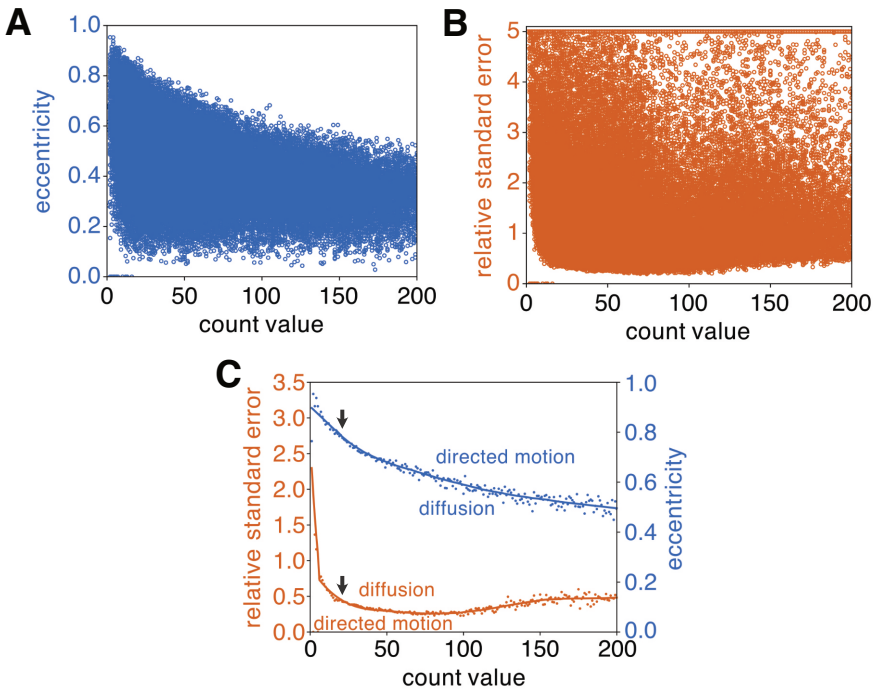

Figure 39: Determination of threshold values to correctly identify diffusion based on random walk simulations. **A** Eccentricity of the diffusion tensor of a superpixel as a function of the statistics (count value) in the superpixel. **B** Dependency of the relative standard error on the statistics of the corresponding superpixels. A cut off was set at a relative standard error of 5. **C** Representation of the threshold values set for the relative standard error and the eccentricity to decide on the dominant motion mode. The relative standard error threshold was set to 1 % of the data from (A) allowing 99 % of the data to be assigned to diffusion. The threshold for the eccentricity was set to 99 % of the data from (B) resulting in 99 % of the data being attributed to diffusion. Black arrows mark statistics at $N = 20$.

The eccentricity threshold started at 0.9 for small statistics and decreased with increasing statistics (Figure 39 C). However, even in case of $N = 200$, the threshold was still 0.5. Thus, it was above the theoretically predicted value of 0 indicative of perfectly isotropic diffusion. The threshold for the relative standard error of a hypothetical velocity was large at small statistics. It was 2.3 at N = 1. As the statistics in superpixels increased, two opposing effects took place when calculating SE_v as follows:

$$SE_v = \frac{err_{\overline{v}}}{\sqrt{N}} \qquad \text{with} \qquad err_{\overline{v}} = \frac{err_{\Delta}}{\overline{v}}, \tag{12}$$

and $err_{\overline{v}}$ indicating the relative error, N the local statistics, err_{Δ} the systematic error of the measured displacement, and $\overline{v}$ the average velocity. The consideration of the statistics by $\sqrt{N}$ resulted in an increasing value in the denominator, while the average velocity, $\overline{v}$, in the denominator tended to zero. As a result the threshold of the relative standard error of the velocity first decreased strongly as N increased. Then, a saddle point around $N = 50$ was reached and finally the relative standard error increased again slowly before it saturated around $N = 200$.
At low statistics ($N < 8$), the eccentricity was close to 1 and the relative standard error diverged. Thus, superpixels with statistics in the unreliable regime were excluded from the decision which of the two motion modes dominated.

For the assignment of superpixels to diffusion or directed motion, a decision guideline was established which is depicted in Figure 40. First, superpixels for which both criteria, eccentricity and relative standard error, pointed towards the same motion mode were assigned to the according motion model (Figure 40, path 1). This implies that superpixels with a small eccentricity ε ($\varepsilon < \varepsilon_{thres}$) and a large relative standard error ($SE_v > SE_{v\,\mathrm{thres}}$) were attributed to diffusion. Alternatively, if the relation was *vice versa* the superpixel was assigned to directed motion. Afterwards, a large number of superpixels remained that could not be attributed as clearly because the two criteria were contradictory (Figure 40, path 2). In order to decide which of the two motion contributions dominated in those cases, the deviation from the threshold was quantified to determine how well the measured parameter can be distinguished from its corresponding threshold: $\Delta\varepsilon = (\varepsilon/\varepsilon_{thres})-1$ and $\Delta SE_v = (SE_v/SE_{v\,\mathrm{thres}})-1$. If the difference between the two deviations was < 0.25, the superpixels remained unassigned as no criterion dominated the other. On the other hand, if the difference was > 0.25, the criterion with the greater deviation from its threshold was selected for the assignment. If the decisive parameter was the eccentricity ($\Delta\varepsilon > \Delta SE_v$), the superpixel was attributed to diffusion in the case of $\varepsilon < \varepsilon_{thres}$ and to directed motion in the case of $\varepsilon > \varepsilon_{thres}$. Conversely, if the relative standard error was found to be the parameter for a reliable attribution ($\Delta\varepsilon < \Delta SE_v$), the superpixel was assigned to diffusion if $SE_v > SE_{v\,\mathrm{thres}}$ or to directed motion if $SE_v < SE_{v\,\mathrm{thres}}$.

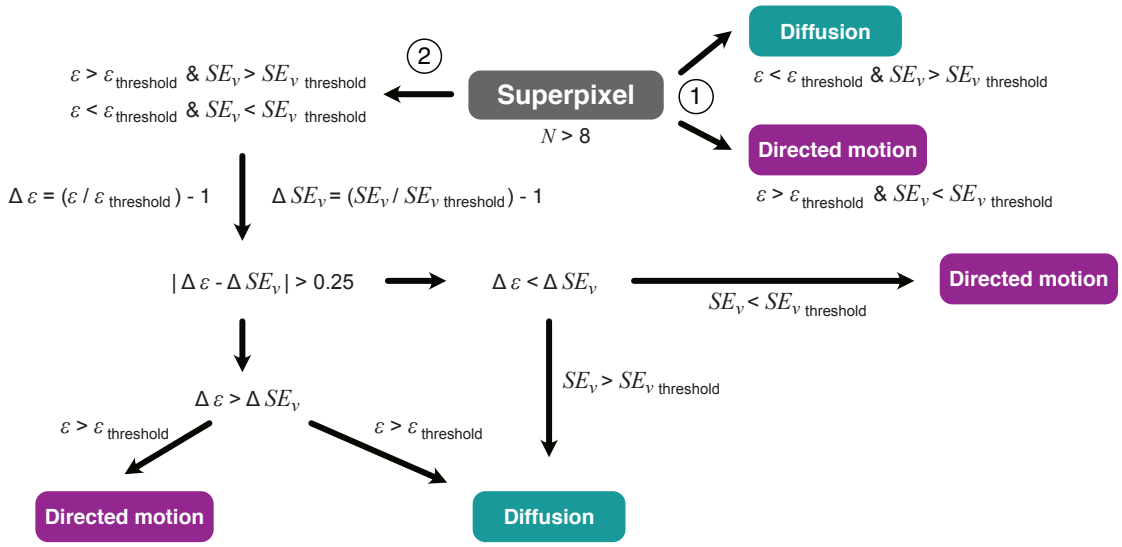

Figure 40: Flow chart illustrating the decision guideline for supermaps. The assignment of superpixels to a motion mode was based on the eccentricity ε and the relative standard error SE_v. The threshold values were determined by random walk simulations and are depicted in Figure 39 C. Path 1 displays the assignment if both criteria point to the same motion mode. Path 2 indicates the assignment if both criteria were contradictory.

Even after this assignment, unassigned superpixels remained. I categorised these orphan pixels based on their neighbouring superpixels by utilising a moving-box kernel (size = 3 superpixel) to also account for superpixels on the diagonal. If the environment was uniform (7 and 8 superpixels of the same motion type), the centre was attributed accordingly. This filtering process continued until no more orphan superpixels could be filled following this principle.

To validate the assignment principle, the guideline was applied to the shortTrAn results of simulations performed to determine the threshold values. When applied to the shortTrAn results of simulations having the lowest statistics (1 - 30 data points per superpixel), 99.4 ± 0.2 % of the assigned superpixels were attributed to diffusion and 0.6 ± 0.2 % to directed motion. On average, $11{,}2 \pm 0.34$ % orphan superpixels remained. Applying the guideline to the shortTrAn results of simulations with the highest statistics (7 - 254 data points per superpixel), 98.8 ± 0.5 % of the assigned superpixels were dominated by diffusion and 1.1 ± 0.5 % by directed motion. On average, 3.15 ± 0.22 % of the superpixels remained without assignment.

2.4.4.2 VSG dynamics is mainly characterised by diffusion

Applying the guiding principle introduced in Section 2.4.4.1 to the 20 investigated cells revealed that the resulting supermaps can be sorted into three different groups. Representative supermaps for each group are depicted in Figure 41, while an overview of all supermaps is shown in Figure 55 (Appendix). If diffusion was the dominant motion mode the superpixels are depicted in green. Magenta superpixels represent superpixels which were dominated by a directed motion and gray superpixels indicate orphan superpixels which could not be clearly assigned. I visually examined the supermaps and classified them into three groups based on prominent features. Group 1 was characterised by a high proportion of superpixels attributed to diffusion and only a few, isolated superpixels assigned to directed motion (Figure 41 A). This group comprised 7 cells. In contrast, group 2 showed a larger proportion of superpixels assigned to directed motion, yet distributed as patches on the surface (Figure 41 B). This group contained 7 cells. Group 3 ($N = 6$ cells) was distinctive from both groups as these trypanosomes showed a high proportion of superpixels associated to directed motion, that clustered in contiguous, elongated arrays (Figure 41 C). The sinks found in the directed motion maps, correlating with slow diffusion, were also noticeable in the supermaps. In the supermaps, the domains were characterised by a centre of diffusion surrounded by superpixels attributed to directed motion. From the quiver plot of the directed motion maps it is known that the direction of the velocity pointed to the centre, which is reminiscent of a trap. For this reason, the sinks were then referred to as round traps in supermaps.

I further specified the supermap groups by analysing the relative prevalence of the two motion modes as well as the connectivity of a superpixel's associated motion mode to the immediate surrounding.

The relative prevalence is shown in Figure 41 D. The majority of superpixels were assigned to be dominated by diffusion (group 1: $68.0 \pm 5.7\,\%$; group 2: $56.6 \pm 4.8\,\%$; group 3: $43.3 \pm 3.9\,\%$). In contrast, an attribution to be dominated by directed motion was less abundant (group 1: $9.4 \pm 2.0\,\%$; group 2: $16.1 \pm 4.1\,\%$; group 3: $32.1 \pm 4.4\,\%$) in all three groups. The fraction of orphan superpixels was similar in all three groups (group 1: $22.6 \pm 5.8\,\%$; group 2: $27.4 \pm 6.8\,\%$; group 3: $24.6 \pm 1.3\,\%$). In contrast to groups 1 and 2, which exhibited significantly more superpixels associated to diffusion, diffusion and directed motion were almost equally prevalent in group 3.

To quantify the connectivity of one motion mode, I extracted the number of the adjacent superpixels attributed to the same motion mode. If up to two adjacent superpixels exhibited the same motion model, they were grouped in category I. Category II and category III represented superpixels with three to five or six to eight neighbours of the same motion model, respectively. When assessing the connectivity of superpixels assigned to diffusion (Figure 41 E), 68 % of all superpixels of cells in

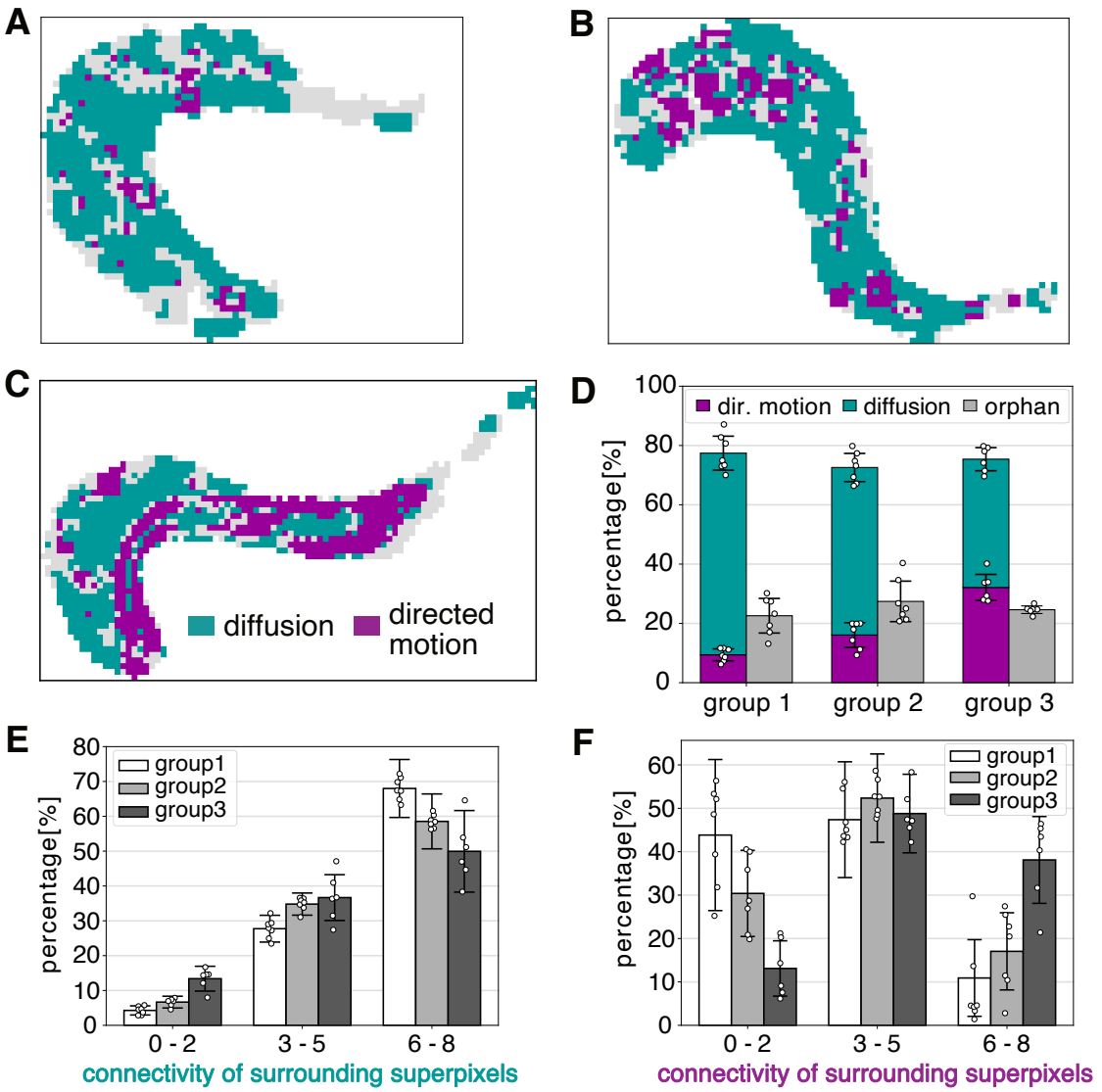

Figure 41: Quantification of the locally dominant motion mode of the VSG dynamics on 13-90 eYFP::MORN1 cells. **A - C** Supermaps of the locally dominating motion mode. Green superpixels are attributed to diffusion, magenta ones to directed motion and grey ones depict orphan superpixels. The number and the arrangement of superpixels dominated by directed motion facilitated supermaps to be grouped. An example is shown for each group. **A**, group 1; **B**, group 2; **C**, group 3. **D** Relative prevalence of the predominant motion mode, diffusion or directed motion, within the three supermap groups. In orphan superpixels, neither of the two types dominated. Bars represent the mean percentage and error bars indicate the SD. **E** Connectivity of superpixels attributed to diffusion to their surrounding for the three different groups. **F** Connectivity of superpixels assigned to directed motion to their surrounding for the three different groups. The percentage of superpixels with 0 - 2, 2 - 5, 6 - 8 neighbours exhibiting the corresponding motion type is represented in E and F (group 1 in white, group 2 in grey, and group 3 in dark grey). Error bars indicate the SD. Individual values of the supermaps within the groups are depicted by circles in D, E and F (N = 7 for group 1 and 2, N = 6 for group 3).

group 1 had six to eight neighbours assigned to the diffusion model (category III). If, on the other hand, the connectivity of superpixels assigned to directed motion was

examined (Figure 41 F), the highest percentage (38 %) of contiguous pixels (category III) was found in group 3. This high fraction relative to the other two groups correlated with the contiguous, elongated arrays of superpixels characterised by directed motion. However, it should be noted that the direction of the velocity did not run along these elongated arrays but pointed perpendicular into the centre, reminiscent of elongated traps. In most cases, there was even an area in the centre that was attributed to diffusion. Hence, the contiguous, elongated arrays were then termed elongated traps.

2.5 *In silico* experiment on the achievability of a fast turnover by VSG randomisation with the newly determined diffusion coefficient

In 2004, Engstler et al. postulated that the entire VSG surface pool is internalised and recycled once in ~12 min. In order to check whether the newly determined average diffusion coefficient of 1.00 µm^2/s is sufficient for a rapid randomisation of VSGs in the surface coat and thus allowing fast turnover, random walk simulations were performed. The VSG uptake through the small FP resembles the narrow escape problem (NEP). This problem deals with a Brownian particle that is confined to a bounded domain (cell surface), except for a small window (FP) through which it can escape. This process can be quantified by the mean first passage time (τ).

First, τ was determined by simulations of VSG diffusion on three trypanosome-shaped masks derived from the shortTrAn (Section 4.8.1). The masks were composed of two layers to mimic the $3D$ surface area of a trypanosome which is known to be 100 µm^2 (Hartel et al., 2015). I selected three trypanosome-shaped masks which had an area of 28.2 µm^2, 34.3 µm^2, and 40.0 µm^2 per layer. The area per layer was still less than half of the total surface area. This can be attributed to the measurements that captured only the part of the membrane in focus. In accordance with the requirements for the NEP, the cells which served as blueprints for the masks were in the G1 or S phase of the cell cycle and thus had only one FP. In the simulations only one layer contained the exit site, the FP region. I extracted the exit site region manually from the part of the outline of the hook complex wrapped around the FP neck indicating the entrance to the FP. 2,000 trajectories of diffusing particles were simulated per mask. 1,996 - 2,000 trajectories escaped by hitting the FP exit site within a predefined time window of 500 s. τ_{sim} was 50 - 78 s (Table 1). The determination of τ_{sim} was complemented further by theoretical considerations to achieve τ_{th}. VSGs are only diffusing in the plane of the membrane and thus effectively in two dimensions. Hence, a theoretical model of a $2D$ domain was chosen with an escape site in the centre. τ_{th} was calculated according to the simplified Equation 13 (Holcman and Schuss, 2013):

$$\tau_{th} = \frac{A_{tryp}}{2\pi D} \ln \frac{1}{e} \qquad \text{with } e = a/C. \tag{13}$$

Here, A_{tryp} denoted the surface area of a trypanosome, D the diffusion coefficient, a the FP radius, and C the circumference of the trypanosome mask. The calculation of τ_{th} required the FP radius. It was derived from the area of the FP mask, which was extracted by a built-in function in MATLAB, assuming a circular shape. τ_{th} was 51 - 73 s for the three cell masks (Table 1) and thus in good agreement with τ_{sim}.

Table 1: Determination of the mean first passage times (τ) of diffusive particles on trypanosome-shaped masks by theory and simulation. A_{tryp}: surface area of a trypanosome; FP: flagellar pocket; e: ratio of the FP radius to circumference of the trypanosome mask; τ_{th}:mean first passage time determined by theory; τ_{sim}: mean first passage time determined by simulation; $\tau_{99\,\%}$: time until 99 % of the particles escaped.

	A_{tryp} [µm^2]	FP radius [µm]	e [%]	τ_{th} [s]	τ_{sim} [s]	$\tau_{99\,\%}$ [min]
Simulation 1	68.6 (2 x 34.3)	0.36	0.34	62 ± 12	76 ± 9	5.7
Simulation 2	80.0 (2 x 40.0)	0.36	0.31	73 ± 15	78 ± 10	6.0
Simulation 3	56.4 (2 x 28.2)	0.31	0.35	51 ± 10	50 ± 9	3.5

In order to determine the time required for VSGs to randomise within the entire VSG coat to finally reach the FP, the time until 99 % of the simulated VSGs have escaped through the FP was approximated. To this end, the time, $\tau_{99\,\%}$, was extracted from the cumulative distribution of the individual escape times. $\tau_{99\,\%}$ was in a range of 3.5 - 6.0 min (Table 1). Thus, the approximated escape time of VSGs to the FP by simulations is sufficient to allow for a turnover time of ~12 min published by Engstler et al. (2004).

2.6 Studying the influence of cytoskeletal anchoring on the distribution and dynamics of surface VSGs *in vivo*.

Since the proposal of the fluid mosaic model by Singer and Nicolson in 1972, the understanding of the plasma membrane organisation has changed considerably. The fluid mosaic model characterised the plasma membrane as homogenous, equilibrated lipid bilayer in which different integral and peripheral membrane proteins are embedded like a mosaic. However, today we know that membranes are far from a well-equilibrated organisation as elaborated in the introduction (Jacobson et al., 2019; Kalappurakkal et al., 2020). Moreover, it was shown that the anchoring of the cytoskeleton influences dynamics of membrane proteins which can be explained by the picket-fence model (Kusumi et al., 2012). Raghupathy et al. (2015) even showed that the anchoring of the actin skeleton to the plasma membrane in Chinese hamster ovary cells influences the distribution of GPI-anchored proteins in the outer leaflet of the membrane via interleaflet coupling. Thus, in the next section of this thesis, I aimed to investigate the dynamics of GPI-anchored VSGs with respect to a possible influence of cytoskeletal anchoring via interleaflet coupling.

In a first approach to detach the anchoring of the plasma membrane from the cytoskeleton, in the case of *T. brucei* the sub-pellicular microtubule corset, the parasites were subjected to osmotic swelling. For this, two procedures were tested: trypanosomes were embedded in hydrogels under hypotonic conditions with or without preswelling of the cells. For preswelling, trypanosomes were incubated in a hypotonic medium consisting of TDB and ddH20 (1:1) for ~2 min before immobilisation in the hydrogel. Microscopic examination in a Neubauer chamber confirmed that cells in hypotonic medium became swollen due to the influx of water. The flagellum of the swollen trypanosomes was still recognisable and beating. The morphology of the cells was reminiscent of a balloon. In both approaches, the individual VSGs of the coat were stained with a nanomolar quantity of Atto-647 N-NHS dye. Subsequently, the cells were embedded in a hydrogel under hypotonic conditions. It should be noted that the morphology of most cells in the hydrogel, with or without preswelling, appeared similar to the slender shape and were no longer swollen. As a possible explanation for the low number of swollen cells in the hydrogel, I suspect that cells experienced counteracting forces from osmotic swelling (expansion) and the hydrogel (compression). The compression could be initiated by the cross-linking of the hydrogel and the natural end of compression is reached at the cytoskeleton. In the following, slender form cells were microscopically examined. VSG dynamics were acquired in 10,000 - 20,000 consecutive images at 100 Hz and 37 °C. Single-molecule localisations were identified by comparison to the known footprint as described in Section 4.7.1. A mask was set around the profile of the cell to eliminate background

signal. On average $4.49\,\mathrm{x}\,10^4 \pm 1.73\,\mathrm{x}\,10^4$ VSG localisations were found per cell. The localisation precision was determined from the error in the Gaussian fit of the x- and y-position and was 31 ± 3 nm.

Before the localisations were studied on a deviation from a random distribution, artificial clusters were removed as described in Section 4.7.7. Subsequently, the nearest neighbour analysis Ripley $L(r) - r$ was carried out. The potential cluster radius was estimated from the maximum of the plot of the Ripley's $L(r) - r$ function. The potential cluster size was 240 ± 26 nm (Figure 42 A). Clusters were also visible in the super-resolved images (Figure 42 B). On, average 489 ± 118 VSG localisations per µm^2 were detected.

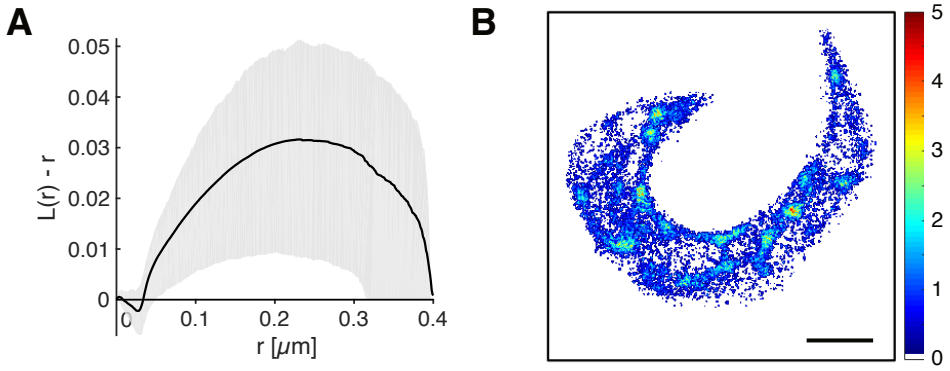

Figure 42: Cluster analysis of labelled surface VSG on osmotically swollen trypanosomes. **A** Ripley's $L(r) - r$ analysis with the $1\,\sigma$ confidence interval represented as grey area. The function averaged over 10 imaged cells and showed a maximum of 240 ± 26 nm. **B** Super-resolved image of the VSG localisations at a localisation precision of 31 nm. The quantity of localisations is colour-coded. The scale bar is 2 µm and applies to A and B. Artificial clusters were removed beforehand.

Using the probabilistic algorithm to compute single-molecule trajectories, on average $6.3\,\mathrm{x}\,10^3 \pm 2.0\,\mathrm{x}\,10^3$ trajectories were identified. The average trajectory length was 7 steps.

The evaluation with shortTrAn showed that the average diffusion coefficient was 0.77 ± 0.15 µm^2/s. This was slower than the measured diffusion coefficient of 1.00 ± 0.15 µm^2/s on the surface of non-swollen 13-90 eYFP:MORN1 cells (Figure 43 A). The eccentricity was 0.79 ± 0.03 and thus similar to the determined eccentricity of 0.78 ± 0.04 measured on non-swollen 13-90 eYFP:MORN1 cells (Figure 43 B). The average velocity of a directed motion was 1.94 ± 0.27 µm/s. This was in the same range as the determined average velocity of 1.99 ± 0.20 µm/s on the non-swollen cells (Figure 43 C). Domains that were described as round traps in the course of this work were also present on the maps. They were characterised by a low diffusion coefficient in the diffusion maps, and by a set of arrows pointing to a common centre in the quiver plots with small velocities at the centre in the heat maps of the directed motion analysis.

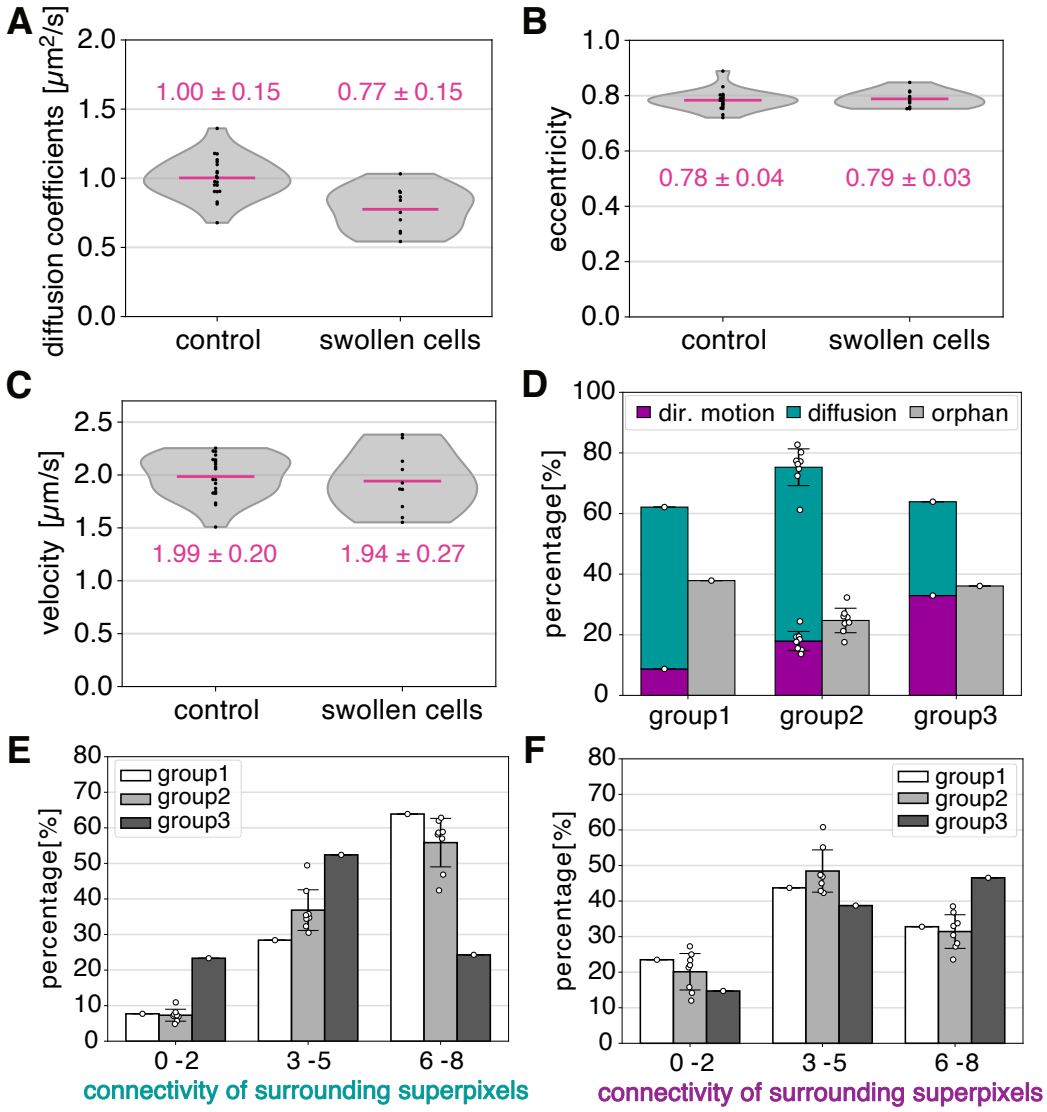

Figure 43: Quantification of VSG dynamics on osmotically swollen trypanosomes. **A - C** Violin plots representing the results of VSG trajectories evaluated by shortTrAn. The average diffusion coefficient (A), the average eccentricity (B) and the average velocity of a directed motion (C) of individual cells are compared to non-swollen trypanosomes (magenta lines). control: non-swollen 13-90 eYFP:MORN1 (N = 20); swollen cells: swollen 13-90 eYFP:MORN1 (N = 10). **D** Relative prevalence on the locally dominating motion mode in obtained supermaps. Diffusion is displayed in green, directed motion in magenta and orphaned superpixels in grey. **E** Connectivity of superpixels dominated by diffusion to adjacent superpixels attributed to the same motion mode. **F** Connectivity of superpixels dominated by directed motion to neighbouring superpixels assigned to the same motion mode. In B and C, group 1 is represented in white (N = 1 cell), group 2 in light grey (N = 8 cells), and group 3 in dark grey (N = 1 cell). The statistics accounts for all three graphs. Error bars indicate the SD. Individual values representing a supermap of one cell are depicted by circles.

The comparative analysis of trajectories obtained from cells that were not preswollen or were preswollen before embedding showed no significant difference when evaluated with shortTrAn. Based on the results from shortTrAn, supermaps were generated

that present the results of the decision which motion mode dominated locally. Supermaps of the swollen cells were classified by visual examination into the three groups previously defined in the analysis of the non-swollen cells (Section 2.4.4.2). All supermaps obtained from swollen trypanosomes are displayed in Figure 56 (Appendix).

Visual classification of the swollen cells resulted in one cell being assigned to group 1, eight cells to group 2 and one cell to group 3. The analysis of the relative prevalence of the two motion modes in supermaps showed that diffusion clearly dominated in groups 1 and 2 (Figure 43 D, group 1: 53 %, group 2: 57 ±6 %, group 3: 31 %). The dynamics on the surface of the cell in group 3, on the other hand, was characterised by directed motion (Figure 43 D, group 1: 9 %, group 2: 18 ±3 %, group 3: 33 %). The share of orphaned superpixels was 38 % for group 1, 25 ± 4 % for group 2, and 36 % for group 3. Checking the connectivity of superpixels dominated by diffusion reinforced that in group 1 and group 2 contiguous areas of the surface were characterised by diffusion. For a superpixel dominated by diffusion, 64 % in group 1 and 56 % in group 2 had six to eight superpixels as neighbours that were also assigned to diffusion (Figure 43 E). Checking the connectivity of superpixels dominated by directed motion revealed that 47 % of superpixels dominated by directed motion were surrounded by six to eight superpixels of the same motion mode. This confirmed the contiguous proportion of the surface dominated by directed motion observed in the visual examination for group 3. Analysis of the relative prevalence and the connectivity of superpixels dominated by diffusion or directed motion underpinned the classification of the swollen cells into the three previously defined groups (Figure 43 F). In contrast to the dynamics of VSGs on non-swollen 13-90 eYFP:MORN1 cells, which showed a balanced distribution into all three groups, VSG dynamics on swollen 13-90 eYFP:MORN1 cells were characterised by an assignment of the majority to group 2. Domains observed earlier in the diffusion and directed motion maps of shortTrAn were again recognisable in the supermaps as round traps. The round traps were frequently characterised by a centre of diffusion surrounded by superpixels dominated by directed motion in which the velocity pointed to the centre.

However, since it remained elusive whether cells had lost the anchoring of the microtubule skeleton to the plasma membrane, another approach was pursued: depletion of whole cell body protein (WCB, Tb427.7.3550), a possible connector protein using RNA interference (RNAi).
As part of Paula Büttner's master project (Büttner, 2021), a 2T1 WCB RNAi cell line was established according to Baines and Gull (2008). Upon induction in BSF trypanosomes, the following phenotypes were observed: cells started to round at the posterior end (~ 6 - 12 h) and during depletion the cell morphology changed. More-

over, rounded cells and multiflagellated cells were observed after ~16 - 24 h. Baines and Gull (2008) showed in electron microscope images that in PSF trypanosomes parts of the plasma membrane had detached from the sub-pellicular corset 48 h after induction. To investigate the dynamics of VSGs under the conditions of a detached plasma membrane and taking into account the faster cell cycle of BSF trypanosomes, the measurements were performed 24 h after RNAi induction. Three different phenotypes were imaged: cells that resembled the shape of a non-induced cell, cells that rounded up posteriorly and completely round cells. Round cells deviated from previously described round phenotypes, like the big-eye phenotype. Big-eye cells are characterised by an enlarged FP which is accompanied by a membranous bulge around it. Such a bulge was not observed for the round phenotype in my experiment.

Before performing single-molecule imaging, I examined the viability of the cells after 24 h of WCB RNAi induction. This aimed to ensure that the membrane integrity of the posterior swollen and round phenotypes was still maintained. Cells were embedded in a hydrogel supplemented with PI. The number of viable cells was determined by enumeration at the microscope. Trypanosomes of the 2T1 cell line served as a control and the viability was checked in two hydrogels with 50 cells each. The viability of posterior swollen and round trypanosomes was checked in triplicates with 10 to 13 cells and 7 to 15 cells, respectively. The viability and thus the plasma membrane integrity of posterior swollen and round trypanosomes was only slightly decreased with $99 \pm 0.1\,\%$ and $91 \pm 7\,\%$ compared to 2T1 cells with

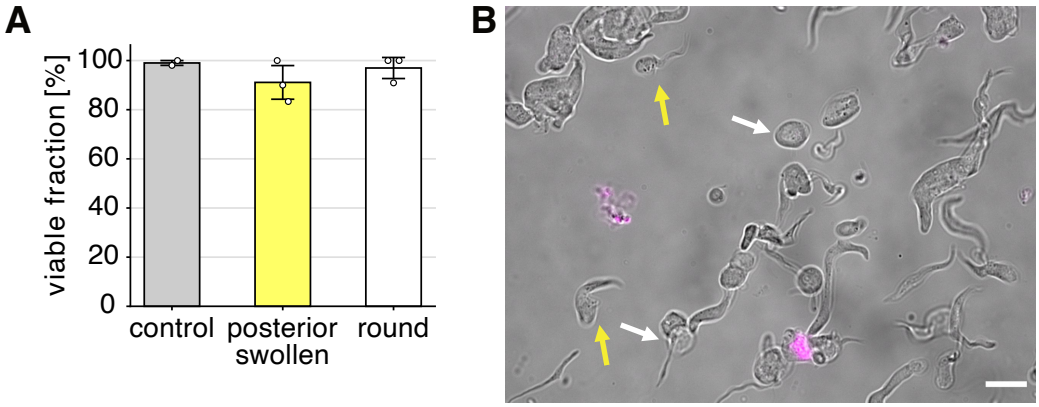

Figure 44: Viability of hydrogel-embedded trypanosomes after 24 h of WCB RNAi induction. **A** Viable fraction of two phenotypes observed after RNAi induction was assessed by PI staining. Examined phenotypes were posterior swollen (N = 3 hydrogels á 10 - 13 cells) and completely round trypanosomes (N = 3 hydrogels á 7 - 15 cells). 2T1 cells embedded in hydrogels served as control (N = 2 hydrogels á 50 cells). **B** Exemplary overview of the viability assay of WCB-depleted trypanosomes. Shown is an overlay image of the transmitted light channel with the PI signal (magenta), indicating dead cells. Yellow arrows point to cells that correspond to the 'posterior swollen' phenotype. Two rounded cells are marked with white arrows as an example. The scale bar is 10 µm.

$97 \pm 4\,\%$ (Figure 44 A). An overview of the viability assay of 24 h WCB-depleted trypanosomes is shown in Figure 44 B.

After successful verification of the membrane integrity of WCB-depleted trypanosomes, single-molecule tracking was conducted at 205 Hz and 37 °C. Trypanosomes were embedded in hydrogels 24 h after induction. Single-molecule tracking was also performed on non-induced 2T1 WCB RNAi cells. VSG dynamics were recorded in 10,000-30,0000 consecutive images. Single-molecule localisations were identified by comparison to the known footprint as described in Section 4.7.1. To eliminate background signal, a mask was set around each trypanosome outline. On average $8.50 \,\mathrm{x}\, 10^4 \pm 5.12 \,\mathrm{x}\, 10^4$ VSG localisation were found per cell for non-induced cells (- Tet, N = 14) and $5.18 \,\mathrm{x}\, 10^4 \pm 3.01 \,\mathrm{x}\, 10^4$ VSG localisation for WCB-depleted cells (+ Tet, N = 20). The localisation precision was 30 ± 2 nm and 28 ± 3 nm, respectively. The localisation precision was determined from the error in the Gaussian fit of the x- and y-position.

First, single-molecule localisations were studied for clusters. For this, artificial clusters were removed beforehand as described in Section 4.7.3. Subsequently, super-resolved images were reconstructed, which are shown in Figure 45. The cell surface of non-induced and induced trypanosomes revealed a uniform distribution of VSG localisations. Thus, no Ripley analysis was performed. On average, 1099 ± 498 and 744 ± 332 VSG localisations per µm^2 were present on non-induced and induced trypanosomes, respectively.

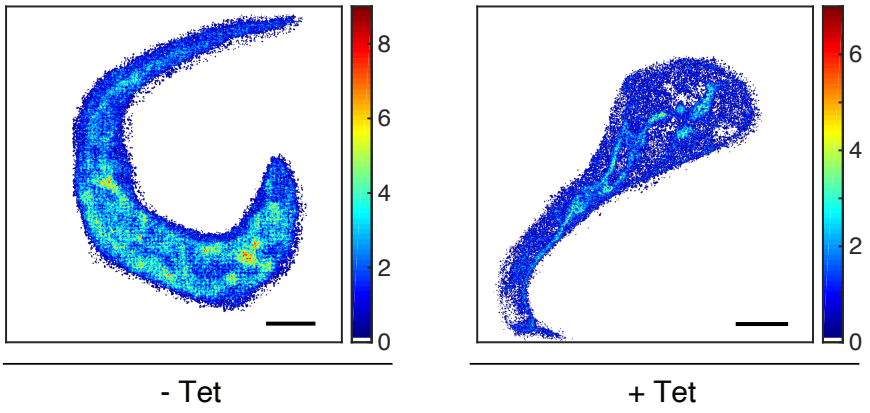

Figure 45: Super-resolved images of VSG localisations on trypanosomes of non-induced and 24 h induced WCB-depletion. Localisations are displayed at a localisation precision of 30 nm (- Tet) and 28 nm (+ Tet). The quantity of localisations is colour-coded. The scale bar is 2 µm. Artificial clusters were removed in advance.

Second, single-molecule trajectories were computed by applying a probabilistic algorithm. On average $1.42 \,\mathrm{x}\, 10^4 \pm 1.02 \,\mathrm{x}\, 10^4$ trajectories were identified on non-induced trypanosomes. On average $6.76 \,\mathrm{x}\, 10^3 \pm 4.18 \,\mathrm{x}\, 10^3$ trajectories were found on WCB-depleted cells. In both cases, the average trajectory length was 4 steps.

Analysing the obtained trajectories with shortTrAn revealed that the average diffusion coefficient of non-induced cells was $1.92 \pm 0.34\,\mu m^2/s$. This was higher than the average diffusion coefficient determined on cells after 24 h of WCB depletion, which was $1.51 \pm 0.32\,\mu m^2/s$ (Figure 46 A). When the WCB-depleted cells were grouped and evaluated according to their phenotypes, the following average diffusion coefficients were measured (Figure 46 B): $1.36 \pm 0.22\,\mu m^2/s$ for cells appearing similar in shape to the slender form (N = 6), $1.61 \pm 0.31\,\mu m^2/s$ for posterior swollen cells (N = 9) and $1.50 \pm 0.35\,\mu m^2/s$ for round trypanosomes (N = 5).
A comparison of the mean eccentricity of non-induced cells of 0.69 ± 0.04 with induced trypanosomes of 0.71 ± 0.04 (Figure 46 A), revealed no significant difference.

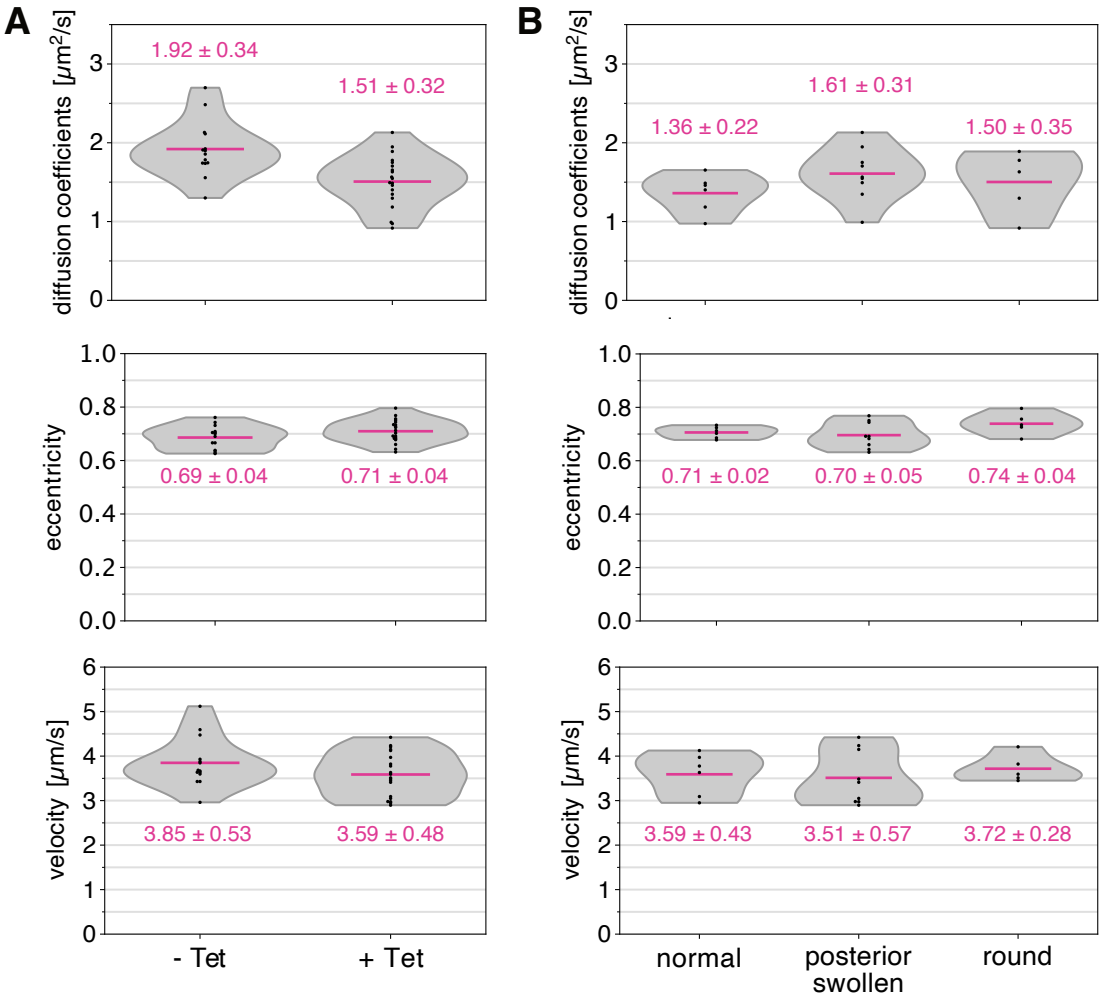

Figure 46: Quantification of VSG dynamics on 2T1 WCB RNAi cells 24 h after induction by shortTrAn. **A** Comparison of the average diffusion coefficient, the average eccentricity, and the average velocity (magenta lines) on the cell surface of cells not induced (- Tet, N = 14) and induced (+ Tet, N = 20) for WCB depletion. **B** Representation of the average diffusion coefficient, the average eccentricity, and the average velocity (magenta lines) of WCB depleted trypanosomes grouped by their phenotypes. Cells appearing similar to non-induced cells (normal, N = 6), cells swollen only at the posterior part (posterior swollen, N = 9), and rounded cells (normal, N = 5).

In addition, when the induced cells were grouped according to their phenotypes, they could not be distinguished. The mean eccentricity for cells with a normal shape was 0.71 ± 0.02, for posteriorly swollen trypanosomes 0.70 ± 0.05 and for rounded cells 0.74 ± 0.04 (Figure 46 B).
The average velocity measured on non-induced cells was 3.85 ± 0.53 µm/s and 3.59 ± 0.48 µm/s on WCB-depleted cells (Figure 46 A). When WCB-depleted cells were categorised, the velocity of normal-appearing cells was 3.59 ± 0.43 µm/s, of posterior swollen cells 3.51 ± 0.57 µm/s, and of round cells 3.72 ± 0.28 µm/s (Figure 46 B).

Next, to decide on the local predominance of diffusion or directed motion, the supermaps were created based on the results of shortTrAn.
First, I compared the relative prevalence and connectivity of superpixels of WCB-depleted cells versus non-induced cells. The cells of the two groups were first classified into the three groups already defined in Section 2.4.4.2 based on the presence of a directed motion and its coverage of a contiguous area. In the case of the VSG dynamics of non-induced cells, five of the trypanosomes were assigned to group 1, six of the trypanosomes to group 2 and three trypanosomes to group 3. All supermaps generated from the VSG dynamics of non-induced cells is depicted in Figure 57 (Appendix). Diffusion dominated on the surface of all three groups (Figure 47 A, group 1: 74 ± 5 %, group 2: 69 ± 4 %, group 3: 49 ± 3 %). In group 1, superpixels in which diffusion dominated covered the largest contiguous area. This was indirectly determined from the connectivity of superpixels assigned to diffusion to their immediately neighbouring superpixels. 75 ± 4 % of superpixels were surrounded by six to eight neighbouring superpixels also assigned to diffusion. In contrast, the rate was 71 ± 8 % in group 2 and 58 ± 7 % in group 3 (Figure 47 B). The share of directed motion increased from 7 ± 2 % with increasing group number and was 22 ± 5 % for group 3 (Figure 47 A). The connectivity of superpixels dominated by directed motion to neighbouring superpixels with the same motion mode was highest for group 3. Here it was 52 ± 3 % for superpixels surrounded by three to five superpixels of the same motion model and 26 ± 6 % for superpixels surrounded by six to eight superpixels of the same motion model (Figure 47 B). Similar to the study on 13-90 eYFP::MORN1 cells, the superpixels dominated by directed motion were arranged in elongated, contiguous clusters for cells of group 3. In contrast to the measurements on the 13-90 eYFP::MORN1 cells, no superpixels of diffusion were localised in the centre of the elongated, contiguous clusters. Additionally, the orientation of a directed motion in these superpixels did not point towards each other, which was the characteristic for the before observed elongated traps. Interestingly, round traps with superpixels dominated by a directed motion pointing to a common centre characterised often by diffusion were still present. On average, three round traps were located on each cell. Orphan superpixels were slightly more abundant in group 3 with 29 ± 2 % than in groups 1 and 2 with 19 ± 6 % and 18 ± 5 %, respectively (Figure 47 A).

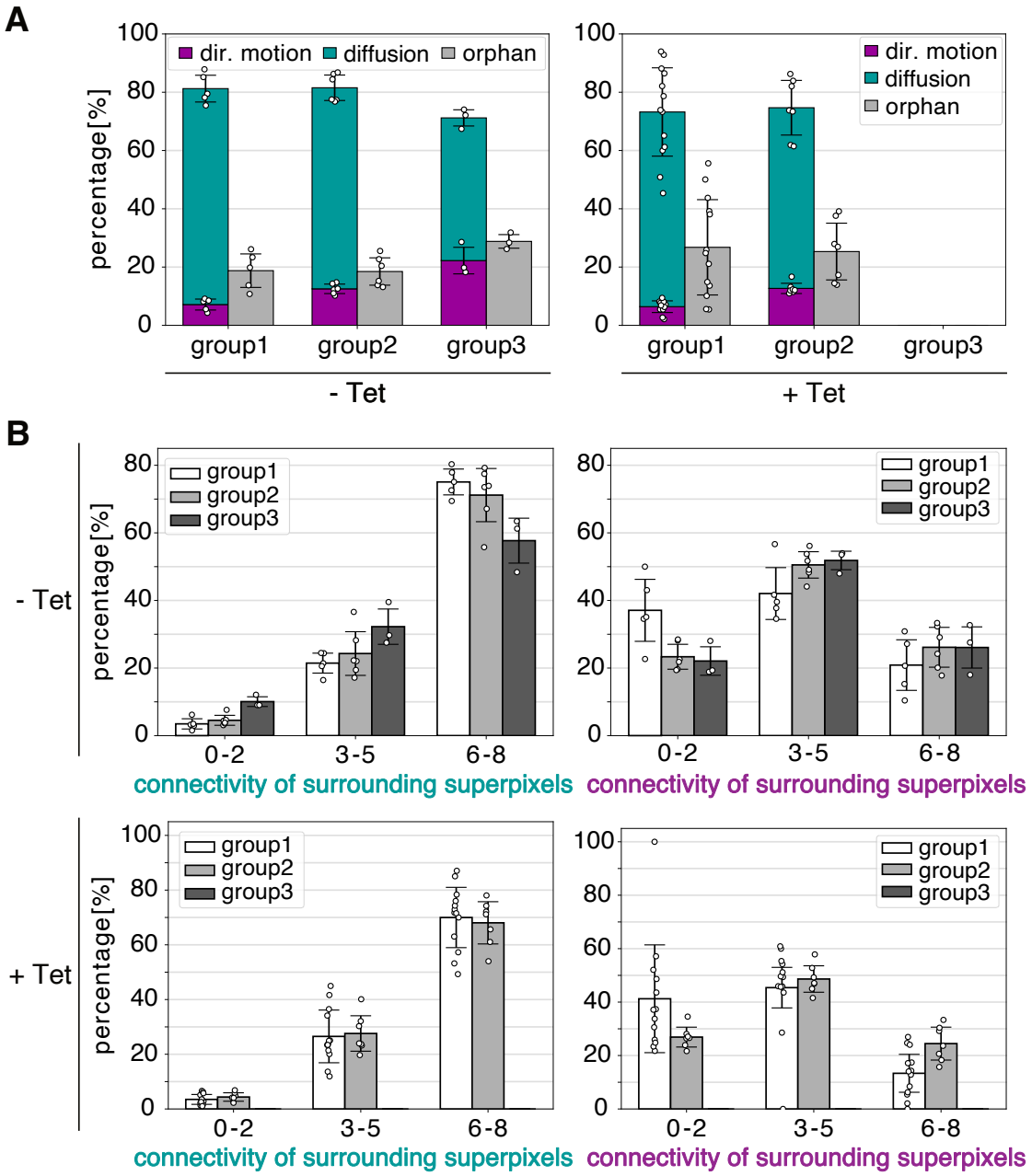

Figure 47: Quantification of supermaps obtained from VSG dynamics on trypanosomes 24 h after induction of WCB depletion. **A** Comparison of the relative prevalence on the locally dominating motion mode on not induced (- Tet) and induced (+ Tet) cells. Diffusion is represented in cyan, directed motion in magenta, and orphaned superpixels in grey. Cells were grouped according to the relative prevalence of the motion mode specified in Section 2.4.4.2. **B** Comparison of the connectivity of superpixels dominated by diffusion or directed motion to superpixels of the same motion mode in the surrounding. Connectivity of non-induced (- Tet) cells is compared to induced (+ Tet) cells. Group 1 is depicted in white (- Tet: N = 5; + Tet: N = 13), group 2 in light grey (- Tet: N = 6; + Tet: N = 7), and group 3 in dark grey (- Tet: N = 3; + Tet: N = 0). The number of cells per groups accounts also for A. In A and B, error bars show the SD. Individual values representing a supermap of one cell are indicated by circles.

When analysing the predominant motion mode of VSGs on the surface of trypanosomes after 24 h of WCB depletion, it was observed that no cells could be assigned to group 3. Of the 20 cells examined, thirteen cells were classified into group 1 and seven cells into group 2. All supermaps obtained from the VSG dynamics on WCB-depleted cells are shown in Figure 58. Group 1 and group 2 were again dominated by diffusion with 67 ± 15 % for group 1 and 62 ± 9 % for group 2. The average proportion of superpixels assigned to a directed motion increased from group 1 with 6 ± 2 % to group 2 with 13 ± 2 % (Figure 47 A). Whereas the proportion of orphan superpixels was similar (group 1: 27 ± 16 %, group 2: 25 ± 10 %). The connectivity of superpixels dominated by diffusion was similar in both groups. Superpixels of diffusion with six to eight neighbours of the same mode of motion were found with a prevalence of 70 ± 11 % in group 1 and 69 ± 8 % in group 2 (Figure 47 B). Thus, diffusion dominated over a wide area of contiguous superpixels. For the connectivity of superpixels dominated by directed motion, group 2 distinguished itself from group 1 by having 24 ± 6 % of superpixels with six to eight neighbours of the same mode compared to 13 ± 7 % (Figure 47 B). The small number of superpixels dominated by directed motion was in many cases arranged in round traps. Again, the round traps were often characterised by superpixels in the centre, which were dominated by diffusion. On average, three round traps were present per cell. Consequently, the assignment of cells on the basis of the local predominant motion mode showed a tendency towards a decrease in contiguous areas dominated by directed motion linked to the depletion of WCB.

Second, to investigate whether differences were detectable between phenotypes of cells after 24 h of WCB depletion, trypanosomes were grouped according to normal appearing cells, posteriorly swollen cells and round trypanosomes. Compilation of supermaps according to the phenotypes of the trypanosomes is shown in Figure 59 (Appendix). Subsequently, these groups were examined for the relative prevalence of the dominant motion modi and their connectivity.

The VSG dynamics for all three phenotypes were dominated by diffusion with an average of 65 ± 14 % in normal-appearing trypanosomes, 70 ± 12 % in posteriorly swollen cells and 65 ± 6 % in round trypanosomes (Figure 48 A). The fraction of superpixels dominated by directed motion was found to be minor in all three groups. This was 10 ± 3 % for normal appearing trypanosomes, 8 ± 4 % for posteriorly swollen cells and 7 ± 5 % for round cells. The average share of orphan pixels ranged from 22 ± 13 % for posteriorly swollen trypanosomes to 28 ± 11 % for round trypanosomes.

The analysis of the connectivity of superpixels dominated by diffusion revealed that over 60 % of the superpixels in the supermaps of the three phenotypes were surrounded by six to eight neighbouring superpixels with the same motion model (Fig-

ure 48 B, normal-appearing: $68 \pm 9\,\%$, posterior swollen: $73 \pm 9\,\%$, round: $64 \pm 10\,\%$). Thus, VSG dynamics on the surface were characterised by diffusion over a large contiguous surface area. The analysis of the connectivity of superpixels dominated by directed motion revealed that the majority of the small proportion of superpixels were surrounded by three to five surrounding superpixels of the same motion mode in all three phenotypes with over 40 % (Figure 48 C, normal-appearing: $47 \pm 4\,\%$, posterior swollen: $49 \pm 8\,\%$, round: $42 \pm 6\,\%$). Followed by superpixels with up to two adjacent superpixels of directed motion (normal-appearing: $33 \pm 10\,\%$, posterior swollen: $34 \pm 11\,\%$, round: $45 \pm 28\,\%$). This demonstrated that the few superpixels dominated by directed motion did not span contiguous surface areas but were mostly isolated or arranged in round traps. In conclusion, the relative prevalence

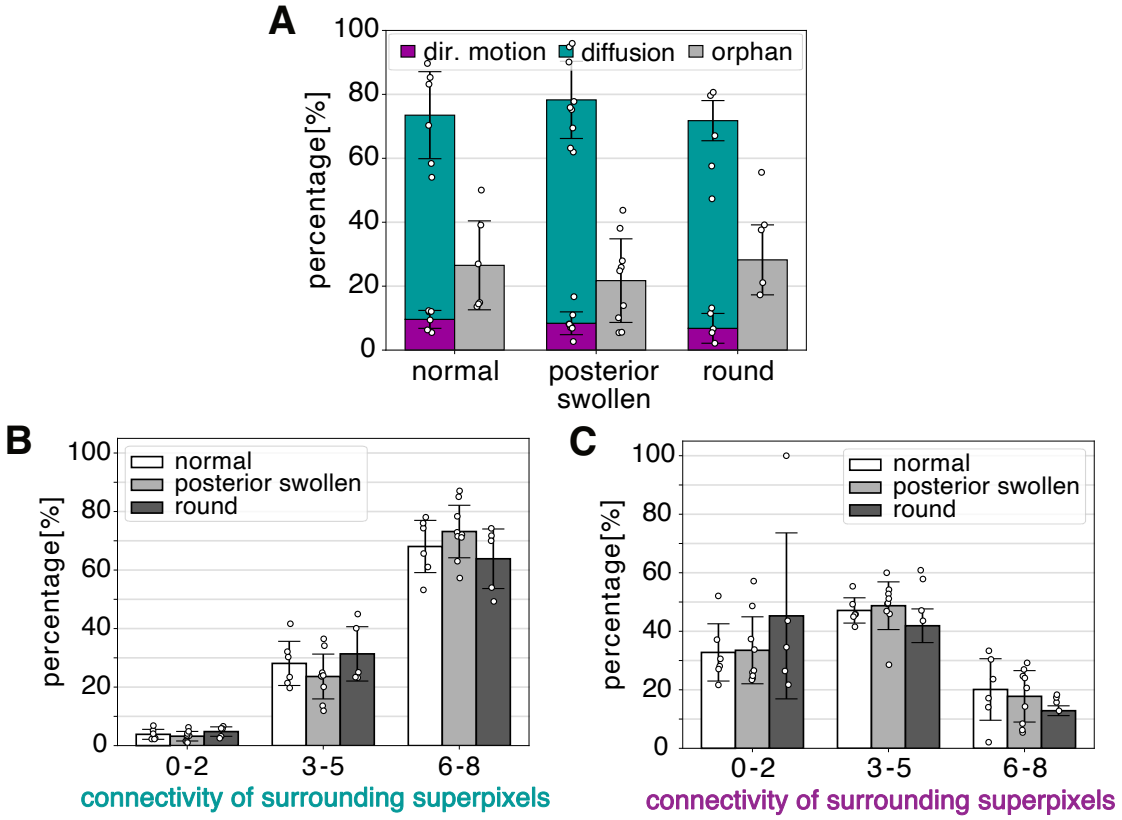

Figure 48: Quantification of supermaps obtained from VSG dynamics on WCB-depleted trypanosomes with respect to their phenotypes. **A** Relative prevalence on the dominating motion mode on trypanosomes after 24 h of WCB depletion. Phenotype groups represent cells appearing similar to non-induced cells (normal, $N = 6$), cells swollen only at the posterior part (posterior swollen, $N = 9$), and rounded cells (round, $N = 5$). **B** Connectivity of superpixels dominated by diffusion to adjacent superpixels of the same motion mode. **C** Connectivity of superpixels dominated by directed motion to surrounding superpixels of the same motion mode. In B and C, cells appearing like non-induced cells are depicted in white, posterior swollen cells in light grey, and rounded cells in dark grey. The number of cells in A accounts also for B and C. In all graphs, error bars indicate the SD. Individual values representing a supermap of one cell are shown by circles.

of diffusion and directed motion, as well as the connectivity of motion modes, was similar for all three phenotypes, and no phenotype was particularly prominent.

In summary, to study the distribution and dynamics of VSGs on the surface of trypanosomes in dependency of the cytoskeletal anchoring two experiments were performed. Firstly, single-molecule tracking was conducted on osmotically swollen 13-90 eYFP::MORN1 cells. Secondly, the distribution and dynamics were investigated on trypanosomes which had the possible connector protein, WCB, depleted by RNAi. In both cases the determined average diffusion coefficient was slower than determined for the control groups that were not osmotically swollen or in which the RNAi had not been induced with tetracycline. However, the average eccentricity and the average velocity of a directed motion were quite similar. When analysing the locally dominating motion mode on the surface by creating supermaps, no osmotically swollen trypanosomes or WCB-depleted trypanosomes could be assigned to group 3. This group was characterised by elongated, contiguous arrays of superpixels dominated by directed motion, so-called elongated traps. In contrast, round traps still existed. In both experiments, diffusion dominated and superpixels dominated by directed motion were spatially isolated.

3 Discussion

In this thesis, VSG dynamics were examined with single-molecule fluorescence microscopy (SMFM) in living trypanosomes to provide a better temporal as well as spatial resolution of the dynamics compared to FRAP analysis. First, in Section 3.1 the adjustments in sample assembly are discussed, including the implementation for the correction of the stage drift. In the second Section 3.2, I will elaborate on the adaptation of an algorithm for the evaluation of short VSG trajectories and the requirement for two extensions. In the third Section 3.3, I discuss the results of single-molecule microscopy and subsequent single-molecule tracking on living trypanosomes. This includes the discussion of the calculations of the escape time of VSGs into the FP, which were complemented by simulations on long time scales not accessible in the experiment. Simulations were used to estimate the randomisation of VSGs on the surface, whether a turnover of the complete VSG coat is feasible within a few minutes.

3.1 Establishment of the experimental setup for two-colour single-molecule measurements in living trypanosomes

Live-cell single-molecule fluorescence microscopy (SMFM) on highly motile trypanosomes requires the immobilisation of the parasite in a nanometre range. In this thesis, I studied the VSG dynamics using SMFM at the physiological temperature of the parasite's host at 37 °C. Prior to this, drift correction at a nanometre scale was implemented for two-colour measurements, as the investigation of VSG dynamics in relation to the labelled FP entrance was performed by two-colour experiments.

Embedding strategies employing in low-melting agarose (Bülow et al., 1988) or gelatine (Hartel et al., 2015; Hartel et al., 2016; Hempelmann et al., 2021) used in previous studies were not suitable for my project. Although low-melting agarose cross-links irreversibly and allows measurements at 37 °C, the hydrogel stiffness is not sufficient to immobilise the highly motile trypanosomes at the nanometre scale. To facilitate measurements in low-melting agarose, the movement of the trypanosomes needs to be additionally reduced or prevented. Therefore, Bülow et al. (1988) inhibited the glycolytic enzyme glyceraldehyde 3-phosphate dehydrogenase with pentalenolactone. This resulted in the depletion of cellular levels of ATP, and motionless trypanosomes. However, the impairment of the ATP metabolism is a severe interference and is expected to have a drastic effect on all cellular processes. On the other hand, gelatine cross-links to a hydrogel with sufficient stiffness to enable embedding of trypanosomes without ATP depletion. However, it restricts the measurements to room temperature due to its temperature-dependent, reversible cross-linking.

Non of the two above described hydrogels is sufficient for a nanometre immobilisation of living, and untreated trypanosomes at a temperature of 37 ℃. For this reason, I opted for an alternative immobilisation strategy. Hydrogels based on the thiol-ene click chemistry enable an efficient immobilisation of living trypanosomes at a nanometre scale (Glogger et al., 2017a; Glogger et al., 2017b; Glogger, 2018). Due to their irreversible cross-linking, single-molecule experiments can be performed even at 37 ℃. The reaction of thiols with enes can either proceed by a catalysed thiol Michael addition or a thiol-ene free-radical addition (reviewed in Hoyle and Bowman (2010)). Hydrogels cross-linked by free-radical addition include hydrogels based on allyl functionalised poly-glycidol (P(AGE-co-G)) and thiol-modified hyaluronic acid (HA-SH) or 8-arm poly (ethylene glycol)-norbornene (PEG-NB) and linear PEG-dithiol (Glogger et al., 2017a; Glogger et al., 2017b; Glogger, 2018). They were cytocompatible and provided efficient immobilisation. However, both hydrogels required the addition of a photoinitiator and exposure to UV-light to cross-link within several minutes. Upon UV exposure the photoinitiator forms free radicals, which initiate polymerisation by the reaction with hydrogel components. Although, only low concentrations of the photoinitiator were used, the free radicals also might interact with molecules on the surface. Furthermore, UV light in particular is associated with the production of reactive oxygen species that can cause severe cell damage (McMillan et al., 2008). Even though the presence of an photoinitiator and UV illumination showed no effect on the integrity of the plasma membrane (Gould et al., 2008; Glogger, 2018), an influence on other cellular processes can not be excluded. For this reason, I chose the embedding in a self-polymerising hydrogel of 8-arm poly (ethylene glycol)-vinylsulfone (PEG-VS) and thiol-modified hyaluronic acid (HA-SH), which is based on Michael addition (Glogger, 2018). Cross-linking required no UV light and is fast (∼one minute) under an alkaline pH of 8.3 [3]. This hydrogel provided good cytocompatibility (Glogger, 2018). In order to check on the immobilisation efficiency, I utilised the 13-90 kin-MORN1::eYFP cell line, which expresses an eYFP-labelled protein located in the axoneme of the flagellum (Glogger et al., 2017a; Glogger, 2018). As the flagellum is the origin of the cell's motility, determining the structural diameter of the axoneme in super-resolved images followed by comparison to the diameter obtained from fixed cells or from electron micrographs provided information on the efficiency of immobilisation. The diameter of the axoneme obtained from 32 super-resolved images was 172 ± 18 nm and thus smaller than the diameter of fixed cells (214 ± 39 nm, Glogger et al. (2017a) ,Glogger (2018)) or in electron micrographs (210 - 230 nm, Nicastro et al. (2006); Koyfman et al. (2011)). In the high-resolution images, the signal of the axoneme could be depicted clearly and no blurring was observed and thus it can be concluded that an immobilisation efficiency in the nanometre range was achieved.

[3] Corresponds to the standard pH value used for labelling with NHS dyes.

Artificial sharpening resulting from a still too high label density for single-molecule measurements was identified as the cause of the surprisingly small diameter. Further artefacts such as false structures and multiple features collapsing into one can also be induced (Burgert et al., 2015; Sage et al., 2015; Fox-Roberts et al., 2017). To identify artificial sharpening as the cause, the single-molecule data were analysed with HAWK (Haar Wavelet Kernel), which separates the single molecules based on their blinking behaviour (Marsh et al., 2018). The algorithm was applied to data sets of four cells and the axonemal diameter increased by $\sim 34\,\mathrm{nm}$. Accounting for this previous underestimation, the average diameter of the axoneme increases from 172 nm to 206 nm, which is in good agreement with the diameters of fixed cells or extracted from electron microscopy.

The Young's modulus of the hydrogel, a measure of the stiffness of a hydrogel, was assayed with the support of Leonard Forster. An average Young's modulus of $105 \pm 29\,\mathrm{kPa}$ was determined for the PEG-VS/HA-SH hydrogel based on the 10 kDa HA-SH. This value is high compared to the stiffness of hydrogels typically used in cell culture ($< 40\,\mathrm{kPa}$, Le et al. (2016)) and for tissue engineering ($\leq 34\,\mathrm{kPa}$, Huang et al. (2012)), excluding the differentiation of stem cells to bone and cartilage, which require higher Young's moduli. In comparison to the previous employed 15 % P(AGE-co-G)/HASH hydrogel with a stiffness of $154 \pm 22\,\mathrm{kPa}$, the Young's Modulus of the PEG-VS/HASH hydrogel is lower to sufficiently immobilise swimming trypanosomes that generate forces of $< 10\,\mathrm{pN}$ (Stellamanns et al., 2014). However, we find that a Young's modulus of 105 kPa is also sufficient to successfully immobilise the cells at the nanometre scale.

The lateral drift of the microcopy stage is a common issue in single-molecule microscopy given the acquisition time of several minutes. Consequently, static structures or outlines appear blurred and, in the case of the study of dynamic processes, directionality is introduced, intensified or cancelled. Potential sources of the drift include mechanical instability of instruments, vibrations as well as temperature control (Han et al., 2015) and thus, a drift at a nanometre scale is hard to avoid. In the measurements presented here, the drift occurred uneven and varied in severity over time rather than being uniform and constant.
The drift can be estimated from the single-molecule localisation alone using image cross-correlation (McGorty et al., 2013; Wang et al., 2014). This requires caution and stationary structures, e.g. microtubules, and can not be applied on moving emitters. Alternatively, the lateral drift can be measured by incorporation of fiducial markers into the sample, e.g. gold nanoparticles or fluorescent beads. Tracking of immobile fiducial markers then allows for the drift correction by subtracting the estimated drift also from moving particles. Hereby two strategies exist: First, fiducial markers can be used for an active, real-time adjustment of the stage position.

To this end, fiducial markers are tracked with a second camera and a closed loop system is utilised to drive piezoelectrical actuators that precisely reposition the stage (Grover et al., 2015). This strategy is favoured as it is highly precise. However, it is technically more demanding and requires additional space at the microscopic setup. A second possibility is to track the localisations of the fiducial markers and to subtract the registered drift *a posteriori*. In this work the second strategy was chosen as it was easier to implement and less costly. TetraSpeck™ (TS) beads (⌀ 100 nm) with a diameter below the diffraction limit were used as fiducial markers. Three major challenges exist when using fluorescent fiducial markers: Firstly, when conducting two-colour microscopy, the fiducial markers need to be detected in both color channels. To this end, the multifluorescent TS beads were employed. Secondly, the fluorescence of the dyed TS beads may outshine the fluorescence of the Atto-647 N NHS labelled VSGs in the surface coat of the trypanosomes or the eYFP signal of the labelled hook complex. To prevent this, the TS beads were pre-bleached with UV light. Thereby, the fluorescence intensity was sufficiently reduced, but at the same time the fluorescence of the beads remained stable throughout the measurements. Thirdly, the TS beads must be in the same field of view. For this the assembly of the sample was adjusted. The addition of the TS beads directly to the hydrogel solution containing the cells, resulted in accumulation of the TS beads in close contact to the trypanosomes. No known reasons exist why the beads would have an affinity to the trypanosomes. An explanation might be, that the hydrodynamic flow generated by the swimming motion of the trypanosomes could be responsible for the preferential localisation of the beads to the trypanosomes while the hydrogel is polymerising. To circumvent this problem, pre-bleached TS beads were spin-coated on the cleaned cover slips. To locate cells at the bottom cover slip and thus, in close proximity to the TS beads, the self-polymerising hydrogel solution containing the cells was placed between two cover slips. Subsequently, a weight was placed on the sandwich to accelerate the distribution of the viscous and already polymerising hydrogel. To prevent squeezing of the cells during the weighting process, non-fluorescent spacer beads (⌀ 6 µm) were added to the hydrogel mixture. A final centrifugation step facilitated the positioning of the trypanosomes close to the bottom cover slip and the TS beads. In addition, the centrifugation enabled a beneficial orientation of the cells for SMFM with the entire longitudinal axis in the field of view.

In a proof-of-principle experiment, I showed that spin-coated TS beads in the field of view were immobile and thus exhibited a similar drift. Hereby, the drift fluctuations of a reference bead ($bead_{ref}$) in the field of view, used for correction, was compared to the drift of a bead located underneath a trypanosome ($bead_{tryp}$). The drift of ($bead_{ref}$) was tracked and only fluctuations above the localisation precision were

corrected. For the example in this thesis, application of the correction determined by $bead_{ref}$ was able to reduce the drift fluctuations $bead_{tryp}$ to ~1 nm ($bead_{ref}$) and ~8 nm ($bead_{tryp}$). Thus, the drift fluctuation was clearly below the localisation precision, which allows me to exclude an intrinsic movement of the fiducial markers. Therefore, spin-coated TS beads can be used to correct the global drift in the VSG localisations recorded on trypanosomes embedded in the hydrogels. This minimises significantly the occurrence of a blurring of a structure and the introduction, reinforcement or elimination of a directionality from a dynamic process.

As the standard labelling condition of pH 8.3 for NHS dyes induces stress to trypanosomes and the self-polymerisation time of ~ 1 minute complicated the whole assembly procedure, the polymerisation was prolongated by adjusting the pH to 7.0 - 7.5 and reducing the temperature. The hydrogel mix was stored on ice and the centrifuge was pre-cooled at 4 ℃. Both adjustments resulted in a polymerisation of approx. two minutes, which provided sufficient time for assembling the sample.
Subsequently, cytocompatibility was examined under the adapted conditions, as the weighting and centrifugation step in the assembly process induces additional stress for the cells. Propidium iodide (PI) is a common life/dead marker and was used in this work. Previous studies showed that PI is suitable to evaluate the viability of trypanosomes in hydrogels (Glogger et al., 2017a; Glogger, 2018). The fraction of viable cells was high for up to one hour, which corresponds to a high cytocompatibility. This period is sufficient for single-molecule microscopy in living trypanosomes. No measurements were performed longer than this period, as Marius Glogger demonstrated that viability decreased significantly after one hour (Glogger, 2018). Possible reasons could be the insufficient supply of the trypanosomes with glucose or side effects of an incomplete cell division process that might be impeded by the immobilisation.

In conclusion, embedding trypanosomes in PEG-VS/HA-SH hydrogels provided sufficient stiffness to immobilise living trypanosomes at a nanometre scale. The implementation of multifluorescent TS beads on the glass allowed for the successful correction of the stage drift. A high cytocompatibility guarantees live-cell single-molecule studies in living trypanosomes for up to one hour even after adjustments in the hydrogel assembly.

3.2 shortTrAn: Adaptation of an algorithm for the evaluation of short trajectories and its extensions

The MSD analysis is a widely used tool to characterise diffusive SPT data and to determine the corresponding diffusion coefficient. It is an especially robust method to determine the diffusion coefficient when free Brownian motion is present. For this purpose, the MSD is plotted over time and the diffusion coefficient can be determined from the slope of the fit. If long trajectories can be obtained from the measurements, the progression of the curve in the $MSD\,vs\,\Delta t$ plot can even be used to reliably identify the type of diffusion and the influence of a directed motion (Figure 4). In particularly, dynamic processes in the crowded biological environment are hampered to diffuse freely. The deviation from free Brownian motion is generally termed anomalous diffusion. To quantify anomalous diffusion α is determined from the $MSD(t)$. While free diffusion is characterised by $MSD(t) = Dt^{\alpha}$ with $\alpha = 1$, confined diffusion and active transport results in $\alpha < 1$ and $\alpha > 1$, respectively. However, in order to yield reliable results, only the first 10 - 20 % of the time lags of an ensemble of trajectories should be used to determine the diffusion coefficient (Qian et al., 1991). The same applies to the characterisation of the type of diffusion. If this recommendation is ignored, deviations from linearity can appear at large time lags even in the case of free diffusion. This emerges since the MSD is less averaged at large time lags, as the number of contributing displacements decreases which results in large statistical fluctuations (Michalet, 2010). VSG trajectories in the present thesis were short with an average length of 13 steps on 13-90 eYFP::MORN1 cells. However, to observe a deviation in linearity at least three time lags are required. This in turn would require a trajectory length of a minimum of 24 steps.

An alternativ evaluation which does not require a minimum step length is the analysis of the $1D$ displacements. Hereby, free Brownian motion is characterised by a Gaussian distribution. Deviations from Gaussian distribution indicate confined diffusion or an influence of directed forces. Performing the $1D$ displacements analysis on the trajectories obtained on 13-90 eYFP::MORN1 cells, showed a deviation from Gaussian distribution. This can be interpreted as a first indication that VSG dynamics may not only be characterised by free diffusion.

Another analysis that is independent of the trajectory length is the approach by Hoze et al. (2012). Here, Trajectories are decomposed into their one-step displacements (OSDs), which are then further evaluated. Theoretically, this approach is based on the Langevin model (Lemons and Gythiel, 1997). It states how the motion of a particle evolves if subjected to a combination of external forces (directed motion) and random due to stochastic influences (diffusion). This model permits to examine OSDs in both scenarios. Thus, both scenarios were quantified and diffusion

coefficients as well as velocities are obtained. The results were then registered to each steps origin into predefined feature spaces that resembled the surface of the trypanosomes. In order to be able to draw meaningful conclusions, the dynamics were evaluated as an ensemble which originated from the same pixel. To improve statistics, individual local results were binned to larger spatial groups (superpixels). The results in a superpixel were then averaged, as the size of the superpixels was sufficiently small to assume homogeneous behaviour in these superpixels. Ultimately, the local diffusion coefficient and velocity represent the average of the locally collected ensemble. This ensemble was still subject to the equation of motion and is composed of a directional component (directed motion) and a stochastic component (diffusion). Both components are always present, but can differ in their strength, length and time scale. The differences can also occur spatially distributed, which can be visualised by partitioning the monitored surface into spatial units. In this way, local differences on the surface can be assessed. This method therefore enables a spatially resolved analysis in contrast to the MSD analysis or the analysis of the $1D$ displacements. In principle, local heterogeneities could also be identified with the analysis of the $1D$ displacements, but significantly higher statistics per superpixel would be required to test a Gaussian distribution.

Settings for the adapted algorithm to evaluate short VSG trajectories and its extensions

The adaptation of the method introduced by Hoze et al. (2012) is referred as short trajectory analysis and abbreviated as shortTrAn. The following settings were used in shortTrAn:

Trajectories of all length were used for shortTrAn, as their reliability was tested by plotting the time course of randomly chosen trajectories on the underlying localisations and video sequences. The reliability of the localisations used was ensured by the fit of localisation parameters to the Atto-647 N footprint, such as signal width and intensity, and the application of a cell mask.

After the calculation of the diffusion coefficients and velocities of each OSD and their registration to the predefined feature spaces resembling the trypanosome surface, the subpixels of 1 nm were binned to larger superpixels to yield sufficient statistics. The smallest binning factor that can be chosen should encompass at least the localisation precision σ. σ of the VSG localisations was 26 nm. Thus, the smallest binning factor should yield a superpixel with 52 nm side length. However, in order to get reasonable statistics without loosing good resolution, a binning factor of 160 was selected. With this binning factor, 50 % of the superpixels comprised a minimum of 13 data points.

For the application of the spatial filters, the following settings were chosen. The first filter removed all entries with low statistics, which served to ensure reliable results. All entries with less than or equal to 5 entries were removed. Dynamics of VSGs in the surface coat of the trypanosomes were assumed to be homogeneous. However, this filter alone is not the only basis for obtaining reliable results. The second spatial filter of the original algorithm was retained. This removed completely isolated superpixels from the surface as a precautionary measure for the third filter, since these lacked information about VSG dynamics of the immediate environment. In contrast to the original algorithm by Hoze et al. (2012), the third spatial filter was a combination of two filters. One filter to smooth out the data assuming similar conditions on the scale of neighbouring superpixels, removing outliers that could be due to noise. The second filter removed $3D$ to $2D$ projection artefacts. I will elaborate on the cause of these artefacts in the following Section '$3D$ to $2D$ projection artefacts in shortTrAn maps'.

The adapted algorithm was further extended to consider the localisation errors that limit SPT: the static and dynamic localisation error (elucidated in Section 1.1.3). Both localisation errors were corrected in the calculation of the diffusion coefficient according to the literature (Martin et al., 2002; Savin and Doyle, 2005; Berglund, 2010; Michalet and Berglund, 2012; Backlund et al., 2015). The implementation is described in Section 2.3.2. The necessity of implementation is elaborated on in the Section 'Consideration of localisation errors has a significant influence on the measured diffusion coefficient'. For the calculation of the velocity of a directed motion, no established consideration of the localisation precision σ exists. Nevertheless, in order to measure the impact of σ, the relative standard error SE_v in the velocity was determined (Section 2.3.2). Finally, the presentation of the following information in the shortTrAn maps was validated: (i) the correct orientation of the ellipses with a Jupyter Notebook written by Torsten Paul (Section 2.3.3.1) and (ii) the orientation of the arrows by the evaluation of a single trajectory with shortTrAn (Section 2.3.3.2). The latter ensured that the arrows followed the course of the trajectory.

$3D$ to $2D$ projection artefacts in shortTrAn maps

During the validation of the implementation of shortTrAn on the VSG tracking data, an accumulation of high velocities especially in superpixels at the rim of the cell surface projection was observed (Figure 30). This observation can be attributed to a $3D$ to $2D$ projection artefact, which arose from the local registration of the results. This has necessitated the introduction of an additional $3D$ to $2D$ projection filter in the third spatial filter.

The results presented in a superpixel are an average value over an area resulting from displacements, which originated from this area. For clarification of the origin of the rim artefacts, a superpixel at the rim of the surface projection is compared with a superpixel in the centre of the surface projection. Thereby, free diffusion of particles is assumed.

If the superpixel was located in the centre of the cell surface, movements in all directions in the $2D$ plane could be registered from this superpixel. In the case of diffusion quantification, isotropic diffusion results in a circle in the ellipse plot, which can be characterised by an eccentricity tending towards zero. In the case of the directed motion quantification, the calculated velocities would cancel each other out due to the uniform contribution to all directions (upper panel in Figure 49).

If the superpixel of interest was located directly at the rim of the cell surface projection, movements following the $3D$ shape and thus out of the focal plane could not be accounted for. As a consequence, free diffusion appeared anisotropic, which is characterised by an increased eccentricity, whereas in the directed motion scenario, the result was an unusually large velocity in direction perpendicular to the rim. Velocities could no longer cancel each other out and instead accumulated (lower panel in Figure 49).

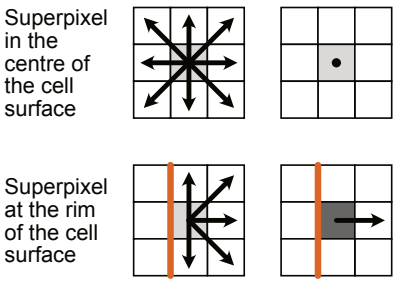

Figure 49: Scheme of the emergence of $3D$ to $2D$ projection artefacts. The measured velocity within a superpixel is an averaged value from one-step displacements emanating from this superpixel. In the case of free diffusion, calculated velocities within a superpixel would cancel each other out due to the uniform contribution to all directions. This is clearly recognisable in a superpixel in the centre of the surface projection. If the superpixel of interest is located at the rim of the projection, movements following the $3D$ shape are out-of-focus and could not be accounted for. Consequently, superpixels show a large net effect of velocities in direction perpendicular to the rim. The velocity amplitude is indicated in different shades of grey. The darker, the higher is the value.

To correct for the $3D$ to $2D$ projection artefacts, a Gaussian filter was implemented in the third spatial filter. The width as well as the strength of the filter was validated by random walk simulations on a trypanosome mask which were then evaluated with shortTrAn (Section 2.3.3.3). The filter was adjusted until the velocities of the superpixels at the rim of the surface projection were found to be in the same range as the velocities in the remaining superpixels. The orientation of the arrows

indicating the direction of the velocities were not modified. The filter simply reduces the magnitude of a velocity rather than counteracting contrary movements. The application of the projection filter to the results in the diffusion scenario also removed the deviation of the eccentricity at the rim to the remaining ellipses in the ellipse plot.

It should be noted, even though free diffusion was simulated, the eccentricity of ellipses located in the centre of the projection did not tend to zero. Instead, the eccentricity was 0.58. This observation was confirmed by simulations to determine which eccentricity values represent free diffusion depending on the statistics in superpixels. Hereby, the eccentricity decreased with increasing statistics, but was still 0.5 at $N = 200$. The eccentricity is known to be very sensitive to even small deviations from a perfect circle. For this reason, even small deviations from a uniform contribution in the movements assigned to a superpixel could lead to eccentricities that only tend towards zero at infinite statistics.

In conclusion, the $3D$ to $2D$ projection artefacts at the rim of the surface projection, which result from the local registration of results to the surface projection, can be addressed by the implementation of an additional spatial filter. Hereby, the velocity of a directed motion and the eccentricity ε are corrected. The correction of both values was particularly important as they were used to decide on the locally dominant motion mode.

Consideration of localisation errors has a significant influence on the measured diffusion coefficient

SPT suffers from sampling errors, also known as the static and dynamic localisation error. As already mentioned, their correction is for shortTrAn particularly important as it is based on the absolute values of the $MSD(\Delta t = 1)$. In order to determine their contribution in the measurements of this study and to verify the necessity for consideration, I back calculated an uncorrected diffusion coefficient for comparison.

The measured average diffusion coefficient in $2D$ corrected for both errors (D_{corr_2D}) of VSG diffusion on 13-90 eYFP::MORN1 cells was $1.00\,\mu m^2/s$ ($N = 20$). To extract the net effect of both corrections contributing to the resulting diffusion coefficient, the uncorrected diffusion coefficient $D_{noncorr\_2D}$ was determined for comparison. The determination of the $D_{noncorr\_2D}$ is based on the uncorrected $MSD_{noncorr\_2D}$ and is defined as follows:

$$D_{noncorr\_2D} = \frac{MSD_{noncorr\_2D}}{4\,\Delta t}. \tag{14}$$

The back calculation of $MSD_{noncorr\_2D}$ was done under consideration of the implementation of the static localisation error on the MSD with

$$MSD_{statt\_corr\_2D} = MSD_{noncorr\_2D} - 4\,\sigma^2 \tag{15}$$

and of the dynamic localisation error on the time lag, Δt, with

$$\Delta t_{dyn\_corr} = \Delta t - \frac{1}{3}\frac{t_{exp}}{\Delta t} t_{exp}, \tag{16}$$

resulting in:

$$MSD_{noncorr\_2D} = 4\,D_{corr\_2D}(\Delta t - \frac{1}{3}\frac{t_{exp}}{\Delta t} t_{exp}) + 4\,\sigma^2. \tag{17}$$

If the known parameters of the localisation precision $\sigma = 0.026\,\mu m$, time lag $\Delta t = 0.01\,s$ and exposure time $t_{exp} = 0.009\,s$ are used in Equation 17, the following calculation was obtained:

$$\begin{aligned} MSD_{noncorr\_2D} &= 4 * 1.00\,\mu m^2/s * (0.01\,s - \frac{1}{3} * \frac{0.009\,s}{0.01\,s} * 0.009\,s) \\ &\quad + 4 * (0.026\,\mu m)^2 \\ &= 4.00\,\mu m^2/s * 7.3\,x\,10^{-3}\,s + 2.704\,x\,10^{-3}\,\mu m^2 \\ &= 0.0319\,\mu m^2 \end{aligned} \tag{18}$$

Was the determined $MSD_{noncorr\_2D}$ used in the Equation 14, this resulted in:

$$\begin{aligned} D_{noncorr\_2D} &= \frac{0.0319\,\mu m^2}{4 * 0.01\,s} \\ &= 0.80\,\mu m^2/s \end{aligned} \tag{19}$$

Back calculation determined $D_{\text{noncorr\_2D}}$ to be only $0.80\,\mu m^2/s$. Thus, if both localisation errors were ignored, the average real diffusion coefficient would have been underestimated significantly by 20 %.

Out of interest in the individual and relative contributions of the two errors, these were calculated as follows:
The static localisation error is considered with the subtraction of $4\,\sigma^2$ (Equation 15). Thus, the $MSD_{noncorr\_2D}$ of $0.0319\,\mu m^2$ was overestimated by $2.7\,x\,10^{-3}\,\mu m^2$. This corresponds to an overestimation of 8 %. The correction of the static localisation error was carried out according to Equation 16. This results in a reduction of the time lag from 10 ms to 7.3 ms. This corresponds to a prior underestimation of 27 %. Hence, the impact of the static localisation error was minor compared to the dynamic localisation error.

In conclusion, although both localisation errors could in principle cancel each other out, a large net effect was found for this study. This emphasises the importance of taking both localisation errors into account.

Guideline based on random walk simulation enables the determination of the locally dominant motion mode

Evaluation of the VSG tracking data by shortTrAn used the same measured set of displacements to quantify the dynamics at two distinct scenarios: diffusion and directed motion. However, the dynamics of biological processes in crowded environments are always made up of a combination of both types of motion and is stated by the Langevin equation (Lemons and Gythiel, 1997). That also applies to the VSG dynamics here.

In order to determine the predominant type of motion and to detect spatial separation, superpixels in which one type of motion clearly dominated were to be identified. In this thesis, I proposed a guideline which identifies the dominant type of motion according to criteria indicating the probability of one of the motion types. In the case of diffusion, information is obtained on the local diffusion coefficient and whether isotropic or anisotropic diffusion was observed. Deviation from isotropic diffusion (circle) were quantified by means of the eccentricity ε of the ellipses ($\varepsilon \in [0, 1]$ with $\varepsilon_{circle} = 0$ and $\varepsilon_{line} = 1$). If the eccentricity approaches 1, this may be indicative of a strong anisotropic diffusion behaviour as well as the influence of a directing force or falsely induced by bad statistics. The latter was addressed by excluding superpixels with bad statistics. ε was considered to be a suitable criterion of the diffusion quantification to conclude on the probability of a type of motion, as anisotropic diffusion could be a first indication for the potential presence of directing forces.
The quantification of directed motion provided local velocities, direction of the velocities, as well as the relative standard error (SE_v) in the local velocities. SE_v indicates the fraction of the localisation error in the velocity. SE_v equals 1, if the measured velocity is caused solely by the inherent localisation precision of the measurement. There are two reasons for the existence of a large SE_v: Firstly, the average velocity in a superpixel is small. This reason will be true if either slow directed motion exists or in case of diffusion because random displacements add up to a zero net displacement. The second reason is that the corresponding error is very large. In contrast, a very small SE_v is obtained for a fast directed motion ($SE_v \to 0$). Thus, it is a measure of the likelihood of a directed motion and was considered a suitable criterion.

In the evaluation of the VSG dynamics on 13-90 eYFP::MORN1 cells by shortTrAn, the ε took all possible values between 0 and 1, whereas the SE_v ranged between 0.029 and 215. In order to finally determine whether diffusion was prevalent or not, appropriate thresholds for both criteria were required.
For this purpose, I simulated random walk processes. Due to a large isoperimetric ratio of the trypanosome projection of $\sim 25\pi$, which is only 4π for a circle of the same circumference, rim effects needed to be considered. Thus, simulations were performed on a trypanosome-shaped mask. Different data sets of trajectories with $D = 1.00\,\mu m^2/s$ were simulated from starting points randomly distributed on the trypanosome mask and subsequently analysed by shortTrAn. In the simulations, the trajectory length and the number of trajectories in a data set were adjusted to cover different numbers of data points per superpixel and thus the underlying statistics were varied. I found that instead of a single threshold, the threshold for ε as well as for SE_v had to be chosen depending on the statistics. The threshold values for both parameters were set under the premises that 99 % of the simulated diffusion data are assigned to a domination by diffusion and only 1 % of the superpixels would be wrongly classified as non-diffusive. These represent very strict threshold values and were based on the fact that simulations reflect the unambiguous case of free diffusion. If in the subsequent application of the guideline a superpixel is assigned to be dominated by directed motion, a false assignment can be excluded. As anticipated, ε was close to 1 at low statistics. Additionally, SE_v diverged at this regime. For this reason, superpixels with statistics in the unreliable regime, $N < 8$, were excluded from the decision which of the motion modes dominated.

To ensure that superpixels were only assigned to a motion type if there was a clear domination towards it, the following three safety measures were implemented: Firstly, superpixels were assigned which pointed to the same motion type with both criteria. Secondly, if the criteria of a superpixel indicated a contrary classification, the assignment was done on the basis of the criterion that deviated greater from its threshold value. The difference between the two deviations to their limit values was measured and had to exceed a threshold value. Thirdly, unassigned superpixels were characterised on the basis of their environment. That was possible due to the assumption of similar conditions on the scale of neighbouring superpixels. To prevent a misclassification, an assignment was only done if the environment was uniform. Specifically, this means that 7 out of 8 neighbouring superpixels had to show the same dominant type of movement. The results of the assignment were presented in supermaps, which showed superpixels dominated by diffusion or directed motion as well as unassigned, so-called orphan superpixels, colour-coded. Finally, the guideline was verified by applying it to the shortTrAn results of the random walk simulations used to determine the threshold values. Thereby it was shown that 99 % of the superpixels were assigned to diffusion and 1 % to directed motion as intended.

In summary, I developed a guideline to determine the locally dominant motion type on the basis of random walk simulations. Hereby, the ε and SE_v were found to be suitable decision criteria. The clear, colour-coded supermaps allow to grasp the VSG surface dynamics on trypanosomes at a glance.

3.3 Single-molecule microscopy in living trypanosomes

Sequential two-colour imaging was established to study VSG dynamics in relation to static structures at a high spatial and temporal resolution. Subsequent evaluation of the dynamic and static single-molecule data with shortTrAn and application of the guideline developed in this thesis enabled me to characterise the dynamics of VSGs. Furthermore, it was attempted to investigate whether the anchoring of the cytoskeleton in the plasma membrane exerts a potential bias on the dynamics of GPI-anchored VSGs.

Sequential two-colour imaging facilitates the investigation of fast dynamics in relation to a static reference structure

In order to investigate the highly dynamic VSGs in the surface coat of trypanosomes in relation to a super-resolved reference structure, two-colour single-molecule fluorescence microscopy was employed.

To analyse the localisations obtained in each colour channel, the information needs to be spatially or temporally separated. Spatial separation can be achieved by the implementation of an emission light splitter into a microscope setup. The projection of the two colour channels onto two separated regions on the sensor chip of the camera facilitates of recording record both information simultaneously. However, for this the imaging area on the sensor chip is doubled and thus is limiting the acquisition speed, as more time is needed to read and process the information. Two-color imaging employing a splitter was utilised by Marius Glogger on trypanosomes. This way the dynamic and static information could be recorded simultaneously, but at a time resolution of 28 Hz only (Glogger, 2018). To adequately resolve the movement of highly dynamic VSGs enabling the generation of meaningful trajectories, VSGs dynamics should be at least recorded at 100 Hz. For this reason, simultaneous two-colour imaging could not be utilised in the work presented here. To achieve high acquisition rates, the occupied region on the sensor chip was reduced by recording the two-colour information temporally separated. While sequential two-colour imaging is not suitable to study two dynamic processes in spatial correlation, it offers the possibility to examine a dynamic process in a spatial correlation to a static structure. This strategy allowed for an acquisition speed of up to 205 Hz.
In order to enable sequential two-colour imaging with spatial correlation at high precision, both colour channels were shifted horizontally to each other by a few pixels on the sensor chip. This allowed for a computational superposition in the two-digit nanometre range, whereas manual superimposition on the sensor chip would introduce an uncertainty of at least one pixel, which corresponds to 160 nm. Computational registration of both colour channels was based on the concept of utilising

immobilised multifluorescent TS beads (Semrau et al., 2011). This concept was already used by Marius Glogger to register the two-colour information in simultaneous two-colour imaging (Glogger, 2018). To generate a transformation matrix from the obtained TS bead localisations a built-in Matlab function fitted a local weighted mean transformation to a set of defined fixed and moving reference points that are related by a global second degree polynomial across the entire region of interest (ROI). It was already shown before that fitting by second degree polynomial provide good results for the registration of two-colour information distorted by lateral chromatic aberrations (Erdelyi et al., 2013). The distorting effect correlates with the image size and increases towards the edge of an image. However, the algorithm does not take into account rotational image distortions. These can arise from the rotation of one channel versus the other. However, to guarantee precise registration, the two colour channels need to be coarsely aligned manually. The adaptation of the registration to sequential two-colour imaging finally enabled registration with a precision of 55 ± 5 nm. This was slightly higher than the localisation accuracy for Atto-647 N and eYFP (~ 26 nm), but significantly improved compared to manual registration.

Thus, sequential two-color single-molecule experiments and the registration of the two-colour information is generally facilitated at a high temporal resolution without adding substantial imprecisions to the experiments.

Generation and analysis of single-molecule trajectories

To analyse the VSG dynamics, trajectories were generated from the VSG single-molecule localisations using a probability-based algorithm. The algorithm developed by Thomas Schmidt and his colleagues identifies the connection of the localisations with the highest probability under defined conditions in consecutive frames (Schmidt et al., 1996). This required an estimation of the diffusion coefficient of the particles. To prevent false positive connections, a repetitive D_{in} vs D_{out} analysis was performed prior to each analysis. Subsequently, the result served as input to generate the trajectories. This probability-based algorithm is suited when single molecules are present in low density and display moderate dynamics. These aspects are relevant to ensure that individual particles can be unambiguously tracked. If the particle density is too high or dynamics too fast, the probability increases that the paths of individual trajectories will cross too often, leading to an impeded tracking. For these cases, alternative methods have been developed, such as Particle Image Correlation Spectroscopy (Semrau and Schmidt, 2007) or Raster Image Correlation Spectroscopy (Digman et al., 2005). To ensure a low density in the case of VSG localisations as well as the prerequisite to follow individual particles, VSGs were stained with a nanomolar quantity, resulting in the detection of ~ 7 particles per

frame. Considering an average cell surface of $\sim 35\,\mu m^2$ in the focus, which was determined from the generated trypanosome masks in shortTrAn, this implies that one particle is present every $5\,\mu m^2$. Additionally, dynamics were recorded with a suitable frequency of 100 - 205 Hz. All this together with plotting the time course of randomly selected trajectories on the underlying localisations and video sequences, led to the conclusion that the generated trajectories could be considered reliable. Single-molecule trajectories were further analysed using shortTrAn to calculate local diffusion coefficients and the velocities of a directed motion. Subsequently, the guideline proposed in this thesis was used to decide on the locally dominating motion behaviour of surface VSGs.

Generation of the structural reference outline from single-molecule localisations

Fluorescently labelled static structures were used as a reference to investigate VSG dynamics in relation to structural features, like the entrance to the FP or the flagellum. In order to resolve the position of the structures with a precision of a few nanometres and thus matching the resolution of the VSG dynamics, SMFM was utilised to conduct super-resolution microscopy (SRM). The structures were then reconstructed by the sum of all temporally separated single-molecule localisations, which were depicted with the corresponding localisation precision. To resolve the complete structure high label densities are required to fulfil the Nyquist-Shannon theorem (Shannon, 1949). It basically states that the required distance between two labels needs to be less than half the feature size to completely resolve a structural feature.

In this thesis, proteins that are part of the structure used as reference were endogenously labelled with eYFP. Subsequently, the intrinsic blinking behaviour of eYFP (Dickson et al., 1997) was exploited to separate single emitters. The comparison of the obtained localisations to the known footprint of a single eYFP molecule, such as signal width and intensity, guaranteed to exclude false-positive localisations. To eliminate possible artificial clusters that falsely result from localising the same immobile emitters multiple times, a correction according to Annibale et al. (2011) was introduced. Eventually, a concave hull was placed around the single-molecule localisations to generate the outline of the structural feature.

The hook complex was chosen as a reference for the FP entrance. The structure is located directly underneath the plasma membrane and one end is wrapped around the FP neck, the constricted invagination of the plasma membrane to the FP. Structures like the FP collar or the FP itself were not considered as reference structures. Although the FP collar is also wrapped around the FP neck, it is located underneath the hook complex. This increases the distance to the plasma membrane and

the offset to the VSGs in the outer leaflet of the plasma membrane increases. Furthermore, the FP itself gives no indication of the location of the FP neck.
One component of the hook complex is MORN1 which is present in the complete structure (Morriswood et al., 2009; Esson et al., 2012). A bloodstream form (BSF) cell line, 13-90 eYFP::MORN1, was established which expressed an endogenously N-terminally tagged MORN1 (Section 2.2.1). Only one allele was labelled to ensure the detection of single molecules. Integration of the eYFP sequence in the MORN1 locus was tested by PCR. Expression and functionality of the fusion protein was verified by Western Blot analysis and the observation of cell growth. The correct localisation of the fusion protein was checked by Immunofluorescence analysis (IFA). Additionally, SRM showed that the hook-like structure could be resolved with a minimum of $1.1\,\mathrm{x}\,10^3$ localisation per µm^2. Taking into account the Nyquist-Shannon Theorem, the structure could be resolved with a mean distance between the particles of ~68 nm.
Similarly, to resolve the spatial course of the flagellum on the cell surface, the 13-90 kinesin-MORN::eYFP cell line was employed. Analogously, the fusion protein was expressed from only one of the kinesin-MORN alleles to ensure detection of single molecules. SRM successfully resolved the flagellar structure with on average $2\,\mathrm{x}\,10^3$ localisation per µm^2. Consequently, the structure was resolved with a mean particle distance of ~50 nm, considering the Nyquist-Shannon theorem.

VSG dynamics are fast and dominated by diffusion

VSG dynamics have been characterised several times by FRAP analyses. However, the diffusion coefficient determined would not be sufficient to achieve rapid randomisation of the VSGs in the surface coat and thus to explain the recycling of the complete VSG coat within a few minutes (Engstler et al., 2004). Consequently, the question arose whether VSG dynamics might be biased, for example, in proximity to the FP, the sole site for endo- and exocytosis, or whether the diffusion coefficient was underestimated. This question was addressed using SMFM. For the first time VSG dynamics were characterised at a high spatial and temporal resolution by single-molecule trajectories in living cells. The 13-90 eYFP::MORN1 cell line was used to enable additionally the investigation in a local context to the FP. Analysis of the SPT data with shortTrAn provided first insights into locally differentiated VSG dynamics.

Application of the guideline presented in Section 2.4.4.1 revealed that diffusion was indeed the dominating motion mode. However, cell-to-cell variability was observed in the proportion of superpixels dominated by diffusion ranging from 48 % to 91 %. The analysis of the VSG trajectories at a diffusion scenario considering the static and dynamic localisation errors resulted in an average diffusion coefficient of $1.00 \pm$

0.15 µm^2/s. Thus, the diffusion coefficient was two orders of magnitude faster than the diffusion coefficients of 0.01 - 0.03 µm^2/s determined by FRAP analyses (Bülow et al., 1988; Hartel et al., 2015; Hartel et al., 2016; Hempelmann et al., 2021). How can this great difference be explained? The following three considerations could contribute to the difference. Firstly, the methodological aspect. FRAP and SPT are both techniques to quantify dynamics, but the probed spatial and temporal scales differ. SPT works in the nanometre and milliseconds range, while basic FRAP operates at a micrometre and seconds scale (Chen et al., 2006). Moreover, FRAP implicitly assumes that the specimen under investigation is homogeneous and that all particles of an ensemble behave similarly. However, this is usually not the case for the plasma membrane of living cells, as they are heterogeneous due to various interactions of the individual components (reviewed in Kalappurakkal et al. (2020)). Consequently, FRAP provides an average of all possible different spatial behaviours and typically only one measurement per cell. Additionally, FRAP measurements require high label densities. In all studies that investigated VSG dynamics, including this study, VSGs were labelled with NHS-functionalised dyes. While these dyes introduce only a small label uncertainty, the NHS dye is a unspecific label and reacts with any primary amine group. However, in the case of the high abundance of VSGs (90 - 95 %) in relation to the remaining cell surface proteins of trypanosomes, NHS dyes offer an adequate choice, as VSGs labelled with a fluorescent protein do not reach the cell surface and show an restriction to intracellular membranes (Hartel et al., 2015). Even though VSG is the most abundant protein on the surface, it is likely that the high dye concentrations also label less abundant surface proteins. In this way, the average dynamics of several, possibly much slower protein families will be probed. In contrast, SPT distinguishes between individual proteins and acquires spatially highly resolved information. The nanomolar dye quantity in the case of trypanosomes additionally guarantees to label mainly the easily accessible VSGs. Secondly, the labelling strategy itself. As already mentioned, FRAP experiments require extensive labelling of the full surface coat to investigate the dynamics of the entire ensemble of surface proteins. This might result in artefacts due to steric hindrance, which are introduced by dye-dye interactions. In contrast, SPT has the advantage of working with nanomolar quantities to detect individual emitters and thus minimising the risk of steric hindrance. Thirdly, the influence of environmental conditions. The diffusion coefficient itself is dependent on the temperature, which is described by the Einstein relation: $D = \mu\, k_b\, T$, where D is the diffusion coefficient, μ is the mobility of the diffusive particle, k_b is the Boltzmann's constant, and T the absolute temperature. All measurements in the current literature, with the exception of Bülow et al. (1988), were conducted at 20 °C, which was due to the restriction imposed by gelatine embedding (Hartel et al., 2015; Hartel et al., 2016; Hempelmann et al., 2021). Although Bülow et al. (1988) performed experiments at

37 °C, a global ATP depletion was needed to immobilise the trypanosomes efficiently in the low-melting agarose gel. This was a severe interference and drastic effects on all cellular processes as well as on the plasma membrane are expectable. For this reason, the diffusion coefficient determined by Bülow et al. (1988) most probably would not represent a diffusion coefficient of VSGs in the coat of unaffected trypanosomes. In my studies, thermostable hydrogels were employed to allow for measurements of the VSG dynamics at 37 °C. When considering the temperature difference from 293 K to 310 K, this can account for a minor increase in the diffusion coefficient of ~6 %. However, the temperature does not only affect the diffusion of the VSGs. The fluidity of a lipid membrane is also influenced by the temperature directly via its phase behaviour (Bassereau and Sens, 2018). In general, the fluidity of the lipid matrix increases at higher temperatures and thus indirectly affected the dynamics of the anchored proteins. Ultimately, I conclude that not only one of the above considerations is the only valid reason, but that an interplay of all the factors mentioned contribute to the great increase in the VSG diffusion coefficient.
Examining the diffusion coefficient on a local level, a heterogeneity in the coefficient can be observed. Structural analysis by X-ray scattering implies that VSGs can adopt two main conformations (Bartossek et al., 2017). A relaxed conformation which possess a wider footprint, while a compact conformation is extended and slim. The authors assume this could be a dynamic adaptation to changes in the protein density in the membrane allowing to maintain the fluidity as well as the shielding function of the VSG coat. The presence of two freely diffusing populations of VSG in artificial lipid bilayers indicated that VSGs can adapt the two different conformational states in a lipid bilayer. In addition, the different conformations may allow the protein to adapt its structure to different environmental conditions, e.g. to float in the compact form over present receptors. Furthermore, the conformations are correlated with a difference in the diffusion coefficient. In the case of the recognised inhomogeneous diffusion, this could imply that due to different conditions or obstacles in the lipid membrane, a certain conformation is locally conditioned, which subsequently results in a local heterogeneity of the diffusion coefficients.

The proportion of local areas, dominated by directed motion ranged from ~9 - 52 % in the cell ensemble studied. The regions dominated by directed motion formed round or elongated traps. Both traps were characterised by superpixels dominated by directed motion enclosing an area that was often characterised by diffusion. While every cell had at least one round trap, elongated traps could only be observed on six of the 20 cell surfaces. Additionally the size of the round traps differed. All this together facilitated the categorisation into three groups. Hereby, the velocity vector pointed towards the centre. In elongated traps, this resulted in biased diffusion along the traps.

In order to identify a possible cause for the emergence of the round traps in the supermaps, videos were visually examined and reference maps were created that illustrated the dwelling time of particles. Slow, confined emitters were identified as the origin. There might be four possible causes for the confined particles on the cell surface which could be responsible for the appearance of the traps in the supermaps.

A first possibility could be that confined particles originate from artefacts of the sample arrangement, e.g. from embedding in the hydrogel or from interactions of the labelled VSGs with the glass surface. In control experiments investigating the dynamics of VSGs in supported lipid bilayers (SLB) with and without a hydrogel layer on top, the induction of confined particles by the hydrogel could be excluded (Section 2.4.3). Furthermore, the presence of immobile emitters on trypanosomes deeply embedded in the hydrogel or on the surface of trypanosomes facing the hydrogel that have been spun onto the glass indicated that the confined particles were not the result of interactions of the labelled particles with the glass surface (Section 2.4.3). This suggests that confined particles were not introduced by artefacts of the sample arrangement.

The second possible explanation is that the confined particles represent endocytosed, labelled VSGs that are located in endosomes. Their signal might be detected even though they are not in the plane of the plasma membrane because a widefield setup was used. However, single-molecule localisations were compared with the Atto-647 N footprint, and in particular the comparison with the error in the fit should reduce the number of particles outside the focus from being considered false-positive localisations. It can be ruled out that the focus was accidentally chosen within the cell as trajectories were collected over the entire cell surface and not only in a restricted area. Moreover, the size of the traps and their location contradict the endosome hypothesis. The size of the round traps was considered including the directed corona, as the $3D$ plasticity of the endosomes could also introduce the projection artefacts observed in this work. Round traps span at least three superpixels, which corresponds to a diameter of 480 nm and is thus significantly larger than the average diameter of endosomes with 135 nm (Grünfelder et al., 2003). In addition, round traps were also detected in the anterior part of the cell. However, endosomes usually localise in the area between the FP and the nucleus, which corresponds to the posterior part of the cell. Based on the numerous arguments against this possibility, I consider it extremely unlikely that the trapped particles could be endocytosed, labelled VSGs.

A second possibility might be that they are physically confined VSGs. This could be possibly caused by interleaflet coupling, as VSGs are linked by GPI-anchors to the outer leaflet of the plasma membrane. The presence and influence of interleaflet coupling has been investigated already extensively in solid supported model mem-

branes (Merkel et al., 1989; Jönsson et al., 2011; Camley and Brown, 2013; Hill and Wang, 2014) and has also been reported to affect the distribution of GPI-anchored proteins in living cells (Raghupathy et al., 2015). Raghupathy et al. (2015) observed that GPI-anchored proteins couple to complementary inner leaflet nanodomains of phosphatidylserine which were associated with connector proteins of the actin cytoskeleton in Chinese hamster ovary cells. However, long chain GPI-anchored proteins were investigated in this study. In contrast, the GPI-anchor of VSGs consists of two short (C14:0) myristate fatty acids. For this reason, an interleaflet coupling of the short GPI-anchor of the VSGs with fatty acids of potential lipid nanodomains in the inner leaflet of the plasma membrane is unlikely. Furthermore, phosphatidylserine represents only a very small fraction of the total cell lipidome in bloodstream form trypanosomes (Richmond et al., 2010). Whether the small fraction of phosphatidylserine is mainly localised in the plasma membrane where it forms lipid nanodomains enriched in phosphatidylserine remains elusive. Furthermore, an association of VSGs with lipid domains, in case of trypanosomes, is unlikely, as it would interfere with the functionality of the coat. However, interleaflet coupling is not the only possibility to explain confined VSGs. Interaction of VSGs with other proteins present in the outer leaflet of the plasma membrane might bias VSG dynamics. Possible candidates are integral proteins including proteins serving as connectors anchoring the cytoskeleton to the plasma membrane. Proteins of the inner leaflet of the plasma membrane are directly influenced, whereas proteins of the outer leaflet are only directly affected if the connectors are transmembrane proteins. Both can be explained by the picket-fence model (Kusumi et al., 2012). Glogger et al. (2017b) showed by insertion of a fluorescent probe that the inner leaflet of trypanosomes is structured and hypothesised the organisation of the inner leaflet in trypanosomes might be affected by the anchoring of the microtubule cytoskeleton to the plasma membrane. In the absence of transmembrane connector proteins, the pattern of the inner leaflet could be transferred to the outer leaflet by interleaflet coupling. Even though a direct interleaflet coupling of the short GPI-anchors of VSGs is highly unlikely, other proteins in the outer leaflet of the membrane could be influenced which then restrict VSGs in their dynamics. The existence of interleaflet coupling in trypanosomes has not yet been investigated, but based on the expanding knowledge of the complex interactions in the plasma membrane and with its environment, it is most likely that it exists.

The third hypothesis explains the existence of confined particles by non-specific binding of the NHS dye to a primary amine, resulting in labelling one of the less abundant proteins on the surface. A potential candidate could be a protein from the invariant surface glycoprotein (ISG) family, which are transmembrane proteins (Ziegelbauer et al., 1992; Ziegelbauer and Overath, 1992; Jackson et al., 1993; Nolan et al., 1997). Given that some ISGs, such as ISG-65 and ISG-75, have a similar size

to VSGs (Schwede et al., 2015), the VSG coat might not completely shield these proteins. In contrast to VSGs with $\sim 1 \times 10^7$ proteins on the surface, the total number of ISGs is estimated to $\sim 2 \times 10^5$ proteins. Thus, ISGs are 50-times less abundant than VSGs (Schwede et al., 2015). Consequently, the probability of a labelled ISG is at least 50 times less compared to a labelled VSG. The existence of an average of 3-4 round traps is comparatively small for the observed cell surface. This could indicate that a much less abundant protein has been labelled. The dynamics of ISGs within the cell surface have not yet been investigated due to the lack of adequate labelling strategies.

Currently, it is not possible to distinguish whether the confined particles are VSGs or less abundant surface proteins. To investigate this, click chemistry could be used to label VSGs specifically, which has proven successful for labelling proteins in living cells (Nikic et al., 2015). Click chemistry offers the advantage compared to endogenous labelling with fluorescent proteins that a natural amino acid is replaced by a noncanonical one that posses custom-designed functional handles (Wang and Schultz, 2004; Liu and Schultz, 2010; Lemke, 2014), also termed genetic code expansion. These variants react specifically with the dye and therefore the tertiary structure of the protein is hardly changed in advance.

Structural elements were considered as potential causes for the elongated traps that appeared on a few trypanosome surfaces. Elongated traps, were already recognised by a contiguous arrangement of aligned and elongated ellipses in the ellipse plot of the diffusion maps. To investigate a potential correlation with the flagellum, the spatial course of the flagellum of was probed (Section 2.4.1). To this end, (i) the spatial course of the flagellum was approximated by transmission light images, as the 13-90 eYFP::MORN1 cell line did not express a marker for the flagellum, and (ii) VSG tracking was performed on the 13-90 kinesin-MORN::eYFP cell line which has the flagellum fluorescently labelled. Both approaches showed no correlation between the flagellum and the arrangement of the aligned and elongated ellipses.

Supermaps generated from VSG tracking in the presence of a fluorescently labelled flagellum confirmed that there is no correlation between elongated traps and the flagellum (Appendix, Figure 60). Elongated traps were observed in 30 % of the cells, hence a possible correlation with the cell cycle was considered. The number as well as the distance in the case of two hook complexes was used to estimate the cell cycle stage. There was no correlation to the cell cycle found, as different cell cycle stages were detected in each group. However, a correlation cannot be completely excluded. This is because in the presence of two hook complexes, the progress of the cell cycle was approximated by the distance between the two complexes, which in turn was a $2D$ projection. Although I assume that it is more likely that the traps originate from a passive effect, e.g. trapping by an underlying structure, an active contribution cannot be ruled out.

The VSG dynamics was also analysed with regard to the area in which the FP is located. The hypothesis was whether VSG dynamics could be biased in the area in which the entrance of the FP is located. The outline of the hook complex was used to determine the position of the entrance. It should be noted that the FP entrance was often at the rim of the cell surface projection, which made evaluation challenging. No clear distinctions for the area of the FP entrance could be identified, neither in supermaps nor in parameters obtained by shortTrAn, such as local diffusion coefficients or local velocities. For the supermaps in general, both superpixels dominated by diffusion and dominated by directed motion were mapped to the FP region. In the case of an active transport process to and from the FP by e.g. molecular motors, I expect clear streams of directed motion around the pocket and not the patchwork we have seen. Furthermore, there was no preferential localisation of round traps directly to the area of the FP entrance. As only VSGs that were already on the surface were labelled with the dye, it was expected that if they were close to the FP, they would localise in the pocket and be endocytosed. Consequently, in the analysis of the directed motion, the orientation of the arrows representing the direction would point to each other and indicate a sink. However, this could not be observed. It might be that a net flow could not be resolved in superpixels as large as 160 nm. In addition, labelled VSGs that were close to the FP could also be pushed away by the exocytosis of unlabelled VSGs that takes place at the same time, resulting in an equalisation of the direction of movements in a local area. These are only presumptions and further experiments are needed to elucidate the movement of the VSGs into or out of the FP.

The intrinsic movement of the trypanosomes and its consequences on the observed results remained unconsidered in this thesis. At the present time, an influence of the the trypanosomes' swimming behaviour on the VSG diffusion cannot yet be studied experimentally in high resolution due to the long acquisition times. However, the additional energy introduced by the intrinsic motion is expected to increase the random mixing of laterally moving membrane-associated particles such as VSGs. Hence, an impact on the randomisation of VSGs as well as on the observed round and elongated traps cannot be excluded.

In summary, I presented the first characterisation of VSG dynamics in living trypanosomes based on single-particle tracking at the host's physiological temperature of 37 °C. Evaluation with shortTrAn enabled the analysis of VSG trajectories and showed that VSG dynamics are characterised mainly by diffusion at the resolution of the study. Diffusion was revealed to be fast with an average diffusion coefficient of 1.00 µm^2/s. Furthermore, a local heterogeneity in the VSG dynamics was recognised. Examining VSG dynamics in proximity to the FP entrance yielded no evidence of a guidance of VSGs into the FP. However, confined particles and confined diffusion

of particles in elongated regions were observed, indicating passive trapping possibly by underlying structures.

Random walk simulations reveal that rapid VSG randomisation allows for fast turnover of the VSG coat

The first single-molecule measurements of the VSG dynamics revealed a fast diffusion coefficient ($\overline{D} = 1.00 \pm 0.15\,\mu m^2/s$), which could be sufficient for fast randomisation of VSGs in the surface coat allowing the VSG surface pool to be recycled within ~12 minutes (Engstler et al., 2004). Endo- and exocytosis in trypanosomes is restricted to the FP, which is located at the posterior end of the cells. VSGs are forced to pass through this small invagination on their way into the cell. The FP accounts for only 5 % of the complete cell surface and thus the whole scenario resembles a narrow escape problem in biology. To test whether the newly determined diffusion coefficient is sufficient to ensure the escape of VSGs through the FP on the expected timescale, I performed experimentally-inspired random walk simulations on trypanosome-shaped masks with a small region representing the FP as well as theoretical calculations to extract the mean first passage time of VSGs diffusing with $D = 1.00\,\mu m^2/s$ on trypanosomes surfaces (Section 2.5). The simulated and the theoretically calculated mean first passage time for all three exemplary trypanosome surfaces was in the order of one minute and thus in good agreement with each other. The verification of the simulations by theory allowed for the extraction of the more relevant time scale, $\tau_{99\,\%}$, characterising the arrival of 99 % of the surface VSGs at the FP entrance from the simulations. The ascertained time was in the range of 3.5 - 6.0 minutes for surface areas of 56 - 80 µm² (Table 2). However, the surface area of trypanosomes is ~100 µm². Although trypanosome-shaped masked were derived from shortTrAn and consisted of two layers to mimic $3D$ plasticity, the used surface masks were smaller than 100 µm². This can be attributed to the fact that the area per layer was still less than half of the total surface area, which was due to to the measurements that captured only the part of the membrane in focus. Hence, $\tau_{99\,\%}$ was extrapolated for all three simulations to 100 µm² based on the direct proportionality of the surface area (A) and the escape time (τ) in theory (Section 2.5, Equation 13).

Table 2: Extrapolation of the escape time through the FP of VSGs distributed on the entire surface. A_{tryp}: surface area of a trypanosome; $\tau_{99\,\%}$: time until 99 % of the particles escaped.

A_{tryp} [µm²]	$\tau_{99\,\%}$ [min]	$\tau_{99\,\%}$ for 100 µm² [min]
68.6	5.7	8.3
80.0	6.0	7.5
56.4	3.5	6.2

This finally resulted in an increase in the arrival time to 6.2 - 8.3 min, which emphasises that VSGs distributed on the entire surface area can reach the FP entrance by free diffusion with an average diffusion coefficient of 1.00 µm^2/s to achieve a turnover time of ~12 min.

To ensure that the VSG coat retains its shielding function, recycling of the VSG coat includes the exocytosis of VSGs. Exocytosis as well as endocytosis take place simultaneously in the FP. This raises the question of how it is ensured that most of the exocytosed VSGs are not immediately re-endocytosed, and whether the newly determined diffusion coefficient may contribute to this. Hence, the following approximation was made:
The endocytosis rate in BSF trypanosomes is 7 Hz, which means that 7 vesicles are endocytosed per second (Engstler et al., 2004). The average diameter of clathrin-coated vesicles is 135 nm (Grünfelder et al., 2003; Engstler et al., 2004), which corresponds to a radius, r, of 67.5 nm. To determine whether the diffusion coefficient of 1.00 µm^2/s is sufficient for VSGs to escape the area endocytosed in one second, the endocytosed area (A_{endo}) was derived from the surface area of seven vesicles as follows:

$$\begin{aligned} A_{endo} &= 7 * (4 * r^2 * \pi) \\ &= 7 * (4 * 0.0675\,\mu m^2 * \pi) \\ &= 0.401\,\mu m^2 \end{aligned} \tag{20}$$

Thus, the area endocytosed per second is 0.401 µm^2. A VSG diffusing with $D =$ 1.00 µm^2/s has a high probability of escaping from the endocytosed surface. On the contrary, a $D = 0.01$ - 0.03 µm^2/s as determined by FRAP analyses would certainly not be sufficient to escape the endocytosed area. This suggests that the fast diffusion coefficient alone is sufficient to bring the majority of exocytosed VSGs to the cell surface and that no active processes are necessarily required.

In conclusion, the average diffusion coefficient of 1.00 µm^2/s determined in this study allows for a fast randomisation of VSGs in the surface coat of trypanosomes. It simultaneously enables VSGs distributed on the entire surface area to reach the FP entrance to allow for a turnover time of ~12 min and contributes to the prevention of exocytosed VSGs being directly re-endocytosed. This guarantees that the shielding function of the VSG coat is sustained during the recycling process and the maintenance of the VSG integrity.

Investigation of VSG dynamics with respect to a potential correlation to the trypanosome's cytoskeleton

Glogger et al. (2017b) found a structured inner leaflet in trypanosomes in a previous study and hypothesised that the cytoskeleton is at the origin of the pattern in accordance with the picket fence model. Here, I would like to test whether the structuring of the inner leaflet can be propagated to the outer leaflet of the membrane and thus potentially influence the distribution and dynamics of VSGs. A prerequisite for this is the interleaflet coupling of the inner leaflet with the outer leaflet of the plasma membrane. To address this question, VSG dynamics was investigated in trypanosomes that were osmotically swollen and in trypanosomes in which a microtubule-associated protein was depleted.

In the first experiment, 13-90 eYFP::MORN1 cells were osmotically swollen to detach the anchoring of the plasma membrane from the rigid cytoskeleton. ShortTrAn analysis followed by the generation of supermaps revealed that in nine out of ten swollen cells diffusion was the dominating motion mode. The proportion of superpixels that could not be assigned to a dominating motion scenario was larger then in the studies of non-swollen 13-90 eYFP::MORN1 cells. The average diffusion coefficient was $0.77 \pm 0.15\,\mu m^2/s$, and thus lower than the diffusion coefficient of non-swollen trypanosomes. Round traps, which are due to confined particles, were also visible in the supermaps of these cells. In comparison to the analysis of VSG dynamics on non-swollen trypanosomes, the proportion of cells with an elongated trap decreased and only one cell was found with a mild manifestation. In general, the cell-to-cell variability in the proportions of superpixels dominated by diffusion or directed motion decreased. Whether the detachment of the cytoskeleton has also potentially affected the area that can be probed by VSGs, the distribution of VSG locations was investigated using Ripley's $L(r) - r$ analysis. Prior to the analysis, artificial clusters were removed according to Annibale et al. (2011), which falsely arise from localising the same immobile emitters multiple times. A minimal increase in the radius of the potential clustered areas that can be probed by VSGs on swollen cells was found. The average potential radius of these areas on swollen trypanosomes was $240 \pm 26\,nm$, while on non-swollen 13-90 eYFP::MORN1 cells it was $225 \pm 20\,nm$. Although the cells were pre-swollen before embedding, hardly any swollen trypanosomes was found in the hydrogel. I suspect that cells experienced counteracting forces from osmotic swelling (expansion) and the hydrogel (compression). This could also lead to the connector proteins re-localising to the plasma membrane when the plasma membrane is again close to the cytoskeleton. Moreover, both radii deviated from the cluster size as well as the size of the diluted areas observed in the inner leaflet of the plasma membrane ($r_{cluster}$ =$170 \pm 5\,nm$, $r_{diluted} > 115 \pm 15\,nm$) (Glogger et al., 2017b). As anticipated due to the short GPI-anchor of

VSGs, no direct correlation was found between the size of the clusters in the inner leaflet of the plasma membrane and the potential clusters of the area probed by VSGs.

As osmotic swelling represented severe stress for the trypanosomes and its effects on the cellular processes could not be gauged, furthermore it remained unclear whether the cells had lost the anchoring of the microtubule skeleton to the plasma membrane, another possibility was sought to detach the anchoring from the membrane.

The depletion of the whole cell body protein (WCB, Tb427.7.3550) using RNA interference (RNAi) was pursued as a second strategy to study the VSG dynamics in light of a potential influence of the cytoskeleton. The WCB was selected as a promising candidate, as WCB localises between the sub-pellicular microtubule skeleton and the inner leaflet of the plasma membrane (Woods et al., 1992). Baines and Gull (2008) identified one domain each at the N- and C-termini in a bioinformatic analysis. The domains enable the protein to mediate the attachment of the microtubule skeleton to the plasma membrane which is the proposed function of the protein (Baines and Gull, 2008). Upon RNAi induction in BSF cells, the same phenotype as in PCF trypanosomes was observed (Baines and Gull, 2008): cells started to round at the posterior end (~6 - 12 h) and during depletion the cell morphology changed. Furthermore, rounded cells and multiflagellated cells (~16 - 24 h) were observed. The latter indicated a defect in cytokinesis. In BSF trypanosomes, the phenotypes established within half the time period described for PCF cells. This can be attributed to the cell cycle of BSF cells (~6 h) being twice as fast as that of PCF cells (~12 h).
VSG dynamics was investigated on three phenotypes: trypanosomes that resembled the shape of a non-induced cell, trypanosomes that rounded up posteriorly and completely round trypanosomes. By examining the round cells in bright field microscopy, it was ruled out that these were cells with a big-eyed phenotype. Indicators as the enlarged FP encircled by a membranous bulge were absent. Prior to SPT, the integrity of the plasma membrane was confirmed by the viability assay with propidium iodide (PI). VSG dynamics on trypanosomes 24 h after RNAi induction with tetracycline (N = 20 cells) was then compared to non-induced trypanosomes (N = 14).
Evaluation with shortTrAn and the subsequent generation of supermaps illustrated that diffusion dominated clearly the local surface areas in non-induced and induced cells. However, the diffusion coefficients differed. VSG diffusion on non-induced cells was faster ($\overline{D}_{non-ind} = 1.92 \pm 0.34\,\mu m^2/s$) than diffusion on induced cells ($\overline{D}_{ind} = 1.51 \pm 0.32\,\mu m^2/s$). This revealed the same tendency as observed on osmotically swollen cells. In addition, the average diffusion coefficient itself is significantly higher compared to the measured coefficients on the 13-90 eYFP::MORN1 cell line. This could be due to the fact that the VSGs trajectories were recorded in the background

of different cell lines: 13-90 vs 2T1. Nevertheless, both cell lines express the VSG MITat 1.2, hence this should not be the source of the difference. As a reference to the induced cells, the VSG dynamics were examined on non-induced cells. Although depletion was not initiated with tetracycline, it is still possible that the RNAi system is leaky and WCB was depleted. To exclude this, measurements on 2T1 cells have to be performed, which do not have the RNAi construct integrated in their genome.

The supermaps of induced and non-induced trypanosomes also showed round traps corresponding to the presence of confined particles on the cell surface. However, a difference was observed in the presence of elongated traps. While mild manifestations of elongated traps were still present on the non-induced trypanosomes, such traps were no longer present on the surface of induced cells. This could be an indication that elongated traps previously observed on the trypanosome surface might due to underlying structures which are influenced by the anchoring of the cytoskeleton. Additionally, the cell-to-cell variability of WCB-depleted cells was reduced. At the same time, the proportion of orphaned superpixels was also slightly increased in comparison to the non-induced trypanosomes. Analysis of the induced cells according to their phenotypes showed that diffusion dominated in all three and the diffusion coefficients were similar, ranging between $1.36 \pm 0.22\,\mu m^2/s$ and $1.61 \pm 0.31\,\mu m^2/s$. Thus, there was no clear distinction of a phenotype.

When examining the area probed by VSGs, no Ripley $L(r) - r$ analysis was performed in this case, as the VSG localisations on non-induced and induced cells were homogeneously distributed on the surfaces, despite the removal of artificial clusters. On average, 1099 ± 498 and 744 ± 332 VSG localisations were present on non-induced and induced cells, respectively. Nevertheless, diluted areas in the VSG localisations were present on cells of the 13-90 eYFP::MORN1 line at similar numbers of 863 ± 307 localisations per μm^2. This could be a first indication that possibly the RNAi system in the non-induced cells could be leaky and WCB was depleted in the control as well. In order to exclude the absence of diluted regions to be an artefact, measurements of VSG dynamics on 2T1 cells without RNAi construct should also be performed. In general, we cannot rule out the possibility that the change in VSG dynamics is exclusively due to a lack of the anchorage, it might also be related to cytokinesis defects. WCB is essential and its absence could trigger stress response mechanisms in trypanosomes that could also affect VSG dynamics.

In conclusion, I presented the first attempts to investigate VSG dynamics probing the influence of the anchoring of the cytoskeleton to the plasma membrane. For this, VSG dynamics were studied on osmotically swollen cells as well as on WCB-depleted trypanosomes. The supermaps generated for both experiments revealed that diffusion was the dominating motion mode and elongated traps were absent.

The latter indicates that elongated traps could be due to underlying structures which are connected to the anchoring of the cytoskeleton. In addition, a tendency was found that the diffusion coefficient decreased when the cytoskeleton was supposedly detached. However, further experiments need to be performed to confirm these results.

4 Materials and Methods

4.1 Materials

4.1.1 Bacteria

Table 3: Bacteria.

Name	Genotype	Provider
E. coli TOP 10	F- mcrA Δ(mrr-hsdRMS-mcrBC) Φ80lacZΔM15 ΔlacX74 recA1 araD139 Δ(ara leu) 7697 galU galK rpsL (StrR) endA1 nupG	Invitrogen (Darmstadt, DE)

4.1.2 *Trypanosoma brucei brucei*

Table 4: *Trypanosoma brucei brucei* cell lines and transgenic cell lines.

Cell line	Characterisation	Reference
MITat 1.6	Molteno Institut Trypanozoon Antigentype 1.6, Lister 427. Wild type strain. Expression of VSG MITat 1.6.	Carrington et al. (1991)
MITat 1.2 13-90 (13-90)	Molteno Institut Trypanozoon Antigentype 1.2, Lister 427. Expression of VSG MITat 1.2. Integrated copy of pLew13 (Addgene plasmid 24007, G. Cross) in the tubulin locus directing expression of a T7 RNA-polymerase and a Tetrepressor. Integrated copy of pLew90 (Addgene plasmid 24008, G. Cross) in the tubulin locus directing Tet-repressor expression under the control of T7-promotor. Selection: 5 µg/ml hygromycin and 2.5 µg/ml geneticin (G-418).	Wirtz et al. (1999)
MITat 1.6 eYFP::MORN1	Parental cell line: MITat 1.6. Construct: pTP_bla_YFP_MORN1. Constitutive expression of an N-terminally eYFP tagged TbMORN1 from one endogenously tagged TbMORN1 locus. One WT allele remained. Selection: 2.5 µg/ml phleomycin.	
13-90 eYFP::MORN1	Parental cell line: MITat 1.2 13-90. Construct: pTP_bla_YFP_MORN1. Constitutive expression of an N-terminally eYFP tagged TbMORN1 from one endogenously tagged TbMORN1 locus. One WT allele remained. Selection: 5 µg/ml hygromycin, 2.5 µg/ml geneticin and 2.5 µg/ml phleomycin.	

To be continued on the next page.

Cell line	Characterisation	Reference
13-90 HASP::eYFP	Parental cell line: MITat 1.2 13-90. Construct: pLew100_HASP_eYFP. Tetracycline-inducible expression of C-terminally SNAP tagged HASP protein (*Leishmania major*) from RRNA locus. Selection: 5 µg/ml hygromycin, 2.5 µg/ml geneticin and 5 µg/ml blasticidin.	Glogger et al. (2017b)
13-90 kinesin-MORN::eYFP	Parental cell line: MITat 1.2 13-90. Construct: plasmid 3329 kinesin-MORN::eYFP. Constitutive expression of an C-terminally eYFP tagged kinesin-MORN from one endogenously tagged kinesin-MORN locus. One WT allele remained. Selection: 5 µg/ml hygromycin, 2.5 µg/ml geneticin and 1 µg/ml puromycin.	Glogger et al. (2017a)
2T1 WCB RNAi	Parental cell line: MITat 1.2 2T1. Construct: pGL2084 WCB RNAi. Tetracycline-inducible depletion of WCB. Selection: 5 µg/ml hygromycin and 2.5 µg/ml phleomycin.	Büttner (2021) (Master thesis)

4.1.3 Antibiotics

Table 5: Antibiotics.

Antibiotic	Abbreviation	Manufacturer	Final concentration
Blasticidin	Bla	InvivoGen, (San Diego, USA)	5 µg/ml
Geneticin	G418	AppliChem (Darmstadt, DE)	2.5 µg/ml
Hygromycin	Hyg	AppliChem (Darmstadt, DE)	5 µg/ml
Phleomycin	Phleo	InvivoGen, (San Diego, USA)	2.5 µg/ml
Puromycin	Puro	AppliChem (Darmstadt, DE)	1 µg/ml
Tetracycline	Tet	AppliChem (Darmstadt, DE)	1-5 µg/ml

4.1.4 DNA oligonucleotides

Table 6: DNA oligonucleotides. Ampl.: Amplification; Recognition sequences for restriction enzymes: HindIII - AAGCTT, SpeI - ACTAGT, XhoI - CTCGAG.

Name	Sequence 5' → 3'	Description
BlaR	ttagccctcccacacataaccaga	Integration-PCR
MORN1-5'UTR-seqF	ccgtctgttggaagtaacctttcg	Integration-PCR

4.1.5 Plasmids

Table 7: Plasmids. Amp: Ampicilin; Phleo: Phleomycin; Bla: Blasticidin; RRNA: ribosomal RNA; ORF: open reading frame.

Name	Description	Selection	Reference
pTP_bla_YFP-_MORN1	Plasmid for the endogenous tagging of TbMORN1. The pCR4 Blunt_TOPO plasmid contained the ~3 kbp fragment 5'-UTR::Bla::α/β tubulin::eYFP::TbMORN1 ORF. Linearisation with CaiI & NdeI.	Amp (*E. coli*) Bla (*T. brucei*)	Morriswood et al. (2009); Esson et al. (2012)

4.1.6 Antibodies

Table 8: Antibodies. AB: Antibody; WB: Western Blot; IFA: Immunofluorescence analysis

Name	Origin	AB type	Dilution	Reference
Primary Antibodies				
α GFP	rabbit		1:5,000 (WB)	Markus Engstler
α H3	guinea pig	polyclonal	1:1,000 (WB)	Pineda (Berlin, DE)
α TbMorn1 (1340)	rabbit	polyclonal	1:10,000 (WB) 1:5,000 (IFA)	Brooke Morriswood
Secondary Antibodies				
Alexa 594 α rabbit	goat	polyclonal	1:2,000 (IFA)	Thermo Fisher Scientific (Waltham, USA)
IR Dye 680 α rabbit	donkey	polyclonal	1:20,000 (WB)	Invitrogen (Darmstadt,DE)
IR Dye 800 α guinea pig	donkey	polyclonal	1:20,000 (WB)	Invitrogen (Darmstadt,DE)

4.1.7 Kits and enzymes

Table 9: Kits and enzymes.

Name (Kits)	Provider
NucleoBond®PC 100	Macherey-Nagel (Düren, DE)
NucleoSpin®Gel and PCR clean-up	Macherey-Nagel (Düren, DE)
Phusion Human Specimen Direct PCR	Thermo Fisher Scientific (Waltham, USA)

Name (Enzymes)	Provider
Phusion High-Fidelity DNA Polymerase	Thermo Fisher Scientific (Waltham, USA)
T4-DNA Ligase	Thermo Fisher Scientific (Waltham, USA)

4.1.8 Chemicals, buffer and working solutions

All chemicals were purchased from Carl Roth (Karlsruhe, DE), AppliChem (Darmstadt, DE), Sigma-Aldrich (St. Louis, USA) and Thermo Fisher Scientific (Waltham, USA) unless otherwise stated in the text.

Table 10: Fluorescent dyes and microspheres.

Name	Provider
ATTO-488 NHS-ester	ATTO-TEC GmbH (Siegen, DE)
ATTO-647 N NHS-ester	ATTO-TEC GmbH (Siegen, DE)
Polystyrene Dragon Green Microspheres (⌀ 0.042 µm)	Bangs Laboratories, Inc. (Fishers, USA)
Polystyrene Flash Red Microspheres (⌀ 0.19 µm)	Bangs Laboratories, Inc. (Fishers, USA)
SeTau-647-NHS	SETA BioMedicals (Urbana, USA)
TetraSpeck™ Microspheres (⌀ 0.1 µm)	Thermo Fisher Scientific (Waltham, USA)

Table 11: Hydrogel.

Name	Provider
8-arm PEG-Vinylsulfone (10 kDa,tripentaerythritol core)	Sigma-Aldrich (St. Louis, USA)
Thiol-functionalised hyaluronic acid (HA-SH), ~54% substituted, 24 kDa	Simone Stichler (AG Groll, University of Würzburg)
Thiol-functionalised hyaluronic acid (HA-SH), ~40% substituted, 10 kDa	Leonard Forster (AG Groll, University of Würzburg)
Unlabelled FACS calibration beads (⌀ 6 µm)	BD Biosciences (Franklin Lakes, USA)

Table 12: Miscellaneous chemicals.

Name	Provider
Agarose	PeQLab Biotechologie (Erlangen, DE)
Amino acids	Sigma-Aldrich (St. Louis, USA)
dNTPs	Thermo Fisher Scientific (Waltham, USA)
GeneRuler™ DNA Ladder Mix	Thermo Fisher Scientific (Waltham, USA)
Hellmanex® III	Hellma GmbH & Co. KG (Müllheim,DE)
Immersion oil	Leica (Wetzlar, DE)
PageRuler Prestained Protein Ladder	Thermo Fisher Scientific (Waltham, USA)
Propidium iodide (1 mg/ml in 1x PBS)	Sigma-Aldrich (St. Louis, USA)
Triton X-100	A. Hartenstein GmbH (Würzburg, DE)
VECTASHIELD®	Vector Laboratories (Burlingame, USA)

Table 13: Media, buffer and solutions.

Medium, buffer, solutions	Components
Cultivation of bacteria	
LB agar	10 g Bacto-Tryptone; 5 g Yeast Extract; 10 g NaCl; 16 g Agar; 100 µg/ml ampicillin; in 1 l ddH_2O; pH 7.4-7.6
LB medium	10 g Bacto-Tryptone; 5 g Yeast Extract; 10 g NaCl; in 1 l ddH_2O; pH 7.4 - 7.6
SOC medium	0.5 % (w/v) Yeast Extract; 2 % (w/v) Bacto-Tryptone; 10 mM NaCl; 2.5 mM KCl; 10 mM MgCl2; 10 mM $MgSO_4$; 20 mM Glucose
Cultivation of trypanosomes	
BSF freezing buffer	HMI-9 with 10 % Glycerol
HMI-9 medium	176.6 g IMDM (Iscove's Dulbeccoo's Medium); 30.24 g $NaHCO_3$; 143 µl beta-Mercaptoethanol; 100 ml Penicillin/Streptomycin; 282 mg Bathocuproine sulfonate; 390 mg Thymidine; 1.36 g Hypoxanthine; 1.82 g L-Cystine; 10 % (v/v) FCS; in 10 l ddH_2O; pH 7.5
PBS	10 mM Na_2HPO_4; 1.8 mM KH_2PO_4; 140 mM NaCl; 2.7 mM KCl; in 1 l ddH_2O; pH 7.4
TDB	5 mM KCl; 80 mM NaCl; 1 mM $MgSO_4$; 20 mM Na_2HPO_4; 2 mM NaH_2PO_4; 20 mM Glucose; pH 7.4
Transfection buffer	90 mM Na_2PO_4; 5 mM KCl; 0.15 mM $CaCl_2$; 50 mM HEPES; pH 7.3
vPBS	1x PBS with 10 mM Glucose; 46 mM Sucrose
Agarose gel electrophoresis	
DNA loading buffer	0.4 % (w/v) Orange G; 15 % Ficoll 400
TAE buffer	40 mM Tris-HCl; 20 mM NaOAc; 1 mM EDTA; in ddH_2O; pH 8

To be continued on the next page.

Medium, buffer, solutions	Components
SDS-PAGE and WB	
Acrylamide solution	37.5 Acrylamide : 1 Bisacrylamide
Anode buffer	25 mM Tris-HCl; 20 % (v/v) Methanol; pH 7.6
APS solution	10 % Ammonium persulfate in ddH_2O
Cathode buffer	300 mM Tris-NaOH; 20 % (v/v) Methanol; 40 mM ε-aminocaproic acid; pH 10,4
SDS sample buffer 2x	126 mM Tris-HCl pH 6.8; 20 % (v/v) Glycerol; 4 % (w/v) SDS; 0.02 % (w/v) Bromphenol blue; 60 mM DTT
SDS running buffer	25 mM Tris; 0.1 % (w/v) SDS; 192 mM Glycine; pH 8.8
Separation gel buffer	1.5 M Tris-HCl; 0.4 % (w/v) SDS; pH 8.8
Stacking gel buffer	0.5 M Tris-HCl; 0.4 % (w/v) SDS; pH 6.8

4.1.9 Labware and consumables

Table 14: Labware and consumables.

Name	Provider
Blotting Paper BP0055858 (1,2 mm)	Sarstedt AG & Co. KG (Nümbrecht ,DE)
Centrifuge tubes 15, 50 ml	Sarstedt AG & Co. KG (Nümbrecht ,DE)
Chamber for cover lips	Workshop Biocenter (Würzburg, DE)
Cover slips, selected thickness (0.17 ± 0.01 mm)	Glaswarenfabrik Karl Hecht GmbH & Co. KG (Sondheim, DE)
Cover slips, Menzel-Gläser	Thermo Fisher Scientific (Waltham, USA)
Cryotubes, 2 ml	Sarstedt AG & Co. KG (Nümbrecht ,DE)
Electroporation cuvettes	BTX Havard Apparatus (Massachusettes, USA)
Falcon® 5ml round bottomed test tubes	VWR International (Radnor, USA)
Glass Pasteur pipettes	Sarstedt AG & Co. KG (Nümbrecht ,DE)
Immobilon ®-FL PVDF Membrane	MilliporeSigma (Burlington, USA)
Lens paper	Karl Hecht GmbH (Sondheim, DE)
Object slides, Menzel-Gläser	Thermo Fisher Scientific, Waltham (USA)
Pipette tips 10, 20, 100, 1000 µl	Sarstedt AG & Co. KG (Nümbrecht ,DE)
Reaction tubes 1.5, 2 ml	A. Hartenstein GmbH (Würzburg, DE)
Serological pipettes 1, 2, 5, 10, 25 ml	Sarstedt AG & Co. KG (Nümbrecht ,DE)
Sterile syringe filter, 0.2 µm pore	VWR International (Radnor, USA)
Vented cell culture flasks	Greiner Bio-One (Frickenhausen, DE)
Well-plates	Sarstedt AG & Co. KG (Nümbrecht ,DE)

4.1.10 Equipment

Table 15: Equipment.

Name	Provider
Cell culture	
Airstream Class II BSC	Esco Gb Ltd (Hoyland, UK)
Amaxa NucleofectorTM 2b Device	Lonza Group AG (Basel, CH)
CO_2 Incubator	Binder GmbH (Tuttlingen, DE)
Neubauer chamber	Paul Marienfeld GmbH & Co. KG (Lauda-Königshofen, DE)
Centrifuges, shaker and sonicator	
Centrifuge 1-14K	Sigma Laborzentrifugen (Osterode a. Harz, DE)
Centrifuge 6-16 K, rotors: 12169/12170	Sigma Laborzentrifugen GmbH (Osterode a. Harz, DE)
Centrifuge Z 216 MK, rotor: 220.87	Hermle Labortechnik GmbH (Wehingen, DE)
Elmasonic P30H (320 W)	Elma Schmidbauer GmbH (Singen, DE)
Shaker celltron	Infors AG (Bottmingen, CH)
Shaker TS-100C	SIA BioSan (Riga, LVA)
DNA and protein analysis	
Electrophoresis chamber	A. Hartenstein GmbH (Würzburg, DE)
iBright CL1500	Thermo Fisher Scientific (Waltham, USA)
Mini PROTEAN® Tetra System	Bio-Rad Laboratories (Munich, DE)
Odyssey Infrared Imaging System	LI-COR Bioscience (Lincoln, USA)
T-100™ Thermal cycler	Bio-Rad Laboratories (Munich, DE)
Tecan Infinite M200 NanoQuant	Tecan Group (Männerdorf, DE)
TRANS-BLOT® SD Semi-Dry Transfer Cell	Bio-Rad Laboratories (Munich, DE)

4.1.11 Microscopes

Table 16: Fluorescence microscope.

Name	Provider
Leica Control Unit super z	Leica (Wetzlar, DE)
Leica CTR 6500 HS	Leica (Wetzlar, DE)
Leica DMI 6000B	Leica (Wetzlar, DE)
Incubator, Heating Unit 2000	PeCon GmbH (Erbach a. d. Donau, DE)
TempController, Co_2 Controller	PeCon GmbH (Erbach a. d. Donau, DE)

Table 17: Single-molecule microscope setup.

Name	Provider
AOTF control unit	costum made
AOTFnc-400.650-TN & Multi-Digal Synthesizer	AA Opto Electronic (Orsay, FRA)
Cobolt Fandango 515 nm, 50 mW	Cobolt AB (Solna, SWE)
Cobolt MLD 640 nm, 100 mW	Cobolt AB (Solna, SWE)
Dichroic filter F48-635	Chroma Technology (Brattleboro, USA)
Dichroic filter zt405/514/633rpc	Chroma Technology (Brattleboro, USA)
Emission filter 550/49 BrightLine HC	Semrock (Rochester, USA)
Emission filter 698/70 BrightLine HC	Semrock (Rochester, USA)
Function Generator HM81-50	Rohde & Schwarz (Munich, DE)
HCX PL APO 100x objective lens (NA 1.47 OIL CORR TIRF)	Leica (Wetzlar, DE)
iXon3 DU-897 Em-CCD camera	Andor (Belfast, UK)
Leica DMI 6000B	Leica (Wetzlar, DE)
OptoSplit II	CAIRN (Faversham, UK)
Oscilloscope HM010-22	HAMEG (Frankfurt, DE)
Photometer PM100D	Thorlabs (Newton, USA)
VCM-D1 (shutter)	UniBlitz (Rochester, UK)

4.1.12 Software and graphical user interface

Table 18: Software and graphical user interface.

Name	Provider
Affinity Designer	Serif Europe Ltd (West Bridgford, UK)
Anaconda-Navigator	Anaconda, Inc. (Austin, USA)
CLC Main Workbench 6	CLC bio software, QIAGEN (Venlo, NLD)
Cobolt Monitor™	Cobolt AB (Solna, SWE)
EndNote X9	Clarivate Analyitcs (London, UK)
GitHub	GitHub, Inc. (San Francisco, USA)
iBright Imaging System	ThermoFisher Scientific (Waltham, USA)
ImageJ 64 (FIJI)	National Institute of Health (Bethesda, USA)
ImageStudio	Li-COR Biosciences (Lincoln, USA)
ImageStudioLite	Li-COR Biosciences (Lincoln, USA)
jupyter Notebook (6.1.4)	Project Jupyter (open-source)
LAS X	Leica (Wetzlar, DE)
MatLab R2013, R2014a, R2017a	The Math Works Inc. (Natick, USA)
MicroManager 1.4/2.0	Micro-Manager (open-source)
Microsoft Office	Microsoft (Redmond, USA)
Spyder (4.1.5)	Spyder IDE (open-source)
TeXShop (LaTeX)	University of Oregon (Eugene, USA)

4.2 Bacterial Methods

4.2.1 Cultivation of *E. coli*

Bacteria were cultured either in liquid 'lysogeny broth' (LB)-medium shaking at 225 rpm or on LB agar plates at 37 °C. In both cases, the substrate was supplemented with the selective antibiotic ampicillin.

4.2.2 Transformation of chemically competent *E. coli*

Transformation is a method to introduce plasmid DNA into chemically competent *E. coli* TOP10. For this purpose, a 100 µl bacterial aliquot stored at -80 °C was thawed on ice for 10 min. 10 ng of the plasmid of interest was added. This was followed by a 30 min incubation on ice prior to a heat shock at 42 °C for one minute. The aliquot was then incubated on ice for 2 min. After the addition of 500 µl pre-warmed SOC medium, the cells were incubated for another 30 min at 37 °C on a shaker (225 rpm) to regenerate the cells. Before plating the bacteria, the culture was pelleted at 500 g for 5 min and resuspended in 150 µl LB medium. From the concentrated bacterial culture, 50 µl and/or 80 µl were spread on a pre-warmed LB agar plate containing appropriate selections and incubated at 37 °C.

4.2.3 Isolation of plasmid DNA from *E. coli*

For the isolation of high-copy plasmids, bacteria were cultured in 3 ml to 15 ml liquid LB-medium over night. The 'NucleoSpin® Plasmid Mini kit' was used according to the manufacturer's instructions to isolate the plasmid DNA. For larger quantities of plasmid DNA, cultures of 50 ml to 100 ml liquid LB-medium were inoculated and the 'NucleoBond® PC 100 Midi kit' was utilised.

4.3 Trypanosomal methods

4.3.1 Cultivation of *T. brucei* bloodstream forms

Bloodstream form (BSF) trypanosomes of *T. brucei* were cultivated in HMI-9 medium at 37 °C, 5 % CO_2 atmosphere and under constant selection with appropriate antibiotics. For daily culture, cells were maintained in 10 ml medium in vented T25 flasks. The parasites were kept in their logarithmic growth phase. For BSF trypanosomes, this corresponds to a cell density below 1×10^6 cells/ml. For this, the cell density was determined using the Neubauer chamber.

4.3.2 Freezing and thawing

Stabilates of BSF cells were generated by harvesting 2×10^6 cells at 1500 g and 4 °C for 10 min. The cell pellet was resuspended in 500 µl ice-cold BSF freezing-medium and transferred to cryotubes. The stabilates were stored for short periods at -80 °C, while long term storage was conducted at -150 °C.
To thaw stabilates of trypanosomes, they were thawed in a water bath at 37 °C and immediately transferred to 10 ml cold HMI-9 medium. The cells were then centrifuged at 1500 g and RT for 10 min. The cell pellet was resuspended in 1 ml pre-warmed HMI-9 before being transferred to a culture flask filled with 10 ml pre-warmed HMI-9 medium.

4.3.3 Generation of transgenic cell lines by transfection

Transfection is a method that allows the introduction of DNA fragments into eukaryotic cells. The transfection was electroporation-based and carried out with the AMAXA Nucleofector II and the X-001 programme. Prior to this, the DNA to be integrated was precipitated with isopropanol (see Section 4.4.3). For each transfection, 2×10^7 trypanosomes were harvested by centrifugation (1500 g, 10 min, RT). The cell pellet was then washed with 10 ml TDB and resuspended in 400 µl pre-warmed transfection buffer. Before transferring the cell suspension into a BTX cuvette, the appropriate amount of DNA was added (linearised plasmid: 10 µg). After successful electroporation, the cells were transferred into 30 ml of pre-warmed HMI-9 medium supplemented with parental selection, referred as 'cell pool'. Subsequently, 1:10 and 1:100 dilutions of the cell pool were prepared in 25 ml HMI-9 medium and transferred to the cavities of 24 well plates, each cavity containing 1 ml. After a regeneration time of at least 8 h for BSF cells, the same volume of HMI-9 medium was added, supplemented with the parental selection and the double concentration of the new selection. Successful transfection resulted in proliferating cell populations after 4-7 days. The obtained transgenic cells were then transferred to cell culture flasks.

4.3.4 Growth curves

The doubling rate of trypanosome cell lines was determined by generating growth curves in triplicates. At the beginning, the BSF cells were diluted to 1×10^5 cells/ml in a total volume of 2 ml. The cell density was determined on five consecutive days at intervals of 24 h using the Beckmann Coulter Counter or the Neubauer chamber. Then the populations were diluted according to their density, so that an exponential growth of the populations was ensured. For plotting on a graph, the cell numbers of the triplicates were averaged and plotted with its standard deviation.

4.3.5 Isolation of genomic DNA

The isolation of genomic DNA allowed for the verification of the correct integration of the endogenous tag within the genome. The 'Human Specimen Direct PCR kit' (Invitrogen) was used to purify genomic DNA. In short, 1×10^6 cells were sedimented (1,400 g, RT, 10 min). After the removal of the supernatant, the pellet was resuspended in 20 µl dilution buffer and 0.5 µl DNA release was added. The suspension was vortexed and incubated for 5 min at RT. It was followed by a 2 min incubation at 98 °C. Cell fragments were pelleted (2,000 g, 5 min). The supernatant was stored at 4 °C and 0.5 µl were then used as template for the integration analysis by PCR.

4.3.6 Preparation of whole-cell lysates

For this purpose, BSF cells were harvested and washed with 1 ml TDB (1,400 g, 4 °C, 10/1 min). Subsequently, the cell pellet was resuspended in 2 x SDS sample buffer, resulting in a final concentration of 2×10^5 cells/µl. Finally, these were incubated at 98 °C for 10 min. The cell lysates were then either directly loaded in an SDS-polyacrylamide gel to perform Western Blotting or stored at -20 °C until further use.

4.3.7 Osmotic swelling of trypanosomes

Preswelling, osmotic swelling of cells before embedding in a hydrogel, was performed by taking up cells in hypotonic medium consisting of TDB and ddH_2O (1:1). For this, 1×10^7 cells were harvested by centrifugation (1,400 g, 4 °C, 10 min). Cells were washed three times with 1 ml TDB (1,400 g, 4 °C, 1 min). The cell pellet was resuspended in 10 - 15 µl TDB. Subsequently, ddH_2O was added to the cell suspension in the equal amount as the suspension volume. Cells were preswollen ~ 2 min until embedding in the hydrogel under hypotonic conditions. To ensure hypotonic conditions in the hydrogel, components were solved in hypotonic medium composed of TDB and ddH_2O. The final conditions in the hydrogel resembled a 1:1 ratio of TDB and ddH_2O.

4.4 DNA methods

4.4.1 Polymerase chain reaction (PCR)

The PCR enables the amplification of DNA. In this work, this was carried out with the Phusion™ High Fidelity DNA Polymerase (Thermo Fisher Scientific). The amplification of genomic DNA for the integration analysis was conducted by an PCR using the 'Phusion Human Specimen Direct PCR kit' according to the manufacturer's instructions. The pipetting schemes and the thermocycler protocols are

shown in Table 19 and Table 20. DNA oligonucleotides (primer) used for PCR reactions are listed in Table 6 in the Material section. The temperature for primer hybridisation was set individually to fulfil the requirements of the used primer pair. The PCR products were either separated by agarose gel electrophoresis and subsequently cleaned up or directly cleaned up using the 'NucleoSpin Gel and PCR clean-up Kit' (Macherey-Nagel). The cleaned up products were either used for digestion or ligated directly into the pJET1.2 cloning vector using the 'CloneJET PCR Cloning Kit' (Thermo Fisher Scientific).

Table 19: PCR pipetting scheme. fw: forward; rev: reverse.

PCR for integration analysis	
0.5 µl	genomic DNA
each 0.5 µM	primer fw / rev
200 µM	dNTPs
-	-
0.02 U/µl	Phusion™ High Fidelity DNA Polymerase
4 µl	5x HF Buffer
x µl	ddH_2O
20 µl	total volume

Table 20: Thermocycler protocol.

Setps	**Temeprature**	**PCR for integration analysis**
1. Initial denaturation	98 °C	5 min
2. Denaturation	98 °C	10 s
3. Annealing	x °C	20 s 30 x
4. Elongation	72 °C	15 s per 1 kb
5. Final elongation	72 °C	1 min
6. Hold	4 °C	∞

4.4.2 Agarose gel electrophoresis and gel extraction

Agarose gel electrophoresis was used to separate the DNA according to its molecular size. For this, the DNA was mixed with 6x DNA loading buffer and separated in a 0.8 % agarose gel supplemented with SYBR Safe DNA Gel Stain (1:50,000, Thermo Fisher Scientific) (30 - 40 min, 110 - 120 V, 1x TAE buffer). The 'GenRuler Mix' (Thermo Fisher Scientific) served as a molecular size standard. Separation of the DNA was checked under UV-light and documented with the iBright Imaging System (Thermo Fisher Scientific). DNA extraction was performed by excising the specific DNA fragments under UV-light and subsequent DNA purification was done using the 'NucleoSpin® Gel and PCR clean up' kit (Macherey-Nagel).

4.4.3 Isopropanol precipitation

For DNA precipitation, 1 volume of isopropanol and 0.1 volume of 3 M NaAc were mixed with 1 volume of the DNA to be precipitated. It was incubated on ice for 30 min, followed by a 20 min centrifugation step at 20,000 g and 4 °C. The pellet was washed twice with 500 µl of 70 % EtOH at 20,000 g and 4 °C. The supernatant was then removed under a sterile bench and the pellet was dried under sterile conditions for at least 1.5 h. Finally, the pellet was resuspended in 15 µl sterile H_2O. Quantification was carried out using a 1:10 dilution on the Infinite M200 (Tecan).

4.4.4 Quantification of DNA

The obtained DNA was quantified by photometric analysis on the Infinite M200 (Tecan) measuring the absorbance at 260 nm and 280 nm. The ratio of OD_{260} and OD_{280} provided information about the purity of the DNA. The quotient with a value of 1.8 was considered ideal.

4.4.5 DNA sequencing

Sequencing was carried out by the GATC service of Eurofins Genomics (Ebersberg, DE). The company's instructions were followed for the sample preparation. In short, 20 µl of plasmid DNA (conc. 80 - 100 ng/µl) or 20 µl of PCR product (conc. 5 - 10 ng/µl) with 20 µl sequencing primer (conc. 10 µM) were sent to the company. The sequencing results were analysed using CLC software (CLC bio, Quiagen).

4.4.6 Restriction digest

DNA digestion was performed with restriction enzymes (Thermo Fisher Scientific or NEB) according to the manufacturer's instructions.

4.5 Protein methods

4.5.1 Sodium dodecyl sulfate polyacrylamide gel electrophoresis (SDS-PAGE)

Protein separation according to their molecular mass was achieved with a discontinuous SDS-PAGE. The gels consisted of a stacking and separation gel. The concentration of acrylamid/bisacrylamid (5:1) was 5 % (w/v) in the stacking gel and 15 % (w/v) in the separation gel. Electrophoresis was performed in SDS running buffer for at least 20 min at 120 V and then increased to 160 V using the EV265 electrophoresis power supply (Consort). The 'PageRuler Prestained Protein Ladder' (10 - 170 kDa, Thermo Fisher Scientific) was used as a size standard. The whole cell lysate of 1.4×10^6 cells were loaded onto the gel. Further analysation of the separated proteins were conducted by western blot (WB).

4.5.2 Western blot

Proteins separated by SDS-PAGE were transferred from SDS gels onto Immobilon® polyvinylidene fluoride (PVDF) membranes (Merck Millipore) with the semi-dry blotting technique. For this purpose, a sandwich from bottom to top was assembled: two Whatman paper soaked in anode buffer, one in Methanol (15 s) activated PVDF membrane, SDS gel, and one Whatman paper soaked in cathode buffer. The transfer was performed using a graphite blotter (TRANS-BLOT SD, Bio-Rad) at 0.8 mA/cm^2 gel for 1 h using the Consort EV265 electrophoresis power supply (Hoefer). Subsequently, the membrane was blocked in 1x PBS mixed with 5 % (w/v) skimmed milk powder for 1 h at RT or overnight at 4°C. Incubation with the primary antibody took place in 5 ml of 0.1 % Tween-20 in 1x PBS mixed with 1 % (w/v) skimmed milk powder for 1 h. The antibody solution was removed and the membrane was washed three times with 0.1 % Tween-20 in 1x PBS. The secondary antibodies were diluted in 10 ml of 0.1 % Tween-20 in 1x PBS with additional SDS (final conc. 0.02 %). The supplement of SDS prevented non-specific binding of the secondary antibodies. The incubation period was 1 h at RT in the absence of light. It was followed by three washing steps with 0.1 % Tween-20 in 1x PBS (5 min, RT, light exclusion). The dry membrane was analysed with the Odyssey CLx (LI-COR) and the signals were quantified with the ImageStudio software (LI-COR).

4.6 Microscopy and associated methods

4.6.1 Preparation of glass cover slips

In order to ensure the ideal conditions for microscopic studies, clean and hydrophilic cover slips were required. Thickness-corrected cover slips (22 x 22 mm, 17 µm, Karl Hecht GmbH & Co KG) were prepared for the usage at the single-molecule setup, while standard cover slips (22 x 22 mm) were used for diffraction-limited microscopy. The cover slips were sonicated in 2 % Hellmanex-II/ddH_2O for 10 min (37 kHz, 100 % power, sweep mode) and extensively rinsed with deionised water. This process was repeated with deionised water before the cover slips were dried in an oven at 80 °C for 30 min and treated with plasma using ambient air for 30 min (PDC-002 CE, Harrick Plasma). The plasma cleaned cover slips were then stored in deionised water and used within one week. For the experiments, the cleaning step in 2 % Hellmanex III/ddH_2O was repeated twice and once with deionised water. Between the cleaning steps, the cover slips were rinsed extensively with deionised water. Cover slips were stored for a maximum of 2 days.

4.6.2 Spin coating of glass cover slips for super-resolution microscopy

To post-process the single-molecule data for the drift of the microscopic stage, multifluorescent TetraSpeck™ Beads (⌀ 0.1 µm, Thermo Fisher Scientific) were spin coated onto half of the cover slips. For this purpose, the cover slip was placed in the Spin Coater WS-650MZ-23NPPB (Laurell Technologies Corporation). 20 µl of a 1:250 dilution of multifluorescent beads were placed in the center of the cover slip and spin coated at 1000 rpm for 1 min. The spin coated cover slips were directly used for the assembly of the hydrogel.

4.6.3 Preparation of trypanosomes for *in vivo* studies and labelling of the VSG coat

To immobilise trypanosomes in a hydrogel, 1×10^7 cells were harvested for 10 min at 1,400 g and 4 °C. After the removal of the supernatant, the cells were washed three times with 1 ml of TDB/vPBS (1 min, 1,200 g, 4 °C). The supernatant was removed so that the cells remained in a volume of 10 - 15 µl. Trypanosomes were now ready to be embedded in a hydrogel or further processed to label VSG on their surface.

4.6.3.1 VSG labelling for single-molecule tracking

For single-molecule tracking of individual VSGs, the cell pellet was taken up in 100 µl of TDB/vPBS and chilled on ice-water (0 °C) for 5 min to halt endo- and exocytosis. Meanwhile, 1 µM Atto-647 N NHS dye was diluted 1:200 in TDB/vPBS pH 7.4 and stored on ice-water. After the incubation, 80 µl of the 5 nM dye dilution was added to the cells, gently flicked and incubated for 5 min on ice-water allowing binding of the NHS dye. Subsequently, washing steps were performed to remove unbound dye. The volume was filled up to 1 ml with TDB/vPBS and centrifuged at 1,200 g and 4 °C for 1 min. The supernatant was removed and the washing step was repeated with 1 ml of TDB/vPBS. The supernatant was removed, leaving the cells resuspended in 10 - 15 µl. The concentrated trypanosomes were directly used for hydrogel embedding. By taking up the cells in 1 ml of TDB/vPBS, the cells could be stored on ice-water for up to 2 h before being embedded in the hydrogel.

4.6.3.2 Labelling of the entire cell surface

When the entire cell surface of trypanosomes was labelled, the cell pellet was taken up in 200 µl TDB/vPBS and chilled on ice-water (0 °C) for 5 min to stop endo- and exocytosis. In the mean time, 10 mM Atto-647 N NHS or 10 mM Atto-NHS 488 was diluted 1:10 in TDB/vPBS pH 7.4 and stored on ice-water. 2 µl of the dye were added to 200 µl of cell suspension at a final concentration of 100 µM. After a incubation for 5 min, the unbound dye was removed by three washing steps. For this, 1 ml of TDB/vPVS was added and centrifuged at 1,200 g and 4 °C for 1 min. The supernatant was removed and the cells remained in a volume of 10 - 15 µl. The

uptake of the cells in 1 ml of TDB/vPBS allowed the storage in ice-water for up to 2 h before being embedded in the hydrogel.

4.6.4 Chemical fixation

For the fixation of trypanosomes, 1×10^7 cells were centrifuged at 1,400 g and 4 °C for 10 min. The trypanosomes were washed three times with 1 ml TDB/vPBS. The cells were either first incubated with a nanomolar quantity of Atto-647 N NHS (see Section 4.6.3) or used directly for fixation. For the fixation in methanol, cells were resuspended in 200 µl TDB/vPBS and transferred to an 1.5 ml reaction tube coated with 3 % BSA overnight to prevent the cells from adhering to the tube wall. 800 µl methanol (- 20 °C) was added dropwise under constant, but slow agitation. The suspension was incubated at - 20 °C for 15 min. For the fixation with para-formaldehyde (PFA), the trypanosomes were taken up in 500 µl TDB/vPBS and transferred to an 1.5 ml reaction tube coated with 3 % BSA. 500 µl of 4 % PFA were added to the cell suspension for a final concentration of 2 % PFA. The cells were incubated at RT for 15 min. Subsequently, the cells of both fixation solutions were washed three times with 1 ml TDB/vPBS (1 min, 1,200 g, 4 °C). After the removal of the supernatant, cells remained in 10 - 15 µl TDB/vPBS and could now be used for embedding in the hydrogel.

4.6.5 Immunofluorescence analysis

The first steps of the immunofluorescence analysis (IFA), including the cell harvesting and fixation with para-formaldehyde were performed according to Section 4.6.4. After fixation the cells could be stored at 4 °C for up to one week. However, for the IFA in this work, the cells were harvested, fixed and incubated with antibodies on the same day.
For one sample, 100 µl of the fixed cell suspension was added to a poly-L-lysine microscope slide. After 20 - 30 min, the samples were checked under a light microscope to check whether the cells adhered to the slide. Subsequently, the remaining liquid was removed, the cells were permeabilised with 200 µl of 0.2 % Triton X100 for 15 min and followed by a washing steps with 1x PBS. This was followed by blocking with 200 µl 3 % BSA in PBS at 37 °C for 30 min. The primary antibody diluted in 200 µl 0.1 % BSA in PBS was added and incubated for 1 h. Before incubation of the cells with the secondary antibody, four washing steps were carried out for 2 min each in 1x PBS. The secondary antibody was diluted in 200 µl 0.1 % BSA in PBS and mixed with DAPI (1:1000). The total volume of 200 µl was added to the cells, followed by an incubation of 30 min. Finally, the specimens were washed four times for 2 min each with 1x PBS and embedded with 3 - 4 µl VECTASHIELD. Sealing of the cover slips was achieved by the use of nail polish. The samples were stored at 4 °C until analysis.

4.6.6 Hydrogel

4.6.6.1 Embedding of trypanosomes

Embedding of trypanosomes became a prerequisite to perform *in vivo* super-resolution studies of the highly motile trypanosomes. For this, trypanosomes were immobilised in a hydrogel of 10 % (w/v) vinylsulfone-functionalised polyethylenglycol (PEG-VS, tripentaerythritol core, Sigma-Aldrich) and 5.6 % (w/v) thiol-functionalised hyaluronic acid (HA-SH, 24 kDa, ~ 54 % SH-substituted, provided by Simone Stichler) or 5 % (w/v) thiol-functionalised hyaluronic acid (HA-SH, ~ 10 kDa, ~ 40 % SH-substituted, provided by Leonard Forster). The hydrogel is cross-linked by the thiol-Michael addition click chemistry and the speed of the polymerisation is dependent on the pH value of the solutions as well as the temperature. The more alkaline the solution or the higher the temperature the faster the polymerisation. In order to handle the components better and prevent early polymerisation, they were dissolved individually. In case of PEG-VS, a 50 % (w/v) solution was prepared in TDB/vPBS pH 7.0. The solution was placed on ice until use and stored at - 20 °C until re-use. HA-SH was dissolved to a 25 % (w/v) solution in TDB/vPBS pH 7.0. The pH was adjusted to 7.0 - 7.5 by adding 5 M and 1 M NaOH. This solution was stored on ice and had to be used within the same day. For immobilisation, trypanosomes were prepared according to Section 4.6.3 for studies of living cells or were fixated *a priori* (Section 4.6.4). In both cases the cells were finally resuspended in a volume of 10 - 15 µl. The final hydrogel mixture was prepared in a total volume of 10 µl. 2 µl of PEG-VS (final conc. 10 % w/v), 2 - 3 µl of the concentrated trypanosomes and 1 µl of TDB/vPBS washed spacer beads (non fluorescent FACS calibration, ⌀ 6 µm, BD Biosciences) were mixed with the appropriate volume of TDB/vPBS pH 7.0. The addition of HA-SH at a final concentration of 5/5.6 % (w/v) started the polymerisation and was therefore added immediately before 3 - 4 µl of the hydrogel mixture were placed between a bead-coated cover slip (bottom) and a non-coated cover slip (top). After quickly weighing down the top cover slip with 90 mg, the hydrogel sandwich was immediately centrifuged in a centrifugation chamber to settle the cells in close proximity of the multifluorescent beads located on the bottom cover slip (1500 xg, 1 min).

For single-molecule tracking, freely diffusing Atto-647 N NHS dye was added to the mixture at a final concentration of 0.1 nM and the volume of TDB/vPBS was adjusted accordingly. This low concentration of initially unbound dye in the background, may bind VSGs and replace bleached signals during imaging. In this way, the label density was optimised. For the viability assay, propidium iodide was added (final conc. 5 µg/ml) to the mixture and the volume of TDB/vPBS was adjusted accordingly. Table 21 shows the pipetting scheme for both experiments.

Table 21: Hydrogel pipetting schemes for single-molecule tracking and viability assay.

Single-molecule tracking		Viability assay	
2 µl	trypanosomes	2 µl	trypanosomes
1 µl	spacer beads	1 µl	spacer beads
2 µl	50 % (w/v) PEG-VS	2 µl	50 % (w/v) PEG-VS
1 µl	1 nM Atto-647 N NHS	1 µl	50 µg/ml propidium iodide
2 µl	25 % (w/v) HA-SH	2 µl	25 % (w/v) HA-SH
2 µl	TDB/vPBS pH 7.0	2 µl	TDB/vPBS pH 7.0
10 µl	total volume	10 µl	total volume

4.6.6.2 Mechanical testing of hydrogel properties

The immobilisation of trypanosomes at a nanometer scale requires hydrogels of a specific stiffness. This mechanical property was tested at the Department for Functional Materials in Medicine and Dentistry (University of Würzburg) and were conducted together with Leonard Forster (Ph.D. student). For this, hydrogels with a polymer content of 10 % (w/v) PEG-VS and 5 % (w/v) HA-SH were poured in a cylindrical glass form with a height of 4 mm and a diameter of 6 mm. After cross-linking, the measurements were performed using a BOSE 5500 system (ElectroForce) for dynamical and mechanical testing. The total displacement was 2 mm, which means a total compression of 50 % with a constant displacement rate of 0.005 mm/s. The Young's Modulus was calculated from the raw data as the slope of the true stress-strain curve in the linear elastic range of 5 - 10 % strain. The measurement was carried out in triplets.

4.6.7 Viability assay

Propidium iodide (PI) was used to assess the viability of trypanosomes in the hydrogel or TDB. The dye serves as marker because it intercalates into DNA when membrane integrity is disrupted, which is the case for dead cells. This is then accompanied by an increase in fluorescence intensity. Living cells, in contrast, do not show any fluorescence. To monitore the viability in the hydrogel, PI was added to the hydrogel mixture at a final concentration of 5 µg/ml (see Section 4.6.6.1 and Table 21). In order to monitore the viability in TDB, 1×10^7 cells were harvested (1,400 xg, 4 °C, 10 min) and washed three times with 1 ml TDB (1,200 xg, 4 °C, 1 min). Cells were kept in TDB supplemented with 5 µg/ml PI also during image acquisition.

4.6.8 Diffraction limited microscopy

Image acquisition was performed with a DMI6000B inverted-widefield fluorescence microscope (LEICA) equipped with a DFC365FX camera (pixel size 6.45 µm, LEICA) and a mercury short-arc reflector lamp (HXP-R120W/45C VIS, Osram) using the Leica Application Suite X software (Leica). The immersion objectives used had a magnification of 63 x (glycerol, NA 1.3) or 100 x (oil, NA 1.4). When Z-planes

were recorded, 50 Z-planes were acquired over a total range of 10 µm. Fluorescent images were presented as maximum intensity projections of 20 - 100 planes and differential interference contrast (DIC) images as average projections of 20 -100 planes. All images were false coloured with ImageJ (green fluorescence channel in cyan, red fluorescence channel in magenta). To normalise the signals in the images, the minimum and maximum intensity values of the images in one figure were set to the same values using a reference in ImageJ.

4.6.9 Single-molecule imaging

The single-molecule measurements were conducted at our single-molecule setup based on an inverted-widefield microscope (Leica DMI6000B) equipped with a high numerical lens (HCX PL APO 100x 1.47 OIL CORR TIRF), a dichroic color filter (zt405/514/633rpc, Chroma) and an EMCCD camera (iXon697, Andor technology, pixel size = 160 nm). The synchronisation of exposure time and camera readout was achieved using an acousto-optical tunable filter (AOTFnc-400.650-TN). The camera signal triggered the function generator (HM81-50, Rohde), which transmitted rectangular signals to the AOTF and thus controlled the illumination starting point and duration. Exposure times and acquisition frequency depended on the specific experimental setup, the readout mode of the camera sensor chip and the defined region of interest (ROI) on the camera sensor chip. The used ROIs and read-out modi are listed with the corresponding acquisition frequency, exposure time (t_{exp}) and the time lag (Δt) in Table 22. For the excitation, one solid-state diode laser (Cobolt Fandango 514 nm) and one diode laser (Cobolt MLD 640 nm) were used. Atto-647 N NHS and SNAP-Cell 647-SiR were excited with the 640 nm laser beam at an mean intensity of 1 or 2 kW/cm^2, while eYFP molecules were excited with a 514 nm laser beam at an mean intensity of 1 or 2 kW/cm^2. Each measurement comprised 10,000 - 30,000 consecutive images. The laser beams were shifted a few pixels horizontally relative to each other by the OptoSplit (CAIRN) allowing sequential image acquisition with nanometre precision due to the post-process superimposition of the two-colour information. Signal detection by the camera was enabled by a dichroic mirror (F48-635, Chroma) and the usage of the appropriate filter combination 550/49 BrightLine HC and 698/70 BrightLine HC (emission filters, Semrock) within the OptoSplit. The open source software MicroManager2.0 was used to control the settings of the camera and AOTF. The built-in function Flat Field Correction in MicroManager2.0 was used to remove the background signal detected in the dark. To do this, 100 images of the entire, non-illuminated camera chip (512 x 512 px, except for pulsed illumination & cropped mode & FT: 512 x 511 px) were stacked and served as input for the Flat Field Correction.

Table 22: Read-out modi in context with the region of interest. It shows all used combinations of region of interests (ROIs) and camera chip read-out modi with their corresponding acquisition frequency (f), exposure time (t_{exp}) and the time lag (Δt). FT: frame transfer.

ROI [px]	**Camera chip read-out modus**	f **[Hz]**	t_{exp} **[ms]**	Δt**[ms]**
120 x 120	pulsed illumination + ROI mode	28	10	32
120 x 120	pulsed illumination + cropped mode + FT	100	9	10
95 x 95	pulsed illumination + cropped mode + FT	205	4.3	4.9

4.6.10 Two-colour single-molecule fluorescence microscopy

4.6.10.1 Acquisition of bead localisations for generation of the registration matrix

To enable nanometre precision in the superimposition of the two-colour information *a posteriori*, a registration matrix had to be computed. For this, the same ROI and acquisition mode were used as for the actual measurements including the flat-field correction to remove background signal detected in the dark. On the camera, both spots are basically in the same position, but with a few pixel offset in the horizontal direction. A cover slip homogeneously coated with TetraSpeck® beads was manually and slowly moved to sample the ROI while both colour channels were alternately recorded in an imaging sequence. At least 4 movies with 10,000 consecutive images each were acquired with all movies starting with the same colour channel, e.g. either red or yellow. The bead positions were then localised as described in Section 4.7.1 and further used for the generation of a registration matrix (Section 4.7.8).

4.6.10.2 Sequential imaging of the two-colour channels

In order to guarantee a high acquisition frequency for the single-molecule tracking, the image section on the camera chip had to be kept small. This eliminated the possibility of placing the ROIs of the dark red and yellow colour channels adjacently on the camera chip and recording them simultaneously. Therefore, the ROIs were placed basically in the same position with a few pixel offset in the horizontal direction. The information from the two channels was then recorded sequentially. The dynamic information was always recorded first, then the static information. The movies for VSG tracking comprised 20,000 - 30,000 images and those of eYFP localisations 10,000 - 20,000 images.

4.7 Analysis of single-molecule data

4.7.1 Single-molecule localisation

The single-molecule localisations were determined computationally by using programs written in MatLab (Mathworks Inc., Version R2013a & R2017a) as previously described in Schmidt et al. (1996) and Fenz et al. (2012). Images fed into the routine had the background signals removed that were detected in the dark. Briefly, a 2D-Gaussian, an estimation for the point-spread function (PSF) of the microscope, was applied to the intensity profiles. Subsequently, a threshold was set to distinguish noise from fluorophore signals, and only signals greater than 5-fold the noise were typically categorised as single molecules. Remaining single-molecule peaks were fitted to the PSF to obtain information about the signal parameters including x- and y-position, signal width, signal intensity, and background signal as well as localisation precision in x and y. Then, the resulting list of molecule positions, width and intensities was filtered with respect to the known single-molecule footprints (width and intensity) as well as for detection error thresholds. The remaining localisations (x_i, y_i) with their parameters were stored in a data matrix and served as input for further data analysis.

4.7.2 Drift correction

For high-resolution images and single-molecule tracking, a large number of consecutive images is required, which is associated with a long acquisition time. During this time, the stage of the microscope can potentially drift. To post-process this drift, multifluorescent beads (TetraSpeck® beads, $\varnothing$ 0.1 µm) were spin-coated on cover slips to ensure at least one immobile reference in the field of view during measurements (see Section 4.6.2). The function furthermore removed double localisations and filled in gaps of missing localisations in reference to previous localisations. The x- and y-positions of the reference object were then smoothed with a built-in MatLab function 'smoothdata' to disregard fluctuations in the magnitude of the localisation precision. In short, a Gaussian filter with the filter size 500 frames was used to calculate reference positions. The discrepancy between the reference position and the starting point was then employed to correct the single-molecule positions in the corresponding frames.

4.7.3 Removal of artificial clusters

Static fluorophores with on-off blinking behaviour are localised multiple times within the localisation precision and gave rise to artificial cluster although signals originated from the same, immobile emitter (Annibale et al., 2011). To remove these artefacts, a self-written MatLab script removed localisations that reappeared within the image

sequence of 1.8 s (at 100 Hz = 180 consecutive images) and were found within the localisation precision of the first localisation.

4.7.4 Super-resolution image

Single-molecule localisations were determined as described in Section 4.7.1 and subsequently artificial clusters were removed as detailed in Section 4.7.3. Then, super-resolution images of eYFP signals were computed as the sum of all fitted single-molecule positions. Each localisation (x_i, y_i) was plotted as a $2D$ Gaussian spot, with the respective width corresponding to the achieved localisation accuracy σ_i for the eYFP molecule.

4.7.5 Quantification of the axoneme width, label density and autofluorescent background in super-resolution images

Super-resolution images were computed from signals recorded of immobilised trypanosomes expressing kinesin-MORN::eYFP as described in Section 4.7.4. To quantify the width of the eYFP signal and thus the width of the axoneme, a contour line was manually drawn along the axonemal signal. Then, perpendicular lines to the contour lines were drawn and the average profile widths were calculated as full-width-half-maximum from a Gaussian fit to the data points. The comparison of their mean axoneme diameter with the mean axoneme diameter of chemically fixed and immobilised trypanosomes as well as trypanosomes embedded in the poly(allyl glycidyl ether-co-glycidyl)/HA-SH hydrogel by Marius Glogger exhibited the immobilisation efficiency of the embedded trypanosomes. For the determination of the label density and the autofluorescent background, the specific axoneme eYFP signals had to be extracted in a two-step process from the total localisations, which included fluorescent background signals such as hydrogel impurities or intracellular autofluorescence. In the first step, a nearest-neighbour analysis was applied to the single-molecule localisations in the super-resolved images to remove sparsely distributed signals from hydrogel impurities and intracellular fluorescence. A minimum of 10 localised emitters within a square of side length 240 nm effectively removed non-specific noise pixels and small clusters. In a second step, remaining clustered emitters were removed by first manually masking everything except the axoneme. To redefine the flagellum region, a fine grained mask was computed by multiplying the resulting coarse-grained mask with the mask generated from the remaining localisations after nearest neighbour analysis. Subsequent application of the final fine grained mask to the image stack identified eYFP molecules (N_{eYFP_F}) localised in the flagellar area (A_F). The label density p was then calculated by $p = \frac{N_{eYFP_F}}{A_F}$ and the average density of the background signal p_{BG} by $p_{BG} = \frac{N_{eYFP} - N_{eYFP_F}}{A - A_F}$ where N_{eYFP} was the number of all localisations found and A was the area of the ROI.

The false-positive single-molecule localisations in the flagellar region were estimated from the ratio $r = \frac{p_{BG}}{p}$.

4.7.6 Determination of collected photons by count conversion

In order to determine the localisation precision based on the theory (Ober et al., 2004), the number of photons collected on the sensor chip per single molecule of the EMCCD camera was required. The count conversion guide provided by Andor enabled me the approximation of collected photons (N_i) based on the counts (C) and is represented in the following Equation:

$$N_i = \frac{(C - \Theta)\gamma}{EM_{gain}QE_s}. \tag{21}$$

θ was the offset of the background, the camera sensitivity γ was 10.7 electrons per A/D unit and the EM gain (EM_{gain}) was 150. The sensor quantum efficiency (QE_s) was extracted from camera specification sheet for the emission wavelength 664 nm of the Atto-647 N NHS dye and was 0.94. The offset of the background θ was negligible because the background signal in the dark was already removed by application of a flat field correction during the measurements.

4.7.7 Cluster identification using Ripley's analysis

The Ripley's $L(r) - r$ function was used to find out whether the localisations deviate from the random distribution. Based on a nearest neighbour analysis the function is defined as (Ripley, 1979):

$$L(r) - r = \sqrt{\frac{K(r)}{\pi}}. \tag{22}$$

$K(r)$ counts the mean number of neighbours, N, up to a radius (r) normalised N by the particle density ($r = N/A$):

$$K(r) = \frac{A}{N^2} \sum_{i \neq 1}^{N} w_{ij}^{-1} I_r(d_{ij}). \tag{23}$$

The distance between two localisations is denoted with d_{ij} and the counting measure is for the distance $d_{ij} \leq r$ with $I_r(d_{ij}) = 1$ and otherwise $I_r(d_{ij}) = 0$. The weighing factor $w_{ij} \leq 1$ accounts for edge effects, which is the proportion of the circumference of a circle with its centre in i lying within the area A . The analysis was performed using MatLab scripts developed by Thomas Schmidt and followed the method described by Pezzarossa et al. (2015). Briefly summarised, occupancy maps were generated from single-molecule localisations. Next, the maps were refined by

dividing each original pixel into nine subpixels. The occupancy was determined as the number of all localisations per subpixel. The Ripley's $L(r)-r$ function was then applied to the data set of maps. The function returns 0 in the case of complete spatial randomness and positive values in the case of clustering. The radius of potential clusters can be obtained by plotting the results from the analysis as a function of examined radii. The radius exhibiting the highest score correlates with the radius of the domains. The parameters used in the analysis were, 0.8 µm as the side length of the square tiles for the subdivision of the ROI and a radius (r) of 0.5 µm, meaning that the function was calculated for each tile up to a radius of 0.5 µm. Finally, the results were averaged over all tiles and all imaged trypanosomes.

4.7.8 Generation of the registration matrix for two-colour imaging

To enable two-colour imaging at a high acquisition frequency, the red and yellow spots were basically placed at the same position on the camera, with a few pixels shifted horizontally (Figure 20). This allowed both channels to be registered to nanometre accuracy using a registration matrix. Such a matrix was generated by recording multifluorescent beads spread on a cover slip according to Section 4.6.10.1 and determining the single-molecule localisation as described in Section 4.7.1. Further analysis was conducted with the self-written MatLab script Overlay_2_Colors_mainFuncSeq.m that used localisations filtered only with respect to the detection error. The script executed following MatLab scripts:

1. separateBeadPos.m:
   The function iterated over all matrices containing bead localisations and separated localisations of the red and yellow colour channel, which are recorded alternately. Separated bead localisations from all movies were then pooled to one data matrix according to the colour channel. Discrimination was necessary, as images of the yellow channel contained both the red and green signals which was due to cross talk (see Section 2.2.2.1). Red signals were removed based on the localisation information obtained from the previous image.
2. mainFuncClearV3.m:
   It displayed the signal width and intensity profile and a pop-up window allowed the filter parameters to be specified. The localisations were then filtered with respect to the signal width and intensities of the known single-molecule footprints and for detection error thresholds. The script without the pop-up window was established by Susanne Fenz.
3. EstimateInputOverlay_2_ColorSeq.m:
   The script enabled the coarse overlay of the red and yellow localisations by entering the number of pixels to be shifted in a pop-up window. The overlay was optimised with respect to localisations in the center, while an offset was

tolerated at the ROI margins. The script is based on a function written by Susanne Fenz and Marius Glogger and was adapted to the two-colour acquisition mode established in this thesis.

4. Overlay_2_ColorSeq.m:
   This script used the build-in function images.geotrans.LocalWeightedMeanTransformation2D. It fitted a local weighted mean transformation to a set of fixed and moving control points which were related by a global second degree polynomial transformation across the entire plane. The script is based on a function written by Susanne Fenz and Marius Glogger and was modified to fit the two-colour acquisition mode established in this work.

4.7.9 Registration of two-colour channels

Evaluation of the two-colour information required the registration of the slightly horizontally shifted colour channels. For this, the generated registration matrix was used and the application was facilitated by the self-written MatLab script EvaluationTrackingInRelationRefObj.m. The function deployed the registration parameters of the registration matrix to the experimentally obtained data set and shifted the yellow localisations (FP localisations) on the red ones (VSG localisations). The function utilised data sets only filtered with respect to the detection error, otherwise too many bead localisations were lost, which were necessary for the drift correction implemented in the analysis. The function contained the following scripts:

1. Drift Correction.m:
   The drift correction for both channels was performed as described in Section 4.7.2.
2. removeBeadSignal.m:
   The TS bead signals were removed to allow a correct representation of the width and intensity profiles of the signals of interest. This required the specification of the number of fiducial markers in focus.
3. MainFuncClearV3.m:
   Explained in Section 4.7.8 'Generation of the registration matrix for two-colour imaging'.
4. DiffusionAnalysisV3.m/DifusionAnalysisV3_DinVSDout.m:
   Analysis was performed as stated in Section 4.7.10.
5. Apply_tformLocalWeightedMeanSeq.m:
   For the final registration, the generated registration matrix was applied to the filtered localisations of the yellow channel. The script is based on a function written by Susanne Fenz and Marius Glogger and was adjusted to the two-colour acquisition mode established in this work.

6. Generation of overlay images containing trajectories from single-molecule tracking and the super-resolution images of the structure.

4.7.10 Single-molecule tracking

To extract the information on dynamics, the tracking algorithm used a correlation of single-molecule localisations in a frame to localisations in subsequent frames. These localisations were obtained and processed according to Section 4.7.1 and the data sets were also corrected for the drift according to Section 4.7.2. The MatLab algorithm was developed by Schmidt et al. (1996) and was further extended. In summary, a probabilistic algorithm related localisations in two frames, i and j of a movie. The probability (p) that a localisation k in an image I_i was identical to a localisation l in an frame I_j depended on the diffusion coefficient D of the molecule and is stated by:

$$p(k,l) = exp(-\frac{(s_{k,i} - s_{l,j})^2}{4\,D\,\Delta t}) \tag{24}$$

with the time lag Δt between the consecutive frames. All probabilities of localisation k in I_i being the localisation l in I_j were collected in a transition matrix. These connections were then evaluated in terms of the overall probabilities within the time lag and from these a combination of connections was chosen to maximise the overall probability. The algorithm required an estimate of the diffusion coefficient of the molecules studied as an input parameter (D_{in}) to compute the probabilities of connections and the resulting diffusion coefficient (D_{out}). To minimise incorrect connections of localisations, an analysis was conducted *a priori* that iterated over a range of D_{in} and determined the corresponding D_{out}. The final input parameter D_{in} was chosen to be independent of D_{out} (D_{in} vs D_{out} analysis) (Hartel et al., 2016). The algorithm also accounted for photobleaching of emitters and diffusion in and out of the field of view. The entire set of trajectories was then fed into the short trajectory analysis (shortTrAn, Section 4.7.11) for further analysis.

4.7.11 Short trajectory analysis (shortTrAn)

Due to the short length of trajectories obtained from the single-molecule tracking on trypanosomes, an alternative evaluation method to the MSD fit was required to be able to distinguish diffusion from other means of motion modes. Therefore, the method published by Hoze and Holcman (2014) was adapted to our data sets. This method allowed the extraction of the local diffusion tensor and forces from a large number of short trajectories and was therefore abbreviated by shortTrAn (**short tr**ajectory **an**alysis). ShortTrAn was realised in cooperation with Torsten Paul und Philip Kollmannsberger (CCTB, University of Würzburg). The basic core scripts

feeding in the tracking data, pre-processing the data and calculating the diffusion tensors as well as the directed motion vectors was developed by Torsten Paul. The further improvement of the scripts, such as the consideration of the localisation errors, and their adaption to our data sets as well as the graphical output was established and extensively evaluated during this thesis under the supervision of Torsten Paul und Philip Kollmannsberger. The routines are written in Python with Spyder and executed by Jupyter Notebooks. ShortTrAn is shared with the research community via the GitHub repository `https://github.com/MarSc13/shortTrAn`.

4.7.11.1 Evaluation of trajectories by shortTrAn

The calculation principle of the diffusion coefficient and the directed motion was based on the Langevin model.

The local diffusion coefficient was determined by centring a square with the side length r at the position X. The one-dimensional local diffusion tensor $D^{i,j}(X,r)$ at position X was calculated from the mean square displacement of the total number of data points $N(X,r)$ collected from trajectories k =1, 2, 3, ..., N traversing the local square:

$$2D^{ij}(X) \approx \frac{1}{N(X,r)} \sum_{k=1}^{N(X,r)} \frac{(X_k^i(t+\Delta t) - X_k^i(t))(X_k^j(t+\Delta t) - X_k^j(t))}{\Delta t}, \qquad (25)$$

with Δt as the time lag. The static localisation error ($corr_{stat}$) was considered according to Martin et al. (2002) and the dynamic localisation error ($corr_{dyn}$) at non-continuous illumination according to Berglund (2010) and Michalet and Berglund (2012). Thus, Equation 25 resulted in

$$2D^{ij}(X,r) \approx \frac{1}{N(X,r)} \sum_{k=1}^{N(X,r)} \frac{(X_k^i(t+\Delta t) - X_k^i(t))(X_k^j(t+\Delta t) - X_k^j(t)) - corr_{stat}}{\Delta t - corr_{dyn}}, \qquad (26)$$

with $corr_{stat} = 2\sigma^2$ and $corr_{dyn} = \frac{1}{3}\frac{t_{exp}}{\Delta t} t_{exp}$. The localisation precision was represented by σ and the exposure time by t_{exp}.

The one-dimensional contribution of a local velocity $b_\alpha(X,r)$ at position X was approximated by

$$b_\alpha(X,r) \approx \frac{1}{N(X,r)} \sum_{k=1}^{N(X,r)} \frac{X_{\alpha k}(t_k+\Delta t) - X_{\alpha k}(t_k)}{\Delta t} \qquad (27)$$

with $\alpha = i, j$, indicating one of the two dimensions. The static localisation error was not considered immediately in the velocity calculation. Instead, the relative

standard error in the velocity was estimated and visualised in an additional map showing the directed motion results (described in Section 4.7.11.4).

The final evaluation routine was performed with the Jupyter Notebook 'shortTrAn_loop.ipynb' and contained the following scripts:

1. loadmat.py:
   Matrices comprising the information about trajectories gained by tracking of single molecules (4.7.10) or from simulations (4.8.2) were fed into the routine and an unit transformation was conducted to convert x- and y-coordinates to virtual pixel size of 1 nm, the so-called subpixels. This was achieved by dividing the coordinates by a factor corresponding to the resolution of the camera chip (px = 160 nm) or the resolution of the simulation masks (px = 10 nm).
2. remove_singlepart.py:
   This scripts implements a filter which removed single localisations representing one trajectory. This filter became necessary for the evaluation of the simulations (4.8.2) as particles travelling back and forth on both leaflets had only a single localisation per leaflet. In addition, a filter was included to set a threshold for a minimum step length that was required for further analysis of the trajectories. In the final evaluation settings, all trajectories were permitted (step length ≥ 1).
3. padding.py:
   Here the later image boundaries were defined by extracting the minimum and maximum values of the x- and y-coordinates. To create sufficient space for later binning, the matrices were padded by adding a total of 320 nm of empty space per dimension. The final lengths of the feature space matrices was calculated by subtracting the minimum from the maximum value and adding the total pad space of 320 nm. This scripts saved also the minima and maxima, enabling the synchronisation of the structural information on the diffusion and directed motion maps.
4. create_fields.py:
   The feature spaces were set up using the lengths calculated in the previous script.
5. calc_fields_out.py:
   For the calculation of the local diffusion tensors xx, xy, yx and yy as well as vectors x and y of a velocity, iterations over all trajectories were performed. The trajectories were decomposed into their individual steps and for each the diffusion tensors and velocity vectors were computed, respectively. The results were then assigned to the subpixel in the feature spaces from which the step originated. The statistical information was stored in an additional matrix, the count field, and each subpixel contained the number of steps that emanated

from it. An option to enable or disable the correction of the localisation error has been implemented. This option could be specified in the input parameters and allowed for the analysis of simulated trajectories which did not posses any localisation errors.

6. binning.py:
   Binning was performed to increase the local statistics. For this, the size of the count field, tensor and vector matrices was divided by the binning factor. By rounding down to the next smallest integer, the number of superpixels of the newly binned matrices was determined and the discrepancy was truncated equally on both sides for each dimension. The preceding padding prevented the removal of populated subpixels. Subsequently, all superpixels of the tensor and vector fields were averaged based on their statistics in the count field. The final binning factor used for the analysis was 160.
7. remove_isolated_px.py:
   Two spatial filters were implemented. The first filter masked superpixels with low statistics. The masking was accomplished by the application of a threshold to the count field cf. This resulted in binerisation and set superpixels S at position i, j with statistics N of ≤ 5 to zero (Equation 28). The entries in the corresponding superpixel $S_{i,j}$ were removed by multiplying Filter 1 with the count field itself, the tensor fields and the vector fields.

$$\text{Filter 1: } cf^{i,j} = \begin{cases} 0 & \text{if } N \leq 5 \\ 1 & \text{if } N > 5 \end{cases} \tag{28}$$

   The purpose of the second spatial filter was it to remove isolated superpixels from the analysis. The binarised count field served as *input* to Equation 29 as follows:

$$\text{Filter 2: } F^{i,j} = bin\left[thresh\left[mask \cdot (input * kernel)\right]\right] \tag{29}$$

   Convolution of the binarised count field determined the number of populated superpixels in the adjacent neighbourhood. For this, a box kernel of size 3 superpixels was utilised and the maximal connectivity could be 8, which corresponded to 8 populated superpixels. The convoluted matrix was then multiplied by the input referred to as $mask$, which resulted in the elimination of superpixels that were filled even though they were not originally populated. Application of a threshold ($thresh$) that populated superpixels with a connectivity ≤ 1 with 0 resulted in the removal of isolated superpixels. To obtain the final filter matrix $F^{i,j}$, another binarisation was performed, masking empty

superpixels with 0 and populated superpixels with 1. The filter matrix was then applied to the tensor and vector fields as well as to the count field itself to mask isolated superpixels. The workflow of the second spatial filter described by Equation 29 is depicted in Figure 50.

8. smoothing.py:
   A combination of two filters has been used here. In order to smooth the data, a sliding box kernel of the size 3 x 3 superpixels was simultaneously utilised on the count field cf and input field if to calculate the weighted average at position i, j (Equation 30). The input field if was either a tensor or a vector field.

$$\text{Filter 3.1: } \widetilde{if}(i,j) = \frac{\sum_k^{-1,0,1} \sum_l^{-1,0,1} if(i+k, j+l) \cdot cf(i+k, j+l)}{\sum_k^{-1,0,1} \sum_l^{-1,0,1} cf(i+k, j+l)} \tag{30}$$

   The $3D$ to $2D$ projection issue at the rim of the trypanosomes, which was due to the entry of the results in the superpixels from which the step originated, was taken into account by applying filter 3.2. It used the Python built-in Gaussian scipy.ndimage.gaussian_filter on the duplicated matrix, that was already processed with Filter 3.1. The radius of the Gaussian filter was 6 superpixels, with a standard deviation σ for the Gaussian kernel of 1 and constant mode with a value of zero. This padded the superpixels outside the trypanosome mask, required for the Gaussian at superpixels close to the rim, with the value 0. Subsequently, the results from Filter 3.1 and Filter 3.2 were combined. Superpixels at the rim were populated with the output of the projection Filter 3.2, while superpixels of the surface area were populated with the output of the smoothing Filter 3.1. The combination of both filters is additionally illustrated in Figure 27.

9. SaveInputParameter.py:
   This script saved all input parameters specified in the Jupyter Notebook to a text file.

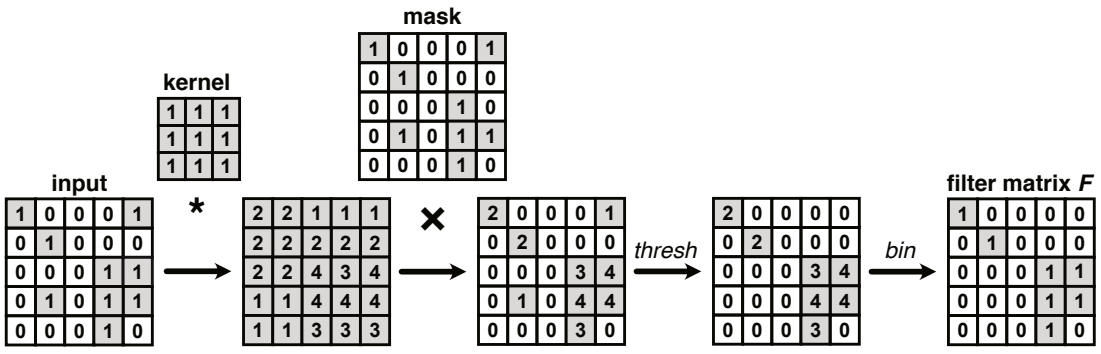

Figure 50: Scheme of the second spatial filter. **A** Illustration of the generation of the filter matrix F used in the second spatial filter. It depicts the convolution by the box kernel, the multiplication by the mask, the application of the threshold ($thresh$), and the binarisation (bin).

4.7.11.2 Generation of the outline of reference structures

In order to study the dynamics of VSGs in relation to a reference structure, the location of the structure should be indicated in the resulting maps. For this, the outline of the structure was generated by a self-written python routine ('outline_signal_marker.py'). The single-molecule localisations of the eYFP-labelled fusion protein served as input, which were obtained and processed according to Section 4.7.1 and drift corrected (Section 4.7.2). Removing artificial clusters was not performed as only the contour of the reference structure was of interest and the more data points were available, the more refined the contour was. Then, the first steps of the shortTrAn were performed to ensure compatibility with the tracking results of shortTrAn. This included the unit transformation to nm, the padding of 320 empty nm-pixels in each dimension to create sufficient space for later binning, the selection of the same image area by means of the saved parameters from Section 4.7.11.1 as well as the binning with the same binning parameters from the corresponding cell in shortTrAn. Background and localisation outliers were manually removed by masking with a polygon. The number of reference structures was specified and the localisations of each extracted separately. Next, a concave hull of the remaining localisations of each structure was compiled with the python built-in function 'alphashape.alphashape' with 0.85 (hook complex) or 0.90 (flagellum) for the parameter α. Scaling the coordinates of the extracted hull vertices with the binning factor 160 guaranteed compatibility with the shortTrAn created maps. In addition, the part of the hook complex which was potentially wrapped around the flagellar pocket neck could be highlighted by running the python script 'Highlighting_fp.py'. For this purpose, the part of the outline to be highlighted was selected by a polygonal area and saved separately to draw this part in a different colour in the maps.

4.7.11.3 Representation of the results on diffusion by shortTrAn

The results of the local diffusion coefficients were presented in an ellipse plot, which was colour-coded for the two-dimensional diffusion coefficient. The shape of the ellipses provided also information on the (an-)isotropic diffusion behaviour by the determination of the eccentricity. First, the tensor units were converted from nm^2/ms to $\mu m^2/s$. Second, a transformation matrix was used to calculate the two one-dimensional diffusion coefficients from the four diffusion tensors. This was realised by the Python function 'numpy.linalg.eig', which returned the eigenvalues and eigenvectors. The eigenvalues corresponded to the two one-dimensional diffusion coefficients and the length of the ellipse axis, while the eigenvectors characterised the orientation of the ellipse axis. The angle of the orientation of the ellipses was calculated using a transformation matrix ([cos,-sin;sin,cos]). The correct orientation of the ellipses was checked with a Python routine written by Torsten Paul, which

compared the input parameters of the ellipses fed into the transformation process with their output. Third, the two-dimensional average diffusion coefficient (D_{2D}) was then derived from the one-dimensional diffusion coefficients (D^{ii}, D^{jj}).

Fourth, the eccentricity ε of an ellipse was calculated by the diffusion coefficients of the minor (D_{minor}) and major axis (D_{major}) of the ellipse as follows:

$$\varepsilon = \sqrt{1 - \frac{D_{minor}}{D_{major}}} \tag{31}$$

The Python scripts 'sim_diffusion.py' or 'sim_diffusion_plus_outline.py' were executed by the Jupyter Notebooks 'Create_Maps.ipynp' or 'Create_Maps_Plus_Outline.ipynp'. The latter enabled also the registration of the structural outline onto the maps and the registration of a highlighted part potentially wrapped around the flagellar entrance. If a part was highlighted, this region (e.g. FPE region) was extracted ± 2 superpixels in each dimension. All parameters and the image section for the extracted region were saved separately for individual analysis.

4.7.11.4 Representation of the results on directed motion by shortTrAn

In case of the directed motion, the information on the velocity was presented in a heat map, colour-coding the amplitude of the velocity, and a quiver plot, indicating the direction of the motion. Additionally the length of the quiver correlated with the amplitude of the velocity. A third map depicted the relative standard error of the velocity, resulting from the consideration of the static localisation error and was used as an indicator for the probability of the presence of directed motion. For this purpose, the two-dimensional directed motion $b(X, r)$ at position X was determined from the two directed motion vectors by:

$$b(X, r) = \sqrt{b_i(X, r)^2 + b_j(X, r)^2}. \tag{32}$$

The plotting of the arrows was accomplished by means of the one-dimensional vectors. The following assumption was made to consider the static localisation error: To determine the velocity of a particle, it has to be localised twice. The detection of each particle is limited by the localisation precision σ, resulting in $\pm 2\,\sigma$ for two particles in one dimension. In order to consider this static localisation error in the local directed motion, the relative standard error at the position X was determined by using the classical error propagation of Equation 32 with $\sigma = 26\,\text{nm}$. The local statistics were taken into account by the division by $\sqrt{(N(X, r))}$. The results were then displayed in a heat map, for which a cut off at 1 was set.

The Python scripts 'sim_directed_motion.py' or 'sim_directed_motion_plus_outline.py' were executed by the Jupyter Notebooks 'Create_Maps.ipynp' or 'Create_Maps_Plus_Outline.ipynp'. The latter allowed for the registration of the structural outline onto the maps and the registration of a highlighted part potentially wrapped around the flagellar pocket entrance. If a part of the outline was highlighted, this region (e.g. FPE region) was extracted ± 2 superpixels in each dimension. All parameters as well as the image section for the extracted region were saved separately for individual analysis. The consideration of the static localisation error and thus the generation of a relative standard error map could be activated or deactivated by specifying the input parameter 'error correction'.

4.8 Random walk simulations on trypanosome-shaped masks

Simulations were run to define thresholds for the guideline to generate supermaps and to check whether the newly determined diffusion coefficient was sufficient to explain the fast turnover rate of the VSG coat. Random walk simulations were performed with an MatLab routine written by Susanne Fenz, which realised the following principle:
For each step, a random angle was chosen $\alpha \in [0, 2\,\pi]$, while the step lengths (l) fulfilled the criterion for the probability (p) in Equation 33 (Fenz et al., 2012):

$$p(l,t) = \frac{2\pi}{4Dt}\, l\, exp\left(-\frac{l^2}{4Dt}\right), \tag{33}$$

where D was the diffusion coefficient and t the time.

4.8.1 *In silico* experiment to estimate the time of turnover with a fixed diffusion coefficient

This *in silico* experiment was performed with an experimentally determined mean diffusion coefficient of $1.00\,\mu m^2/s$ and a time lag of 10 ms. The random walk was simulated on three different trypanosome-shaped masks based on Equation 33. The masks were a composite of a trypanosome outline and the corresponding flagellar pocket entrance region (FPR) indicating the escape site. The cellular outline was defined by the count field, while the FPR was manually selected from the part of the structural outline wrapped around the FP entrance. Both were results of shortTrAn (4.7.11). The resolution of the masks was 10 nm. The cellular outline layer with the FPR (first layer) was achieved by partitioning one pixel of the count field matrix into 16 x 16 subpixels and keeping the occupancy information. In the case of the FPR, the localisations of the manually selected area were placed in the cell outline matrix masking the FPR. Next, the cellular outline layer was doubled excluding the FPR (second layer) to approximate the $3D$ shape of a trypanosome. 1,000 starting points

were then randomly distributed on the first layer and 2,000 dimensionless particles were simulated to perform a random walk on layers until escaping through the FPR. When interacting with the boundaries of the current layer, the particle was relocated to the other layer. Thus, the first position on the entered layer corresponded to the last position of the previous layer. The trajectory length with 50,000 steps was chosen long enough to ensure almost all particles were able to escape during the simulation. Subsequently, the individual escape times (ET) from all particles were collected and plotted in a probability density histogram. The mean first passage time (τ) was then determined from the fit in the exponential tail of the histogram:

$$\left(\frac{1}{\tau}\right) exp\left(\frac{-ET}{\tau}\right). \tag{34}$$

The tail region was found automatically by minimising the corresponding R^2 value. Simulations and their evaluation were carried out by Susanne Fenz.

4.8.2 *In silico* experiment to define thresholds for the motion model assignment in supermaps

In order to investigate the influence of statistics on the ellipticity and the relative standard error determined by shortTrAn, simulations were designed as follows. The experimentally determined mean diffusion coefficient of 1.00 µm^2/s and a time lag of 10 ms were used in this *in silico* experiment. The random walk was simulated on one trypanosome-shaped mask based on Equation 33. The mask was composed of one layer, which represented a trypanosome outline with its corresponding flagellar pocket entrance region (FPR) marking the escape site. The resolution was 10 nm. The outline and FPR were achieved as described in Section 4.8.1. Two sets of simulations were then performed with a trajectory length of either 15 or 50 to mimic the trajectory length of the single-molecule tracking on trypanosomes. Each simulation, contained 20,000 starting points randomly distributed on the layer. 10,000 dimensionless particles were simulated to perform a random walk. For this experiment, only localisation of the trajectories were kept until they hit the boundary for the first time. Subsequently, different stacks with a varying number of trajectories (2,000 - 10,000 trajectories) were bundled for each trajectory length and fed to shortTrAn. Additionally, two data sets containing either 4,000 or 5,000 trajectories of each trace length were evaluated with shortTrAn. From the shortTrAn results, the eccentricity and relative error were extracted with the corresponding statistics of the superpixels and pooled respectively. From these data sets, look-up tables were generated. In order to be able to decide which parameter values may still be treated as indicators of diffusion, threshold values were introduced. It was ensured that 99 % of the data on the eccentricity and relative standard error were assigned to diffusion and only

1 % were falsely assigned to directed motion for a given statistics. Therefore, the limit for the eccentricity was set to 99 % and for the relative standard error to 1 %. Based on these threshold values, the decision was made whether diffusion or directed motion was the predominant motion model in a superpixel (4.9).

4.9 Generation of supermaps - the representation of the decision on the motion model

After the shortTrAn, information about diffusion as well as of directed motion were available for each superpixel. The next step was to decide whether diffusion or directed motion was the locally predominant motion model. For this purpose, a Python routine was established which used the look-up tables of the eccentricity ε and the relative standard error SE_v as an additional input together with the results of single-molecule tracking data analysed with the shortTrAn. By iterating over all superpixels, the routine compared the calculated eccentricity and relative standard error of an superpixel to the statistics-dependent thresholds ε_{thres} and $SE_{v\,thres}$ determined in Section 4.8.2. If both criteria were pointing towards diffusion ($\varepsilon < \varepsilon_{thres}$ & $SE_v > SE_{v\,thres}$) or directed motion ($\varepsilon > \varepsilon_{thres}$ & $SE_v < SE_{v\,thres}$), the superpixel was assigned accordingly. If the two criteria were contradictory, the criterion that could be assigned to a motion model with higher certainty was identified. The better the criterion could be distinguished from its corresponding threshold, the higher the certainty. For this purpose, the discrepancy between the two deviations from their threshold values was calculated ($\mid \Delta\varepsilon - \Delta SE_v \mid$). If the discrepancy was < 0.25, the superpixel remained unassigned, while if the discrepancy was > 0.25, the criterion with the more significant discrepancy to its threshold was used. If the eccentricity was identified to be the parameter for the reliable assignment ($\Delta\varepsilon > \Delta SE_v$), the superpixel was assigned to the diffusion in the case of $\varepsilon < \varepsilon_{thres}$ and to the directional movement in the case of $\varepsilon > \varepsilon_{thres}$. However, if the decisive parameter was the relative standard error ($\Delta\varepsilon < \Delta SE_v$), the superpixel was allocated to diffusion for $SE_v > SE_{v\,thres}$ or to directional motion for $SE_v < SE_{v\,thres}$. Subsequently, the remaining unassigned superpixels were characterised with the help of their neighbours. For this, a moving box kernel (kernel size = 3 superpixels) was employed to consult also superpixels on the diagonal. If the environment was strictly characterised by diffusion (7 and 8 superpixels), the orphan superpixel was categorised to diffusion. While the predominance of a directed motion resulted in the assignment to the directed motion model. This filtering process was repeated until no unassigned superpixels could be filled according to this principle. Python scripts as well as the Jupyter Notebooks for generation of the supermaps, which optionally show the outline of a structure, are available in the ShortTrAn GitHub repository `https://github.com/MarSc13/shortTrAn`.

References

Abbe, E. (1873). Beiträge zur Theorie des Mikroskops und der mikroskopischen Wahrnehmung. *Archiv für Mikroskopische Anatomie*, 9(1):413–468.

Airy, G. B. (1835). On the diffraction of an object-glass with circular aperture. *Transactions of the Cambridge Philosophical Society*, 5:283.

Annibale, P., Vanni, S., Scarselli, M., Rothlisberger, U., and Radenovic, A. (2011). Identification of clustering artifacts in photoactivated localization microscopy. *Nat Methods*, 8(7):527–8.

Backlund, M. P., Joyner, R., and Moerner, W. E. (2015). Chromosomal locus tracking with proper accounting of static and dynamic errors. *Phys Rev E Stat Nonlin Soft Matter Phys*, 91(6):062716.

Baines, A. and Gull, K. (2008). WCB is a C2 domain protein defining the plasma membrane - sub-pellicular microtubule corset of kinetoplastid parasites. *Protist*, 159(1):115–125.

Balzarotti, F., Eilers, Y., Gwosch, K. C., Gynna, A. H., Westphal, V., Stefani, F. D., Elf, J., and Hell, S. W. (2017). Nanometer resolution imaging and tracking of fluorescent molecules with minimal photon fluxes. *Science*, 355(6325):606–612.

Bargul, J. L., Jung, J., McOdimba, F. A., Omogo, C. O., Adung'a, V. O., Kruger, T., Masiga, D. K., and Engstler, M. (2016). Species-specific adaptations of trypanosome morphology and motility to the mammalian host. *PLoS Pathog*, 12(2):e1005448.

Barry, J. D. and McCulloch, R. (2001). Antigenic variation in trypanosomes: enhanced phenotypic variation in a eukaryotic parasite. *Adv Parasitol*, 49:1–70.

Bartossek, T., Jones, N. G., Schafer, C., Cvitkovic, M., Glogger, M., Mott, H. R., Kuper, J., Brennich, M., Carrington, M., Smith, A. S., Fenz, S., Kisker, C., and Engstler, M. (2017). Structural basis for the shielding function of the dynamic trypanosome variant surface glycoprotein coat. *Nat Microbiol*.

Bassereau, P. and Sens, P. (2018). *Physics of biological membranes*. Springer Nature Switzerland, Springer, Cham, 1 edition.

Bastin, P., Ellis, K., Kohl, L., and Gull, K. (2000). Flagellum ontogeny in trypanosomes studied via an inherited and regulated RNA interference system. *J Cell Sci*, 113 (Pt 18):3321–8.

Bastin, P., Pullen, T. J., Sherwin, T., and Gull, K. (1999). Protein transport and flagellum assembly dynamics revealed by analysis of the paralysed trypanosome mutant snl-1. *J Cell Sci*, 112 (Pt 21):3769–77.

Bastin, P., Sherwin, T., and Gull, K. (1998). Paraflagellar rod is vital for trypanosome motility. *Nature*, 391(6667):548.

Baumgart, T., Hess, S. T., and Webb, W. W. (2003). Imaging coexisting fluid domains in biomembrane models coupling curvature and line tension. *Nature*, 425(6960):821–4.

Berglund, A. J. (2010). Statistics of camera-based single-particle tracking. *Phys Rev E Stat Nonlin Soft Matter Phys*, 82(1 Pt 1):011917.

Bernards, A., De Lange, T., Michels, P. A., Liu, A. Y., Huisman, M. J., and Borst, P. (1984). Two modes of activation of a single surface antigen gene of Trypanosoma brucei. *Cell*, 36(1):163–70.

Betzig, E., Patterson, G. H., Sougrat, R., Lindwasser, O. W., Olenych, S., Bonifacino, J. S., Davidson, M. W., Lippincott-Schwartz, J., and Hess, H. F. (2006). Imaging intracellular fluorescent proteins at nanometer resolution. *Science*, 313(5793):1642–1645.

Bobroff, N. (1986). Position measurement with a resolution and noise-limited instrument. *Review of Scientific Instruments*, 57(6):1152–1157.

Borges, A. R., Link, F., Engstler, M., and Jones, N. G. (2021). The glycosylphosphatidylinositol anchor: A linchpin for cell surface versatility of Trypanosomatids. *Front Cell Dev Biol*, 9:720536.

Bringaud, F., Riviere, L., and Coustou, V. (2006). Energy metabolism of trypanosomatids: adaptation to available carbon sources. *Mol Biochem Parasitol*, 149(1):1–9.

Broadhead, R., Dawe, H. R., Farr, H., Griffiths, S., Hart, S. R., Portman, N., Shaw, M. K., Ginger, M. L., Gaskell, S. J., McKean, P. G., and Gull, K. (2006). Flagellar motility is required for the viability of the bloodstream trypanosome. *Nature*, 440(7081):224–227.

Bruce, D. (1895). Preliminary report on the tsetse fly disease or nagana in Zululand. *Durban: Bennett and Davis*.

Brun, R., Blum, J., Chappuis, F., and Burri, C. (2010). Human African trypanosomiasis. *Lancet*, 375(9709):148–59.

Buehler, L. (2016). *Cell Membranes*. Garland Science, Taylor & Francis Group, New York, NY, 1st edition.

Bülow, R., Overath, P., and Davoust, J. (1988). Rapid lateral diffusion of the variant surface glycoprotein in the coat of Trypanosoma brucei. *Biochemistry*, 27(7):2384–8.

Burgert, A., Letschert, S., Doose, S., and Sauer, M. (2015). Artifacts in single-molecule localization microscopy. *Histochem Cell Biol*, 144(2):123–31.

Bülow, R., Nonnengasser, C., and Overath, P. (1989). Release of the variant surface glycoprotein during differentiation of bloodstream to procyclic forms of Trypanosoma brucei. *Mol Biochem Parasitol*, 32(1):85–92.

Büttner, P. (2021). *A single-molecule view of the cytosolic membrane of Trypanosoma brucei*. Master thesis.

Camley, B. A. and Brown, F. L. H. (2013). Diffusion of complex objects embedded in free and supported lipid bilayer membranes: role of shape anisotropy and leaflet structure. *Soft Matter*, 9(19):4767–4779.

Carrington, M., Miller, N., Blum, M., Roditi, I., Wiley, D., and Turner, M. (1991). Variant specific glycoprotein of Trypanosoma brucei consists of two domains each having an independently conserved pattern of cysteine residues. *J Mol Biol*, 221(3):823–35.

Chalfie, M., Tu, Y., Euskirchen, G., Ward, W. W., and Prasher, D. C. (1994). Green fluorescent protein as a marker for gene-expression. *Science*, 263(5148):802–805.

Chao, J., Ram, S., Ward, E. S., and Ober, R. J. (2013). Ultrahigh accuracy imaging modality for super-localization microscopy. *Nat Methods*, 10(4):335–8.

Chen, Y., Lagerholm, B. C., Yang, B., and Jacobson, K. (2006). Methods to measure the lateral diffusion of membrane lipids and proteins. *Methods*, 39(2):147–53.

Corradi, V., Sejdiu, B. I., Mesa-Galloso, H., Abdizadeh, H., Noskov, S. Y., Marrink, S. J., and Tieleman, D. P. (2019). Emerging diversity in lipid-protein interactions. *Chem Rev*, 119(9):5775–5848.

Cross, G. A. (1975). Identification, purification and properties of clone-specific glycoprotein antigens constituting the surface coat of Trypanosoma brucei. *Parasitology*, 71(3):393–417.

Cross, G. A., Kim, H. S., and Wickstead, B. (2014). Capturing the variant surface glycoprotein repertoire (the VSGnome) of Trypanosoma brucei Lister 427. *Mol Biochem Parasitol*, 195(1):59–73.

Danielli, J. F. and Davson, H. (1935). A contribution to the theory of permeability of thin films. *Journal of Cellular and Comparative Physiology*, 5(4):495–508.

d'Avila Levy, C. M., Boucinha, C., Kostygov, A., Santos, H. L., Morelli, K. A., Grybchuk-Ieremenko, A., Duval, L., Votypka, J., Yurchenko, V., Grellier, P., and Lukes, J. (2015). Exploring the environmental diversity of kinetoplastid flagellates in the high-throughput DNA sequencing era. *Mem Inst Oswaldo Cruz*, 110(8):956–65.

Deschout, H., Cella Zanacchi, F., Mlodzianoski, M., Diaspro, A., Bewersdorf, J., Hess, S. T., and Braeckmans, K. (2014). Precisely and accurately localizing single emitters in fluorescence microscopy. *Nat Methods*, 11(3):253–66.

Dickson, R. M., Cubitt, A. B., Tsien, R. Y., and Moerner, W. E. (1997). On/off blinking and switching behaviour of single molecules of green fluorescent protein. *Nature*, 388(6640):355–358.

Digman, M. A., Brown, C. M., Sengupta, P., Wiseman, P. W., Horwitz, A. R., and Gratton, E. (2005). Measuring fast dynamics in solutions and cells with a laser scanning microscope. *Biophys J*, 89(2):1317–27.

Dixon, H., Ginger, C. D., and Williamson, J. (1971). The lipid metabolism of blood and culture forms of Trypanosoma lewisi and Trypanosoma rhodesiense. *Comp Biochem Physiol B*, 39(2):247–66.

Dixon, H. and Williamson, J. (1970). The lipid composition of blood and culture forms of Trypanosoma lewisi and Trypanosoma rhodesiense compared with that of their environment. *Comp Biochem Physiol*, 33(1):111–28.

Doyle, J. J., Hirumi, H., Hirumi, K., Lupton, E. N., and Cross, G. A. (1980). Antigenic variation in clones of animal-infective Trypanosoma brucei derived and maintained in vitro. *Parasitology*, 80(2):359–69.

Dutton, J. E. (1902). Preliminary note upon a trypanosome occurring in the blood of man. *Thompson Yates Lab*, Rep 4:455 – 468.

Engstler, M., Pfohl, T., Herminghaus, S., Boshart, M., Wiegertjes, G., Heddergott, N., and Overath, P. (2007). Hydrodynamic flow-mediated protein sorting on the cell surface of trypanosomes. *Cell*, 131(3):505–15.

Engstler, M., Thilo, L., Weise, F., Grunfelder, C. G., Schwarz, H., Boshart, M., and Overath, P. (2004). Kinetics of endocytosis and recycling of the GPI-anchored variant surface glycoprotein in Trypanosoma brucei. *J Cell Sci*, 117(Pt 7):1105–15.

Erdelyi, M., Rees, E., Metcalf, D., Schierle, G. S., Dudas, L., Sinko, J., Knight, A. E., and Kaminski, C. F. (2013). Correcting chromatic offset in multicolor super-resolution localization microscopy. *Opt Express*, 21(9):10978–88.

Esson, H. J., Morriswood, B., Yavuz, S., Vidilaseris, K., Dong, G., and Warren, G. (2012). Morphology of the trypanosome bilobe, a novel cytoskeletal structure. *Eukaryot Cell*, 11(6):761–72.

Fenn, K. and Matthews, K. R. (2007). The cell biology of Trypanosoma brucei differentiation. *Curr Opin Microbiol*, 10(6):539–46.

Fenz, S., Pezzarossa, A., and Schmidt, T. (2012). The basics and potential of single-molecule tracking in cellular biophysics. *Comprehensive Biophysics*, 2:260–272.

Ferguson, M. A., Homans, S. W., Dwek, R. A., and Rademacher, T. W. (1988). Glycosyl-phosphatidylinositol moiety that anchors Trypanosoma brucei variant surface glycoprotein to the membrane. *Science*, 239(4841 Pt 1):753–9.

Ferguson, M. A. J., Hart, G. W., and Kinoshita, T. (2015). *Glycosylphosphatidylinositol Anchors*, pages 137–150. Cold Spring Harbor (NY).

Fernandes, A. P., Nelson, K., and Beverley, S. M. (1993). Evolution of nuclear ribosomal RNAs in kinetoplastid protozoa: perspectives on the age and origins of parasitism. *Proc Natl Acad Sci U S A*, 90(24):11608–12.

Fox-Roberts, P., Marsh, R., Pfisterer, K., Jayo, A., Parsons, M., and Cox, S. (2017). Local dimensionality determines imaging speed in localization microscopy. *Nat Commun*, 8:13558.

Franco, J. R., Cecchi, G., Priotto, G., Paone, M., Diarra, A., Grout, L., Simarro, P. P., Zhao, W., and Argaw, D. (2020). Monitoring the elimination of human African trypanosomiasis at continental and country level: Update to 2018. *PLoS Negl Trop Dis*, 14(5):e0008261.

Garcia-Saez, A. J. and Schwille, P. (2010). Surface analysis of membrane dynamics. *Biochim Biophys Acta*, 1798(4):766–76.

Garner, O. B. and Baum, L. G. (2008). Galectin-glycan lattices regulate cell-surface glycoprotein organization and signalling. *Biochem Soc Trans*, 36(Pt 6):1472–7.

Garrison, P., Khan, U., Cipriano, M., Bush, P. J., McDonald, J., Sur, A., Myler, P. J., Smith, T. K., Hajduk, S. L., and Bangs, J. D. (2021). Turnover of variant surface glycoprotein in Trypanosoma brucei is a bimodal process. *mBio*, page e0172521.

Glogger, M. (2018). *Single-molecule fluorescence microscopy in live Trypanosoma brucei and model membranes*. Doctoral thesis.

Glogger, M., Stichler, S., Subota, I., Bertlein, S., Spindler, M. C., Tessmar, J., Groll, J., Engstler, M., and Fenz, S. F. (2017a). Live-cell super-resolution imaging of intrinsically fast moving flagellates. *Journal of Physics D-Applied Physics*, 50(7).

Glogger, M., Subota, I., Pezzarossa, A., Denecke, A. L., Carrington, M., Fenz, S. F., and Engstler, M. (2017b). Facilitating trypanosome imaging. *Exp Parasitol*.

Gorter, E. and Grendel, F. (1925). On bimolecular layers of lipoids on the chromocytes of the blood. *J Exp Med*, 41(4):439–43.

Goswami, D., Gowrishankar, K., Bilgrami, S., Ghosh, S., Raghupathy, R., Chadda, R., Vishwakarma, R., Rao, M., and Mayor, S. (2008). Nanoclusters of GPI-anchored proteins are formed by cortical actin-driven activity. *Cell*, 135(6):1085–97.

Gould, M. K., Vu, X. L., Seebeck, T., and de Koning, H. P. (2008). Propidium iodide-based methods for monitoring drug action in the kinetoplastidae: comparison with the Alamar Blue assay. *Anal Biochem*, 382(2):87–93.

Grandgenett, P. M., Otsu, K., Wilson, H. R., Wilson, M. E., and Donelson, J. E. (2007). A function for a specific zinc metalloprotease of African trypanosomes. *PLoS Pathog*, 3(10):1432–45.

Grover, G., Mohrman, W., and Piestun, R. (2015). Real-time adaptive drift correction for super-resolution localization microscopy. *Opt Express*, 23(18):23887–98.

Gruszynski, A. E., DeMaster, A., Hooper, N. M., and Bangs, J. D. (2003). Surface coat remodeling during differentiation of Trypanosoma brucei. *J Biol Chem*, 278(27):24665–72.

Grünfelder, C. G., Engstler, M., Weise, F., Schwarz, H., Stierhof, Y. D., Boshart, M., and Overath, P. (2002). Accumulation of a GPI-anchored protein at the cell surface requires sorting at multiple intracellular levels. *Traffic*, 3(8):547–59.

Grünfelder, C. G., Engstler, M., Weise, F., Schwarz, H., Stierhof, Y. D., Morgan, G. W., Field, M. C., and Overath, P. (2003). Endocytosis of a glycosylphosphatidylinositol-anchored protein via clathrin-coated vesicles, sorting by default in endosomes, and exocytosis via RAB11-positive carriers. *Mol Biol Cell*, 14(5):2029–40.

Guigas, G. and Weiss, M. (2016). Effects of protein crowding on membrane systems. *Biochim Biophys Acta*, 1858(10):2441–2450.

Gull, K. (1999). The cytoskeleton of trypanosomatid parasites. *Annu Rev Microbiol*, 53:629–55.

Gull, K. (2003). Host-parasite interactions and trypanosome morphogenesis: a flagellar pocketful of goodies. *Curr Opin Microbiol*, 6(4):365–70.

Han, R., Wang, L., Xu, F., Zhang, Y., Zhang, M., Liu, Z., Ren, F., and Zhang, F. (2015). Drift correction for single-molecule imaging by molecular constraint field, a distance minimum metric. *BMC Biophys*, 8(1):1.

Harmsen, M. M. and De Haard, H. J. (2007). Properties, production, and applications of camelid single-domain antibody fragments. *Appl Microbiol Biotechnol*, 77(1):13–22.

Hartel, A. J., Glogger, M., Guigas, G., Jones, N. G., Fenz, S. F., Weiss, M., and Engstler, M. (2015). The molecular size of the extra-membrane domain influences the diffusion of the GPI-anchored VSG on the trypanosome plasma membrane. *Sci Rep*, 5:10394.

Hartel, A. J., Glogger, M., Jones, N. G., Abuillan, W., Batram, C., Hermann, A., Fenz, S. F., Tanaka, M., and Engstler, M. (2016). N-glycosylation enables high lateral mobility of GPI-anchored proteins at a molecular crowding threshold. *Nat Commun*, 7:12870.

Heddergott, N., Kruger, T., Babu, S. B., Wei, A., Stellamanns, E., Uppaluri, S., Pfohl, T., Stark, H., and Engstler, M. (2012). Trypanosome motion represents an adaptation to the crowded environment of the vertebrate bloodstream. *PLoS Pathog*, 8(11):e1003023.

Heilemann, M., van de Linde, S., Schuttpelz, M., Kasper, R., Seefeldt, B., Mukherjee, A., Tinnefeld, P., and Sauer, M. (2008). Subdiffraction-resolution fluorescence imaging with conventional fluorescent probes. *Angewandte Chemie-International Edition*, 47(33):6172–6176.

Hell, S. W. and Wichmann, J. (1994). Breaking the diffraction resolution limit by stimulated-emission - stimulated-emission-depletion fluorescence microscopy. *Optics Letters*, 19(11):780–782.

Hempelmann, A., Hartleb, L., van Straaten, M., Hashemi, H., Zeelen, J. P., Bongers, K., Papavasiliou, F. N., Engstler, M., Stebbins, C. E., and Jones, N. G. (2021). Nanobody-mediated macromolecular crowding induces membrane fission and remodeling in the African trypanosome. *Cell Rep*, 37(5):109923.

Hemphill, A., Lawson, D., and Seebeck, T. (1991). The cytoskeletal architecture of Trypanosoma brucei. *J Parasitol*, 77(4):603–12.

Herschel, J. F. W. (1845). On a case of superficial colour presented by a homogeneous liquid internally colourless. *Philosophical Transactions of the Royal Society of London*, 135:143–145.

Hertz-Fowler, C., Figueiredo, L. M., Quail, M. A., Becker, M., Jackson, A., Bason, N., Brooks, K., Churcher, C., Fahkro, S., Goodhead, I., Heath, P., Kartvelishvili, M., Mungall, K., Harris, D., Hauser, H., Sanders, M., Saunders, D., Seeger, K., Sharp, S., Taylor, J. E., Walker, D., White, B., Young, R., Cross, G. A., Rudenko, G., Barry, J. D., Louis, E. J., and Berriman, M. (2008). Telomeric expression sites are highly conserved in Trypanosoma brucei. *PLoS One*, 3(10):e3527.

Hess, S. T., Girirajan, T. P. K., and Mason, M. D. (2006). Ultra-high resolution imaging by fluorescence photoactivation localization microscopy. *Biophysical Journal*, 91(11):4258–4272.

Hess, S. T., Huang, S., Heikal, A. A., and Webb, W. W. (2002). Biological and chemical applications of fluorescence correlation spectroscopy: a review. *Biochemistry*, 41(3):697–705.

Hill, R. J. and Wang, C. Y. (2014). Diffusion in phospholipid bilayer membranes: dual-leaflet dynamics and the roles of tracer-leaflet and inter-leaflet coupling. *Proc Math Phys Eng Sci*, 470(2167):20130843.

Holcman, D. and Schuss, Z. (2013). Control of flux by narrow passages and hidden targets in cellular biology. *Rep Prog Phys*, 76(7):074601.

Hooke, R. (1665). *Micrographia: Or Some Physiological Descriptions Of Minute Bodies Made By Magnifying Glasses With Observations and Inquiries thereupon.* Printed by Jo. Martyn and Ja. Allestry, London.

Hoyle, C. E. and Bowman, C. N. (2010). Thiol-ene click chemistry. *Angewandte Chemie-International Edition*, 49(9):1540–1573.

Hoze, N. and Holcman, D. (2014). Residence times of receptors in dendritic spines analyzed by stochastic simulations in empirical domains. *Biophys J*, 107(12):3008–3017.

Hoze, N., Nair, D., Hosy, E., Sieben, C., Manley, S., Herrmann, A., Sibarita, J. B., Choquet, D., and Holcman, D. (2012). Heterogeneity of ampa receptor trafficking and molecular interactions revealed by superresolution analysis of live cell imaging. *Proc Natl Acad Sci U S A*, 109(42):17052–7.

Huang, G., Wang, L., Wang, S., Han, Y., Wu, J., Zhang, Q., Xu, F., and Lu, T. J. (2012). Engineering three-dimensional cell mechanical microenvironment with hydrogels. *Biofabrication*, 4(4):042001.

Jablonski, A. (1935). Über den Mechanismus der Photolumineszenz von Farbstoffphosphoren. *Zeitschrift fur Physik*, 94:38.

Jackson, D. G., Owen, M. J., and Voorheis, H. P. (1985). A new method for the rapid purification of both the membrane-bound and released forms of the variant surface glycoprotein from Trypanosoma brucei. *Biochem J*, 230(1):195–202.

Jackson, D. G., Windle, H. J., and Voorheis, H. P. (1993). The identification, purification, and characterization of 2 invariant surface glycoproteins located beneath the surface-coat barrier of blood-stream forms of trypanosoma-brucei. *Journal of Biological Chemistry*, 268(11):8085–8095.

Jacobson, K., Liu, P., and Lagerholm, B. C. (2019). The lateral organization and mobility of plasma membrane components. *Cell*, 177(4):806–819.

Jönsson, P., Gunnarsson, A., and Hook, F. (2011). Accumulation and separation of membrane-bound proteins using hydrodynamic forces. *Anal Chem*, 83(2):604–11.

Kalappurakkal, J. M., Sil, P., and Mayor, S. (2020). Toward a new picture of the living plasma membrane. *Protein Sci*, 29(6):1355–1365.

Kennedy, P. G. (2013). Clinical features, diagnosis, and treatment of human African trypanosomiasis (sleeping sickness). *Lancet Neurol*, 12(2):186–94.

Kimaro, E. and Abiola, P. (2021). *Epidemiology and Economic Importance of African Animal Trypanosomiasis*, pages 24–52.

Kleine, F. K. (1909). Weitere wissenschaftliche Beobachtungen über die Entwicklung von Trypanosomen in Glossinen. *Dtsch. Medizinische Wochenschrift*, 35:924 – 925.

Kohl, L., Robinson, D., and Bastin, P. (2003). Novel roles for the flagellum in cell morphogenesis and cytokinesis of trypanosomes. *Embo Journal*, 22(20):5336–5346.

Koyfman, A. Y., Schmid, M. F., Gheiratmand, L., Fu, C. J., Khant, H. A., Huang, D., He, C. Y., and Chiu, W. (2011). Structure of Trypanosoma brucei flagellum accounts for its bihelical motion. *Proc Natl Acad Sci U S A*, 108(27):11105–8.

Kusumi, A., Fujiwara, T. K., Chadda, R., Xie, M., Tsunoyama, T. A., Kalay, Z., Kasai, R. S., and Suzuki, K. G. (2012). Dynamic organizing principles of the plasma membrane that regulate signal transduction: commemorating the fortieth anniversary of Singer and Nicolson's fluid-mosaic model. *Annu Rev Cell Dev Biol*, 28:215–50.

Kusumi, A., Suzuki, K. G., Kasai, R. S., Ritchie, K., and Fujiwara, T. K. (2011). Hierarchical mesoscale domain organization of the plasma membrane. *Trends Biochem Sci*, 36(11):604–15.

Lacomble, S., Vaughan, S., Gadelha, C., Morphew, M. K., Shaw, M. K., McIntosh, J. R., and Gull, K. (2010). Basal body movements orchestrate membrane organelle division and cell morphogenesis in Trypanosoma brucei. *J Cell Sci*, 123(Pt 17):2884–91.

LaCount, D. J., Gruszynski, A. E., Grandgenett, P. M., Bangs, J. D., and Donelson, J. E. (2003). Expression and function of the Trypanosoma brucei major surface protease (GP63) genes. *J Biol Chem*, 278(27):24658–64.

Lakowicz, J. R. (2010). *Principles of fluorescence spectroscopy*. Springer, New York, NY, 3. (corr. at 4. print.) edition.

Lakshminarayan, R., Wunder, C., Becken, U., Howes, M. T., Benzing, C., Arumugam, S., Sales, S., Ariotti, N., Chambon, V., Lamaze, C., Loew, D., Shevchenko, A., Gaus, K., Parton, R. G., and Johannes, L. (2014). Galectin-3 drives glycosphingolipid-dependent biogenesis of clathrin-independent carriers. *Nat Cell Biol*, 16(6):595–606.

Lamont, G. S., Tucker, R. S., and Cross, G. A. (1986). Analysis of antigen switching rates in Trypanosoma brucei. *Parasitology*, 92 (Pt 2):355–67.

Le, N. N. T., Zorn, S., Schmitt, S. K., Gopalan, P., and Murphy, W. L. (2016). Hydrogel arrays formed via differential wettability patterning enable combinatorial screening of stem cell behavior. *Acta Biomater*, 34:93–103.

Lee, A. G. (2003). Lipid-protein interactions in biological membranes: a structural perspective. *Biochim Biophys Acta*, 1612(1):1–40.

Lee, A. G. (2011). Lipid-protein interactions. *Biochem Soc Trans*, 39(3):761–6.

Lelek, M., Gyparaki, M. T., Beliu, G., Schueder, F., Griffié, J., Manley, S., Jungmann, R., Sauer, M., Lakadamyali, M., and Zimmer, C. (2021). Single-molecule localization microscopy. *Nature Reviews Methods Primers*, 1(1):39.

Lemke, E. A. (2014). The exploding genetic code. *Chembiochem*, 15(12):1691–4.

Lemons, D. S. and Gythiel, A. (1997). Paul Langevin's 1908 paper "On the theory of Brownian motion" ["sur la théorie du mouvement brownien," C. R. Acad. Sci. (Paris) 146, 530–533 (1908)]. *American Journal of Physics*, 65(11):1079–1081.

Link, F., Borges, A. R., Jones, N. G., and Engstler, M. (2021). To the surface and back: Exo- and endocytic pathways in Trypanosoma brucei. *Front Cell Dev Biol*, 9:720521.

Liu, C. C. and Schultz, P. G. (2010). Adding new chemistries to the genetic code. *Annual Review of Biochemistry, Vol 79*, 79:413–444.

Livingstone, D. (1857). *Missionary travels and researches in South Africa*. Project Gutenberg, Champaign, Ill.

Loeb, J. (1904). The recent development of biology. *Science*, 20(519):777–86.

Lukosz, W. (1966). Optical systems with resolving powers exceeding classical limit. *Journal of the Optical Society of America*, 56(11):1463–1471.

MacGregor, P., Savill, N. J., Hall, D., and Matthews, K. R. (2011). Transmission stages dominate trypanosome within-host dynamics during chronic infections. *Cell Host Microbe*, 9(4):310–8.

Manzo, C. and Garcia-Parajo, M. F. (2015). A review of progress in single particle tracking: from methods to biophysical insights. *Rep Prog Phys*, 78(12):124601.

Marsh, R. J., Pfisterer, K., Bennett, P., Hirvonen, L. M., Gautel, M., Jones, G. E., and Cox, S. (2018). Artifact-free high-density localization microscopy analysis. *Nature Methods*, 15(9):689–+.

Martin, D. S., Forstner, M. B., and Kas, J. A. (2002). Apparent subdiffusion inherent to single particle tracking. *Biophys J*, 83(4):2109–17.

McGorty, R., Kamiyama, D., and Huang, B. (2013). Active microscope stabilization in three dimensions using image correlation. *Opt Nanoscopy*, 2(1).

McKean, P. G., Baines, A., Vaughan, S., and Gull, K. (2003). gamma-Tubulin functions in the nucleation of a discrete subset of microtubules in the eukaryotic flagellum. *Current Biology*, 13(7):598–602.

McMillan, T. J., Leatherman, E., Ridley, A., Shorrocks, J., Tobi, S. E., and Whiteside, J. R. (2008). Cellular effects of long wavelength UV light (UVA) in mammalian cells. *J Pharm Pharmacol*, 60(8):969–76.

Mehlert, A., Bond, C. S., and Ferguson, M. A. (2002). The glycoforms of a Trypanosoma brucei variant surface glycoprotein and molecular modeling of a glycosylated surface coat. *Glycobiology*, 12(10):607–12.

Merkel, R., Sackmann, E., and Evans, E. (1989). Molecular friction and epitactic coupling between monolayers in supported bilayers. *Journal De Physique*, 50(12):1535–1555.

Meyer, H. (1899). Zur Theorie der Alkoholnarkose. *Archiv für experimentelle Pathologie und Pharmakologie*, 42(2):109–118.

Meyer, H. (1901). Zur Theorie der Alkoholnarkose. *Archiv für experimentelle Pathologie und Pharmakologie*, 46(5):338–346.

Michalet, X. (2010). Mean square displacement analysis of single-particle trajectories with localization error: Brownian motion in an isotropic medium. *Phys Rev E Stat Nonlin Soft Matter Phys*, 82(4 Pt 1):041914.

Michalet, X. and Berglund, A. J. (2012). Optimal diffusion coefficient estimation in single-particle tracking. *Phys Rev E Stat Nonlin Soft Matter Phys*, 85(6 Pt 1):061916.

Moerner, W. E. and Kador, L. (1989). Optical detection and spectroscopy of single molecules in a solid. *Phys Rev Lett*, 62(21):2535–2538.

Moreira-Leite, F. F., Sherwin, T., Kohl, L., and Gull, K. (2001). A trypanosome structure involved in transmitting cytoplasmic information during cell division. *Science*, 294(5542):610–2.

Morriswood, B. (2015). Form, fabric, and function of a flagellum-associated cytoskeletal structure. *Cells*, 4(4):726–47.

Morriswood, B., He, C. Y., Sealey-Cardona, M., Yelinek, J., Pypaert, M., and Warren, G. (2009). The bilobe structure of Trypanosoma brucei contains a MORN-repeat protein. *Mol Biochem Parasitol*, 167(2):95–103.

Mugnier, M. R., Stebbins, C. E., and Papavasiliou, F. N. (2016). Masters of disguise: Antigenic variation and the VSG coat in Trypanosoma brucei. *PLoS Pathog*, 12(9):e1005784.

Myler, P., Nelson, R. G., Agabian, N., and Stuart, K. (1984a). Two mechanisms of expression of a predominant variant antigen gene of Trypanosoma brucei. *Nature*, 309(5965):282–4.

Myler, P. J., Allison, J., Agabian, N., and Stuart, K. (1984b). Antigenic variation in African trypanosomes by gene replacement or activation of alternate telomeres. *Cell*, 39(1):203–211.

Nicastro, D., Schwartz, C., Pierson, J., Gaudette, R., Porter, M. E., and McIntosh, J. R. (2006). The molecular architecture of axonemes revealed by cryoelectron tomography. *Science*, 313(5789):944–8.

Nikic, I., Kang, J. H., Girona, G. E., Aramburu, I. V., and Lemke, E. A. (2015). Labeling proteins on live mammalian cells using click chemistry. *Nat Protoc*, 10(5):780–91.

Nolan, D. P., Jackson, D. G., Windle, H. J., Pays, A., Geuskens, M., Michel, A., Voorheis, H. P., and Pays, E. (1997). Characterization of a novel, stage-specific, invariant surface protein in Trypanosoma brucei containing an internal, serine-rich, repetitive motif. *J Biol Chem*, 272(46):29212–21.

Ober, R. J., Ram, S., and Ward, E. S. (2004). Localization accuracy in single-molecule microscopy. *Biophys J*, 86(2):1185–200.

Ogbadoyi, E., Ersfeld, K., Robinson, D., Sherwin, T., and Gull, K. (2000). Architecture of the Trypanosoma brucei nucleus during interphase and mitosis. *Chromosoma*, 108(8):501–13.

Ormö, M., Cubitt, A. B., Kallio, K., Gross, L. A., Tsien, R. Y., and Remington, S. J. (1996). Crystal structure of the aequorea victoria green fluorescent protein. *Science*, 273(5280):1392–1395.

Orrit, M. and Bernard, J. (1990). Single pentacene molecules detected by fluorescence excitation in a p-terphenyl crystal. *Phys Rev Lett*, 65(21):2716–2719.

Overath, P. and Engstler, M. (2004). Endocytosis, membrane recycling and sorting of GPI-anchored proteins: Trypanosoma brucei as a model system. *Mol Microbiol*, 53(3):735–44.

Overath, P., Stierhof, Y. D., and Wiese, M. (1997). Endocytosis and secretion in trypanosomatid parasites - tumultuous traffic in a pocket. *Trends Cell Biol*, 7(1):27–33.

Overton, C. E. (1901). *Studien über die Narkose: zugleich ein Beitrag zur allgemeinen Pharmakologie*. G. Fischer.

Paindavoine, P., Rolin, S., Van Assel, S., Geuskens, M., Jauniaux, J. C., Dinsart, C., Huet, G., and Pays, E. (1992). A gene from the variant surface glycoprotein expression site encodes one of several transmembrane adenylate cyclases located on the flagellum of Trypanosoma brucei. *Mol Cell Biol*, 12(3):1218–25.

Patnaik, P. K., Field, M. C., Menon, A. K., Cross, G. A., Yee, M. C., and Butikofer, P. (1993). Molecular species analysis of phospholipids from Trypanosoma brucei bloodstream and procyclic forms. *Mol Biochem Parasitol*, 58(1):97–105.

Patterson, G. H. and Lippincott-Schwartz, J. (2002). A photoactivatable GFP for selective photolabeling of proteins and cells. *Science*, 297(5588):1873–7.

Pays, E. (1985). Gene conversion in trypanosome antigenic variation. *Prog Nucleic Acid Res Mol Biol*, 32:1–26.

Perez-Morga, D., Vanhollebeke, B., Paturiaux-Hanocq, F., Nolan, D. P., Lins, L., Homble, F., Vanhamme, L., Tebabi, P., Pays, A., Poelvoorde, P., Jacquet, A., Brasseur, R., and Pays, E. (2005). Apolipoprotein L-I promotes trypanosome lysis by forming pores in lysosomal membranes. *Science*, 309(5733):469–72.

Pezzarossa, A., Zosel, F., and Schmidt, T. (2015). Visualization of HRas domains in the plasma membrane of fibroblasts. *Biophys J*, 108(8):1870–7.

Pike, L. J. (2006). Rafts defined: a report on the Keystone Symposium on Lipid Rafts and Cell Function. *J Lipid Res*, 47(7):1597–8.

Pinger, J., Nesic, D., Ali, L., Aresta-Branco, F., Lilic, M., Chowdhury, S., Kim, H. S., Verdi, J., Raper, J., Ferguson, M. A. J., Papavasiliou, F. N., and Stebbins, C. E. (2018). African trypanosomes evade immune clearance by O-glycosylation of the VSG surface coat. *Nat Microbiol*, 3(8):932–938.

Plowman, S. J., Muncke, C., Parton, R. G., and Hancock, J. F. (2005). H-ras, K-ras, and inner plasma membrane raft proteins operate in nanoclusters with differential dependence on the actin cytoskeleton. *Proc Natl Acad Sci U S A*, 102(43):15500–5.

Qian, H., Sheetz, M. P., and Elson, E. L. (1991). Single-particle tracking - analysis of diffusion and flow in 2-dimensional systems. *Biophysical Journal*, 60(4):910–921.

Quan, T., Zeng, S., and Huang, Z. L. (2010). Localization capability and limitation of electron-multiplying charge-coupled, scientific complementary metal-oxide semiconductor, and charge-coupled devices for superresolution imaging. *J Biomed Opt*, 15(6):066005.

Quincke, G. (1888). Über periodische Ausbreitung an Flüssigkeitsoberflächen und dadurch hervorgerufene Bewegungserscheinungen. *Annalen der Physik*, 271(12):580–642.

Raghupathy, R., Anilkumar, A. A., Polley, A., Singh, P. P., Yadav, M., Johnson, C., Suryawanshi, S., Saikam, V., Sawant, S. D., Panda, A., Guo, Z., Vishwakarma, R. A., Rao, M., and Mayor, S. (2015). Transbilayer lipid interactions mediate nanoclustering of lipid-anchored proteins. *Cell*, 161(3):581–594.

Ralston, K. S., Kisalu, N. K., and Hill, K. L. (2011). Structure-function analysis of dynein light chain 1 identifies viable motility mutants in bloodstream-form Trypanosoma brucei. *Eukaryotic Cell*, 10(7):884–894.

Rayleigh, L. (1903). On the theory of optical images, with special reference to the microscope. *Journal of the Royal Microscopical Society*, 23(4):474–482.

Reuner, B., Vassella, E., Yutzy, B., and Boshart, M. (1997). Cell density triggers slender to stumpy differentiation of Trypanosoma brucei bloodstream forms in culture. *Mol Biochem Parasitol*, 90(1):269–80.

Richmond, G. S., Gibellini, F., Young, S. A., Major, L., Denton, H., Lilley, A., and Smith, T. K. (2010). Lipidomic analysis of bloodstream and procyclic form Trypanosoma brucei. *Parasitology*, 137(9):1357–92.

Ripley, B. D. (1979). Tests of randomness for spatial point patterns. *Journal of the Royal Statistical Society Series B-Methodological*, 41(3):368–374.

Robertson, J. D. (1957). New observations on the ultrastructure of the membranes of frog peripheral nerve fibers. *J Biophys Biochem Cytol*, 3(6):1043–8.

Robertson, J. D. (1967). Origin of the unit membrane concept. *Protoplasma*, 63(1):218–45.

Robinson, D. R. and Gull, K. (1991). Basal body movements as a mechanism for mitochondrial genome segregation in the trypanosome cell cycle. *Nature*, 352(6337):731–3.

Robinson, D. R., Sherwin, T., Ploubidou, A., Byard, E. H., and Gull, K. (1995). Microtubule polarity and dynamics in the control of organelle positioning, segregation, and cytokinesis in the trypanosome cell cycle. *J Cell Biol*, 128(6):1163–72.

Rodriguez, E. A., Campbell, R. E., Lin, J. Y., Lin, M. Z., Miyawaki, A., Palmer, A. E., Shu, X., Zhang, J., and Tsien, R. Y. (2017). The growing and glowing toolbox of fluorescent and photoactive proteins. *Trends Biochem Sci*, 42(2):111–129.

Rodriguez, J. A., Lopez, M. A., Thayer, M. C., Zhao, Y., Oberholzer, M., Chang, D. D., Kisalu, N. K., Penichet, M. L., Helguera, G., Bruinsma, R., Hill, K. L., and Miao, J. (2009). Propulsion of African trypanosomes is driven by bihelical waves with alternating chirality separated by kinks. *Proc Natl Acad Sci U S A*, 106(46):19322–7.

Rolin, S., Halleux, S., Van Sande, J., Dumont, J., Pays, E., and Steinert, M. (1990). Stage-specific adenylate cyclase activity in Trypanosoma brucei. *Exp Parasitol*, 71(3):350–2.

Rotureau, B., Subota, I., Buisson, J., and Bastin, P. (2012). A new asymmetric division contributes to the continuous production of infective trypanosomes in the tsetse fly. *Development*, 139(10):1842–50.

Rotureau, B. and Van Den Abbeele, J. (2013). Through the dark continent: African trypanosome development in the tsetse fly. *Front Cell Infect Microbiol*, 3:53.

Rust, M. J., Bates, M., and Zhuang, X. W. (2006). Sub-diffraction-limit imaging by stochastic optical reconstruction microscopy (STORM). *Nature Methods*, 3(10):793–795.

Sage, D., Kirshner, H., Pengo, T., Stuurman, N., Min, J., Manley, S., and Unser, M. (2015). Quantitative evaluation of software packages for single-molecule localization microscopy. *Nat Methods*, 12(8):717–24.

Savin, T. and Doyle, P. S. (2005). Static and dynamic errors in particle tracking microrheology. *Biophys J*, 88(1):623–38.

Schmidt, T., Schutz, G. J., Baumgartner, W., Gruber, H. J., and Schindler, H. (1996). Imaging of single molecule diffusion. *Proc Natl Acad Sci U S A*, 93(7):2926–9.

Schuss, Z., Singer, A., and Holcman, D. (2007). The narrow escape problem for diffusion in cellular microdomains. *Proc Natl Acad Sci U S A*, 104(41):16098–103.

Schuster, S., Kruger, T., Subota, I., Thusek, S., Rotureau, B., Beilhack, A., and Engstler, M. (2017). Developmental adaptations of trypanosome motility to the tsetse fly host environments unravel a multifaceted in vivo microswimmer system. *Elife*, 6.

Schwarzer, R., Levental, I., Gramatica, A., Scolari, S., Buschmann, V., Veit, M., and Herrmann, A. (2014). The cholesterol-binding motif of the HIV-1 glycoprotein gp41 regulates lateral sorting and oligomerization. *Cell Microbiol*, 16(10):1565–81.

Schwede, A., Macleod, O. J., MacGregor, P., and Carrington, M. (2015). How does the VSG coat of bloodstream form african trypanosomes interact with external proteins? *PLoS Pathog*, 11(12):e1005259.

Seed, J. R. and Sechelski, J. B. (1989). Mechanism of long slender (LS) to short stumpy (SS) transformation in the African trypanosomes. *J Protozool*, 36(6):572–7.

Semrau, S., Pezzarossa, A., and Schmidt, T. (2011). Microsecond single-molecule tracking (µsSMT). *Biophys J*, 100(4):L19–21.

Semrau, S. and Schmidt, T. (2007). Particle image correlation spectroscopy (PICS): retrieving nanometer-scale correlations from high-density single-molecule position data. *Biophys J*, 92(2):613–21.

Serricchio, M., Schmid, A. W., Steinmann, M. E., Sigel, E., Rauch, M., Julkowska, D., Bonnefoy, S., Fort, C., Bastin, P., and Butikofer, P. (2015). Flagellar membranes are rich in raft-forming phospholipids. *Biol Open*, 4(9):1143–53.

Sezgin, E., Levental, I., Mayor, S., and Eggeling, C. (2017). The mystery of membrane organization: composition, regulation and roles of lipid rafts. *Nat Rev Mol Cell Biol*, 18(6):361–374.

Shannon, C. E. (1949). Communication in the presence of noise. *Proceedings of the Institute of Radio Engineers*, 37(1):10–21.

Sharma, R., Peacock, L., Gluenz, E., Gull, K., Gibson, W., and Carrington, M. (2008). Asymmetric cell division as a route to reduction in cell length and change in cell morphology in trypanosomes. *Protist*, 159(1):137–51.

Shera, E. B., Seitzinger, N. K., Davis, L. M., Keller, R. A., and Soper, S. A. (1990). Detection of single fluorescent molecules. *Chemical Physics Letters*, 174(6):553–557.

Sherwin, T. and Gull, K. (1989). The cell division cycle of Trypanosoma brucei brucei: timing of event markers and cytoskeletal modulations. *Philos Trans R Soc Lond B Biol Sci*, 323(1218):573–88.

Shimogawa, M. M., Ray, S. S., Kisalu, N., Zhang, Y., Geng, Q., Ozcan, A., and Hill, K. L. (2018). Parasite motility is critical for virulence of african trypanosomes. *Sci Rep*, 8(1):9122.

Shimomura, O., Johnson, F. H., and Saiga, Y. (1962). Extraction, purification and properties of aequorin, a bioluminescent protein from the luminous hydromedusan, aequorea. *J Cell Comp Physiol*, 59:223–39.

Simons, K. and Toomre, D. (2000). Lipid rafts and signal transduction. *Nat Rev Mol Cell Biol*, 1(1):31–9.

Simons, K. and Van Meer, G. (1988). Lipid sorting in epithelial cells. *Biochemistry*, 27(17):6197–6202.

Singer, S. J. and Nicolson, G. L. (1972). The fluid mosaic model of the structure of cell membranes. *Science*, 175(4023):720–31.

Slator, P. J., Cairo, C. W., and Burroughs, N. J. (2015). Detection of diffusion heterogeneity in single particle tracking trajectories using a hidden markov model with measurement noise propagation. *PLoS One*, 10(10):e0140759.

Smith, J. D. (1993). Phospholipid biosynthesis in protozoa. *Prog Lipid Res*, 32(1):47–60.

Stellamanns, E., Uppaluri, S., Hochstetter, A., Heddergott, N., Engstler, M., and Pfohl, T. (2014). Optical trapping reveals propulsion forces, power generation and motility efficiency of the unicellular parasites Trypanosoma brucei brucei. *Sci Rep*, 4:6515.

Steverding, D., Stierhof, Y. D., Chaudhri, M., Ligtenberg, M., Schell, D., Beck-Sickinger, A. G., and Overath, P. (1994). ESAG 6 and 7 products of Trypanosoma brucei form a transferrin binding protein complex. *Eur J Cell Biol*, 64(1):78–87.

Steverding, D., Stierhof, Y. D., Fuchs, H., Tauber, R., and Overath, P. (1995). Transferrin-binding protein complex is the receptor for transferrin uptake in Trypanosoma brucei. *J Cell Biol*, 131(5):1173–82.

Stoeckenius, W. (1962). Structure of the plasma membrane. *Circulation*, 26(5):1066–1069.

Stokes, G. G. (1852). On the change of refrangibility of light. *Philosophical Transactions of the Royal Society of London*, 142:463–562.

Tanaka, K. A., Suzuki, K. G., Shirai, Y. M., Shibutani, S. T., Miyahara, M. S., Tsuboi, H., Yahara, M., Yoshimura, A., Mayor, S., Fujiwara, T. K., and Kusumi,

A. (2010). Membrane molecules mobile even after chemical fixation. *Nat Methods*, 7(11):865–6.

Taylor, A. E. and Godfrey, D. G. (1969). A new organelle of bloodstream salivarian trypanosomes. *J Protozool*, 16(3):466–70.

Taylor, J. E. and Rudenko, G. (2006). Switching trypanosome coats: what's in the wardrobe? *Trends Genet*, 22(11):614–20.

Terai, T. and Nagano, T. (2013). Small-molecule fluorophores and fluorescent probes for bioimaging. *Pflugers Arch*, 465(3):347–59.

Thompson, R. E., Larson, D. R., and Webb, W. W. (2002). Precise nanometer localization analysis for individual fluorescent probes. *Biophys J*, 82(5):2775–83.

Tielens, A. G. and van Hellemond, J. J. (2009). Surprising variety in energy metabolism within Trypanosomatidae. *Trends Parasitol*, 25(10):482–90.

Turner, C. M. (1997). The rate of antigenic variation in fly-transmitted and syringe-passaged infections of Trypanosoma brucei. *FEMS Microbiol Lett*, 153(1):227–31.

Tyler, K. M., Fridberg, A., Toriello, K. M., Olson, C. L., Cieslak, J. A., Hazlett, T. L., and Engman, D. M. (2009). Flagellar membrane localization via association with lipid rafts. *J Cell Sci*, 122(Pt 6):859–66.

Van Den Abbeele, J., Claes, Y., van Bockstaele, D., Le Ray, D., and Coosemans, M. (1999). Trypanosoma brucei spp. development in the tsetse fly: characterization of the post-mesocyclic stages in the foregut and proboscis. *Parasitology*, 118 (Pt 5):469–78.

van Leeuwenhoek, A. (1677). Observations, communicated to the publisher by Mr. Antony van Leewenhoeck, in a dutch letter of the 9th Octob. 1676. here english'd: concerning little animals by him observed in rain-well-sea- and snow water; as also in water wherein pepper had lain infused. *Phil. Trans. R. Soc.*, 12::821–831.

van Meer, G., Voelker, D. R., and Feigenson, G. W. (2008). Membrane lipids: where they are and how they behave. *Nat Rev Mol Cell Biol*, 9(2):112–24.

Vanhollebeke, B., De Muylder, G., Nielsen, M. J., Pays, A., Tebabi, P., Dieu, M., Raes, M., Moestrup, S. K., and Pays, E. (2008). A haptoglobin-hemoglobin receptor conveys innate immunity to Trypanosoma brucei in humans. *Science*, 320(5876):677–81.

Vassella, E., Reuner, B., Yutzy, B., and Boshart, M. (1997). Differentiation of African trypanosomes is controlled by a density sensing mechanism which signals cell cycle arrest via the cAMP pathway. *J Cell Sci*, 110 (Pt 21):2661–71.

Veatch, S. L., Cicuta, P., Sengupta, P., Honerkamp-Smith, A., Holowka, D., and Baird, B. (2008). Critical fluctuations in plasma membrane vesicles. *ACS Chem Biol*, 3(5):287–93.

Venkatesan, S. and Ormerod, W. E. (1976). Lipid content of the slender and stumpy forms of Trypanosoma brucei rhodesiense: a comparative study. *Comp Biochem Physiol B*, 53(4):481–7.

Vial, H. J., Eldin, P., Tielens, A. G., and van Hellemond, J. J. (2003). Phospholipids in parasitic protozoa. *Mol Biochem Parasitol*, 126(2):143–54.

Vickerman, K. (1969). On the surface coat and flagellar adhesion in trypanosomes. *J Cell Sci*, 5(1):163–93.

Wang, L. and Schultz, P. G. (2004). Expanding the genetic code. *Angew Chem Int Ed Engl*, 44(1):34–66.

Wang, Y., Schnitzbauer, J., Hu, Z., Li, X., Cheng, Y., Huang, Z. L., and Huang, B. (2014). Localization events-based sample drift correction for localization microscopy with redundant cross-correlation algorithm. *Opt Express*, 22(13):15982–91.

Wheeler, R. J. (2010). The trypanolytic factor-mechanism, impacts and applications. *Trends in Parasitology*, 26(9):457–464.

Wirtz, E., Leal, S., Ochatt, C., and Cross, G. A. (1999). A tightly regulated inducible expression system for conditional gene knock-outs and dominant-negative genetics in Trypanosoma brucei. *Mol Biochem Parasitol*, 99(1):89–101.

Woods, A., Baines, A. J., and Gull, K. (1992). A high molecular mass phosphoprotein defined by a novel monoclonal antibody is closely associated with the intermicrotubule cross bridges in the Trypanosoma brucei cytoskeleton. *J Cell Sci*, 103 (Pt 3):665–75.

Zhou, X. X. and Lin, M. Z. (2013). Photoswitchable fluorescent proteins: ten years of colorful chemistry and exciting applications. *Curr Opin Chem Biol*, 17(4):682–90.

Ziegelbauer, K., Multhaup, G., and Overath, P. (1992). Molecular characterization of two invariant surface glycoproteins specific for the bloodstream stage of Trypanosoma brucei. *J Biol Chem*, 267(15):10797–803.

Ziegelbauer, K. and Overath, P. (1992). Identification of invariant surface glycoproteins in the bloodstream stage of Trypanosoma brucei. *J Biol Chem*, 267(15):10791–6.

Appendix

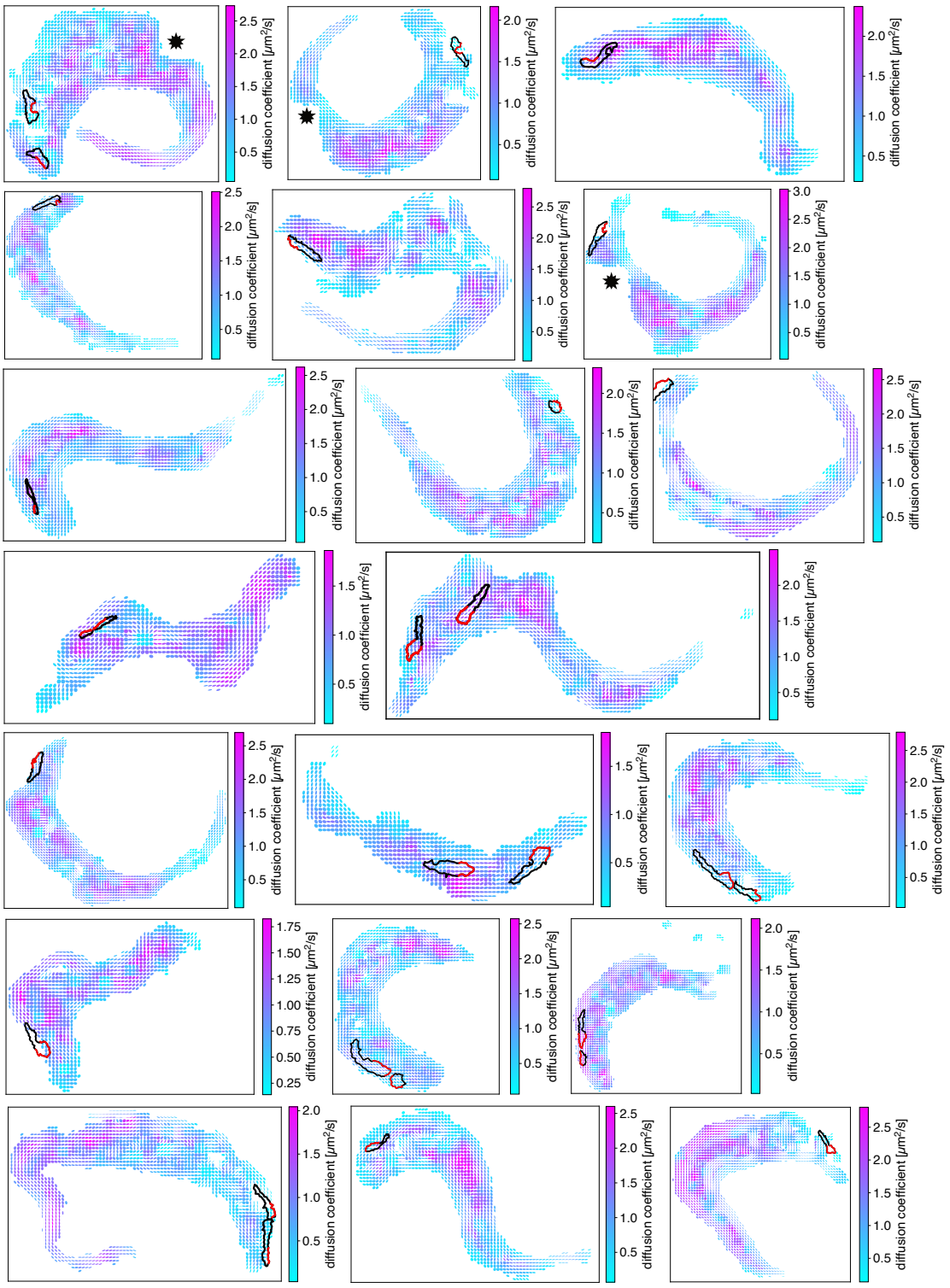

Figure 51: Diffusion maps of VSG dynamics on the 13-90 eYFP::MORN1 cell line. 20 trypanosome surfaces were investigated. The colour code of the ellipses represents the local diffusion coefficient, whereas the shape of the ellipses indicates isotropic (circle) or anisotropic (ellipse) diffusion. The black outline illustrates the position of the hook complex with a red highlighting indicating the part wrapped around the FP neck. Asterisks represent regions outshone by the fluorescence of a TS bead. A superpixel is 0.16 x 0.16 µm.

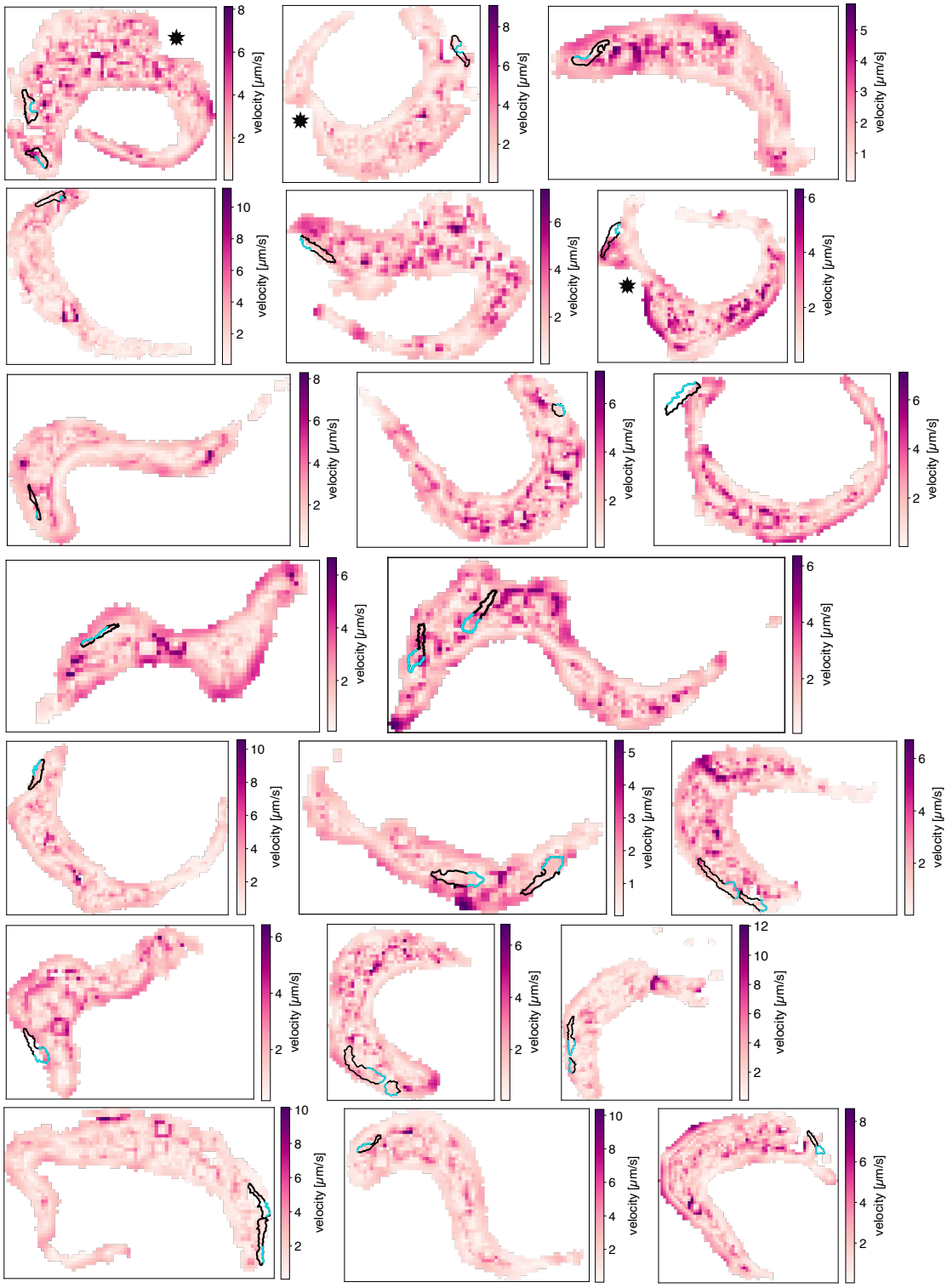

Figure 52: Velocity maps of VSG dynamics on the 13-90 eYFP::MORN1 cell line. 20 trypanosome cell surfaces were examined. The amplitude of local velocities is colour-coded. The outline of the hook complex is shown by a black line with the cyan part highlights the part which is wrapped around the FP neck. Asterisks indicate regions outshone by the fluorescence of a TS bead. A superpixel is 0.16 x 0.16 µm.

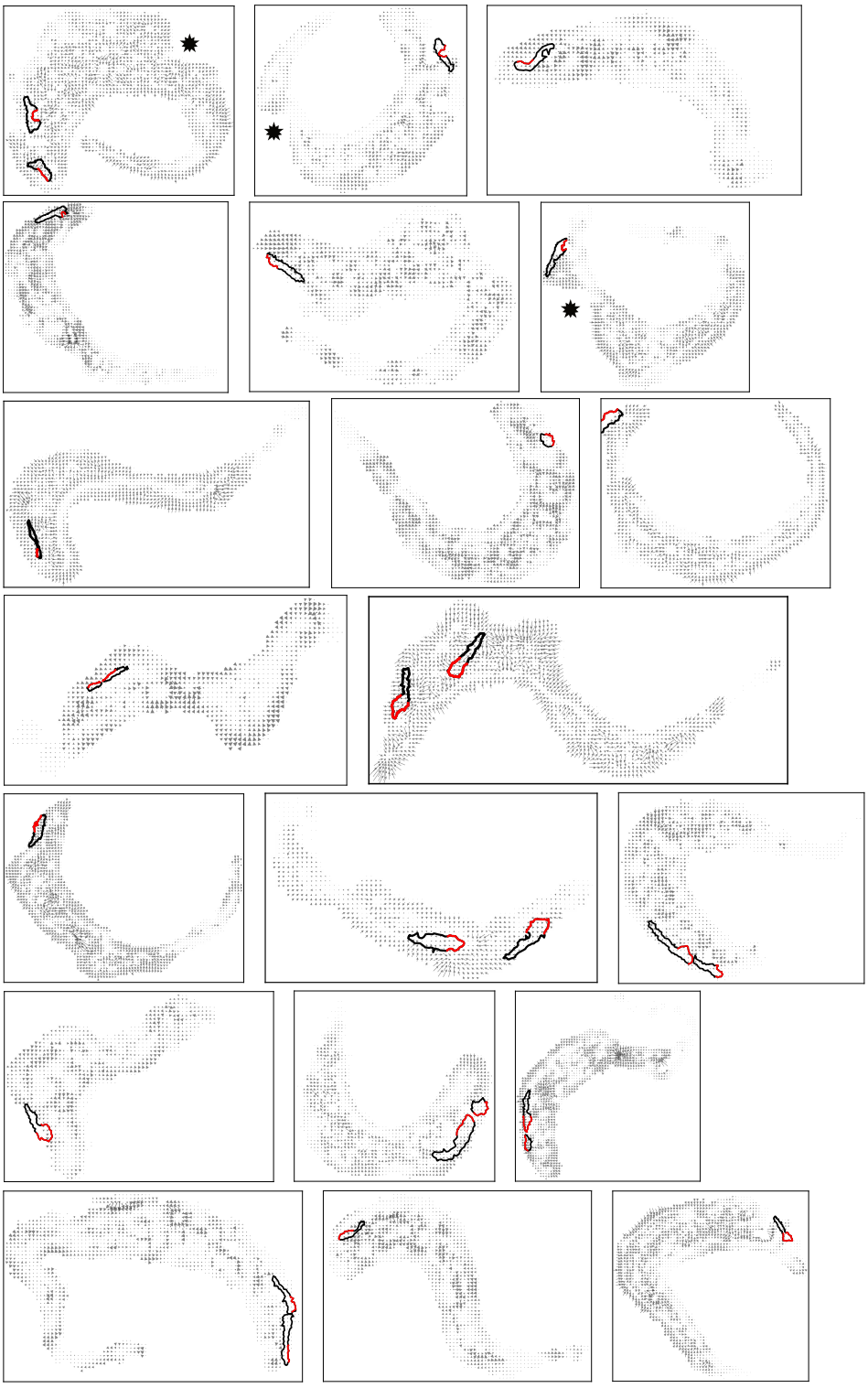

Figure 53: Quiver plots of VSG dynamics on the 13-90 eYFP::MORN1 cell line. Investigation was performed on 20 trypanosomes. Arrows indicate the direction of the local velocities, while the size of the arrows correlate with the with the amplitude of the local velocities. The outline of the hook complex is depicted by a black line with a red part indicating the part wrapped around the FP neck. Asterisks represent regions outshone by the fluorescence of a TS bead. A superpixel is 0.16 x 0.16 µm.

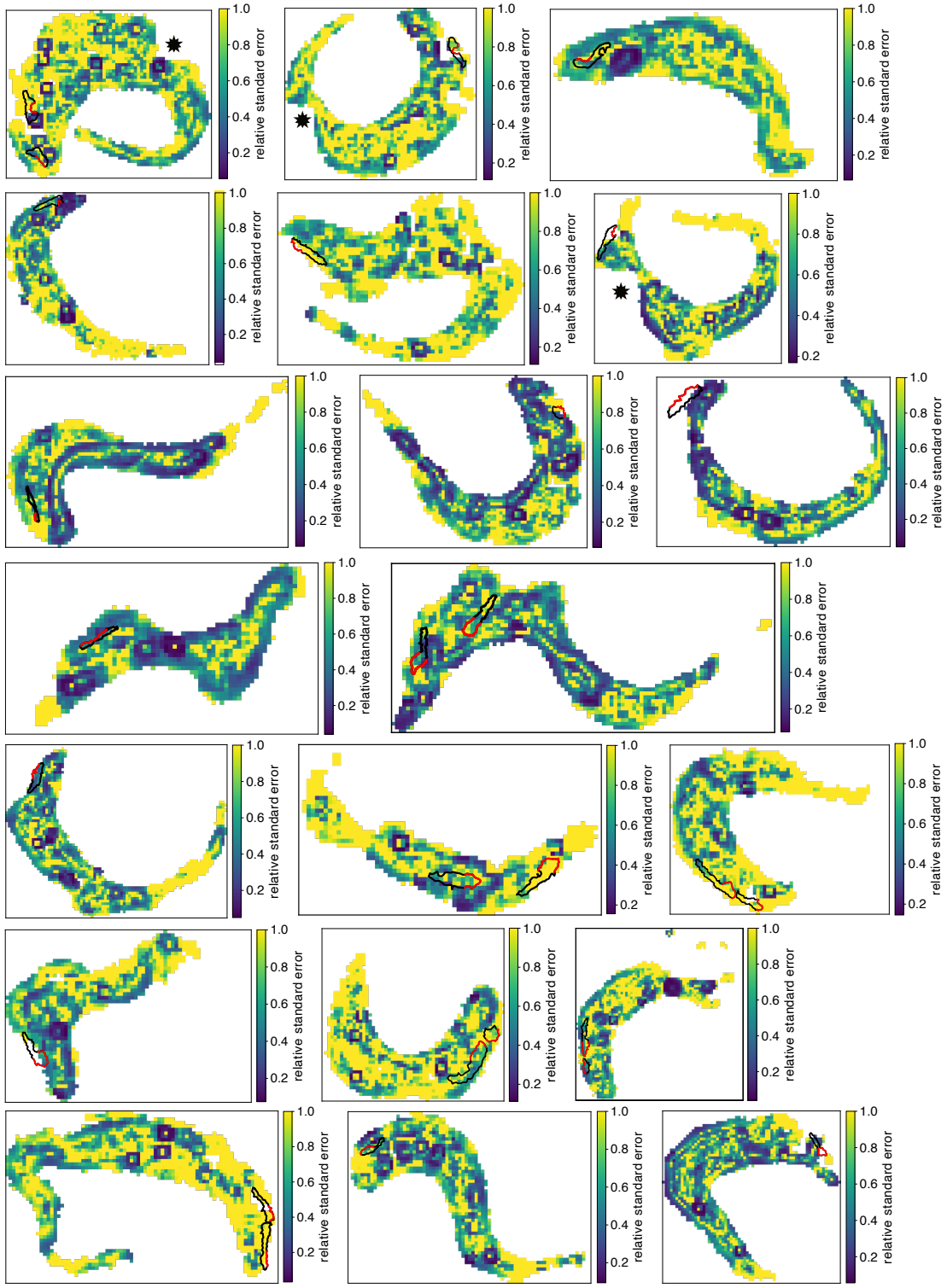

Figure 54: Relative standard error maps of VSG dynamics on the 13-90 eYFP::MORN1 cell line. 20 trypanosomes were analysed. Local relative standard errors in the local velocities are colour-coded. A cut of of the local relative standard errors was set at 1. The black outline with the red highlighting represents the location of the hook complex with the part wrapped around the FP neck. Asterisks indicate the region outshone by the fluorescence of a TS bead. A superpixel is 0.16 x 0.16 µm.

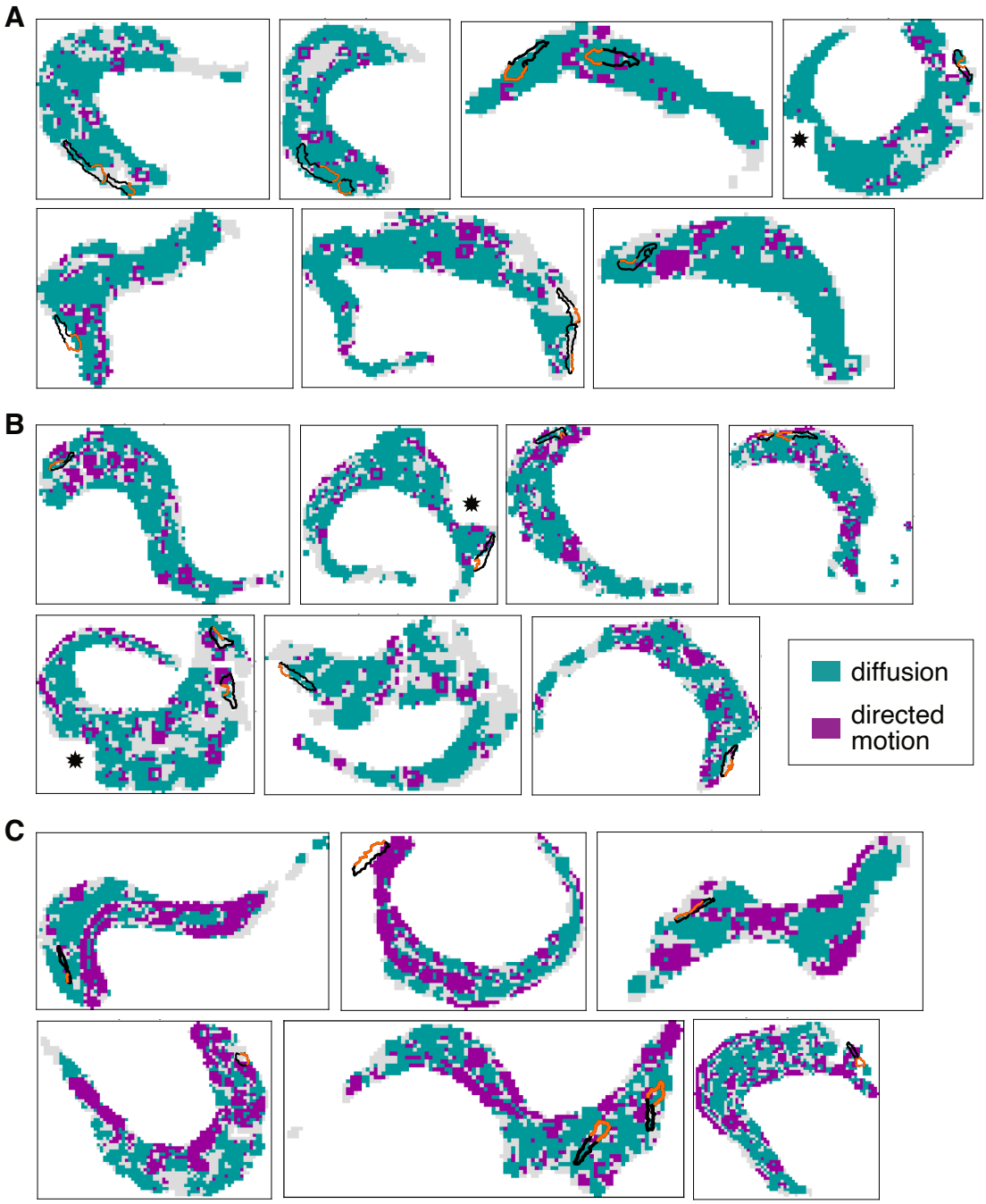

Figure 55: Supermaps depicting the locally dominant motion mode of VSG dynamics on the 13-90 eYFP::MORN1 cell line. A total of 20 trypanosomes were analysed. The colour code indicates the dominant motion mode. Superpixels in green are dominated by diffusion, while superpixels in magenta are dominated by directed motion. Superpixels which could not be assigned are shown in grey. The outline of the hook complex is depicted by a black line, while the part wrapped around the FP neck is depicted in orange. The number of superpixels dominated by directed motion and their arrangement facilitated grouping (A, group 1; B, group 2; C, group 3). Asterisks represent regions outshone by the fluorescence of a TS bead. A superpixel is 0.16 x 0.16 µm.

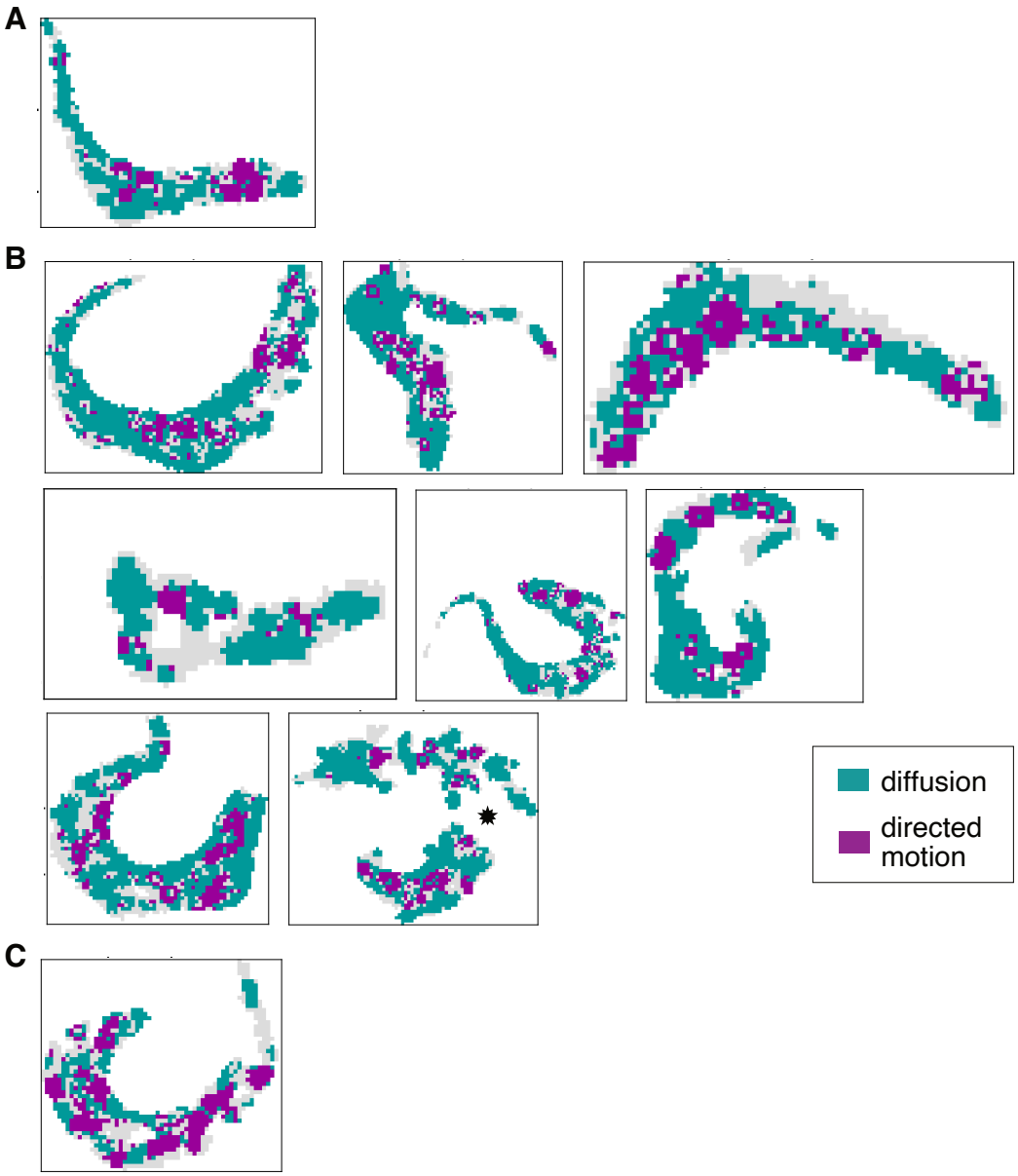

Figure 56: Supermaps illustrating the locally dominant motion mode of VSG dynamics on osmotically swollen trypanosomes. In total 10 trypanosome surfaces were evaluated. The locally dominant motion mode is colour-coded. Green superpixels represent diffusion, magenta superpixels represent directed motion, and grey superpixels could not be attributed. The number of superpixels dominated by directed motion and their arrangement enabled grouping (A, group 1; B, group 2; C, group 3). The asterisk marks a region outshone by the fluorescence of a TS bead. A superpixel is 0.16 x 0.16 µm.

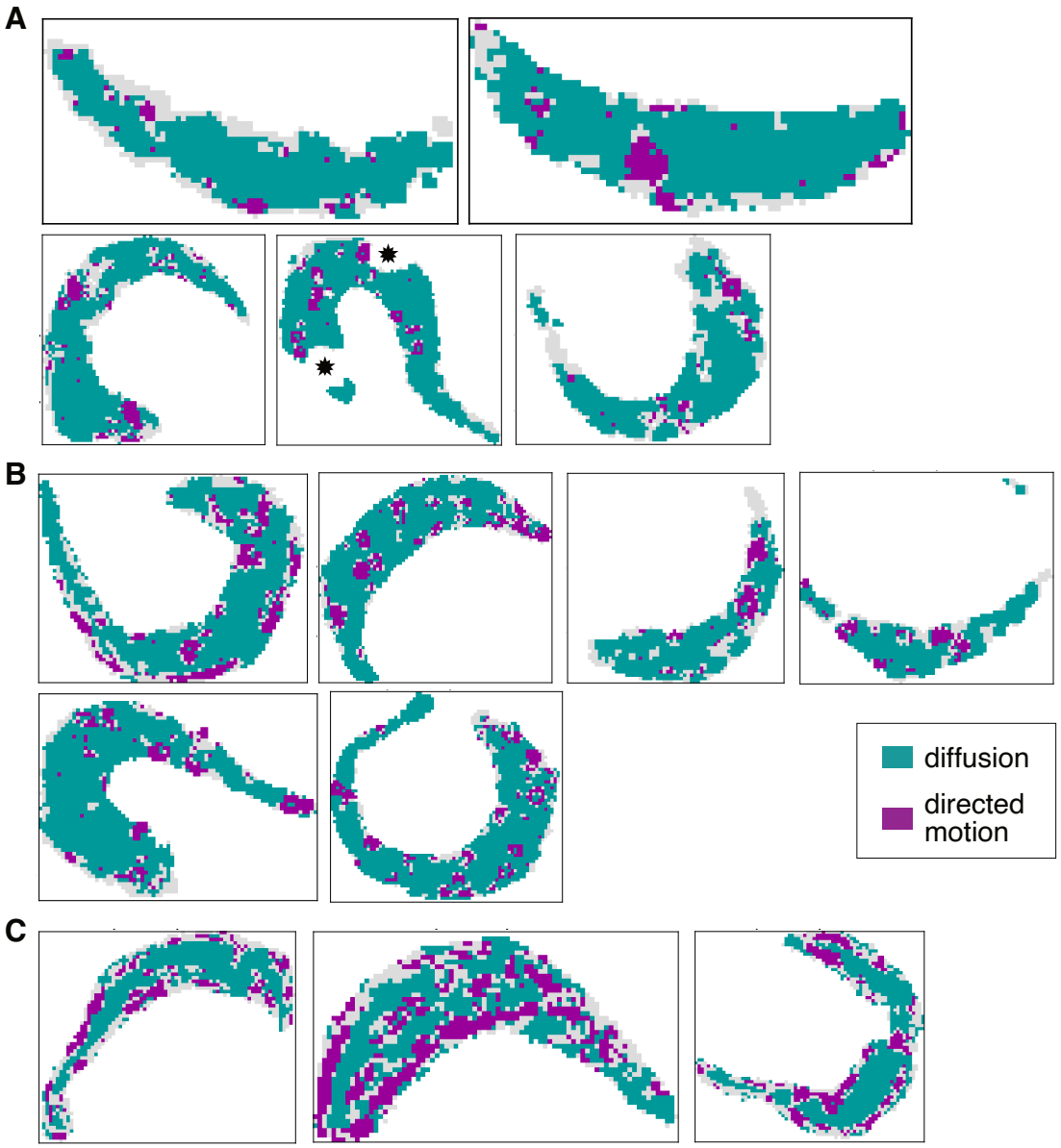

Figure 57: Supermaps depicting the locally dominant motion mode of VSG dynamics on non-induced trypanosomes on the 2T1 WCB RNAi cell line. A total of 14 cells were analysed. The colour code represents the local dominant motion mode. Diffusion is indicated by green, while magenta indicates directed motion. Superpixel in grey could not be assigned. Grouping of the maps was enabled by the number of superpixels dominated by directed motion and their arrangement (A, group 1; B, group 2; C, group 3). The asterisk indicates a region outshone by the fluorescence of a TS bead. A superpixel is 0.16 x 0.16 µm.

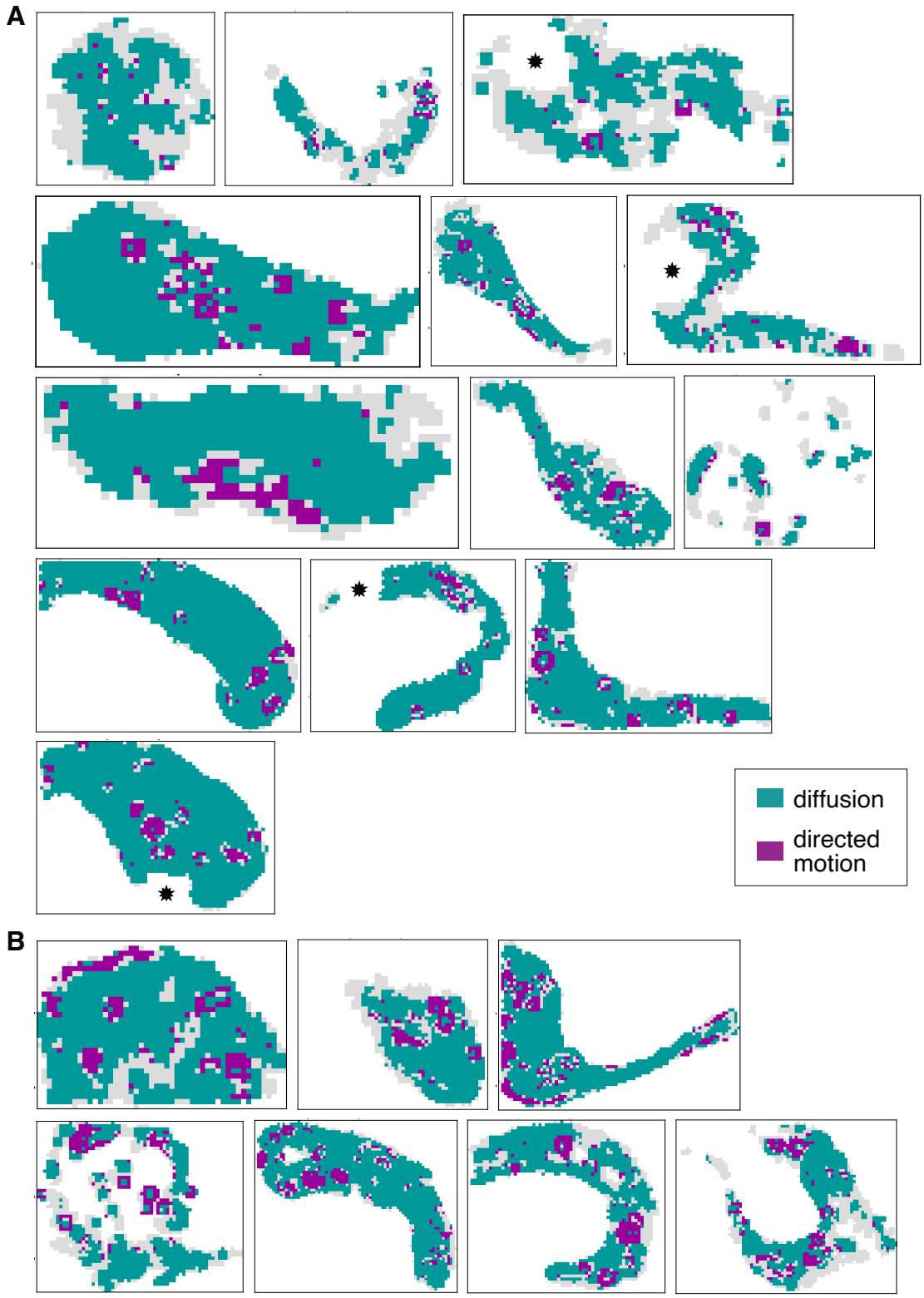

Figure 58: Supermaps illustrating the locally dominant motion mode of VSG dynamics on WCB-depleted trypanosomes. In total 20 cells were evaluated after 24 h of WCB depletion. The colour code shows the local domination motion mode. Green indicates diffusion, magenta indicates directed motion, and grey indicates orphaned superpixels. The number of superpixels dominated by directed motion and their arrangement allowed for grouping (A, group 1; B, group 2; C, group 3). Asterisks represent regions outshone by the fluorescence of a TS bead. A superpixel is 0.16 x 0.16 µm.

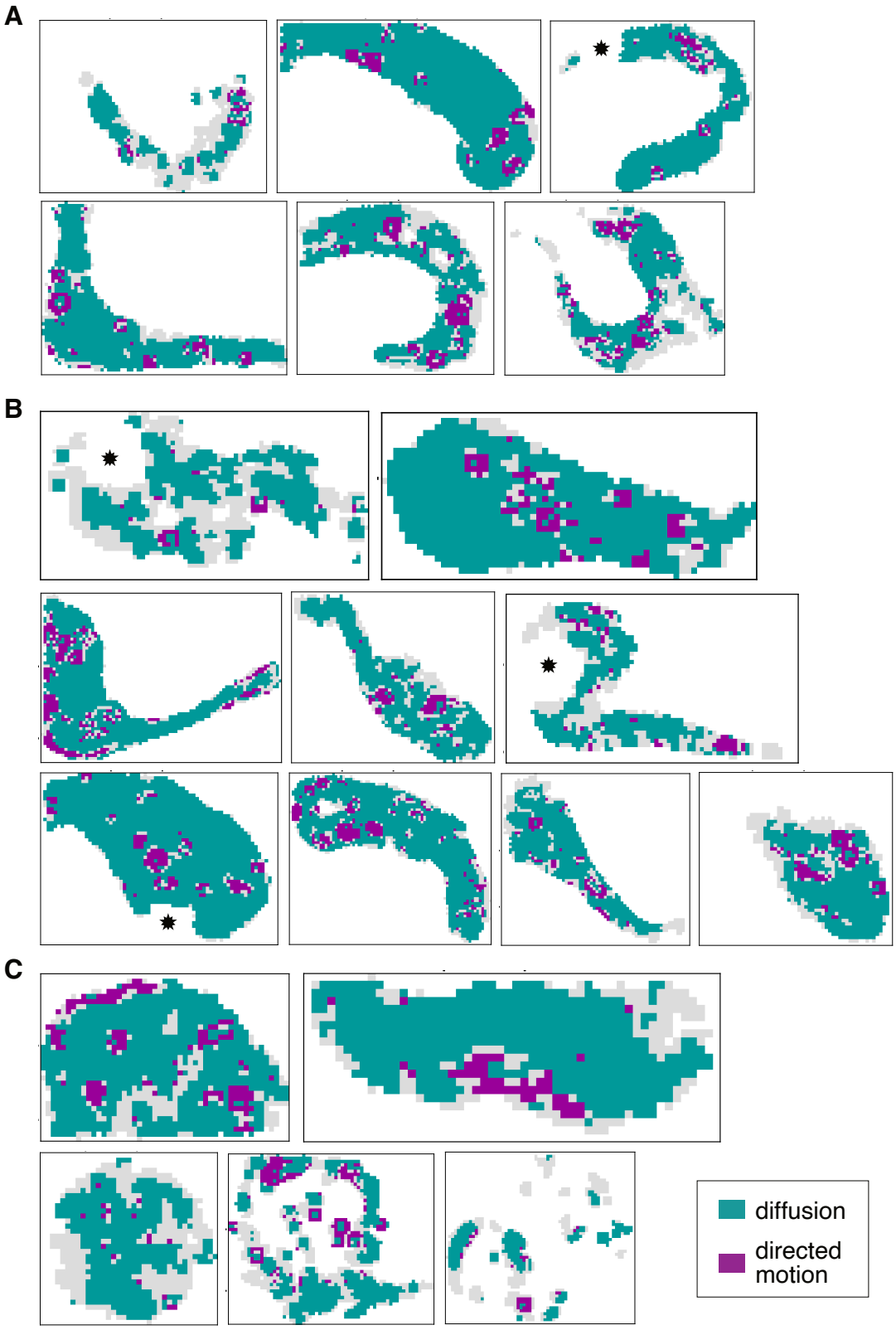

Figure 59: Locally dominant motion mode of VSG dynamics on WCB-depleted trypanosomes in relation to their phenotypes. VSG dynamics were investigated 24 h after WCB RNAi induction. The locally dominating motion mode is colour-coded. Green indicates diffusion, while magenta indicates directed motion. Grey superpixel could not be assigned. The trypanosome surfaces are grouped according to the exhibited phenotype (A, normal; B, posterior swollen; C, round). Asterisks indicate regions outshone by the fluorescence of a TS bead. A superpixel is 0.16 x 0.16 µm.

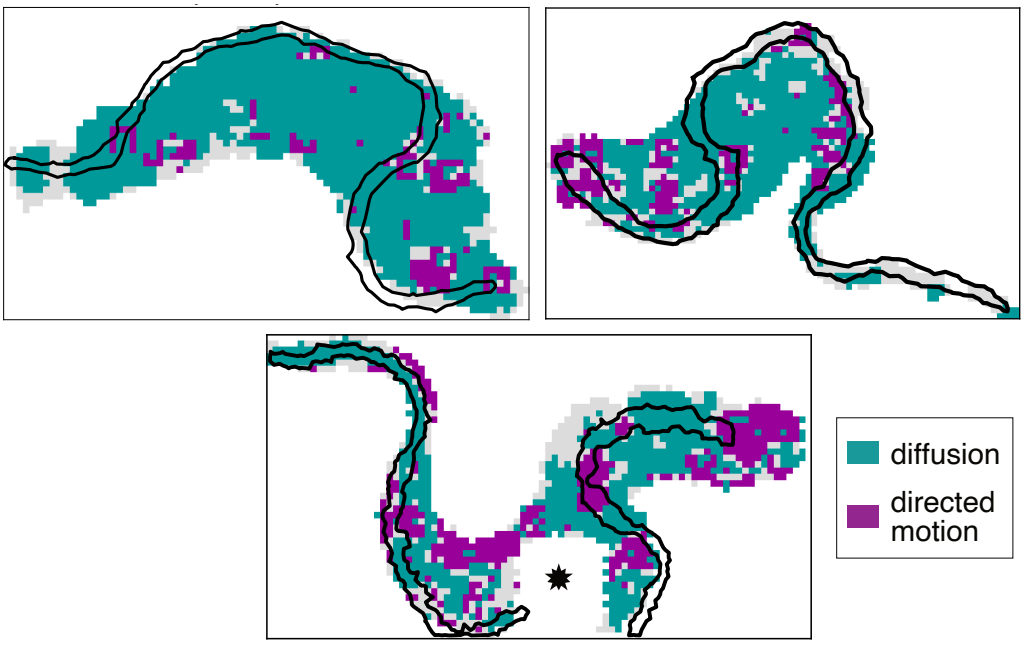

Figure 60: The locally dominant motion mode of VSG dynamics in regard to the flagellum. The colour-code in the supermaps visualise the local dominant motion type. Diffusion is shown in green, and directed motion in magenta. Orphaned superpixels are depicted in grey. The black line indicates the outline of the flagellum. The asterisk marks a region outshone by the fluorescence of a TS bead. A superpixel is 0.16 x 0.16 µm.

List of Abbreviations

&	and
~	approximate
℃	degree Celsius
%	percentage
α	alpha, half-angular of the objective
ε	eccentricity
λ	lambda, wavelength
σ	sigma, localisation precision
Δt	time lag
µm	micrometre
µm/s	micrometre per second
$\mu m^2/s$	square micrometre per second
$1D$	one dimension
$2D$	two dimension
Å	angstrom
ABD	actin binding domain
AOTF	acousto-optic tunable filter
AP	anchored protein
APOL1	apolipoprotein L1
ATP	adenosine triphosphate
BF	bright field
BSF	bloodstream form
C14:0	lipid number, myristic acid
cdf	cumulative density function
CL	cardiolipin
CLEM	correlative light and electron microscopy
CLSM	confocal laser scanning microscopy
CTD	C-terminal domain
D	diffusion coefficient
ddH_2O	double-distilled water
DNA	deoxyribonucleic acid
dyn	dynamic
Dec.	December
dSTORM	direct stochastic optical reconstruction microscopy
e.g.	*exempli gratia*, for example
EMCCD	electron multiplying charge coupled device
EMFM	Einzelmolekül-Fluoreszenzmikroskopie
ER	endoplasmic reticulum
ES	expression site
ESAG4	expression site associated gene 4
et al.	and other
eYFP	enhanced yellow fluorescent protein
FCS	fluorescence correlation microscopy
FOV	field of view
FP	flagellar pocket
FPE region	FP entrance region

FRAP	fluorescence recovery after photobleaching
FWHM	full-width half-maximum
G2 phase	cell cycle phase preceding mitosis
GFP	green fluorescent protein
GPI	glycosylphosphatidylinositol
GT	Geißeltasche
GUVs	giant unilamellar vesicles
h	hour(s)
HA-SH	thiol-functionalised hyaluronic acid
HAT	human African trypanosomiasis
Hz	hertz
IgG	immunoglobulin G
IPC	inositol phosphorylceramide
in situ	on site, in position
ISG	invariant surface glycoprotein
K	kelvin, kinetoplast
kDa	kilodaltons
keV	kiloelectron volt (10^3)
LE	lysosomal endosome
M phase	mitosis
MAP	microtubule-associated protein
MCT	molecular crowding threshold
mg	milligram
min	minute(s)
MITat	Molteno Institut Trypanozoon Antigentype
ml	mililitre
mm	milimetre
mM	millimolar
MORN	membrane occupation and recognition nexus
MSD	mean-squared displacement
MT	microtubule
N	nucleus
NA	numerical aperture
NHS	N-hydroxysuccinimide
nm	nanometre
nM	nanomolar
NTD	N-terminal domain
P(AGE-co-G)	allyl functionalised poly-glycidol
PALM	photoactivated localisation microscopy
PBS	phosphate buffered saline.
PC	phosphatidylcholine
PCF	procyclic form
PCR	polymerase chain reaction
PE	phosphatidylethanolamine
PEG-dithiol	poly (ethylene glycol)-dithiol
PEG-NB	poly (ethylene glycol)-norbornene
PEG-VS	poly(ethylen glycol)-vinyl sulfone
PFR	paraflagellar rod
PG	phosphatidylglyccrol
pH	measure of acidity or alkalinity

PI	phosphatidylinositol, propidium iodide
PLC	phospholipase C
pN	piconewton
PS	phosphatidylserine
PSF	point spread function
px	px
RE	recycling endosome
ROI	region of interest
s	second(s)
S phase	synthesis phase
SE_v	relative standard error
SEM	scanning electron microscopy
shortTrAn	short trajectory analysis
SIF	stumpy inducing factor
SLB	supported lipid bilayer
SM	sphingomyelin
SMFM	single-molecule fluorescence microscopy
SPT	single-particle tracking
SRM	super-resolution microscopy
stat	static
STED	stimulated emission depletion
STORM	stochastic optical reconstruction microscopy
T. brucei	*Trypanosoma brucei*
T. brucei brucei	*Trypanosoma brucei brucei*
T. brucei gambiense	*Trypanosoma brucei gambiense*
T. brcuei rhodesiense	*Trypanosoma brucei rhodesiense*
T. congolense	*Trypanosoma congolense*
T. vivax	*Trypanosoma vivax*
t_{exp}	exposure time
TDB	trypanosoma dilution buffer
TfR	transferrin receptor
TLF	trypanolytic factor
TM	transmembrane
TEM	transmission electron microscopy
TS bead	TetraSpeck™ bead
UTR	untranslated region
UV light	ultraviolet light
vs	versus
VSG	variant surface glycoprotein
v/v	volume per volume
vPBS	'Voorheis' modified PBS

List of Figures

List of Tables

List of publications

Manuscripts related to this PhD thesis:

Schwebs M., Paul T., Glogger M., Forster L., Morriswood B., Teßmar J., Groll J., Engstler M., Kollmannsberger P., Fenz S. Single-molecule fluorescence microscopy reveals fast dynamics of the variant surface glycoprotein coat on living trypanosomes.

Publications that are not part of this thesis:

Leal, A. Z., Schwebs, M., Briggs, E., Weisert, N., Reis, H., Lemgruber, L., Luko, K., Wilkes, J., Butter, F., McCulloch, R., and Janzen, C. J. (2020). Genome maintenance functions of a putative Trypanosoma brucei translesion DNA polymerase include telomere association and a role in antigenic variation. Nucleic Acids Research, 48(17):9660–9680.

Reis, H., Schwebs, M., Dietz, S., Janzen, C. J., and Butter, F. (2018). TelAP1 links telomere complexes with developmental expression site silencing in African trypanosomes. Nucleic Acids Res, 46(6):2820–2833.

Curriculum vitae

Acknowledgement

First of all, I have to express my special gratitude to Susanne Fenz for introducing me to the exciting world of biophysics, programming and single-molecule microscopy. I am very grateful for your enduring support, your ongoing input and our fruitful discussions. My sincere thanks to you for devoting your free time over the past year to continuously support me and Elisabeth!

I also want to thank Philip Kollmannsberger for the fantastic collaboration that made this project possible. I am grateful to you for your input and feedback on a regular basis, and for having me in your group for half a year which gave me the opportunity to expand my programming skills with Python.

My gratitude also goes to Markus Engstler for our regular meetings and all the useful discussions and suggestions. I also appreciated the possibility to come with my questions to your office at any time.

Many thanks to Matthias Weiss for giving me the opportunity to visit your research group in Bayreuth. Also, I would like to thank you for your expertise and advice.

Special thanks also goes to Torsten Paul, who introduced me to the world of Python programming. Working with you was a great pleasure and our discussions broadened my traditional biological way of thinking considerably.

I want to thank Leonard Forster for the excellent and always immediate support regarding any questions about hydrogels as well as for your steady supply of gel components. It was always thrilling to get to know the field of functional materials.

Many thanks to Elisabeth and all the former members of the AG Fenz. To these belong Nico, Katharina, Ivana, Marius and my talented student Paula, who did an excellent work and contributed to this project. I would like to thank you all for the enjoyable working atmosphere, the interesting discussions, but also for our tea breaks and cooking sessions. You have grown very dear to my heart.

I also want to express my appreciation to the current and previous members of the Department for Cell and Developmental Biology. Thank you for your support. It was a wonderful time in a great working atmosphere in which colleagues also became friends! I would especially like to thank Reinhild, Kathrin, Elisabeth, Silke, Elina, Lydia, Uli and Manu. You keep the business running and make sure that everything runs smoothly. I would also like to express my greatest thanks to Patrick. In the last years, you have not only once helped me out of a technical misery!

I would also like to thank the *Graduate School of Life Sciences* for providing a structured PhD programme and the opportunity to participate at diverse workshops and conferences.

Außerdem möchte ich mich bei meinen Freunden bedanken. Ihr habt vor allem in unserer gemeinsamen Freizeit für den nötigen Ausgleich gesorgt!

Ein außerordentlicher Dank geht auch an meinen Freund Christian. Mit deiner Liebe und deinem Humor, der mich immer zum Lachen bringen kann, sowie deiner ausgeglichenen Art hast du mir viel Energie und Ausdauer verliehen. Ich freue mich sehr auf unseren neuen gemeinsamen Abschnitt in München.

Zu guter Letzt möchte ich mich bei meiner Familie und ganz besonders bei meinen Eltern und meiner Schwester bedanken. Eure niemals endende Unterstützung ist die Basis für alles was ich heute erreicht habe. Ich bin euch unendlich dankbar!